DIGITALCOMMONS
@WAYNESTATE

Wayne State University

Wayne State University Dissertations

1-1-2015

Investigation Of New Ligand Architechtures Towards Proton And Water Reduction Catalysis By Cobalt Complexes

Debashis Basu
Wayne State University,

Follow this and additional works at: http://digitalcommons.wayne.edu/oa_dissertations

 Part of the Chemistry Commons

Recommended Citation
Basu, Debashis, "Investigation Of New Ligand Architechtures Towards Proton And Water Reduction Catalysis By Cobalt Complexes" (2015). *Wayne State University Dissertations.* Paper 1284.

This Open Access Dissertation is brought to you for free and open access by DigitalCommons@WayneState. It has been accepted for inclusion in Wayne State University Dissertations by an authorized administrator of DigitalCommons@WayneState.

www.manaraa.com

INVESTIGATION OF NEW LIGAND ARCHITECTURES TOWARDS PROTON AND WATER REDUCTION CATALYSIS BY COBALT COMPLEXES

by

DEBASHIS BASU

DISSERTATION

Submitted to the Graduate School of

Wayne State University,

Detroit, Michigan

In partial fulfillment of the requirements

for the degree of

DOCTOR OF PHILOSOPHY

2015

MAJOR: CHEMISTRY (Inorganic)

Approved by:

_____

Advisor Date

_____

_____

_____

www.manaraa.com

© COPYRIGHT BY

DEBASHIS BASU

2015

All Rights Reserved

www.manaraa.com

DEDICATION

This thesis is dedicated to my fiancée Sudeshna Ganguly for her patience, love, and affection towards me during the period of this study.

www.manaraa.com

ACKNOWLEDGEMENTS

I would like to acknowledge my advisor Prof. Cláudio N. Verani for his supports, guidance, encouragement, and patience. One of the major limitations from my side was my lab and computer skills, which got greatly improved after I joined the Verani Lab. In spite of my limited lab and computer skills, Professor Verani was very patient, supportive and encouraging in guiding me towards the right direction, which gave me tremendous amount of confidence to pursue lab work with much more efficiency. His leadership quality, knowledge, hardwork, passion, tenacity, and enthusiasm motivate me constantly to perform my research studies effectively. During my 6 years stay in the lab, he encouraged and supported me financially to go and participate in several regional, national, and international conferences and symposia, which helped to improve my presentation skills and to make connections with several people in the field. Professor Verani helped me a great deal in improving my writing skills during the manuscript preparation period of my publications. Moreover, he also encouraged me to work with several research collaborators to advance my research to a more refined level. Professor Verani is not only an excellent scientist but also a great human being. He is a very understanding man and he helps his students a great deal in difficult times. Moreover, he is a well-rounded person with interest in science, archeology, space, arts, and music.

I would also like to thank my dissertation committee members, Professor Stephanie Brock, Professor Zhongwu Guo, and Dr. Karen Mulfort for their valuable suggestions during various parts of my Ph.D study.

Strong collaborations are one of the fundamental aspects of interdisciplinary research and I acknowledge and thank Professor H. Bernhard Schlegel for maintaining a very strong collaboration between the Verani and the Schlegel lab. Dr. Shivnath Mazumder and Xuetao Shi

www.manaraa.com

(Sam) are especially appreciated for running most of the DFT calculations and critically analyze relevant results. Dr. Marco M. Allard is also recognized for running calculations for cobalt-phenolate based systems. Prof. John F. Endicott is acknowledged for insightful discussions. Dr. Karen Mulfort and Dr. Anushree Mukherjee from ANL are acknowledged for running transient absorption spectral measurements. Dr. Lew Hryhorczuk, Dr. Yuri Danylyuk, and Nicole Lenca are acknowledged for running mass spectral analysis for several samples. Dr. Mary J. Heeg, Dr. Philip D. Martin, Mr. Kenneth K. Kpogo, and Mr. Habib Baydoun from the Department of Chemistry, Wayne State University and Dr. Richard Staples from the Department of Chemistry, Michigan State University are greatly appreciated for solving X-ray structures. Dr. Zhi Mei is acknowledged for SEM measurements. I would also like to thank Dr. Bashar Ksebati for training me for the NMR instruments. Dr. Oleg Poluektov and Dr. Jens Niklas from ANL are acknowledged for running EPR experiments and critically assign the peaks.

I would like to thank Dr. Regina Zibuck, Dr. Michael Maguire, and Dr. Maryfrances Barber with whom I taught CHM 1250 and CHM 1220/1225 as a teaching assistant in my first two years of study. Dr. Barber is also acknowledged for providing the orientation for the international students to prepare us for the speak test etc.

I would like to acknowledge Melissa Burton for being super organized and helped in every academic related matter. Debbie McCreless is appreciated for all her help with the administrative and financial matter. Nestor Ocampo is acknowledged for handling and solving computer related issues. The science store staff especially Elizabeth Ries and Gregory Kish are acknowledged for all the help regarding the buying of chemicals and other store matter.

I would like to thank Wayne State University for offering me the teaching assistantship position for the first two years of my study. I would also like to thank Department of Energy

www.manaraa.com

(DOE) for providing the necessary funding for my research and salary from the Division of Chemical Sciences, Geosciences, and Biosciences, Office of Basic Energy Sciences of the U.S. Department of Energy (DOE-BES) through the SISGR-Solar Energy Program (Grant DE-FG02-09ER16120 and DE-SC0001907). This funding also helped us to go to various regional (Ohio Inorganic Weekend), national (ACS National meeting in Indianapolis, IN), and international (ISPPCC, Traverse city) conferences.

Life would be tough without the great Verani lab members. Among the seniors, first and foremost, I would like to give a big thanks to Dr. Rajendra Shakya for teaching me all the basic experimental skills required for organic and inorganic synthesis. Dr. Shakya's presence in the lab brought good work ethics as well as good working environment. Dr. Fernando R. Xavier is remembered for the kinetics, spectroscopic, and electrochemical expertise as well as for his cheerful behavior and friendly nature. Dr. Marco M. Allard is acknowledged for sharp chemistry knowledge along with never-ending hour-long scientific discussions. Dr. Frank Lesh is appreciated for the hardworking nature, strong work ethics, and organizing capability. Dr. Rama Shanmugam is remembered for her friendly nature coupled with great technical knowledge about various instruments.

Among my contemporaries, Dr. Dakshika Wanniarachchi, Dr. Dajena Tomco, and Dr. Lanka Wickramasinghe are greatly appreciated and remembered. Dakshika is one of the best physical chemists I have ever seen who establishes water oxidation techniques almost single-handedly. Apart from that, we also worked together as a team to establish proton reduction methodology. An acute physical chemistry background along with hardworking capability was the major strengths of Dakshika. Dajena was one of the very few students who have very strong biological chemistry background in our lab. Dajena will be remembered for her passionate and

www.manaraa.com

logical approach towards science along with her cheerful and friendly nature. Lanka has a very calm and hardworking approach towards solving any problem and will be remembered for her tenacity and dedication towards science. Ryan Thomas is another contemporary of mine. Ryan will be remembered for his physical and analytical chemistry knowledge along with friendly and supportive nature.

Among my juniors, Sunalee Gonawala is recognized for her hardworking and organized nature. Habib Baydoun, Kenneth K. Kpogo, and Brittany M. Venglarcik are the three young bloods in the lab. Habib is gifted with great physical inorganic conceptions coupled with good holistic knowledge of science. Kenneth is a hardworking chap with lot of potentials in synthesis and separation techniques. Brittany is very organized girl and more inclined towards teaching. Pavithra Hettiarachchi and Danushka Ekanayake are in their initial years of study and already started showing promises. Nour is a first year student, just joined our lab few weeks ago, and she seems to be a very intelligent girl.

I would like to acknowledge three very hardworking undergrads Joe, Milan, and Grace who worked with me in various parts of my graduate study.

I would like to thank Dr. Verani's wife Priscilla and daughter Clara for being so nice and kind. We have several gatherings in their house and they are always very warm and hospitable.

I would like to acknowledge my families back in India. Life would be difficult without their constant support and encouragement. I thank them to have trust on me and for all the love, hard work, and sacrifice they made for me.

I also like to thank my sweetheart Sudeshna Ganguly for being so nice, lovely and encouraging. Life would not be the same without her.

I would also like to thank all my friends back in home and in here for constant support.

www.manaraa.com

TABLE OF CONTENTS

www.manaraa.com

LIST OF TABLES

www.manaraa.com

www.manaraa.com

LIST OF FIGURES

www.manaraa.com

www.manaraa.com

www.manaraa.com

www.manaraa.com

www.manaraa.com

www.manaraa.com

www.manaraa.com

www.manaraa.com

www.manaraa.com

www.manaraa.com

www.manaraa.com

LIST OF SCHEMES

www.manaraa.com

CHAPTER 1

INTRODUCTION

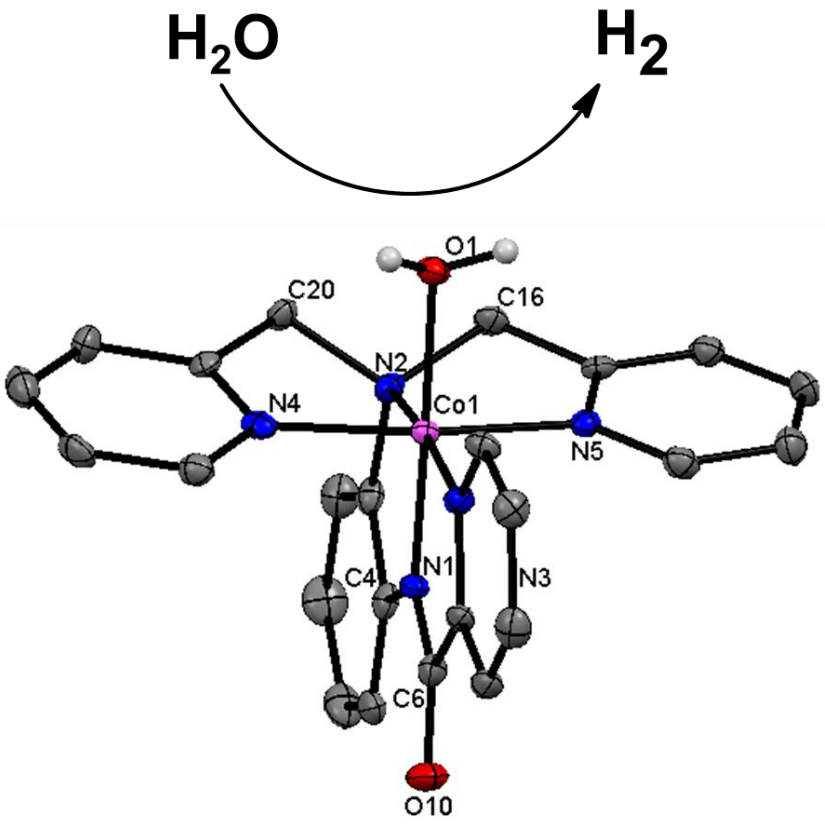

www.manaraa.com

CHAPTER 1

INTRODUCTION

1.1.1 Hydrogen as an Alternative Energy Source

One of the main energy sources for the world population is non-renewable fossil fuels which will be depleted within the next hundred years.[1] Existing fossil fuel sources such as natural gas and coal generate carbon dioxide as a byproduct after usage. Thus, increased CO_2 emissions (**Scheme 1.1**) are responsible for the massive climate changes observed in the last century. The looming energy crisis resulting from this continuous depletion, along with the rapid increase of carbon dioxide in the atmosphere have driven extensive research for obtaining carbon-neutral energy from affordable and abundant sources.[1]

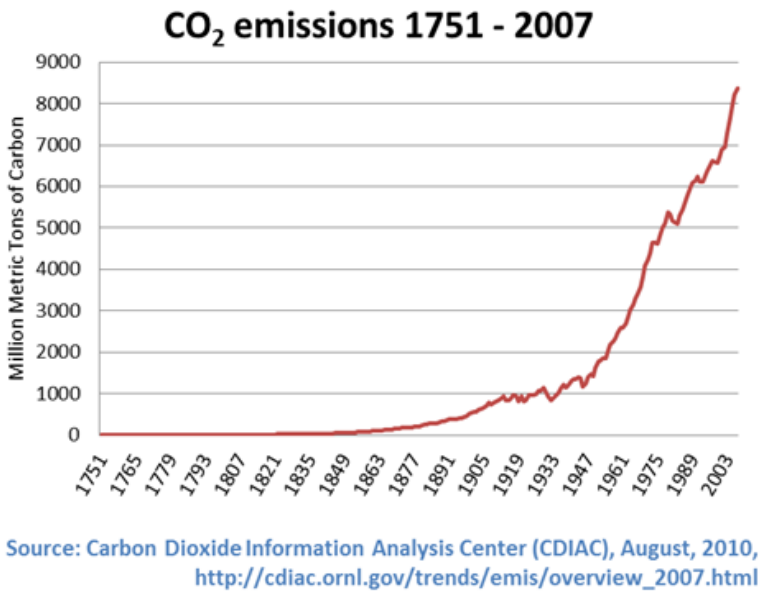

http://www.globalissues.org/article/233/climate-change-and-global-warming-introduction

Scheme 1.1. CO_2 emmisions over the last few hundred years.[1]

Therefore, there is a demand to develop renewable energy sources that will reduce CO_2

www.manaraa.com

emissions. Dihydrogen (H_2) is expected to be a clean and sustainable energy source to meet the ever increasing global energy requirements, while addressing concerns over climate change.[1] Hydrogen is the lightest and the most abundant element in Earth's crust, but is not found in the pure gaseous form instead appear with other elements in various hydrocarbons and water. Gaseous dihydrogen can be generated by either methane reforming or water electrolysis reactions, respectively.

$$\mathbf{CH_4 + H_2O \rightarrow CO + 3\ H_2}\ \textbf{(reforming)}$$

$$\mathbf{2\ H_2O(}\boldsymbol{l}\mathbf{) \rightarrow 2\ H_2(}\boldsymbol{g}\mathbf{) + O_2(}\boldsymbol{g}\mathbf{)}\ \textbf{(electrolysis)}$$

Dihydrogen is capable of generating energy with net zero pollution,[1] thus it is suitable as an alternative energy source. Hydrogen can also be used in many energy-related applications, such as in fuel cells to react with oxygen to generate water and electrical energy.[1] Water can then be recycled for general purposes such as drinking or bathing and also to regenerate hydrogen. The use of hydrogen as fuel has been found in many practical applications as in many hybrid cars. Water is an affordable and abundant source of hydrogen and in order for hydrogen to have practical economical use as a fuel, it has to be generated from such a source. However, two potential challenges are present regarding the use of hydrogen: (i) the efficient generation, and (ii) the proper storage. Therefore, several research groups are investigating efficient hydrogen generation by splitting water. On the other hand, the effective storage of hydrogen is challenging.[2] Several labs have designed and synthesized metallo-organic frameworks (MOFs) with appropriate pore size to store hydrogen.[2] We will not discuss storage in detail, but several reviews have addressed the issue.[2]

www.manaraa.com

1.1.2 Water Splitting to Generate Dihydrogen

Water is a widely available and an affordable potential source of dihydrogen. Thus, there is extensive ongoing research towards splitting water efficiently into its constituents, hydrogen and oxygen gas. Water splitting is a difficult process because of its thermodynamic limitations and multielectronic nature.[3] Electronically there are two steps in water splitting, namely, (i) a four electron oxidation of water to generate oxygen and proton and (ii) a two electron reduction of protons (H^+) to generate hydrogen gas. To achieve effective water splitting, it is necessary to understand the electronic processes governing water oxidation and proton reduction. Equations 1 and 2 summarize these steps.

$$2\ H_2O \longrightarrow O_2 + 4\ H^+ + 4\ e^- \quad (1) \quad E^0\text{: -1.23 V vs. SHE}$$

$$4\ H^+ + 4e^- \longrightarrow 2\ H_2 \quad (2) \quad E^0\text{: 0 V vs. SHE}$$

Both of these steps are energy-demanding due to the uphill nature of the reactions. Thermodynamically, water can be oxidized to dioxygen at -1.23 V, whereas protons can be reduced to hydrogen at 0 V vs. the standard hydrogen electrode (SHE) at pH zero and 25°C. Therefore, the overall water splitting process requires E^0 of -1.23 V, making the free energy change (ΔG) positive for the reaction. Thus, the splitting of water to hydrogen and oxygen involves 56.64 kcal/mol of energy and is thermodynamically unfavorable (**Scheme 1.2**).[1] Water oxidation involves multiple proton-coupled electron transfers (PCET) combined with the O-O bond formation, making this whole process fairly complicated. On the contrary, green plants oxidize water to dioxygen efficiently in Photosystem-II, exploiting a multimetallic [Mn_4Ca] cluster.[4] Hydrogen is commercially produced from natural gas instead of water due to the energy requirements associated with the process. On the contrary, [FeFe] and [FeNi] hydrogenase can reduce protons to dihydrogen very efficiently.[5]

www.manaraa.com

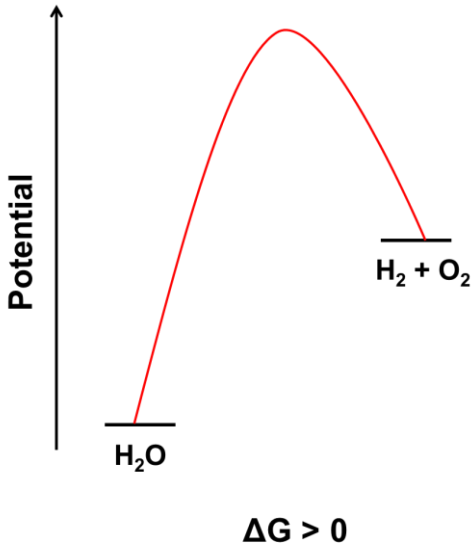

Scheme 1.2. Schematic diagram of the Gibbs free energy change (ΔG) involved with water splitting.

1.1.3 Generation of Hydrogen from Water in Nature

Despite the thermodynamic limitations associated with the water splitting process, green plants are able to split water to oxygen and hydrogen gas very efficiently. In the Photosystem-II, sunlight induces initial electron transfer from a chlorophyll photosensitizer to the quinone electron acceptor through a tyrosine redox-mediator and generates a positive hole in the photosensitizer. This hole can be subsequently transferred to the multimetallic [Mn_4Ca] catalytic center by further electron transfer (**Scheme 1.3**). Multiple electron transfers from the catalytic site can generate high-valent manganese species which can act as the active species for water oxidation catalysis. Subsequent formation of two high-valent manganese-oxo species followed by oxygen generation is the typical pathway of operation.[4] The difficulties of multiple proton-coupled electron transfer steps combined with O-O bond formation are overcome by the use of multimetallic centers and redox mediators coupled with sequential electron transfer in the right direction.[4]

www.manaraa.com

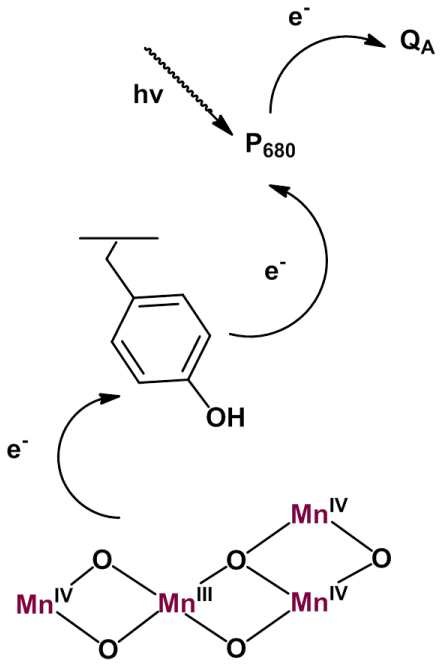

Scheme 1.3. Simplified schematic representation of electron transfer processes between different components of the Photosystem-II. It is adapted from reference 4b.

On the other hand, [FeFe] and [NiFe] hydrogenase enzymes are capable of reducing protons to hydrogen at low overpotentials through multistep pathways.[5] These bimetallic active sites typically contain sulfur-bridged iron-iron or iron-nickel clusters coordinated with carbon monoxide or cyanide ligands. An adjacent electron donor or redox mediator such as ferridoxin (Fe_4S_4 cluster) is typically bound with the active site (**Figure 1.1**). Sequential electron transfer to the metal and the ligand centers (ferridoxin) coupled with amine nitrogen induced hydrogen-bridged pathway generates the active species, which subsequently produces hydrogen. There are typically three kind of hydrogenases: [FeFe], [NiFe] and [Fe]-only.[5] In general, [FeFe] hydrogenase works better than [NiFe] hydrogenases in terms of hydrogen production activity. One such example of [FeFe] hydrogenase is found in clostridium pasteurianum bacteria, where it can generate hydrogen from water with a massive 10,000 s^{-1} turnover frequency (TOF).[5]

www.manaraa.com

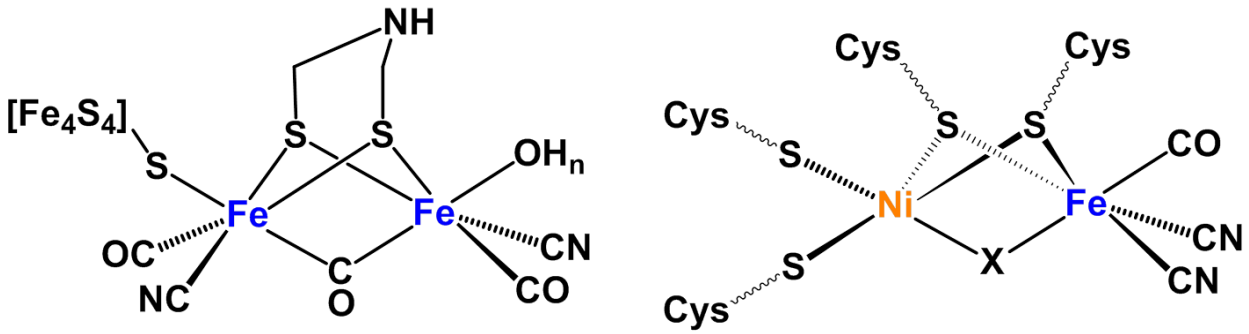

Figure 1.1. Simple schematic representation of active sites for [FeFe] and [FeNi] hydrogenase.

1.2.0 Biomimetic Proton Reduction Catalysis

The Verani group is interested to study the second step of the water splitting process, namely proton reduction, in more detail due to our interest in the hydrogen fuel formation reaction. Several research groups have tried to mimic the active site of [FeFe] and [NiFe] hydrogenase by using synthetic inorganic chemistry. Darensbourg,[6] Rauchfuss,[7] Sun,[8] and Artero[9] are the key players in the field of mimicking the hydrogenase active sites for proton reduction activity. In general, researchers have tried to synthesize the active site of the complex which contains either [FeFe] or [FeNi] centers bridged by thiolate units. The coligands are typically carbon monoxide or cyanide, which ensure a low-spin configuration of the metal ions, and therefore less lability in the active center formed primarily by soft systems. A proton source such as NH was often incorporated in the ligand framework to serve as a proton relay by this moiety. Multiple variations of these complexes were made by changing the coligands from cyanide to phosphine or the bridging unit from thiolate to dithilone.[6-9] Various [FeFe], [FeNi], [Fe], and [Ni] complexes were synthesized and although several groups have succeeded in mimicking the active site of hydrogenase (**Figure 1.2**), the catalytic activities of the biomimetic complexes are considerably lower than those in the actual enzymes. Nonetheless, incorporation of such

www.manaraa.com

biomimetic complexes into micelles or dendrimers improved the catalytic activity to a great extent.

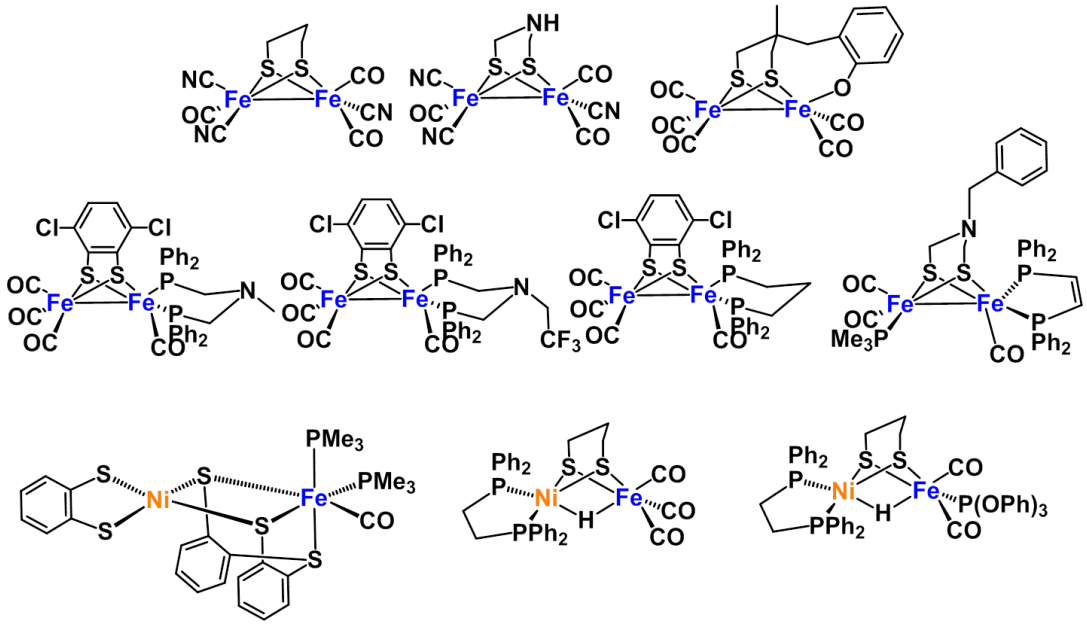

Figure 1.2. Biomimetic synthetic model complexes of [FeFe] and [NiFe] hydrogenases.

1.3.0 Types of Proton and Water Reduction Catalysis

In general, there can be four different categories for such catalysis.[10]

A) **Electrocatalytic proton reduction:** Proton reduction in non-aqueous solvents with a catalyst by using an organic acid. A particular potential is applied electrochemically to generate the active species from the catalyst, which can start the catalytic cycle and eventually generate hydrogen.

B) **Photocatalytic proton reduction:** Proton reduction in non-aqueous solvents with a catalyst in the presence of an organic acid and a photosensitizer under photocatalytic conditions. Here a particular wavelength of light excites the photosensitizer, which then transfers an excited state electron to the catalyst, thus generating the active species which will generate hydrogen from the organic acid. This photosensitizer can be present in

www.manaraa.com

solution as an independent complex or as a subunit in a heterometallic scaffold containing the catalyst and the photosensitizer. There are some advantages associated with strongly coupled heterometallic complexes that may favor catalytic activity, but the synthetic complexity of such systems continues to be an impediment.

C) **Electrocatalytic water reduction:** In contrary to the process with organic acids in non-aqueous solvents which is expensive, water is an affordable and abundant source of protons. In this category neutral water is reduced to generate hydrogen. A fixed potential is applied electrochemically to generate the active species from the catalyst, which will start the catalytic cycle and generate hydrogen.

D) **Photocatalytic water reduction:** Water reduction in the presence of the catalyst and photosensitizer under photocatalytic conditions. Monochromatic light excites the photosensitizer, which will transfer an excited state electron to the catalyst, thus generating the active species, which will generate hydrogen from neutral water. The photosensitizer can be present in the same or as an independent molecule.

1.4.0 Important parameters for proton/water reduction electrocatalysis

There are a few important parameters[10] relevant to proton and water reduction electrocatalysis. Those parameters are listed and discussed below.

A) **Overpotential (η)**: The excess potential required to generate hydrogen from an acid source in comparison with the thermodynamic potential for hydrogen generation, as shown in equation 3.

$$\boldsymbol{\eta} = E_{p/2} - E^{0}_{HA/H2} \qquad (3)$$

$E_{p/2}$: experimental potential for H_2 generation; $E^{0}_{HA/H2}$: standard thermodynamic potential for H_2

www.manaraa.com

generation. A good catalyst should have a low overpotential for hydrogen generation. For water reduction, researchers generally use the "onset" overpotential (the potential from where the catalytic peak starts to increase) instead of regular overpotential due to the ill-behaved nature of the cyclic voltammogram.

B) $\mathbf{k_{obs}}$: Experimental rate constant for hydrogen generation, as shown in equation 4.

$$i_c/i_p = n/0.4463\sqrt{RT\mathbf{k_{obs}}/F\nu} \quad (4)$$

i_c: peak current in the presence of catalyst; i_a: peak current in the absence of catalyst; n: number of electrons transferred to generate one equivalent of hydrogen; R: universal gas constant; T: temperature; F: Faraday constant; ν: scan rate; high k_{obs} indicates faster rate of hydrogen generation.

C) **Turnover number (TON)**: The number of moles of hydrogen generated per mole of catalyst used, as shown in equation 5.

$$\mathbf{TON} = n_{H2}/n_{cat} \quad (5)$$

n_{H2}: The number of moles of hydrogen after bulk electrolysis; n_{cat}: The number of moles of catalysts used for bulk electrolysis.

The TON assesses the overall stability of the complex. The higher the TON, the more stable the catalyst is.

D) **Faradaic efficiency (FE)**: The ratio between numbers of moles of hydrogen generated and half of the charge passed during the bulk-electrolysis experiment, as shown in equation 6.

$$\mathbf{FE} = [(n_{H2})/(Q/2)] \quad (6)$$

n_{H2}: The number of moles of hydrogen generated after bulk electrolysis; Q: The amount of charge passed during the bulk electrolysis experiment.

www.manaraa.com

The Faradaic efficiency is a measure of how much of the total catalytic species is involved in actual catalysis with respect to other bimolecular pathways. A Faradaic efficiency of 100% indicates that the catalyst is only involved in one pathway of electron transfer reaction, namely to generate hydrogen. A good catalyst should present Faradaic efficiencies of 80-100 %.

1.5.0 First-row Transition Metal Complexes for Proton and Water Reduction

Molecular systems containing affordable Earth-abundant transition metals capable of electro-catalytic proton reductions have attracted attention due to the potential improvement in catalytic performance through rational design. Theoretically, the generation of a two-electron reduced species from a metal-complex at a proper potential can generate an active species capable of reducing protons to dihydrogen while oxidizing back to the parent state. Platinum based catalysts are well-known to reduce protons to dihydrogen.[11] However, the expensive nature of noble metals makes these complexes impractical for the hydrogen-based economy. Thus, there is an immediate urge to identify complexes of abundant metals for proton reduction. Complexes of iron, nickel, and cobalt are well-known in the literature to perform proton reduction catalysis.[10] Thus, several groups have tried to design complexes which are not necessarily a structural match with hydrogenase, but serve the functional role. In this regard, manganese,[12] iron,[13] nickel,[14] copper[15] and cobalt[16-23] complexes of various ligand frameworks were designed and tested towards proton and water reduction. Manganese complexes of vinylidene/allenylidene ligands[12] have shown proton reduction activity in the presence of HBF_4 as the acid source in acetonitrile at a potential of -1.60 (vinylidene) and -0.84 $V_{Fc/Fc+}$ (allenylidene). (**Figure 1.3a**).[12a] On the other hand, iron complexes of a fluorine-rich dimethyl glyoxime (dmgH) type ligand exhibited proton reduction in the presence of trifluoroacetic acid (TFA) at a low overpotential of 0.3 V with a TOF of 200 s^{-1} (**Figure 1.3b**).[13a] Several Ni(II) complexes of phosphines,[14a-g] oximes,[14h] and

www.manaraa.com

thiolanes,[14i] (**Figure 1.3c-e**) are also well-known in this regard. Few Ni(II) phosphines, and pyridine-rich complexes (**Figure 1.3f-h**),[14j] are known to generate hydrogen from neutral water. Similarly, Sun *et al.*[15] recently have shown water reduction at pH 2.5 by using copper complexes of such pyridine-rich ligands (**Figure 1.3i**) with an onset overpotential of 420 mV and TON of 1.4 x 10^4 mol of hydrogen. Many cobalt complexes capable of performing proton and water reduction are known in literature,[16-23] and will be discussed in the following section.

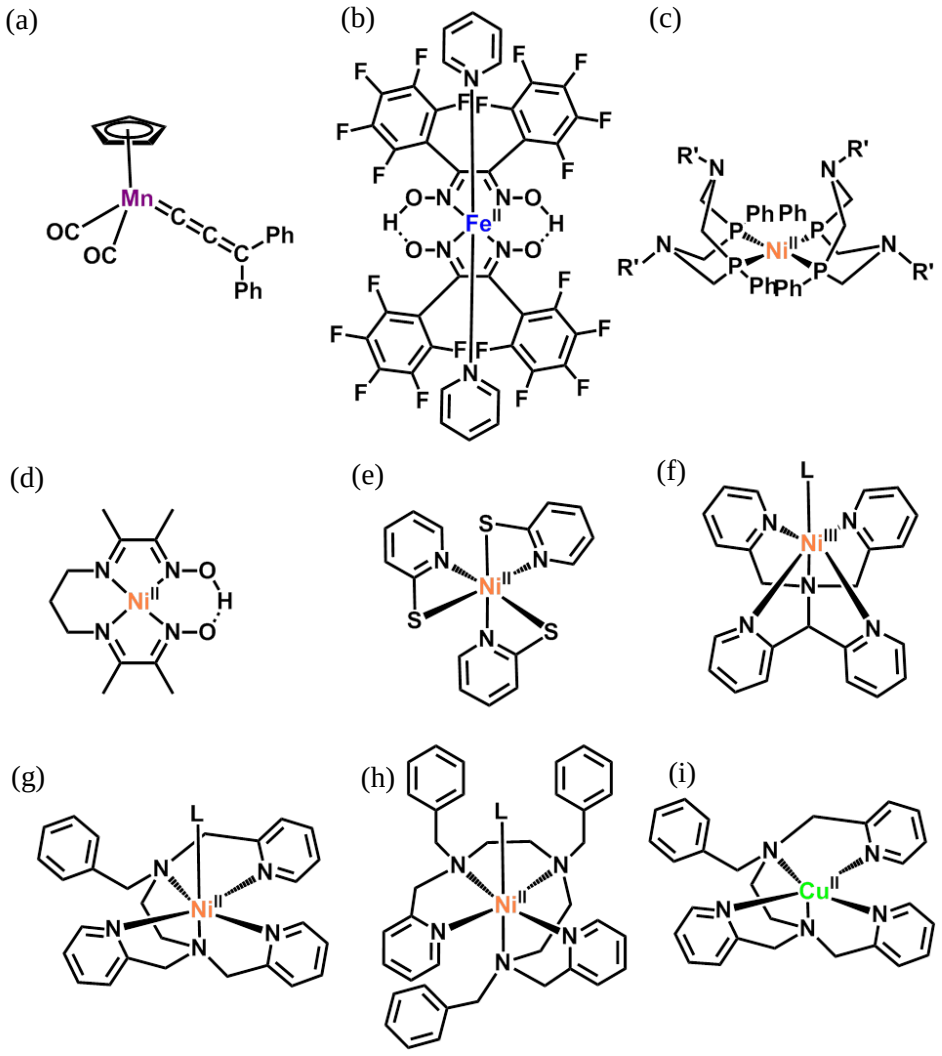

Figure 1.3. (a) Mn, (b) Fe^{II}, (c)-(h) Ni^{II}, and (i) Cu^{II} complexes for proton and water reduction. L = CH_3CN/H_2O.

www.manaraa.com

1.5.1 Proton Reduction Catalysts based on Cobalt Complexes

The cobalt ion has been used in several proton-reduction electrocatalysts because of its energetically viable conversion from $3d^6$ Co^{III} or $3d^7$ Co^{II} into the procatalytic nucleophile $3d^8$ Co^{I} species.[16-23] These electrocatalysts generally stabilize the lower oxidation state of the cobalt center either by direct metal reduction or by assistance from the ligand. The Co^{I}-species for these complexes is extremely nucleophilic, and can attack a proton to generate a Co^{III}-H species, which can subsequently react with another proton to generate dihydrogen. On the other hand, this Co^{III}-H species can undergo further reduction to generate a cobalt(II)-hydride (Co^{II}-H) species which can then react with another proton to generate hydrogen. Among the most studied systems for cobalt, the Espenson catalyst,[16a] a Co^{III} oxime species that stabilizes its monovalent Co^{I} counterpart, is capable of proton reduction in acidic media. It has been widely studied by several groups.[16] While a general consensus has not yet been reached for most Co catalysts,[16] it is widely accepted that a Co^{III}–H species must be generated from a series of reduction and protonation events in the catalytic cycle. Several ligands have been used to accommodate the cobalt ion towards proton reduction, which is described in the following sections.

A) Cobalt Complexes in N_4 Pseudo-macrocyclic Environments

The cobalt-dimethylglyoxime $[Co(dmgH)_2]^0$ complex was first introduced in 1960s by Costa *et al.* as the successful model for vitamin B_{12}.[16b] Later, Espenson *et al.* found this complex as the catalyst for proton reduction to generate hydrogen in 1986.[16a] This series of complexes (**Figure 1.4-1.6**) was investigated extensively in the 2000s by Artero, Peters, Mulfort & Tiede, Gray, Alberto, Eisenberg, Hammes-Schiffer, and Muckermann.[16c-u] Due to the π-acceptor nature of the oxime ligand framework, the Co^{I} state was stabilized upon reduction, which can successively generate hydrogen from various acids.

www.manaraa.com

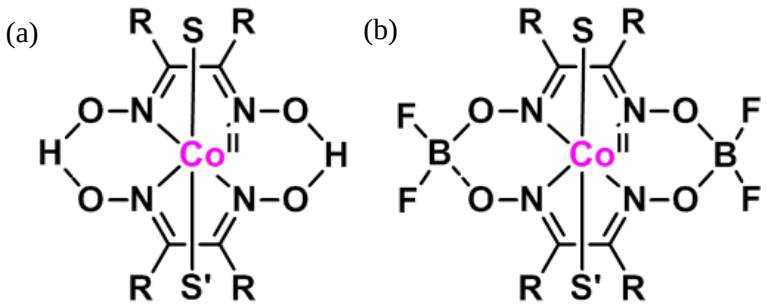

Figure 1.4. (a)-(b) Monometallic (S = S' = H_2O, CH_3CN; R= Me, Ph).

Artero *et al.*[16c-d] have proposed various mechanistic pathways for hydrogen generation with these complexes (**Figure 1.4a,b**) in the presence of acid sources of different strengths. They also studied the kinetic, mechanistic, and catalytic aspects of these complexes with heteroaxially substituted axial ligands. A boron bridge was incorporated to protect these complexes against hydrolysis. Peters *et al.*[16e-f] (**Figure 1.4a,b**) compared the catalytic activity upon changing the equatorial oxime substituents from methyl to phenyl. The methyl substituents have shown optimized activity towards proton reduction. They isolated and crystallized the Co^I complex, the active species for the catalysis, which is 5-coordinated in nature (**Figure 1.4b**). Eisenberg,[16i-l] as well as Mulfort & Tiede[16m-n] used heteroaxially substituted monometallic $Co(dmgH)_2$ complexes towards photocatalytic proton reduction in the presence of organic or inorganic photosensitizers. All of these species can generate hydrogen using strong to mild organic acids at low overpotentials (0-0.5 V) with good turnover numbers (0-50). Several groups have designed tetradentate oxime ligands instead of dimethylglyoxime due to the enhanced stability of the earlier species towards hydrolysis. Artero *et al.*[14h] synthesized and characterized the dibromo analog of such cobalt complexes with a bridging propyl unit in the ligand framework (**Figure 1.5a,b**). These complexes are more robust catalysts than their dimethylglyoxime analogs.[16o]

www.manaraa.com

They studied the mechanism of proton reduction with this series of complexes and proposed that the formation of a Co^{III}-H intermediate from the reaction between an active Co^{I} species with the proton. Moreover, they invoked an oxime-bridged pathway in the generation of hydrogen. Alberto *et al.*[16p-q] proceeded one step further and designed a similar ligand with varying substituents on the propyl bridge (**Figure 1.5c**), which reveals better TON (TON_{Co}: 8/12 h) for the unsubstituted one, whereas the electron-withdrawing fluoro-substituted one shows the lowest TON (TON_{Co}: 2/12 h) in the presence of rhenium containing photosensitizers, TEOA as the sacrificial donor, and HBF_4 as the acid source in aqueous solution. Furthermore, they designed a pentadentate ligand (**Figure 1.5d**) with a similar oxime framework containing a pendant pyridine arm generated from the propyl bridge. They used this cobalt complex (**Figure 1.5d**) as the catalysts for proton reduction in the similar photocatalytic conditions as described before for the complexes in **Figure 1.5c**. This complex (in **Figure 1.5d**) exhibited superior catalytic activity with TON_{Co} reaches to 10 after 12 h of experiment.

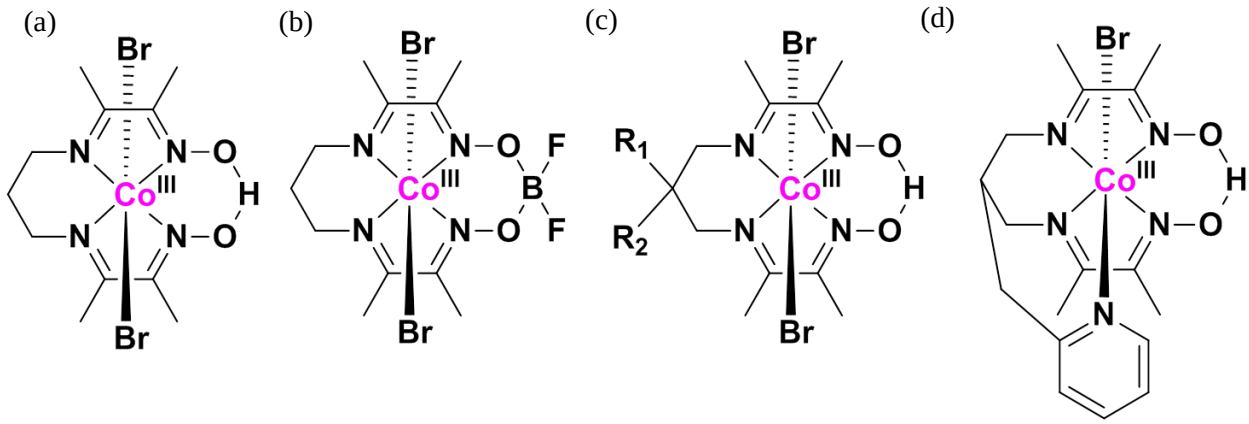

Figure 1.5. Cobalt complexes based on tetradentate oxime ligands (R_1, R_2: CH_2OH; R_1, R_2: F; R_1: H, R_2: OH).

Peters *et al.*[16f] developed cobalt complexes of a tetraaza macrocycle containing four imine moieties connected by two bridging propyl units. The imine units are connected with various alkyl substituents. The alkyl substituents were systematically altered to include a variety of

www.manaraa.com

methyl and phenyl substituents as shown in **Figure 1.6a**. The methyl substituted complexes were able to generate hydrogen in non-aqueous media from both strong and medium strength acids such as p-toluene sulfonic acid (TsOH) and tetrafluoroboric acid (HBF_4), respectively. On the contrary, the phenyl substituted complexes could not catalyze proton reduction with these acid sources. Peters *et al.* also altered the axial ligands from neutral acetonitrile to negatively charged bromides. Additionally, Alberto *et al.*[16q] (**Figure 1.6b**) have explored the photocatalytic activity of similar complexes with substituents on the propyl bridge in the presence of rhenium containing photosensitizers with a TON of ca. 17.

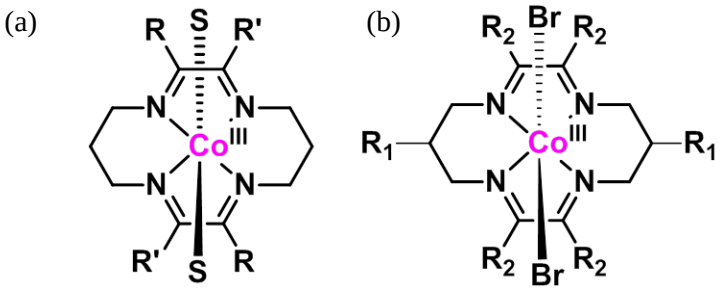

Figure 1.6. Cobalt complexes based on tetraimine macrocycles (S = Br, CH_3CN; R= R' = Me; R = R' = Ph; R = Me, R' =Ph. R_1 = OH, R_2: CH_3).

B) Cobalt Complexes of Pyridine-rich Ligands

Several groups have designed and synthesized pyridine-containing multidentate ligands which can accommodate cobalt and generate cobalt(II) complexes (**Figure 1.7**). Chang *et al.*[17a] have synthesized such complexes using a tetradentate ligand (**Figure 1.7a**), capable of generating hydrogen from trifluoroacetic acid at a low overpotential of 0.4 – 0.6 V in acetonitrile or in an acetonitrile/water (1:1) mixture with TOF of 40. Furthermore, pentadentate redox-active pyridino-bis-bipyridine ligands have been designed and the corresponding cobalt complexes were synthesized (**Figure 1.7b**).[17b] These complexes exhibited electrocatalytic proton reduction at a low overpotential of 0.55 V in presence of a very weak acids such as acetic acid. Ligand-

www.manaraa.com

centered redox activity was found to be responsible to reduce the overpotential with respect to its non-redox counterparts. The incorporation of the electron-withdrawing CF_3 substituent on the para position of the pyridine ring (**Figure 1.7c**) reduces the catalytic activity due to excessive stabilization of the reactive Co^{I}-species.

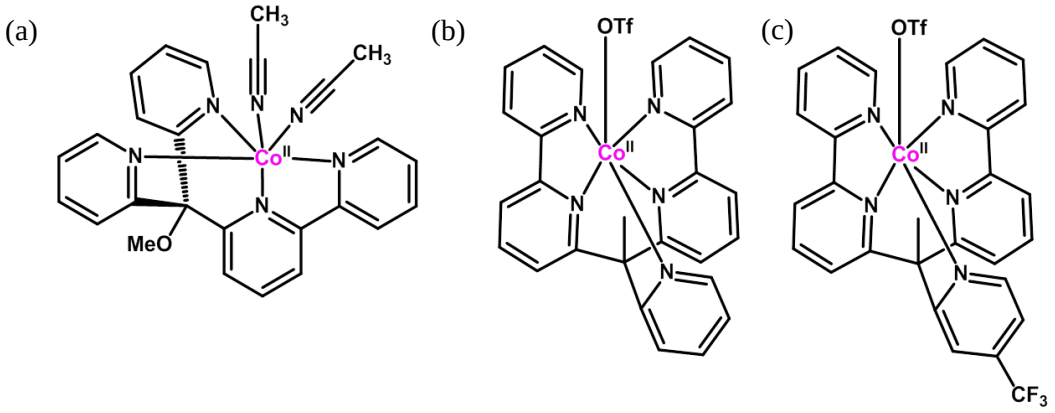

Figure 1.7. Cobalt complexes based on pyridine-rich ligands.

C) Cobalt Complexes of N_4 Aniline-salen Ligands

Gastel *et al.*[18] have synthesized a novel Co^{II} complex based on an aniline-salen type of ligand (**Figure 1.8**).

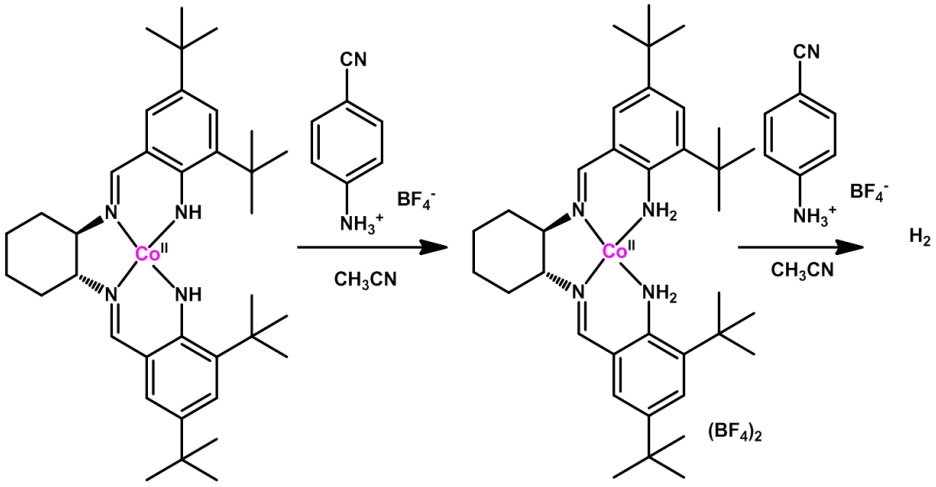

Figure 1.8. Cobalt complex based on aniline-salen ligand. This complex undergoes protonation in the presence of a proton source to generate an anilinium complex which generates hydrogen.

This complex can undergo protonation in presence of two equivalents of acid, p-cyano anilinium

www.manaraa.com

tetrafluoroborate. This protonated complex can induce a 1.0 V positive shift in the Co^{II}/Co^{I} electrochemical potential, thus acting as a proton reduction catalyst which generates hydrogen at an overpotential of 0.9 V with a TON of 30 after 3.7 hours of electrolysis in CH_3CN at -1.9 $V_{Fc/Fc+}$. Furthermore, this aniline group acts as a proton relay to the active site.

D) Homobimellic Cobalt Complexes in Nitrogen-rich Environments

Several groups have designed bimetallic cobalt complexes based on nitrogen-rich ligands where the metal centers stay in close proximity (**Figure 1.9**).[19]

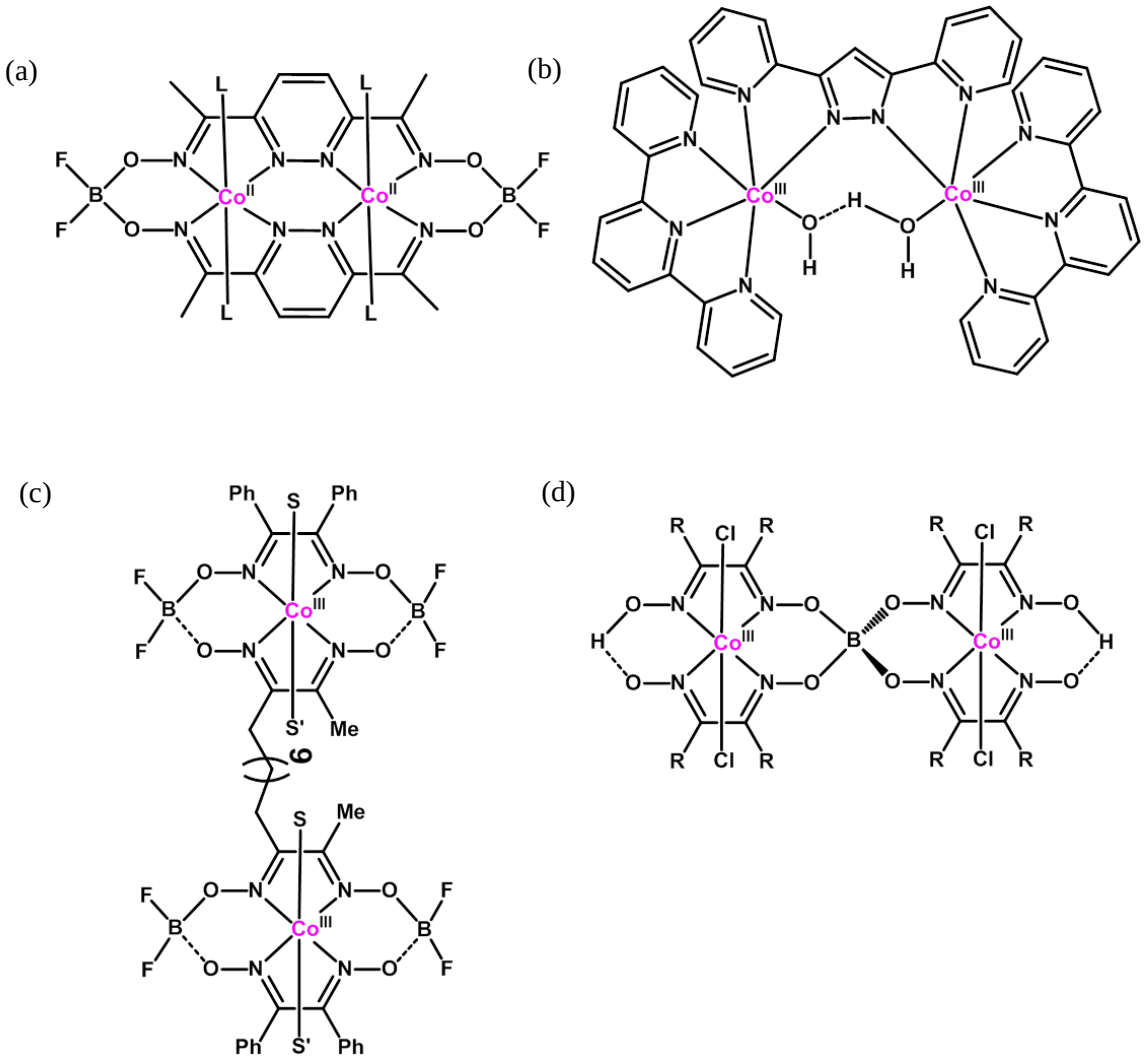

Figure 1.9. Homobimetallic cobalt complexes with nitrogen-rich ligands for proton reduction. L = CH_3CN; S= Cl; S' = Py.

www.manaraa.com

Peters *et al.*[19a] synthesized a bimetallic [$Co^{II}Co^{II}$] complex based on pyridazine as the bridging unit where the other donating units are oxime-based (**Figure 1.9a**). This complex exhibited unique redox properties by stabilizing five different oxidation states, namely [$Co^{III}Co^{III}$], [$Co^{III}Co^{II}$], [$Co^{II}Co^{II}$], [$Co^{II}Co^{I}$], and [$Co^{I}Co^{I}$]. Proton reduction catalysis was observed at a low overpotential with this complex (**Figure 1.9a**) in the presence of 2,6-dichloroanilinium tetrafluoroborate as the acid source. Fukuzami and coworkers[19b] synthesized a bimetallic [$Co^{III}Co^{III}$] complex based on pyrazolate as the bridging moiety, where the other coordination sites of the metal were occupied by terpyridine units (**Figure 1.9b**). This parent complex can undergo three or four electron reductions by $Co(C_p)_2$ or $Co(C_p^*)_2$ to generate $Co^{I}Co^{II}$ or $Co^{I}Co^{I}$ species, respectively. Either of these species can act as the active species and react in the presence of an acid such as TFA to generate the corresponding hydride species, which subsequently generates hydrogen at an overpotential of 0.6 V. A heterolytic pathway was invoked to explain the mechanism of hydrogen generation. Gray *et al.*[19c] have shown catalysis with a bimetallic $Co(dmgBF_2)_2$ type complex bridged with an eight-carbon (8C) long chain (**Figure 1.9c**). This complex exhibited no improvement of catalysis in comparison with its monometallic analog, suggesting that catalysis is occuring in a heterolytic manner. The same group[19d] also synthesized a homobimetallic cobalt complex linked through a boron bridge (**Figure 1.9d**). Surprisingly, this complex generates hydrogen at a higher overpotential (0.954 V) in the presence of ($[DMFH]^+$) and DMF (1:1) in comparison with its monomeric analog.

E) Cobalt Complexes with Oxygen Donor Ligands

A considerably smaller number of research groups is involved with proton reduction catalysis with cobalt complexes using oxygen as the donor moiety. This is due to the expected higher negative potentials associated with the redox processes (**Figure 1.10**).[20] Tilley *et al.* synthesized

www.manaraa.com

and characterized two trimetallic complexes of [$Co^{III}Co^{II}Co^{III}$] type supported by a acylalkoxy ligand framework (**Figure 1.10a,b**).[20a] These complexes exhibited proton reduction in acetonitrile in the presence of TsOH at very low overpotential (<200 mV) with a good TOF of 80 s^{-1}.

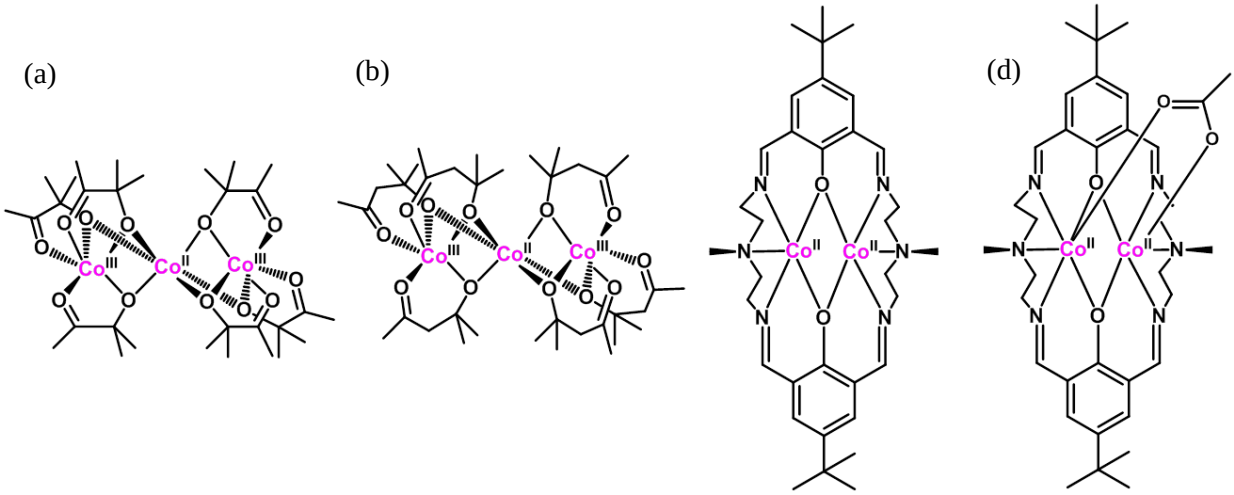

Figure 1.10. Cobalt complexes in oxygen-rich environment for proton reduction.

On the other hand, Dinolfo and coworkers synthesized [$Co^{II}Co^{II}$] complexes based on a modified Robson-type [N_6O_2] macrocycle (**Figure 1.10c,d**).[20b] These complexes displayed proton reduction activity in the presence of a mild acid TFA, and a weak acid HOAc in acetonitrile. In the presence of TFA, this complex generates hydrogen at an overpotential of 0.7 V. The rate constant of proton reduction in the presence of TFA was calculated to be 138 $M^{-2}s^{-1}$ (**Figure 1.10c**), whereas the acetate coordination (**Figure 1.10d**) lowers the rate constant to 63 $M^{-2}s^{-1}$. Moreover, this complex shows electrocatalytic overpotential of 0.6 V in the presence of HOAc with a Faradaic efficiency of 72-94% at -1.88 $V_{Fc/Fc+}$. Generally, these complexes generate [$Co^{I}Co^{I}$] species upon double reduction, which can act as the active species. The catalytic mechanism can either involve heterolytic reaction between a proton with one of the Co^{III}-H species or homolytic combination and cleavage of two Co^{III}-H species. The presence of stable macrocyclic environments support the stability of the lower oxidation states of the metal centers.

www.manaraa.com

These imino-phenolate-based bimetallic cobalt complexes are one of the first examples of phenolate-based ligand framework towards proton reduction.

F) Cobalt Complexes of Dithiolane Ligands

Eisenberg and coworkers[21a] synthesized several cobalt dithiolane complexes (**Figure 1.11a-d**) and studied them for proton reduction. Dithiolane is a potential redox-active ligand and thus, important in understanding the role of ligand-catalysed proton reduction.[21b] They prepared several complexes by either incorporating slightly electron-donating methyl substituents, mild electron-withdrawing chloro, or strongly withdrawing cyano groups (**Figure 1.11a-d)**. All of these complexes exhibited electrocatalytic and photocatalytic proton reduction either in CH_3CN or CH_3CN/H_2O (1:1) mixture.

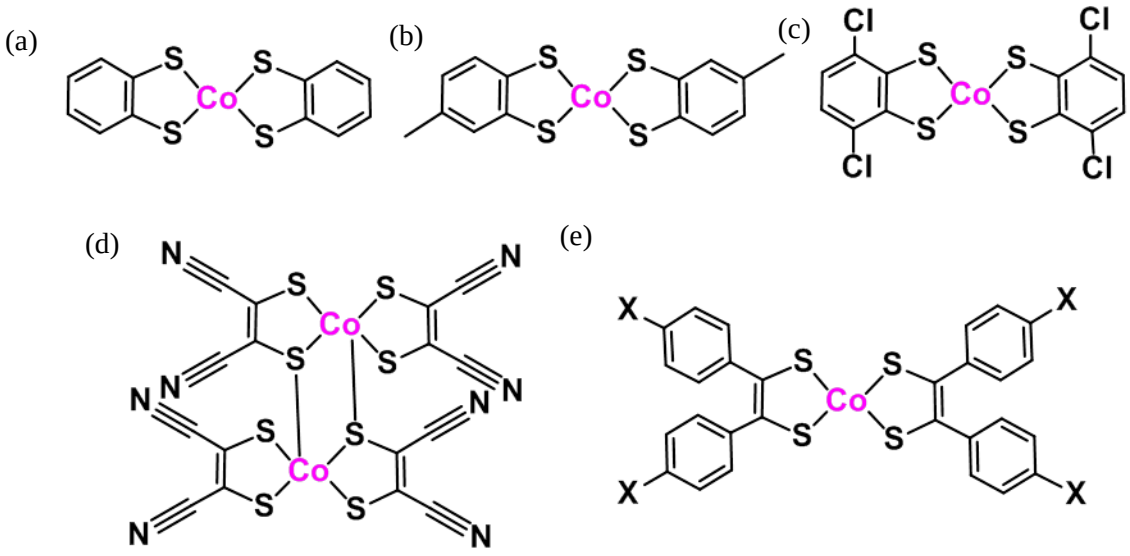

Figure 1.11. Cobalt complexes based on dithiolane ligands (X = F, Cl, I, OMe).

Electrocatalysis was performed with TFA as the acid source. Additionally, photocatalysis was executed with $Ru(bpy)_3^{2+}$ as the photosensitizer and ascorbic acid as the sacrificial electron donor at 520 nm irradiation. The complex containing strongly withdrawing cyano groups displayed superior activity during photocatalysis with a turnover number reaching 9,000. Tilley

www.manaraa.com

and coworkers[21c] varied the aryl substituents on a similar dithiolane ligand (**Figure 1.11e**) and showed a considerable effect of aryl substituents on the catalytic current during electrocatalysis. They used anilinium tetrafluoroborate as the acid source with an overpotential ranging from 0.35 – 0.5 V for different complexes. Furthermore, they proposed the possibility of a bridged protonation pathway through dithiolane from the doubly reduced species.

G) Cobalt Complexes based on Phosphine-rich Ligands

Gray and coworkers[22a] recently synthesized a Co^{I} complex based on the tripodal phosphine-rich ligand (**Figure 1.12a**) which stabilizes a Co^{III}-H species to a significant extent, thus isolable under regular conditions. This complex generates hydrogen from a mild acid source such as TsOH at an overpotential of 1 V. The isolation and ^{1}H-NMR spectroscopic characterization of the Co^{III}-H species enabled them to study the kinetics of the catalytic process in great detail. Homolytic combination of two Co^{III}-H species or heterolytic reactions of Co^{II}-H with a proton are the two most likely pathways to be operative in the generation of hydrogen under these conditions.

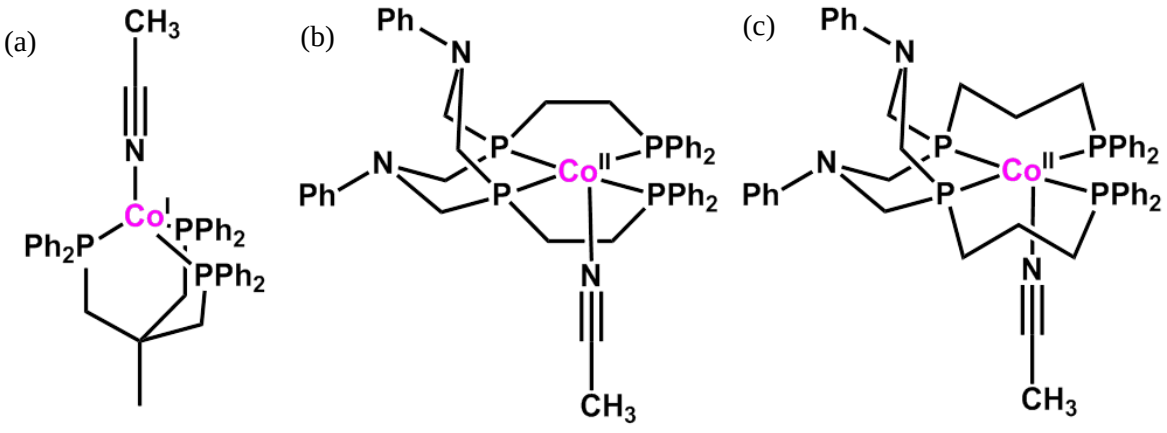

Figure 1.12. Cobalt complexes based on phosphine-rich ligands.

Bullock *et al.*[22b-c] synthesized two new tetradentate phosphine-rich ligands containing two pendant amine moieties. Cobalt complexes of such ligands (**Figure 1.12b,c**) allow isolating two

www.manaraa.com

very important active intermediates, namely Co^{I} and Co^{III}-H species, which in turn helps to understand the catalytic mechanisms. Electrocatalytic proton reduction was exhibited by these complexes in the presence of $[(DMF)H]^{+}$:DMF with a TOF of 980 s^{-1}, and an overpotential ranging between 0.9 – 1.2 V. They were able to analyze various cobalt hydride species and concluded that the Co^{I}-H species can be a potentially active intermediate during catalysis in addition to the Co^{III}-H and Co^{II}-H species. Furthermore, the pendant amine of these complexes facilitates the transfer of protons to the active site.

H) [RuCo] Heterobimetallic Complexes for Photocatalytic Proton Reduction

Several groups have designed supramolecular [RuCo] systems to study electron transfer and photocatalytic hydrogen production instead of using monometallic cobalt complexes for electrocatalytic or photocatalytic (in the presence of an external photosensitizer) proton reduction. Artero *et al.*[23a,b] designed such systems where the photosensitizer is attached to the active site through a pyridine donor in the axial position (**Figure 1.13a,b**). They studied photocatalysis in the presence of triethyl ammonium tetrafluoroborate (Et_3NHBF_4) as the acid source, triethyl amine (Et_3N) as the electron donor, and a cadmium iodide-doped mercury lamp as the light source. The boron-capped bridge shifted the Co^{II}/Co^{I} electrochemical potential to a less negative value, whereas this supramolecular system facilitates the electron transfer and thus proton reduction capability, which is 1.5 to 8.5 times better than the corresponding multicomponent systems. The TONs range from 10-60 after 4 h of operation for various complexes. Sun and coworkers[23c] took a step further and compared the photocatalytic activity between a fully conjugated bridge (**Figure 1.13c**) *versus* a non-conjugated bridge (**Figure 1.13d**) in the presence of Et_3NHBF_4 as the acid source and Et_3N as the electron donor. The complex containing the unconjugated bridge showed better activity (TON: 48 after 8 h) than the

www.manaraa.com

conjugated one (TON: 38 after 8 h), suggesting possible prevention of back electron transfer.

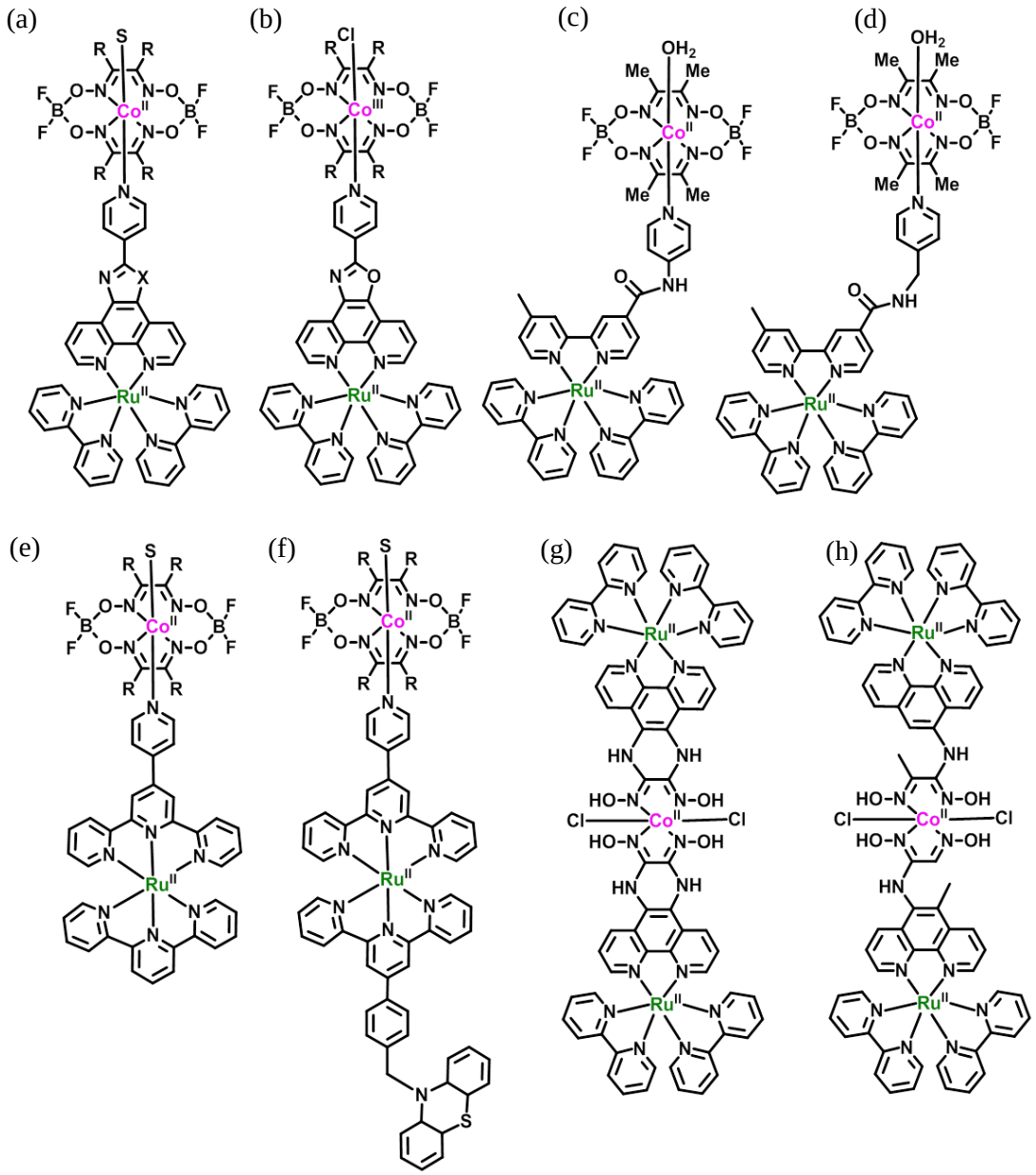

Figure 1.13. [RuCo] complexes; S = H_2O, X = O, R = Me/Ph; X = NH, R = Me.

Mulfort & Tiede[23d] investigated several supramolecular [RuCo] assemblies shown in **Figure 1.13e,f** in detail, focusing on the axial coordination and an electron transfer. X-ray scattering studies revealed an equilibrium between the associated [RuCo] assembly and the dissociated [Ru] and [Co] fragments. On the other hand, transient absorption measurements showed a very

www.manaraa.com

complex kinetic profile with the combination of very fast quenching of the excited state and also a long-lived decay of the exited state. Both these techniques unequivocally suggested the possibility of axial ligand dissociation, thus limiting the electron transfer process from the photosensitizer to the catalytic site. Furthermore, these axially bound systems can promote very fast back electron transfer which can quench the catalytically active species. Therefore, Tiede, Chen & Mulfort explored a new synthetic design[23e] by using an equatorial attachment to assemble the photosensitizer and the catalytic site. Two such complexes based on [RuCoRu] cores (**Figure 1.13g,h**) were synthesized[23e] and thoroughly characterized. The complex shown in **Figure 1.13g** exhibited a charge separated state upon irradiation, as observed from the formation of a high spin Co^{I} state. The complex shown in **Figure 1.13h** did not show any charge separated state. Although limited by the very short-lived charge separated state and multiple ligand state, these equatorial designs are a big step towards photocatalytic hydrogen production.

1.5.2. Water Reduction Catalysts based on Cobalt Complexes

As far as the concern regarding sustainable energy source goes, it is always ecofriendly, greener, and cheaper to generate hydrogen from neutral water rather than expensive organic acids. Most of the complexes are known to catalyze proton reduction in non-aqueous media due to the lack of solubility, stability, and activity in neutral water. Therefore, several ligand systems were recently designed aiming at water soluble complexes.[24,25]

1.5.2.1. Cobalt Complexes of Pyridine-rich Ligands

Several pyridine-rich multidentate ligands were designed to generate water soluble Co(II)/Co(III) complexes, which are capable of generating hydrogen from neutral water (**Figure 1.14**). Thus, in the last few years several groups have synthesized cobalt complexes based on tetradentate imino-pyridine,[24a] (**Figure 1.14a**) and diimino-pyridine[24b] (**Figure 1.14b**) ligand frameworks. On the

www.manaraa.com

other hand, cobalt complexes of several tetradentate ligands based on pyridine, bipyridine, phenanthroline, and carbene moieties were also synthesized[17a,24c-h] (**Figure 1.14c-h**). Moreover, several complexes based on pentadentate ligands (**Figure 1.14i-n**) were also produced for this purpose. Among those, cobalt complexes of pentapyridine,[17b,24i,j] monoamino-tetrapyridine,[24k,l] diamino-tripyridine,[24m] and triamine-bispyridine[24n] complexes are well established. Several of these complexes exhibited electrocatalytic water reduction activity at a low overpotential (0.4 – 1.0 V) with TONs in the thousands. Several of these complexes (**Figure 1.14b-g,i-l,n**) were also investigated in photocatalysis, and they displayed excellent photocatalytic activity in the presence of various photosensitizers.

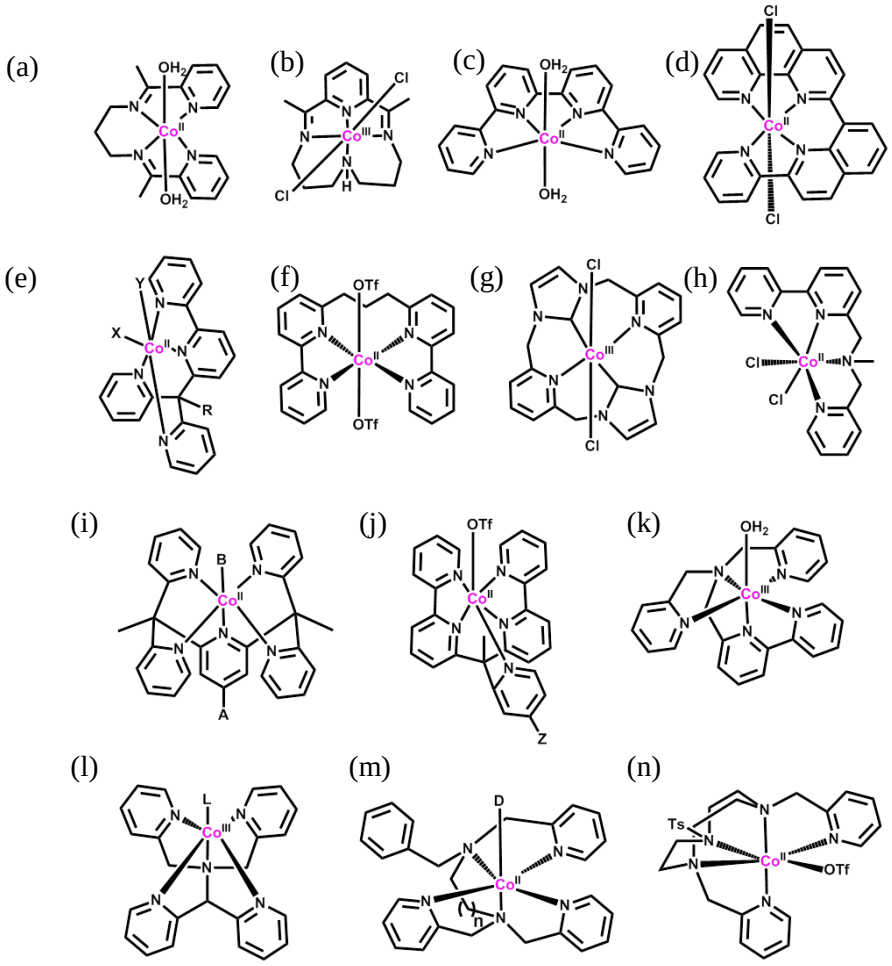

Figure 1.14. Cobalt complexes of several pyridine-rich ligands. R = OH, X = Y = Br; R = OMe, X = Y= CH_3CN; A/Z = H, CF_3, NMe_2, B = H_2O; L = Cl^-, NO_3^-, OTf^-, H_2O; D = CH_3CN, H_2O.

www.manaraa.com

1.5.2.2. Cobalt Complexes based on Phosphine-rich Ligands

To reduce the onset overpotential of hydrogen generation, Sun *et al.* have designed a novel phosphine-rich tetradentate ligand environment that can accommodate a cobalt(II) ion.[25] The Co(II) complex contains two water molecules in the 5th and 6th positions (**Figure 1.15**). This complex exhibited excellent electrocatalytic activity in the presence of neutral water at a very low overpotential of 0.08 V. In addition, it did not decompose over a 20-hour period and generated 1,490 moles of hydrogen per hour with respect to one mole of the catalyst.

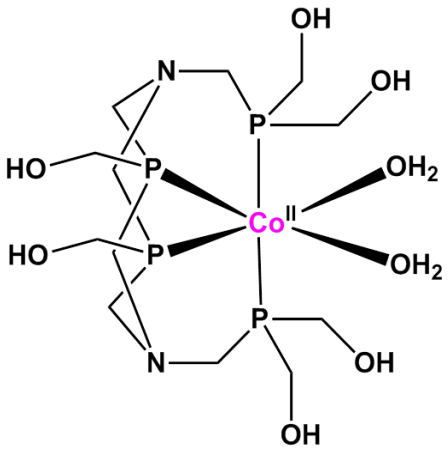

Figure 1.15. Cobalt complex of phosphine-rich ligand.

1.6.0. Generalized Catalytic Mechanisms for Proton Reduction with Cobalt Complexes

In general terms, independent of the nature of the parent species (be it Co^{III} or Co^{II}), it is important for a particular ligand framework to stabilize the Co^{I} state. This state is capable of reducing protons to hydrogen. Usually, a π-acceptor or a soft-donor ligand environment can favor this lower oxidation state upon reduction.[16-25] This Co^{I} is an extremely good nucleophile to attack an electrophile such as the proton and generate the Co^{III}-H species, which is an active intermediate in proton reduction catalysis. In presence of a strong acid source, this Co^{III}-H intermediate can either react with a proton to generate hydrogen in a heterolytic fashion or it can combine with another Co^{III}-H species to generate hydrogen in a homolytic manner. Depending

www.manaraa.com

on the acid strength (mainly for mild/weak acids), the Co^{III}-H intermediate can undergo reduction, either directly from the electrochemical potential available in the system or by electron transfer from the residual Co^{I} species present in solution, to generate the Co^{II}-H species. This Co^{II}-H species can either react with another proton to generate hydrogen heterolytically or it can combine with another Co^{II}-H species homolytically to generate hydrogen (**Figure 1.16**).[10b]

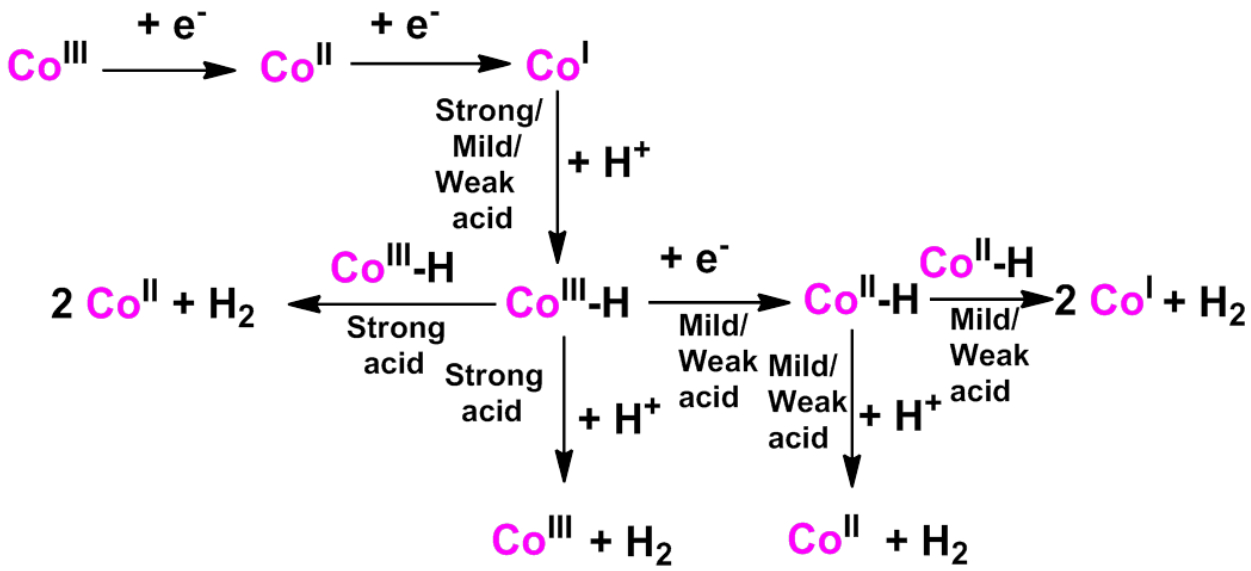

Figure 1.16. Generalized mechanistic scheme for proton reduction.

1.6.0 Summary and Outlook

An extensive body of literature was generated in the last decade regarding proton and water reduction catalysis due to the immediate need to find effective and sustainable alternative energy sources. The inexpensive nature of first-row transition metals has driven the new, yet already extensive, research direction towards Earth-abundant metal catalyzed hydrogen production. Cobalt complexes seem to be the most promising among those studied because of the stabilization of highly nucleophilic Co^{I} species. In spite of the existence of several cobalt-containing proton reduction electro- and photocatalysts reported in the literature (over one hundred), there are only very few known (only one third of them ~ 30) to perform efficient water

www.manaraa.com

reduction. Therefore, a systematic variation of the ligand framework is required to optimize and understand the electronic, spectroscopic, and mechanistic aspects towards proton and water reduction catalysis.

1.8.0 Research Statements and Objectives

It is necessary to understand the electronic processes governing water oxidation and proton reduction to achieve effective electro or photocatalytic water splitting. I am mostly interested in studying the behavior of the catalytic site (Co^{III}/Co^{II}) for proton reduction. Proton reduction involves two-electron transfers to generate one equivalent of dihydrogen. Theoretically, the generation of a two-electron reduced species from a metal-complex at a proper potential, can act as an active species capable of reducing protons to dihydrogen while oxidizing back to the parent species. The doubly reduced species can be generated *via* a two-electron metal-based reduction or *via* a combination of metal and ligand-based reductions. Thus, the Verani group uses ligand design containing redox-active frameworks for the formation of metal complexes for proton reduction. Cobalt has been extensively used to catalyze proton or water reduction to generate dihydrogen because it can stabilize highly nucleophilic reduced species such as Co^{I}. Therefore, the focus of this thesis is to generate Co^{II}/Co^{III} complexes of polydentate ligands for the generation of proton reduction catalysts. To perform the catalysis efficiently, the reduced active species must be basic enough to deprotonate the acid and react with the proton, but excessive basicity is undesirable because it overstabilizes the metal hydride intermediate, thus inhibiting hydrogen formation. Optimization of proton reduction capability can only be systematically achieved by altering the design of the ligand framework around the metal center. Therefore, we have investigated the electronic, redox, electron transfer, and catalytic properties of cobalt complexes in various ligand frameworks: imino-phenolates, imino-oximes, and imino-pyridines

www.manaraa.com

(**Figure 1.17**). Due to our previous experience of synthesizing polydentate ligand frameworks[26a-e] and its corresponding cobalt complexes[26f] in the Verani lab, we were very confident in designing various ligand scaffolds.

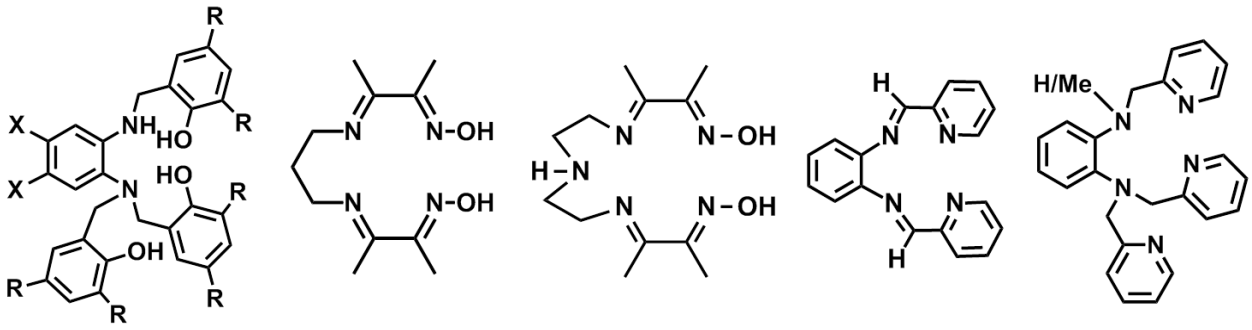

Figure 1.17. The ligand frameworks employed to accommodate cobalt towards proton/water reduction.

Furthermore, we can probe the role of substituents around this ligand framework or alter the axial ligands and the axial ligand substituents to modulate the electronic and redox properties, thus affecting the overall nucleophilic character of the reduced cobalt species which will have a direct influence on catalysis. Therefore, in this thesis I will discuss cobalt complexes of redox-active ligands and their activity towards proton reduction, as well as our progress towards designing various ligand frameworks capable of reducing the overpotential for hydrogen generation.

Moreover, in this thesis I describe the synthetic efforts towards designing photocatalytic assemblies containing the heterobimetallic [$Ru^{II}Co^{III}$] core, where Ru^{II} is the photosensitizer and Co^{III} is the catalytic site. These species were obtained using selected catalytic modules, namely cobalt oxime with a $Ru(bpy)_2^{2+}$ photosensitizer *via* equatorial attachment.

Additionally, we synthesized cobalt complexes that are water soluble, and therefore that can be tested towards their water reduction capability. Hydrogen generation from neutral water is always beneficial and more affordable than the expensive organic acids. Therefore, we

www.manaraa.com

incorporated several polar imine moieties in our ligand design to make the corresponding complex water soluble.

I. Goals and Objectives

The overall objective of this thesis project is to understand the synthetic, geometric, redox, electronic, catalytic, and mechanistic aspects of cobalt complexes in various redox-active ligand frameworks and use this information to attain efficient proton and water reduction. In order to obtain this overarching objective, the following goals have been pursued.

- **Goal # 1:** ***Evaluation of Substitution and H-bond-induced Modulation of the Electronic and Catalytic Properties of Octahedral Co^{III}-complexes in Phenolate-rich Environments towards Proton Reduction.*** We aim to modulate the redox, electronic and catalytic properties for Co^{III}-complexes of phenolate-rich ligands by changing the substituents either in the ligand or on the metal. This goal is addressed in Chapter 3.

- **Goal # 2:** ***Investigation of the Electrochemical and Catalytic Pathways of Co^{III}-oxime Complexes with Homoaxial and Heteroaxial Ligands towards Proton Reduction.*** We address the electrochemical and catalytic pathways for Co^{III}-oxime complexes with various axial ligands for proton reduction in organic solvent and we also investigate the synthetic, electronic, and catalytic implications of a selected $[Ru^{II}Co^{III}]$ complex. This goal is addressed in Chapter 4.

- **Goal # 3:** ***Study of Proton and Water Reduction Catalysis by a Co^{III}-complex of Pentadentate Oxime Ligand.*** Based on the observations for Goal **2** that 5-coordinated species are the active species for the catalysis, we investigate cobalt complex formation with a pentadentate oxime ligand and its activity towards proton and water reduction.

www.manaraa.com

This goal is addressed in chapter 5.

Goal # 4: ***Study of Synthetic, Mechanistic, Geometric, Electronic, and Catalytic Properties of Phenylene-bridged Pyridine-rich Co^{II}/Co^{III}-complexes towards Proton and Water Reduction.*** We aim to examine the reactivity of cobalt complex formation with this series of ligands and the nature of electrochemical and mechanistic pathways for proton and water reduction in organic and aqueous solvents. This goal is addressed in chapter 6.

These topics were developed over the course of the last 6 years and constitute the body of this dissertation. The results follow.

www.manaraa.com

REFERENCES

1. (a) Turner, J. A. *Science* **2004**, *305*, 972. (b) Lewis, N. S.; Nocera, D. G. *Proc. Natl. Acad. Sci. U.S.A.* **2006**, *103*, 15729. (c) Esswein, A. J.; Nocera, D. G. *Chem. Rev.* **2007**, *107*, 4022. (d) Cook, T. R.; Dogutan, D. K.; Reece, S. Y.; Surendranath, Y.; Teets, T. S.; Nocera, D. G. *Chem. Rev.* **2010**, *110*, 6474. (e) Walter, M. G.; Warren, E. L.; McKone, J. R.; Boettcher, S. W.; Mi, Q.; Santori, E. A.; Lewis, N. S. *Chem. Rev.* **2010**, *110*, 6446. (f) Tran, P. D.; Artero, V.; Fontecave, M. *Energy Environ. Sci.* **2010**, *3*, 727. (g) McCusker, J. K. *Science.* **2001**, *293*, 1599. (h) http://cdiac.ornl.gov/ (i) http://www.fuelcells.org /base.cgim?Template = hydrogen_basics (j) Kudo, A.; Kato, H.; Tsuji, I. *Chem. Lett.* **2004**, *33*, 1534. (k) Limburg, B.; Bouwman, E.; Bonnet, S. *Coord. Chem. Rev.* **2012**, *256*, 1451.
2. (a) Goldsmith, J.; Wong-Foy, A. G.; Cafarella, M. J.; Sieg, D. J. *Chem. Mater.* **2013**, *25*, 3373. (b) Tranchemontagne, D. J.; Park, K. S.; Furukawa, H.; Eckert, J.; Knobler, C. B.; Yaghi, O. M. *J. Phys. Chem. C* **2012**, *116*, 13143. (c) Zhao, D.; Yuan, D.; Zhou, H-C. *Energy Environ. Sci.* **2008**, *1*, 222. (d) Murray, L. J.; Dinca, M.; Long, J. R. *Chem. Soc. Rev.* **2009**, *38*, 1294.
3. McEvoy, J.P.; Brudvig, G. W. *Chem. Rev.*, **2006,** *106*, 4457.
4. (a) Loll, B.; Kern, J.; Saenger, W.; Zouni, A.; Biesiadka, J. *Nature.* **2005**, *438*, 1040. (b) Sun, L.; Hammarstrom, L.; Akermark, B.; Styring, S. *Chem. Soc. Rev.* **2001**, *30*, 36.
5. (a) Gloaguen, F.; Rauchfuss, T. B. *Chem. Soc. Rev.* **2009**, *38*, 100. (b) Simmons, T. R.; Berggren, G.; Bacchi, M. Fontecave, M.; Artero, V. *Coord. Chem. Rev.* **2014**, *270*, 127.
6. (a) Hsieh, C. H.; Erdem, Ö. F.; Harman, S. D.; Singleton, M. L.; Reijerse, E.; Lubitz, W.; Popescu, C. V.; Reibenspies, J. H.; Brothers, S. M.; Hall, M. B.; Darensbourg, M. Y.

www.manaraa.com

J. Am. Chem. Soc. **2012**, *134*, 13089. (b) Hsieh, C. H.; Ding, S.; Erdem, Ö. F.; Crouthers, D. J.; Lubitz, W.; Popescu, C. V.; Reibenspies, J. H.; Hall, M. B.; Darensbourg, M. Y. *Nature Communications* **2014**, *5*, 3684. (c) Pinder, T. A.; Montalvo, S. K.; Hsieh, C. H.; Lunsford, A. M.; Bethel, R. D.; Pierce, B. S.; Darensbourg, M. Y. *Inorg. Chem.* **2014**, *53*, 9095. (d) Crouthers, D. J.; Denny, J. A.; Munoz, D. G.; Darensbourg, M. Y. *Organometallics* **2014**, *33*, 4747.

7. (a) Carroll, M. E.; Barton, B. E.; Rauchfuss, T. B.; Carroll, P. J. *J. Am. Chem. Soc.* **2012**, *134*, 18843. (b) Manor, B. C.; Rauchfuss, T. B. *J. Am. Chem. Soc.* **2013**, *135*, 11895. (c) Huynh, M. T.; Schilter, D.; Hammes-Schiffer, S.; Rauchfuss, T. B. *J. Am. Chem. Soc.* **2014**, *136*, 12385.
8. (a) Chen, L.; Wang, M.; Gloaguen, F.; Zheng, D.; Zhang, P.; Sun, L. *Inorg. Chem*. **2013**, *52*, 1798. (b) Zheng, D.; Wang, M.; Chen, L.; Wang, N.; Sun, L. *Inorg. Chem.* **2014**, *53*, 1555. (c) Zheng, D.; Wang, M.; Chen, Lin.; Wang, N.; Chenga, M.; Sun, L. *Chem. Commun.* **2014**, *50*, 9255. (d) Zheng, D.; Wang, N.; Wang, M.; Ding, S.; Ma, C.; Darensbourg, M. Y.; Hall, M. B.; Sun, L. *J. Am. Chem. Soc.* **2014**, *136*, 16817.
9. (a) Canaguier, S.; Fourmond, V.; Perotto, C. U.; Fize, J.; Pe´caut, J.; Fontecave, M.; Field, M. J.; Artero, V. *Chem. Commun.* **2013**, *49*, 5004. (b) Fourmond, V.; Canaguier, S.; Golly, B.; Field, M. J.; Fontecave, M.; Artero, V. *Energy Environ. Sci.* **2011**, *4*, 2417. (c) Canaguier, S.; Field, M.; Oudart, Y.; Pe´caut, J.; Fontecave, M. Artero, V. *Chem. Commun.* **2010**, *46*, 5876. (d) Vaccaro, L.; Artero, V.; Canaguier, S.; Fontecave, M.; Field, M. J. *Dalton Trans.* **2010**, *39*, 3043.
10. (a) Thoi, V. S.; Sun, Y.; Long, J. R.; Chang, C. J. *Chem. Soc. Rev.* **2013**, *42*, 2388. (b) Wang, M.; Chena, L.; Sun, L. *Energy Environ. Sci.* **2012**, *5*, 6763. (c) Eckenhoff, W. T.;

www.manaraa.com

Eisenberg, R. *Dalton Trans.* **2012**, *41*, 13004. (d) Eckenhoff, W. T.; McNamara, W. R.; Du, P.; Eisenberg, R. *Biochim. et Biophys. Acta* **2013**, *1827*, 958. (e) Artero, V.; Chavarot-Kerlidou, M.; Fontecave, M. *Angew. Chem. Int. Ed.* **2011**, *50*, 7238.

11. (a) Zhu, M.; Lu, Y.; Du, Y.; Li, J.; Wang, X.; Yang, P. *Int. J. Hydro. Energy* **2011**, *36*, 4298. (b) Ajayi, F. F.; Chae, K-J.; Kim, K-Y.; Choi, M-J.; Kim, I. S. *Int. J. Hydro. Energy* **2009**, *34*, 110. (c) Best, J. P.; Dunstan, D. E. *Int. J. Hydro. Energy* **2009**, *34*, 7562. (d) Tinker, L. L.; McDaniel N. D.; Curtin. P. N.; Smith, C. K.; Ireland, M. J. *Chem. Eur. J.* **2007**, *13*, 8726.
12. Valyaev, D. A.; Peterleitner, M. G.; Semeikin, O. V.; Utegenov, K. I.; Ustynyuk, N. A.; Sournia-Saquet, A.; Lugan, N.; Lavigne, G. *J. Organometall. Chem.* **2007**, *692*, 3207.
13. (a) Rose, M. J.; Gray, H. B.; Winkler, J. R. *J. Am. Chem. Soc.* **2012**, *134*, 8310. (b) Connor, G. P.; Mayer, K. J.; Tribble, C. S.; McNamara, W. R. *Inorg. Chem.* **2014**, *53*, 5408.
14. (a) Wilson, A. D.; Newell, R. H.; McNevin, M. J.; Muckerman, J. T.; DuBois, M. R.; DuBois, D. L. *J. Am. Chem. Soc*. **2006**, *128*, 358. (b) Dutta, A.; Lense, S.; Hou, J.; Engelhard, M. H.; Roberts, J. A. S.; Shaw, W. J. *J. Am. Chem. Soc*. **2013**, *135*, 18490. (c) Pool, D. H.; DuBois, D. L. *J. Organometall. Chem.* **2009**, *694*, 2858. (d) Helm, M. L.; Stewart, M. P. R.; Bullock, M.; DuBois, M. R.; DuBois, D. L. *Science* **2011**, *333*, 863. (e) Hoffert, W. A.; Roberts, J. A. S.; Bullock, R. M.; Helm, M. L. *Chem. Commun.*, **2013**, *49*, 7767. (f) Yang, J. Y.; Smith, S. E.; Liu, T.; Dougherty, W. G.; Hoffert, W. A.; Kassel, W. S.; DuBois, M. R.; DuBois, D. L.; Bullock, R. M. *J. Am. Chem. Soc.* **2013**, *135*, 9700. (g) Bullock, R. M.; Appel, A. M.; Helm, M. L. *Chem. Commun.* **2014**, *50*, 3125. (h) Jacques, P-A.; Artero, V.; Pecaut, J.; Fontecave, M. *Proc. Natl. Acad. Sci. USA* **2009**,

www.manaraa.com

106, 20627. (i) Han, Z.; McNamara, W. R.; Eum, M-S.; Holland, P. L.; Eisenberg, R. *Angew. Chem. Int. Ed.* **2012**, *51*, 1667. (j) Zhang, P.; Wang, M.; Yang, Y.; Zheng, D.; Hana, K.; Sun, L. *Chem. Commun.* **2014**, *5*0, 14153.

15. Zhang, P.; Wang, M.; Yang, Y.; Yao, T.; Sun, L. *Angew. Chem. Int. Ed.* **2014**, *53*, 13803.
16. (a) Connolly, P.; Espenson, J. H. *Inorg. Chem.* **1986,** *25*, 2684. (b) Costa, G.; Mestroni, G.; Savorgnani, E. D. *Inorg. Chim. Acta* **1969,** 323. (c) Razavet, M.; Artero, V.; Fontecave, M. *Inorg. Chem.* **2005**, *44*, 4786. (d) Baffert C.; Artero, V.; Fontecave, M. *Inorg. Chem.* **2007**, *46*, 1817. (e) Hu, X.; Cossairt, B. M.; Brunschwig, B. S.; Lewis, N. S.; Peters, J. C. *Chem. Comm.* **2005,** 4723 (f) Hu, X.; Brunschwig, B. S.; Peters, J. C. *J. Am. Chem. Soc.* **2007,** *129*, 8988. (g) Berben, L. A.; Peters, J. C. *Chem. Commun.* **2010**, 398. (h) McCrory, C. C.; Uyeda, L. C.; Peters, J. C. *J. Am. Chem. Soc.* **2012**, *134*, 3164. (i) Du, P.; Schneider, J.; Luo, G.; Brennessel, W. W.; Eisenberg, R. *Inorg. Chem.* **2009**, *48*, 4952. (j) Lazarides, T.; McCormick, T.; Du, P.; Luo, G.; Lindley, B.; Eisenberg, R. *J. Am. Chem. Soc.* **2009**, *131*, 9192. (k) McCormick, T. M.; Calitree, B. D.; Orchad, A.; Kraut, N. D.; Bright, F. V.; Detty, M.R.; Eisenberg, R. *J. Am. Chem. Soc.* **2010**, *132*, 15480. (l) McCormick, T. M. Han, Z.; Weinberg, D. J. Brennessel, W. W.; Holland, P.L.; Eisenberg, R. *Inorg. Chem.* **2011**, *50*, 10660. (m) Utschig, L. M.; Silver, S. C.; Mulfort, K. L.; Tiede, D. M. *J. Am. Chem. Soc.* **2011**, *133*, 16334. (n) Mulfort, K. L.; Tiede, D. M. *J. Phys. Chem. B* **2010**, *114*, 14572. (o) Bhattacharjee, A.; Andreiadis, E. S.; Kerlidou, M. C.; Fontecave, M.; Field, M. J.; Artero, V. *Chem. Eur. J.* **2013,** *19*, 15166. (p) Probost, B.; Rodenberg, A.; Guttentag, M.; Hamm, P.; Alberto, R. *Inorg. Chem.* **2010**, *49*, 6453. (q) Probst, B.; Guttentag, M.; Rodenberg, A.; Hamm, P.; Alberto, R. *Inorg. Chem.* **2011,** *50*, 3404 (r) Solis, B.; Hammes-Schiffer, S. *Inorg. Chem.* **2011,** *50*, 11252

www.manaraa.com

(s) Solis, B.; Hammes-Schiffer, S. *J. Am. Chem. Soc.* **2011,** *133*, 19036. (t) Solis, B.; Yu, Y.; Hammes-Schiffer, S. *Inorg. Chem.* **2013,** *52*, 6994. (u) Muckermann, J. T.; Fujita, E. *Chem. Comm.* **2011,** *47*, 12456.

17. (a) Bigi, J. P.; Hanna, T. E.; Harman, W. H.; Chang, A.; Chang, C. J. *Chem. Commun.* **2010**, *46*, 958. (b) Nippe, M.; Khnayzer, R. S.; Panetier, J. A.; Zee, D. Z.; Olaiya, B. S.; Head-Gordon, M.; Chang, C. J.; Castellano, F. N.; Long, J. R. *Chem. Sci.* **2013,** *4*, 3934.
18. Kochem, A.; Thomas, F.; Jarjayes, O.; Gellon, G.; Philouze, C.; Weyhermüller, T.; Neese, F.; Gastel, M. V. *Inorg. Chem.* **2013**, *52*, 14428.
19. (a) Szymczak, N. K.; Berben, L. A.; Peters, J. C. *Chem. Commun.* **2009**, 6729. (b) Mandal, S.; Shikano, S.; Yamada, Y.; Lee, Y-M.; Nam, W.; Llobet, A.; Fukuzumi, S. *J. Am. Chem. Soc.* **2013**, *135*, 15294. (c) Valdez, C. N.; Dempsey, J. L.; Brunschwig, B. S.; Winkler, J. R.; Gray, H. B. *Proc. Nat. Acad. Sci USA* **2012,** *109*, 15589. (d) Laga, S. M.; Blakemore, J. D.; Henling, L. M.; Brunschwig, B. S.; Gray, H. B. *Inorg. Chem.* **2014**, *53*, 12668.
20. (a) Ahn, H. S.; Davenport, T. C.; Tilley, T. D. *Chem. Commun.* **2014**, *50*, 3834. (b) Kal, S.; Filatov, A. S.; Dinolfo, P. H. *Inorg. Chem.* **2014**, *53*, 7137.
21. (a) McNamara, W. R.; Han, Z.; Yin, C-J.; Brennessel, W. W.; Holland, P. L.; Eisenberg, R. *Proc. Natl. Acad. Sci. USA* **2012**, *109*, 15594. (b) Solis, B. H.; Hammes-Schiffer, S. *J. Am. Chem. Soc.* **2012**, *134*, 15253. (c) Letko, C. S.; Panetier, J. A.; Head-Gordon, M.; Tilley, T. D. *J. Am. Chem. Soc.* **2014**, *136*, 9364.
22. (a) Marinescu, S. C.; Winkler, J. R.; Gray, H. B. *Proc. Natl. Acad. Sci. USA* **2012**, 109, 15127. (b) Wiedner, E. S.; Roberts, J. A. S.; Dougherty, W. G.; Kassel, W. S.; DuBois, D. L.; Bullock, R. M. *Inorg. Chem.* **2013**, *52*, 9975. (c) Wiedner, E. S.; Appel, A. M.;

www.manaraa.com

DuBois, D. L.; Bullock, R. M. *Inorg. Chem.* **2013**, *52*, 14391.

23. (a) Fihri, A.; Artero, V.; Razavet, M.; Baffert, C.; Leibl, W.; Fontecave, M. *Angew. Chem. Int. Ed.* **2008**, *47*, 564. (b) Fihri, A.; Artero, V.; Pereira, A.; Fontecave, M. *Dalton Trans.* **2008**, 5567. (c) Li, C.; Wang, M.; Pan, J.; Zhang, P.; Zhang, R.; Sun, L. *J. Organometal. Chem.* **2009**, *694*, 2814. (d) Mulfort, K. L.; Tiede, D. M. *J. Phys. Chem. B* **2010**, *114*, 14572. (e) Mukherjee, A.; Kokhan, O.; Huang, J.; Niklas, J.; Chen, L. X.; Tiede, D. M.; Mulfort, K. L. *Phys. Chem. Chem. Phys.* **2013**, *15*, 21070.

24. (a) Stubbert, B. D.; Peters, J. C.; Gray, H. B. *J. Am. Chem. Soc.* **2011**, *133*, 18070. (b) Leung, C. F.; Chen, Y. Z.; Yu, H. Q.; Yiu, S. M.; Ko, C. C.; Lau, T. C. *Int. J. Hydro. Energy* **2011**, *36*, 11640. (c) Leung, C-F.; Ng, S-M.; Ko, C-C.; Man, W-L.; Wu, J.; Chen, L.; Lau, T. C. *Energy Environ. Sci*. **2012**, *5*, 7903. (d) Tong, L.; Zong, R.; Thummel, R. P. *J. Am. Chem. Soc.* **2014**, *136*, 4881. (e) Guttentag, M.; Rodenberg, A.; Bachmann, C.; Senn, A.; Hamm, P.; Alberto, R. *Dalton Trans.* **2013**, *42*, 334. (f) Khnayzer, R. S.; Thoi, V. S.; Nippe, M.; King, A. E.; Jurss, J. W.; Roz, K. A. E.; Long, J. R.; Chang, C. J.; Castellano, F. N. *Energy Environ. Sci.* **2014**, *7*, 1477. (g) Kawano, K.; Yamauchi, K.; Sakai, K. *Chem. Commun.* **2014**, *50*, 9872. (h) Singh, W. M.; Mirmohades, M.; Jane, R. T.; White, T. A.; Hammarström, L.; Thapper, A.; Lomoth, R.; Ott, S. *Chem. Commun.* **2013**, *49*, 8638. (i) Sun, Y.; Bigi, J. P.; Piro, N. A.; Tang, M. L.; Long, J. R.; Chang, C. J. *J. Am. Chem. Soc.* **2011**, *133*, 9212. (j) King, A. E.; Surendranath, Y.; Piro, N. A.; Bigi, J. P.; Long, J. R.; Chang, C. J. *Chem. Sci.* **2013**, *4*, 1578. (k) Singh, W. M.; Baine, T.; Kudo, S.; Tian, S.; Ma, X. A. N.; Zhou, H.; DeYonker, N. J.; Pham, T. C.; Bollinger, J. C.; Baker, D. L.; Yan, B.; Webster, C. E.; Zhao, X. *Angew. Chem. Int. Ed.* **2012**, *51*, 5941. (l) Xie, J.; Zhou, Q.; Li, C.; Wang, W.; Hou, Y.; Zhang, B.; Wang, X. *Chem.*

www.manaraa.com

Commun. **2014**, *50*, 6520. (m) Zhang, P.; Wang, M; Gloaguen, F.; Chen, L.; Quentel, F.; Sun, L. *Chem. Commun.* **2013**, *49*, 9455. (n) Call, A.; Codolà, Z.; Acuña-Parés, F.; Lloret-Fillol, J. *Chem. Eur. J.* **2014**, *20*, 6171.

25. Chen, L.; Wang, M.; Han, K.; Zhang, P.; Gloaguen, F.; Sun, L. *Energy Environ. Sci.* **2014**, *7*, 329.
26. (a) Lanznaster, M.; Hratchian, H. P.; Heeg, M. J.; Hryhorczuk, L. M.; McGarvey, B. R. ; Schlegel, H. B.; Verani, C. N. *Inorg. Chem.* **2006**, *45*, 955. (b) Lanznaster, M.; Heeg, M. J.; Yee, G. T.; McGarvey, B. R.; Verani, C. N. *Inorg. Chem.* **2007,** *46*, 72. (c) Allard, M. M.; Sonk, J. A.; Heeg, M. J.; McGarvey, B. R.; Schlegel, H. B.; Verani, C. N. *Angew. Chem. Int. Ed.* **2012,** *51*, 3178. (d) Wickramasinghe, L. D.; Perera, M. M.; Li, L.; Mao, G.; Zhou, Z.; Verani, C. N. *Angew. Chem. Int. Ed*. **2013**, *52*, 13346. (e) Wickramasinghe, L. D.; Mazumder, S.; Gonawala, S.; Perera, M. M.; Baydoun, H.; Thapa, B.; Li, L.; Xie, L.; Mao, G.; Zhou, Z.; Schlegel, H. B.; Verani, C. N. *Angew. Chem. Int. Ed*. **2014**, *53*, 14462. (f) Allard, M. M.; Xavier, F. R.; Heeg, M. J.; Schlegel, H. B.; Verani, C. N. *Eur. J. Inorg. Chem.* **2012**, 4622.

www.manaraa.com

CHAPTER 2

MATERIALS, METHODS, AND INSTRUMENTATION

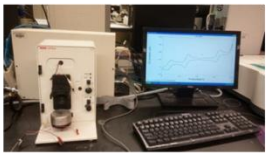

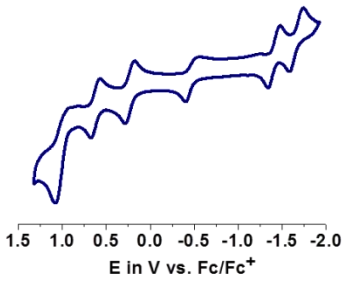

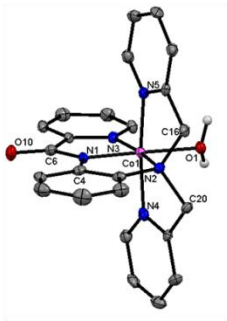

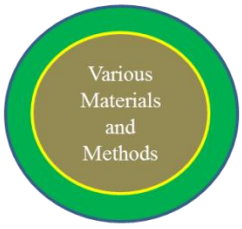

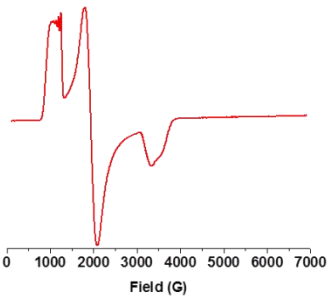

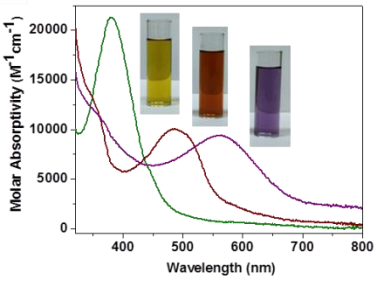

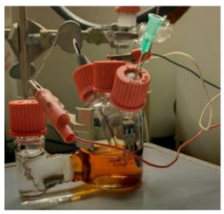

www.manaraa.com

CHAPTER 2

MATERIALS, METHODS, AND INSTRUMENTATION

2.1. Materials

In this research program, several ligands and their corresponding complexes were synthesized. All the precursors including organic molecules and metal salts for this synthesis were purchased from Sigma-Aldrich, Acros Organics, and Alfa Aeser. Solvents were purchased from suitable commercial sources. Dry solvents were used for reactions when necessary.

2.2. Methods and Instrumentations

All the organic products were characterized by multiple physicochemical techniques such as fourier transform infrared spectroscopy (FTIR), proton nuclear magnetic resonance spectroscopy (^{1}H-NMR), and electrospray ionization mass-spectrometry (ESI-MS). Identification of functional groups was achieved from FTIR spectra, whereas ^{1}H-NMR spectra established the presence of various protons in different environments. Additionally, ESI-MS confirmed the presence of molecular ion peaks in solution. Furthermore, to characterize metal complexes, FTIR spectroscopy was used to determine the functional groups and the counterions, when present. For this research, we employed mainly Co(III) complexes with a few exceptions using Co(II) complexes. As Co(III) complexes are $3d^6$ low-spin, we were able to get sharp and well defined ^{1}H-NMR spectra for these species. EPR spectroscopy equipment was employed to understand the spin-state of the Co(II) complexes. In a few instances, we synthesized Ru(II)-based complexes which can again be characterized with ^{1}H-NMR due to its $4d^6$ low-spin diamagnetic nature. ESI-MS spectroscopy equipment was used to confirm the presence of the molecular ion peak in solution and C, H, N elemental analysis equipment were performed to confirm the

www.manaraa.com

identity of the complex. X-ray diffraction techniques were used to solve the structural identities of the complexes when possible. After performing all the techniques to confirm the complex is indeed present in the system, we employed several spectroscopic and electrochemical methods to understand the electronic nature of the complexes. UV-visible spectroscopy revealed the viable electronic transitions in the system, whereas the cyclic voltammograms showed the presence of various redox species in solution upon oxidation or reduction. Spectroelectrochemistry or bulk-electrolysis techniques were used to gain information about the oxidized or reduced redox species. Finally, gas chromatography was used to determine the amount of hydrogen generated during bulk-electrolysis measurements.

2.2.1. Fourier transform infrared spectroscopy (FTIR)

Infrared spectroscopy is an important technique due to its ability to identify various functional groups present in the system. The spectrum is typically obtained between % transmittance *versus* wavelength. Thus the presense of C=O, C=N, C=C, and other moieties were often confirmed by FTIR spectra. Each functional group has different vibrational frequency, thus appeared at different regions of the FTIR spectrum. Furthermore, it can also tell whether or not a particular functional group is present in the metal complex. For example, very often the presence of perchlorate (ClO_4^-), and hexafluorophosphate (PF_6^-) counterions were obtained from FTIR spectra. Infrared spectra were recorded from 4000 to 650 cm^{-1} as KBr pellets on a Bruker Tensor 27 FTIR spectrophotometer in the lab**.**

2.2.2. Nuclear magnetic resonance spectroscopy (NMR)

^{1}H-NMR spectroscopy was employed to identify protons in various environments. The spectrum is typically obtained between intensity *versus* chemical shift. ^{1}H-NMR characterization is essential for organic molecules. For Co(III) and Ru(II) complexes, this technique has been

www.manaraa.com

extensively used due to the diamagnetic nature of the complexes. This technique mainly provides three important parameters such as, i) chemical shift (from the ppm value), ii) proton counts (from the intensity), and iii) splitting pattern (from the nature of the peak). This information allows us to deconvulate the identity of the molecules. Typically, the ^{1}H-NMR spectroscopy was carried out in a Mercury FT-NMR 400 MHz setup using deuterated solvents such as $CDCl_3$, CD_3CN, and d^6-DMSO at 25 °C**.**

2.2.3. Electrospray Ionization Mass spectrometry (ESI-MS)

ESI Mass spectrometry is one of the strongest techniques due to its ability to identify the molecular ion peak in the solution, thus it can tell about the identity of the compound. The spectrum is typically obtained as relative abundance *versus* m/z (mass versus charge). Typical ESI/APCI mass spectra show m/z peaks which are usually associated with the unfragmented molecule due to the soft nature of the technique. Generally, compounds are dissolved in organic solvents such as methanol or acetonitrile before the experiment. During the experiment, these molecules are fragmented with high energetic electrons and generate charged species. Typically, positive mode was used extensively to identify the ligands and the complexes. Low-resolution mass spectrometry is typically used for organic compounds, whereas for metal complexes high-resolution techniques seems to be more useful (due to multi-charge nature). We typically obtain a cluster of peaks together due to the relative abundance of various components in the molecule. ESI-(+) mass spectrometry was measured in a triple quadrupole Micromass Quattro LC equipment where experimental mass patterns were fitted with theoretical isotopic distribution. These experiments were executed with the by Dr. Lew Hryhorczuk and Dr. Yuri Danylyuk form the central instrumental facility of department of chemistry, Wayne State University.

www.manaraa.com

2.2.4. Electron paramagnetic resonance spectroscopy (EPR)

EPR spectroscopy was used to determine the number of unpaired electrons, spin-state, and coordination around the metal. Diamagnetic compounds such as Co(III) and Ru(II) containing complexes (low spin: diamagnetic) can be characterized from ^{1}H-NMR spectra, whereas EPR spectra is essential to determine the spin-state (high spin *versus* low spin) of paramagnetic Co(II) containing complexes. Samples were prepared under a nitrogen atmosphere. A 10^{-3} M solution of the complex was filled in suprasil quartz capillaries with 4 mm outer diameter and frozen in liquid nitrogen. Continuous wave (cw) X-band (9-10 GHz) EPR experiments were carried out with a Bruker ELEXSYS E580 EPR spectrometer (Bruker Biospin, Rheinstetten, Germany), equipped with a Bruker ER 4102ST resonator or a Bruker ER 4122SHQ resonator. The temperature was controlled using a helium gas-flow cryostat (ICE Oxford, UK) and an ITC (Oxford Instruments, UK). Data processing was done using Xepr (Bruker BioSpin, Rheinstetten) and Matlab 7.11.2 (The MathWorks, Inc., Natick) environment, and simulations were performed using the EasySpin software package (version 4.5.5).[1] These experiments were executed with the collaboration with Dr. Oleg Poluektov from Argon National Laboratory (ANL), and the experiments were performed by Dr. Jens Niklas from ANL.

2.2.5. Elemental analyses

In this technique, carbon (C), hydrogen (H), and nitrogen (N) percentages were determined by combustion method. The corresponding oxides such as carbon dioxide (CO_2), water (H_2O), and nitrous oxide (N_2O) were generated and the amounts of carbon, oxygen, and nitrogen were calculated from the amount of the oxides. These elemental analyses (C, H, and N) were performed using Exeter analytical CHN analyzer by Midwest Microlab: Indianapolis, Indiana.

www.manaraa.com

2.2.6. X-ray Crystallography

X-ray crystallography is the most important technique which can unambiguously confirm the structural identities of complexes. X-ray quality crystals were typically obtained by slow evaporation, vapor diffusion, and solvent layering techniques. Diffraction data was usually measured on a Bruker X8 APEX-II kappa geometry diffractometer with Mo radiation and a graphite monochromator. Various programs and software such as APEX-II, SHELX, COSMO APEX II, SAINT, and SADABS were used to solve and refine the structures.[2] Dr. Mary J. Heeg, Dr. Phil Martin, Habib Baydoun, Kenneth K. Kpogo from the Department of Chemistry, Wayne State University and Dr. Richard Staples from the Department of Chemistry, Michigan State University solved the crystal structures.

2.2.7. Ultraviolet-visible Spectroscopy (UV-vis)

UV-visible spectroscopy reveals the electronic absorptions associated with the complexes. Multiple electronic transitions are operative in a complex, some of which are Laporte and/or spin allowed or forbidden. The probability of these transitions very much depends on the selection rules. The intensity/probability of a transition is designated by molar absorption coefficient (ε), which has been defined from Beer-Lambert law as, $A = \varepsilon \times C \times l$, where A is the absorbance, C is the concentration of the complex, and l is the length of the cell. A metal complex typically exhibits different kind of electronic transitions such as ligand based (LLCT), metal to ligand charge transfer (MLCT), ligand to metal charge transfer (LMCT), and d-d transitions. Ligand-based transitions are typically very intense ($\varepsilon \sim 20000 - 60000$); whereas the charges transfer bands appears as medium intense band ($\varepsilon \sim 5000 - 20000$). On the other hand, the d-d transition typically shows very low intense bands ($\varepsilon \sim 50 - 1000$). UV–visible spectra were typically obtained at room temperature using a Varian Cary 50 spectrophotometer operating in the range

www.manaraa.com

of 200 to 1000 nm with quartz cells. Values of ε are given in M^{-1} cm^{-1}. The origin of these electronic spectra typically provides valuable information regarding the frontier orbitals of the complexes. All the spectra are recorded in dichloromethane, acetonitrile, or dimethyl formamide.

2.2.8. Cyclic Voltammetry

Cyclic voltammetry is one of the major characterization techniques in this context. It tells about the various redox species present in the solution. The electrochemical behavior of the complexes was investigated with a BAS 50W potentiostat/galvanostat. Cyclic voltammograms were obtained at room temperature in acetonitrile, dichloromethane or *N*,*N*'-dimethylformamide solutions containing 0.1 M of *n*-Bu_4NPF_6 or *n*-Bu_4NBF_4 as supporting electrolyte under argon atmosphere. The electrochemical cell employed was comprised of three electrodes: glassy-carbon (working), platinum wire (auxiliary) and Ag/AgCl (reference). The ferrocene/ ferrocenium redox couple Fc/Fc^+ (E^o = 400 mV *vs* NHE)[3] was used as the internal standard. Usually, $E_{1/2}$ $(E_{p,c} + E_{p,a})/2$ was reported for reversible processes, whereas $E_{p,c}$ and $E_{p,a}$ are the typical parameters to designate irreversible process. Peak to peak potential separations (ΔE_p = $|E_{p,c} - E_{p,a}|$) and $|i_{pa} / i_{pc}|$ values were measured to evaluate the reversibility of the redox processes. The redox events were normally associated with the frontier orbitals of the complexes.

2.2.9. Spectroelectrochemistry

Spectroelectrochemical measurement coupled with UV-Visible spectroscopy often reveals the electronic nature of oxidized or reduced species. Spectroelectrostatic measurements were carried out in a optically transparent thin-layer cell (*ca.* 0.1 mm) constructed according to a procedure described as follows: a flat platinum wire in a "u" shape was sandwiched between two glass slides where the inner parts were coated with indium-tin oxide (ITO) (8-12 Ω/sq). The flat wire acted as the working electrode and extended outside of the slides for electrical contact. The

www.manaraa.com

solutions were prepared and degassed under an inert atmosphere (argon) and introduced into the cell through a capillary action. The working electrode was located within 4-6 mm of the cell bottom to minimize ohmic potential (iR) drop. All potentials were measured *vs.* a Ag/AgCl reference electrode and a second platinum wire (counter). Potentials were applied to the cell by a BAS 50W potentiostat/galvanostat, and the spectra were collected with a Varian Cary 50 apparatus at the room temperature within a typical time interval of 30 s until the equilibrium between oxidized/reduced species was achieved.

2.2.10. Bulk Electrolysis

Bulk electrolysis measurement coupled with UV-visible and EPR spectroscopy often reveals the electronic nature of oxidized or reduced species. Bulk electrolysis experiment have been performed in a custom-made air-tight H-type cell in the presence of vitreous carbon as the working electrode, Ag/AgCl as the reference electrode placed in the same compartment, and Pt-coil was used as the auxiliary electrode which was placed in the other compartment separated by a frit. Controlled potential electrolysis of the complex has been done in acetonitrile (20 mL) with $TBAPF_6$/$TBABF_4$ as the supporting electrolyte until the calculated final charge was attained. All the potentials were measured against a Ag/AgCl reference electrode. Potentials were applied to the cell by a BAS 50W potentiostat/galvanostat, and the UV-visible spectra after bulk-electrolysis were collected with a Varian Cary 50 apparatus at room temperature.

2.2.11. Chemical Reduction

Chemical reduction experiments were performed to monitor the electron acceptance rate of various complexes. These experiments were performed in CH_3CN/H_2O (90:10% v/v) upon addition of ascorbic acid (reductant) where complexes were evaluated spectrophotometrically on a Varian Cary 50 spectrophotometer, at their λ_{max}, respectively by the disappearance/decrease of

www.manaraa.com

their ligand-to-metal charge transfer (LMCT) at room temperature. The absorption values were converted into concentration using their absorptivity molar coefficient values (ε, $M^{-1}cm^{-1}$). All reactions were monitored throughout time until the absorbance at each λ_{max} value was constant. Reactions were performed using the following conditions: In a 4 mL cuvette (1 cm optical path) 2700 μL of a freshly prepared and degassed acetonitrile solution of the complex was added ($[C]_{final}$ 1.80×10^{-4} M), and the reaction was initiated by the addition 300 μL of a aqueous ascorbic acid (pH ~ 3.0 adjusted with HNO_3; $[AA]_{final} = 1.80 \times 10^{-2}$ M). The concentration of the complexes *versus* the elapsed time was plotted and fitted using a typical first order exponential decaying equation $[C] = [C]_0 \times e^{kt}$ and linearized using the first order rate law $ln[C] = -kt + ln[C]_0$; where [C] is concentration at a given time (M); $[C]_0$ is the initial concentration (M), *k* is the rate constant (s^{-1}) and t is time (s). The half-lives for the compounds were calculated using the expression $t_{½} = ln2/k$ where $t_{½}$ is the half-life and *k* is the rate constant (s^{-1}).

2.2.12. Electrocatalysis (Electrochemistry, Bulk Electrolysis, and Gas Chromatography)

Proton reduction electrocatalysis was tested for complexes *via* cyclic voltammetry in presence of either trifluoroacetic acid (TFA, pKa: 12.7 in CH_3CN), triethyl ammonium chloride (Et_3NHCl, pKa: 18.7 in CH_3CN), or acetic acid (HOAc, pKa: 22.3 in CH_3CN).[4] Glassy carbon was used as the working electrode, platinum wire as the auxiliary electrode, and Ag/AgCl as the reference electrode, with $TBAPF_6$ or $TBABF_4$ as the supporting electrolyte. Overpotentials (η) were calculated from the observed changes in the cyclic voltammogram followed by subtracting the thermodynamic standard potential for H^+/H_2 in CH_3CN in the presence of the corresponding acids (after considering the homoconjugation effect[4]) from the experimental half-wave potential for the catalytic peak in the presence of particular amount of acids. To determine the amount of hydrogen released, bulk electrolysis has been done in a custom-made air-tight H-type cell using a

www.manaraa.com

mercury-pool as the working electrode, Ag/AgCl as the reference, both located in the main chamber. A coiled Pt wire was used as the auxiliary electrode isolated on another compartment separated by a frit. $TBAPF_6$/$TBABF_4$ was used as the supporting electrolyte. The main chamber was filled with an electrolyte solution and a proton source in CH_3CN, whereas the smaller compartment was filled with the electrolyte solution in CH_3CN. The applied potential for bulk electrolysis was measured against Ag/AgCl and potentials are converted against Fc/Fc^+ upon subtracting the electrochemical potential of Fc/Fc^+ from the applied potential *versus* Ag/AgCl in similar condition. In a typical test, the cell was purged with N_2 gas for 20 min followed by sampling of the head space gas (100µl) to ensure an O_2 free environment in the gas-chromatograph. The GC is a Gow-Mac 400 equipped with a thermal conductivity detector and a 8' x 1/8" long 5Å molecular sieve column operating at 60°C with N_2 as the carrier gas. The calibration was carried out with hydrogen (H_2) gas (Hydrogen GC grade 99.99+ %, Scotty analyzed gases, Sigma Aldrich). The solution (no catalyst) was electrolyzed for three hours at appropriate potential and the head space gas was injected into the GC to record the amount of hydrogen generated. Then the cell was purged with N_2 gas for another 20 min followed by injection of the catalyst dissolved in CH_3CN. Bulk electrolysis was conducted for three hours at the same potential and the head space gas (100 µL) was injected to the GC instrument. The amount of hydrogen produced was measuered. The turnover number was calculated after background substraction as the ratio of moles of dihydrogen produced over moles of catalyst used. Faradaic efficiency was calculated from GC measurements.

For water reduction, similar procedure has been followed. A phosphate buffer of 1M was prepared by mixing NaH_2PO_4 (0.454 mol, 27.24 g) and Na_2HPO_4 (0.545 mol, 38.695 g)] in ultrapure water. Then, the pH was adjusted to 7 by adding suitable amounts of NaOH or HCl.

www.manaraa.com

Cyclic voltammetric experiments were performed to determine the onset overpotential for hydrogen generation using Hg-pool as the working electrode, Pt-wire as the auxillary electrode, and Ag/AgCl as the reference electrode. Comparison with the blank (electrode only) was performed to determine the shift of onset overpotential by introducing the complex. For controlled potential experiment, the main chamber was filled with 20 mL of the phosphate buffer solution whereas the glass-fitted chamber was filled with 5 mL of solution. Bulk electrolysis at appropriate potential was applied in presence of the same set of electrodes as the CV experiment for complexes to generate H_2. The GC is a Gow-Mac 400 with a thermal conductivity detector and 8' X 1/8" long 5Å molecular sieve column operating at 60°C was used with N_2 as the carrier gas. The calibration was carried out with hydrogen gas (Hydrogen GC grade 99.99 %, Scotty analyzed gases, Sigma Aldrich).

2.2.13. DFT calculations

DFT calculation is a very important tool for this research. It has been often used to determine the relative energies of the molecular orbitals associated with these complexes. Furthermore, this method gives valuable insight into the redox potentials and sequence during the electrochemistry experiments. It can also provide the energy associated with different processes, thus can predict a plausible mechanistic path, which is very relevant for proton or water reduction catalysis. Furthermore, TD-DFT calculations can simulate the UV-visible spectra in a particular solvent. The DFT calculations were executed by using Gaussian,[5a] after using B3PW91[5b-d] functional with SDD, 6-311++G(d,p), D95 basis sets.[5e-g] These DFT and TD-DFT calculations were executed by the collaboration with Professor H. B. Schlegel's lab in the chemistry department of Wayne State University. Dr. Marco Allard, Dr. Shivnath Mazumder, and Mr. Xuetao Shi performed these calculations.

www.manaraa.com

REFERENCES

1. Stoll, S.; Schweiger, A. EasySpin, a comprehensive software package for spectral simulation and analysis in EPR. *Journal of Magnetic Resonance* **2006**, *178*, 42.
2. (a) COSMO V1.58, *Software for the CCD Detector Systems for Determining Data Collection Parameters.* Bruker Analytical X-ray Systems, Madison, WI (**2008**). (b) APEX2 V2008.5-0 Software *for the CCD Detector System*; Bruker Analytical X-ray Systems, Madison, WI (**2008**). (c) SAINT V 7.34 Software *for the Integration of CCD Detector System* Bruker Analytical X-ray Systems, Madison, WI (**2008**).(d) SADABS V2.008/2 Program for absorption corrections using Bruker-AXS CCD based on the method of Robert Blessing; Blessing, R.H. *Acta Cryst.* **1995**, *A51*, 33. (e) Sheldrick, G.M. "A short history of SHELX". *Acta Cryst*. **2008**, A64, 112. (f) Sluis, P. V. D.; Spex, A.L. *Acta Cryst*. **1990**, *A46*, 194. (g) Spex, A. L. *J. Apply. Cryst*.**2003**, *36*, 7.[a] Obtained with graphite monochromated Mo Kα (*l* = 0.71073 Å) radiation. [b]$R1 = \sum||F_o|-|F_c||/\sum|F_o|$. [c]$wR_2 = \{\sum[w(F_o^2-F_c^2)^2/\{\sum[w(F_o^2)^2]\}^{1/2}$. (h) COSMO V1.61, *Software for the CCD Detector Systems for Determining Data Collection Parameters.* Bruker Analytical X-ray Systems, Madison, WI (**2009**). (i) APEX2 V2010.11-3. Software *for the CCD Detector System*; Bruker Analytical X-ray Systems, Madison, WI (**2010**). (j) SAINT V 7.68A Software *for the Integration of CCD Detector System* Bruker Analytical X-ray Systems, Madison, WI (**2010**). (k) Dolomanov, O. V.; Bourhis,L. J.; Gildea,R. J.; Howard, J. A. K.; Puschmann, H. OLEX2: a complete structure solution, refinement and analysis program. *J. Appl. Cryst.* **2009**, *42*, 339.
3. Gagne, R.; Koval, C.; Licenski, G. *Inorg. Chem.* **1980,** *19*, 2854.
4. Fourmond, V.; Jacques, P. A.; Fontecave, M.; Artero, V. *Inorg. Chem.* **2010,** *49*, 10338.

www.manaraa.com

5. (a) Frisch, M. J.; Trucks, G. W.; Schlegel, H. B. *et al. Gaussian Development Version; Revision H.35 ed.; Gaussian, Inc.: Wallingford, CT* **2010.** (b) Becke, A. D. *J. Chem. Phys.* **1993,** *98,* 5648. (c) Perdew, J. P. *Phys. Rev. B* **1986,** *33,* 8822. (d) Perdew, J. P.; Burke, K.; Wang, Y. *Phys. Rev.* **1996,** *54,* 16533. (e) Dunning, T. H. Jr.; Hay, P. J. *In Modern Theoretical Chemistry, Ed. H. F. Schaefer III, Vol. 3 (Plenum: New York,* **1977**) 1-28. (f) Dolg, M.; Wedig, H.; Preuss, H. *J. Chem. Phys.* **1987,** *86,* 866. (g) Krishnan, R.; Binkley, J.S.; Seeger, R.; Pople, J. A. *J. Chem. Phys.* **1980,** *72,* 650.

www.manaraa.com

CHAPTER 3

MODULATION OF ELECTRONIC AND REDOX PROPERTIES IN PHENOLATE-RICH COBALT(III) COMPLEXES AND THEIR IMPLICATIONS FOR CATALYTIC PROTON REDUCTION

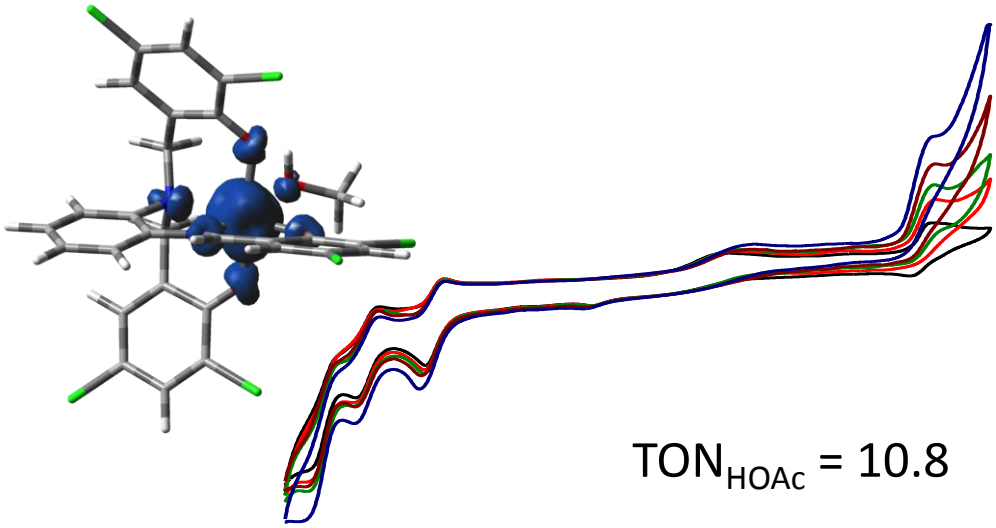

www.manaraa.com

CHAPTER 3

MODULATION OF ELECTRONIC AND REDOX PROPERTIES IN PHENOLATE-RICH COBALT(III) COMPLEXES AND THEIR IMPLICATIONS FOR CATALYTIC PROTON REDUCTION

Portions of the text in this chapter were reprinted or adapted with permission from: Basu, D.; Allard, M. M.; Xavier, F. R.; Heeg, M. J.; Schlegel, H. B.; Verani, C. N.* *Dalton Trans.* **2015**, *44*, 3454. All rights to the work are retained by the authors and any reuse requires permission of the authors.

3.1. Introduction

Considering the impending limitations of fossil fuels and the increasing demand for energy, the search for earth-abundant catalysts capable of hydrogen production is at the core of an economy based on renewable fuels.[1] The cobalt ion has been used in several proton-reduction electrocatalysts because of its energetically viable conversion from $3d^6$ ^{LS}Co(III) or $3d^7$ Co(II) into the procatalytic nucleophile $3d^8$ ^{LS}Co(I) species.[2] This species captures a proton to yield a reactive Co(III)-H species which can either stay in the Co(III)-H state or undergoes reduction to generate a Co(II)-H species; either of them able to react with another proton, thus yielding H_2.[3] Several ligands have been used to accommodate the cobalt ion; among the most studied figure oximes and polypyridines in pending-arm, macrocyclic, and iminopyridine motifs.[4] Although phenolate-based cobalt complexes have been used in olefin and epoxide polymerization,[5] these complexes are less favored for proton reduction because of the high overpotentials associated with the Co(II)/Co(I) couple, but the search for new architectures that either yield new catalysts or allow for rationalizations about catalyst design[6] is impending.

Our group is engaged in the chemistry of cobalt complexes with redox-active phenolate-rich environments focusing on tridentate [NN'O][7] and pentadentate [N_2O_3][8] ligands to predict

www.manaraa.com

structural, electronic, and redox properties of metallosurfactants, and the reactivity of metallodrugs. In [N_2O_3] environments with three *t*-butyl-decorated phenolates[8] four reversible redox-accessible states are present; three involving distinct phenolato/phenoxyl radical couples between 0.3 and 1.0 $V_{Fc+/Fc}$ and one process associated with the Co(III)/Co(II) couple at -0.6 $V_{Fc+/Fc}$. The redox processes were cycled 30 times without major decomposition at the surface of the electrode. These results are encouraging because reversibility of redox processes along with modulation of the Co(III)/Co(II) potential may be relevant for the development of proton reduction catalysts.

With the previous arguments in mind, we hypothesize that the nature of phenolate-linked substituent will modulate the potential by which cobalt(III)/(II) reduction takes place. Furthermore, based on recent literature,[9] we suggest that adventitious hydrogen-bonding may enhance the desired reversibility of the metal-based process.

In this chapter, we investigate the structural, electronic and redox behavior of five complexes, shown in **Scheme 1**, by means of experimental and computational methods. We also evaluate their behavior as electron acceptors in ascorbic acid-mediated reductions and in proton reduction in acidic media. The results follow.

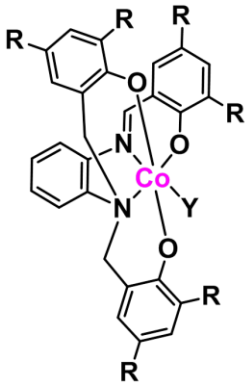

R = Cl; Y = MeOH (1)
R = Br; Y = MeOH (2)
R = I; Y = MeOH (3)
R = *t*-Bu; Y = MeOH (4)
R = *t*-Bu; Y = ^{4}*t*-Bu-Py (5)

Scheme 3.1. Cobalt(III) complexes of phenolate-rich ligands.

www.manaraa.com

3.2. Experimental

3.2.1. X-ray structural determination

Diffraction data for **1** and **2** were measured on a Bruker X8 APEX-II kappa geometry diffractometer with Mo radiation and a graphite monochromator. Frames were collected at 100 K with the detector at 40 mm and 0.3 degrees between each frame and were recorded for 10 s. APEX-II[10] and SHELX[11] software were used in the collection and refinement of the models. Crystals of **1** (CCDC # 1012180) appeared as dark needles. 106022 reflections were measured, yielding 7148 unique data (R_{int} = 0.074). Hydrogen atoms were placed in calculated positions. These neutral molecules crystallized without ions, solvent or appreciable disorder. Crystals of **2** (CCDC # 1012179) were dark rods. 58214 reflections were counted, which averaged to 7895 independent data (R_{int} = 0.089). Hydrogen atoms were placed at calculated positions. The solvate molecules occupied sites of symmetry and this did not refine without disorder in the space group *C*2/c. The PLATON program SQUEEZE[12] was utilized to include the solvate electrons resulting in an empirical formula of 1 complex: 1 dichloromethane molecule.

A red crystal of **5** (CCDC # 1012178) was mounted and collection of data was performed by using a Bruker CCD diffractometer. Omega and phi scans (0.5°/frame in the period of 30 s) were used to measure the data. The program COSMO[13] determined the sum of the images whereas completeness and redundancy was found to be 100% out to 0.83 Å and 4.0, respectively. APEX II software[14] was used to determine all the parameters related to the unit cell and SAINT was used for refinement. SAINT software[15] was used for the reduction of data. SADABS[16] was used to perform absorption and scaling related adjustments. SHELXS-97 program was implemented to solve the crystal structures and further refined by the method of least squares on both F^2 and SHELXL- 97 (SHELXTL-PC V 6.10).[12] This structure of **5** was measured and solved by Dr. Richard Staples from MSU and displayed C2/c (# 15) space group.

www.manaraa.com

Anisotropic corrections for all atoms (non-hydrogen) were executed. Geometrical techniques were used to calculate hydrogen atom and further refined by models based on riding method. T-butyl groups exhibited some sorts of disorder and therefore an implementation of a few restraints were performed. No sign of decomposition was observed during the mounting, collection, and solving processes. All the structural representation was shown at an ellipsoidal probability of 50%.

Table 3.1. Crystal Data for the complexes **1**, **2**, and **5**.

	1	**2**	**5**
Empirical formula	$C_{28}H_{19}Cl_6CoN_2O_4$	$C_{29}H_{21}Br_6Cl_2CoN_2O_4$	$C_{60}H_{82}CoN_3O_3$
Formula weight	719.08	1070.77	952.22
Temperature (K)	100(2)	100(2)	173(2)
Wavelength (Å)	0.71073	0.71073	0.71073
Crystal system, space group	Monoclinic, C2/c	Monoclinic, C2/c	Monoclinic, C2/c
a (Å)	22.0260(10)	28.251(3)	41.003(4)
b (Å)	12.9174(6)	13.5819(10)	14.7728(16)
c (Å)	22.6310(12)	22.091(2)	19.051(2)
α (º)	90	90	90
β (º)	116.109(3)	125.407(7)	102.408(10)
γ (º)	90	90	90
Volume ($Å^3$)	5781.9(5)	6908.9(10)	11270(2)
Z	8	8	8
Calculated density (Mg/m^3)	1.652	2.059	1.122
Absorption coefficient (mm^{-1})	1.187	7.629	0.348
F (000)	2896	4096	4112
R(F) (%)	4.39	8.22	6.03
R_w(F) (%)	6.70	11.29	11.29

[a]$R(F) = \Sigma \| F_o | - | F_c \| / | F_o |$; $Rw(F) = [\Sigma w(F_o^2 - F_c^2)^2/\Sigma w(F_o^2)^2]^{1/2}$ for *$I > 2\sigma(I)$*

3.2.2. Computational methods

Electronic structure calculations were carried out with the Gaussian 09 suite of programs[17] using Density Functional Theory (DFT). The B3PW91/6-31G(d) level of theory[18] was employed throughout. Geometries were fully optimized without symmetry constraints, and stationary

www.manaraa.com

points were verified via frequency analysis. Solvent effects in dichloromethane and/or acetonitrile were estimated using the built-in default settings of the IEF-PCM polarizable continuum model.[19] Vertical electronic excitation energies and intensities were calculated using time-dependent density functional theory (TD-DFT).[20] Molecular orbitals were plotted with GaussView and UV-visible spectral plots were prepared using SWizard with a full width at half-height of 2000 cm^{-1}. All optimized geometries agreed well with the crystallographic data available for all relevant structures.

3.2.3. Catalytic activity

Proton reduction electrocatalysis was tested for **1** and **4** via cyclic voltammetry in presence of acetic acid (HOAc, pKa: 22.3 in CH_3CN)[21a] with tetra-butyl ammonium hexafluorophosphate ($TBAPF_6$) as supporting electrolyte. For bulk electrolysis, the main chamber was filled with an electrolyte solution and proton source ($TBAPF_6$: 1.56 g; HOAc: 0.24 g [4 mmol], 20 mL acetonitrile) and the glass-fitted chamber was filled with another electrolyte solution ($TBAPF_6$: 0.39 g; 5 mL acetonitrile). Bulk electrolysis was conducted with catalyst (0.04 mmol) in acetonitrile (CH_3CN) for 180 minutes at -1.8 $V_{Ag/AgCl}$ and the head space gas (100 µL) was injected into the GC to record the amount of dihydrogen produced. After the background subtraction, the turnover number was calculated as the ratio of the moles of dihydrogen produced over the moles of catalyst used. Faradaic efficiency was calculated from the gas chromatography measurements.

www.manaraa.com

3.2.4. Synthetic procedures

The 2,4-substituted chloromethylphenols (pendant arms) where –R can be Cl or Br were synthesized under similar conditions (*vide infra*). The precursor 2-(chloromethyl)-4,6-diiodo phenol, 2-(chloromethyl)-4,6-di-*tert*-buytl-phenol, and the ligand 6,6′-(((2-((3,5-di-*tert*-butyl-2-hydroxybenzyl)amino)phenyl)azanediyl)bis(methylene)bis(2,4-di-*tert*-butyl-phenol) (**H_3L^{tBu}**) were synthesized according methods already described in the literature.[7c,8]

*The precursor 2,4-substituted-hydroxymethylphenols***.** A 70 mL methanol solution of the 3,5-di-substituted-2-hydroxybenzaldehyde (25.0 mmol) was reduced by $NaBH_4$ (60 mmol) at 0 °C overnight. Then, the solvent was removed under reduced pressure and the residual white solid was dissolved in water and the pH was adjusted to ~ 5.0 with 2.0 M HCl. The product was extracted from water using dichloromethane and dried over anhydrous Na_2SO_4. The solution was filtered and the solvent was removed by rotary evaporation yielding a white colored solid. The crude products were used with no further purification. 2,4-dichloro-6-(hydroxymethyl)phenol: Yield: 70%. IR (KBr, cm^{-1}) 3281(s) (OH); 3050(w) (Ar-CH); 2948(w) (alkyl-CH); 1596(w), 1580(w), 1474(s) (Ar-C-C); 1166(m) (C-O). ^{1}H-NMR [400 MHz, $CDCl_3$, 300 K] δ/ppm = 2.259 [s, 1H (aliphatic-OH)]; 4.779 [s, 2H (CH_2)]; 6.654 [s, 1H (aryl-OH)]; 7.129 [s, 1H (aryl)]; 7.289 [s, 1H (aryl)]. 2,4-dibromo-6-(hydroxymethyl)phenol: Yield: 70%. IR (KBr, cm^{-1}) 3508(m), 3241(m) (OH); 3075(w) (Ar-CH); 2934(w) (alkyl-CH); 1456(s) (Ar-C-C); 1141(s) (C-O). ^{1}H-NMR [400 MHz, $CDCl_3$, 300K] δ/ppm = 2.632 [s, 1H (aliphatic-OH)]; 4.786 [s, 2H (CH_2)]; 4.8 [s, 1H (aryl-OH)]; 6.921 [s, 1H (aryl)]; 7.590 [s, 1H (aryl)].

The precursor 2,4-substituted-chloromethylphenols. Thionyl chloride (50 mmol) was added to the solution of the previously synthesized alcohols (20 mmol) in 30 mL of dichloromethane. After stirring it overnight, the solvent was removed by rotary evaporation and

www.manaraa.com

washed five times with *n*-pentane. The 2,4-disubstituted-6-(chloromethyl)phenols were isolated as a white solid and used with no further purification. 2,4-dichloro-6-(chloromethyl)phenol: Yield: 94%. IR (KBr, cm^{-1}) 3474(s) (OH); 3081(w) (Ar-CH); 2978(w) (alkyl-CH); 1597(w), 1580(w), 1469(s) (Ar-C-C); 1161(s) (C-O). ^{1}H-NMR [400 MHz, $CDCl_3$, 300K] δ/ppm = 4.618 [s, 2H (CH_2)]; 5.775 [s, 1H (OH)]; 7.281 [s, 1H (aryl)]; 7.322 [s, 1H (aryl)]. 2,4-dibromo-6-(chloromethyl)phenol: Yield: 90%. IR (KBr, cm^{-1}) 3462(s) (OH); 3066(w) (Ar-CH); 2971(w) (alkyl-CH); 1461(s) (Ar-C-C); 1143(s) (C-O). ^{1}H-NMR [400 MHz, $CDCl_3$, 300K] δ/ppm = 4.618 [s, 2H (CH_2)]; 5.761 [s, 1H (aryl-OH)]; 7.445 [s, 1H (aryl)]; 7.577 [s, 1H (aryl)].

The proligands. Phenylene diamine (2 mmol) was treated with the appropriate 2,4-disubstituted-6-(chloromethyl)phenol (6.2 mmol) in presence of triethylamine (8 mmol) in 80 mL of dichloromethane for 3 days under reflux to yield a yellow colored solution. The mixture was washed three times with brine solution (3 × 200 mL) to remove excess triethylamine, dried over anhydrous sodium sulfate and the crude product was isolated by solvent rotoevaporation. Unreacted chloride was removed by washing the solid with cold hexane to yield a yellow-colored solid. Upon coordination to the metal these amine proligands are stabilized as imine ligands.[8]

6,6'-(((2-((3,5-dichloro-2-hydroxybenzyl)amino)phenyl)azanediyl)bis(methylene)bis(2,4-dichlorophenol) - ***$H_3L'^{Cl}$*.** Yield: 75%. IR (KBr, cm^{-1}) 3505(w), 3414(w) (OH); 3263(w) (NH); 3078(w) (Ar-CH); 2983(w) (alkyl-CH); 1599(m), 1467(s) (Ar-C-C); 1165(m) (C-O). ^{1}H-NMR [400 MHz, $CDCl_3$, 300K] δ/ppm = 4.093 [s, 4H (CH_2)]; 4.263 [s, 2H (CH_2)]; 6.61 [d, 1H (aryl)]; 6.776 [t, 1H (aryl)]; 6.887 [s, 2H (aryl)]; 7.011 [t, 1H (aryl)]; 7.068 [s, 1H (aryl)]; 7.167 [d, 1H (aryl)]; 7.212 [s, 2H (aryl)]; 7.3 [s, 1H (aryl)]. ESI pos. in MeOH: m/z = 630.9670 for $[H_3L_1 + H^+]^+$.

www.manaraa.com

6,6'-(((2-((3,5-dibromo-2-hydroxybenzyl)amino)phenyl)azanediyl)bis(methylene)bis(2,4-dibromophenol) - $\boldsymbol{H_3L'^{Br}}$. Yield: 70%. IR (KBr, cm^{-1}) 3490(w) (OH); 3252(w) (NH); 3070(w) (Ar-CH); 2982(w) (alkyl-CH); 1598(m), 1455(s) (Ar-C-C); 1144(m) (C-O). ^{1}H-NMR [400 MHz, $CDCl_3$, 300K] δ/ppm = 4.096 [s, 4H (CH_2)]; 4.249 [s, 2H (CH_2)]; 6.644 [d, 1H (aryl)]; 6.798 [t, 1H (aryl)]; 7.023 [t, 3H (aryl)]; 7.157 [d, 1H (aryl)]; 7.268 [s, 1H (aryl)]; 7.475 [s, 2H (aryl)]; 7.542 [s, 1H (aryl)] ESI pos. in MeOH: m/z = 894.7 for $[H_3L_2 + H^+]^+$.

6,6'-(((2-((2-hydroxy-3,5-diiodobenzyl)amino)phenyl)azanediyl)bis(methylene))bis(2,4-diiodophenol) - $\boldsymbol{H_3L'^{I}}$. Yield: 73%. IR (KBr, cm^{-1}) 3385(w) (OH); 3226(w) (NH); 3061(w) (Ar-CH); 2920(w) (alkyl-CH); 1598(m), 1451(s) (Ar-C-C); 1147(m) (C-O). ^{1}H-NMR [400 MHz, $CDCl_3$, 300K] δ/ppm = 4.07 [s, 4H (CH_2)]; 4.238 [s, 2H (CH_2)]; 6.733[t, 2H (aryl)]; 6.867 [t, 1H (aryl)]; 7.077 [t, 2H (aryl)]; 7.183 [d, 2H (aryl)]; 7.526 [s, 1H (aryl)]; 7.809 [s, 1H (aryl)]; 7.961 [s, 1H (aryl)] ESI pos. in MeOH: m/z = 1182.582 for $[H_3L_3 + H^+]^+$.

The Complexes. Caution: Perchlorate salts are potentially explosive and should be handled with utmost care and in small quantities. Complexes **1**-**4** have been synthesized under aerobic conditions using the general procedure described as follows: To a 30 mL solution of ligand (1 mmol) in dichloromethane sodium methoxide (0.162 g, 3 mmol) in 30 mL of methanol, was added and the mixture was stirred for 10 minutes. A 20 mL methanol solution of $[Co(H_2O)_6](ClO_4)_2$ (0.365 g, 1 mmol) was then added dropwise to the mixture in a period of 5 minutes. After the addition was complete, the solution was refluxed for 4 hours to ensure the completion of reaction, then the mixture was concentrated to 10 mL. Slow evaporation of the solvent gives rise to brown colored precipitate which was collected by vaccum filtration. Further recrystalization from different solvent mixtures give crystalline pure product.

www.manaraa.com

[$Co^{III}(L^{Cl})MeOH$] **(1).** Recrystallized from MeOH/diethyl ether (1:1). Yield. 80%. IR (KBr, cm^{-1}) 3444(w) (OH); 3063(w) (Ar-CH); 2950(w) (alkyl-CH); 1612(s), 1450(s) (Ar-C-C); 1584(m) (C=N); 1177(m) (C-O); No ClO_4^-. ^{1}H-NMR [400MHz, d^6-DMSO, 300K] δ/ppm = 3.150 [d, 3H (CH_3)]; 3.967 [d, 2H (CH_2)]; 4.083 [q, 1H (OH)]; 4.767 [d, 2H (CH_2)]; 6.734 [s, 2H (aryl)]; 6.820 [s, 2H (aryl)]; 7.138 [t, 1H (aryl)]; 7.300 [t, 1H (aryl)]; 7.552 [s, 1H (aryl)]; 7.645 [s, 1H (aryl)]; 7.686 [d, 1H (aryl)]; 7.955 [s, 1H (N=CH)]; 8.056 [d, 1H (aryl)]. ESI pos. in MeOH: m/z = 684.8624 for $[Co^{III}(L'^{Cl}) + H^+]^+$. Anal. Calcd for $C_{28}H_{19}Cl_6CoN_2O_4$: C, 46.77; H, 2.66; N, 3.90. Found: C, 46.46; H, 2.64; N, 4.00.

[$Co^{III}(L^{Br})MeOH$] **(2).** Recrystallized from MeOH/DCM (1:1). Yield. 85%. IR (KBr, cm^{-1}) 3263(w) (OH); 3050(w) (Ar-CH); 2945(w) (alkyl-CH); 1612(m), 1442(s) (Ar-C-C); 1584(m) (C=N); 1157(m) (C-O); No ClO_4^-. ^{1}H-NMR [400MHz, d^6-DMSO, 300K] δ/ppm = 3.149 [d, 3H (CH_3)]; 3.977 [d, 2H (CH_2)]; 4.077 [q, 1H (OH)]; 4.8 [d, 2H (CH_2)]; 6.877 [s, 2H (aryl)]; 7.032 [s, 2H (aryl)]; 7.145 [t, 1H (aryl)]; 7.295 [t, 1H (aryl)]; 7.693 [d, 1H (aryl)]; 7.724 [s, 1H (aryl)]; 7.843 [s, 1H (aryl)]; 7.981 [s, 1H (N=CH)]; 8.054 [d, 1H (aryl)]. ESI pos. in MeOH: m/z = 954.5676 for $[Co^{III}(L'^{Br}) + Li^+]^+$. Anal. Calcd for $C_{28}H_{19}Br_6CoN_2O_4$: C, 34.11; H, 1.94; N, 2.84. Found: C, 33.60; H, 1.81; N, 2.95.

[$Co^{III}(L^{I})MeOH$] **(3). ^{i}PrOH** Recrystallized from DCM/isopropanol (1:1). Yield. 90%. IR (KBr, cm^{-1}) 3443(w) (OH); 3047(w) (Ar-CH); 2925(w) (alkyl-CH); 1610(m), 1427(s) (Ar-C-C); 1581(m) (C=N); 1150(m) (C-O); No ClO_4^-. ^{1}H-NMR [400MHz, d^6-DMSO, 300K] δ/ppm = 3.147 [d, 3H (CH_3)]; 3.945 [d, 2H (CH_2)]; 4.01 [q, 1H (OH)]; 4.808 [d, 2H (CH_2)]; 6.978 [s, 2H (aryl)]; 7.065 [t, 1H (aryl)]; 7.116 [t, 1H (aryl)]; 7.271 [s, 2H (aryl)]; 7.718 [d, 1H (aryl)]; 7.843 [d, 1H (aryl)]; 7.945 [s, 1H (N=CH)]; 8.044 [s, 2H (aryl)]. ESI pos. in MeOH: m/z = 1242.4844 for $[Co^{III}(L'^{I}) + Li^+]^+$. Anal. Calcd for $C_{31}H_{27}I_6CoN_2O_5$: C, 28.04; H, 2.05; N, 2.11 Found: C,

www.manaraa.com

28.55; H, 1.55; N, 2.52.

[$Co^{III}(L^{t\text{-}Bu})MeOH$][8] **(4)**. Recrystallized from MeOH/DCM. ^{1}H-NMR [400MHz, d^{6}-DMSO, 300K] δ/ppm = 0.86 [s, 18H (t-butyl)]; 1.00 [s, 18H (t-butyl)]; 1.24 [s, 9H (t-butyl)]; 1.62 [s, 9H (t-butyl)]; 3.145 [d, 3H (CH_3)]; 3.855 [d, 2H (CH_2)]; 4.085 [q, 1H (OH)]; 4.865 [d, 2H (CH_2)]; 6.46 [s, 2H (aryl)]; 6.53 [s, 2H (aryl)]; 6.88 [t, 1H (aryl)]; 7.08 [t, 1H (aryl)]; 7.10 [s, 1H (aryl)]; 7.28 [s, 1H (aryl)]; 7.53 [s, 1H (N=CH)]; 7.645 [d, 1H (aryl)]; 8.035 [d, 1H (aryl)].

[$Co^{III}(L^{t\text{-}Bu})$4-t-bu-pyridine] **(5)**. To a 20 mL solution of complex **4** (0.425g, 0.5 mmol) in DCM, excess 4-t-butyl pyridine (0.135, 1 mmol) in 20 mL of methanol was added and refluxed for 2 hours. To ensure the completion of this reaction it has been further stirred for 2 hours and then concentrated to 10 mL. Slow evaporation of the solvent gives rise to brown colored precipitate which was collected by vaccum filtration. Recrystallization form MeOH/DCM (1:1) gives crystalline pure product. Yield. 95%. IR (KBr, cm^{-1}) 3088(w), 3030(w) (Ar-CH); 2952(s), 2903(m), 2868(m) (t-bu C-H); 1616(m), 1602(m), 1463(m) (Ar-C-C); 1585 (m) (C=N); No ClO_4^-. ^{1}H-NMR [400MHz, d^{6}-DMSO, 300K] δ/ppm = 0.87 [s, 18H (t-butyl)]; 1.00 [s, 18H (t-butyl)]; 1.25 [s, 9H (t-butyl)]; 1.35 [s, 9H (t-butyl)]; 1.64 [s, 9H (t-butyl)]; 3.89 [t, 2H (CH_2)]; 4.40 [d, 1H (CH_2)]; 4.87 [d, 1H (CH_2)]; 6.46 [d, 2H (aryl)]; 6.54 [s, 1H (aryl)]; 6.64 [s, 1H(aryl)]; 7.12 [d, 2H (aryl)]; 7.28 [s, 1H (aryl)]; 7.38 [s, 1H (aryl)]; 7.54 [s, 1H (aryl)]; 7.71 [d, 1H (aryl)]; 7.80 [d, 1H (aryl)]; 7.94 [s, 1H (aryl)]; 8.05 [d, 1H (aryl)]; 8.46 [d, 1H (aryl)]; 9.07 [d, 1H (aryl)]. ESI pos. in MeOH: m/z = 951.5703 for $[Co^{III}(L^{t\text{-}Bu})$4-t-bu-pyridine$]^{+}$. Anal. Calcd for $C_{60}H_{82}CoN_3O_3$: C, 75.68; H, 8.68; N, 4.41 Found: C, 75.21; H, 8.48; N, 4.27.

www.manaraa.com

3.3. Results and discussions

3.3.1. Syntheses and characterizations

A series of asymmetrical pentadentate ligands was synthesized by treatment of 1,2-diaminobenzene with 2,4-disubstituted-chloromethylphenol precursors bearing chloro (**1**), bromo (**2**), iodo (**3**) and *t*-butyl (**4** and **5**) functionalities in presence of triethylamine in dichloromethane (**Figure 3.1**). Pale yellow solids were obtained for each ligand after brine extraction and characterized with spectroscopic (FTIR and ^{1}H-NMR) and ESI-MS spectrometric methods.

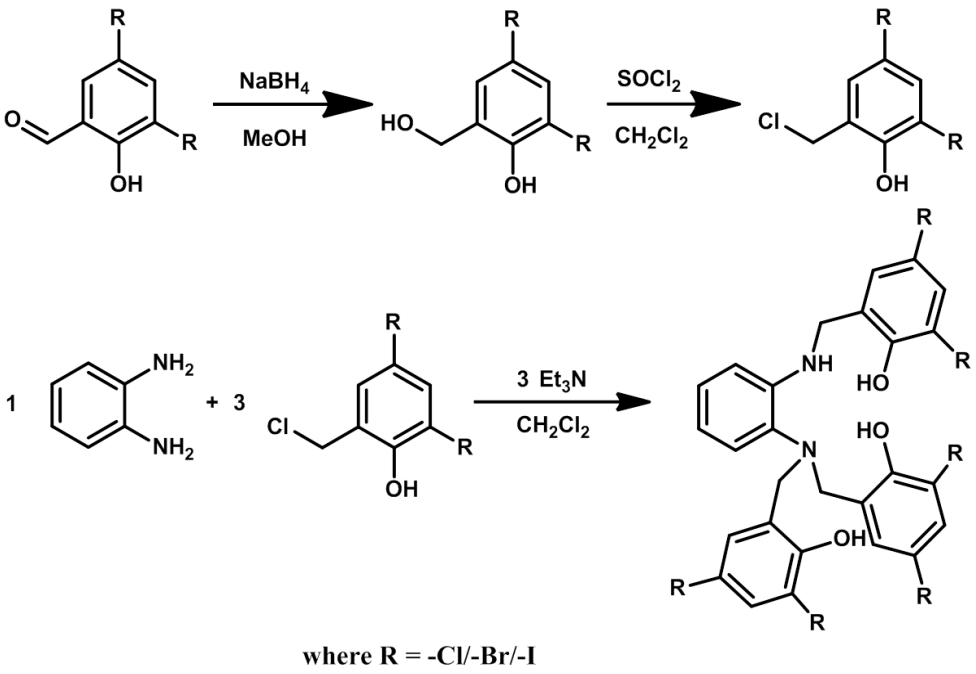

where R = -Cl/-Br/-I

Figure 3.1. Synthesis of the precursors and ligands.

The ligands were dissolved in methanol and treated with cobalt(II) perchlorate under aerobic conditions and in the presence of sodium methoxide to afford the desired cobalt(III) complexes **1-4** (**Figure 3.2.**). During the course of the reaction, the cobalt(II) ion is oxidized into cobalt(III) and the ligand is oxidized from its amine to imine form. Complex **5** has been synthesized by reaction of **4** with excess of 4-t-butyl-pyridine in a MeOH/DCM (1:1) solvent mixture (**Figure**

www.manaraa.com

3.2.).

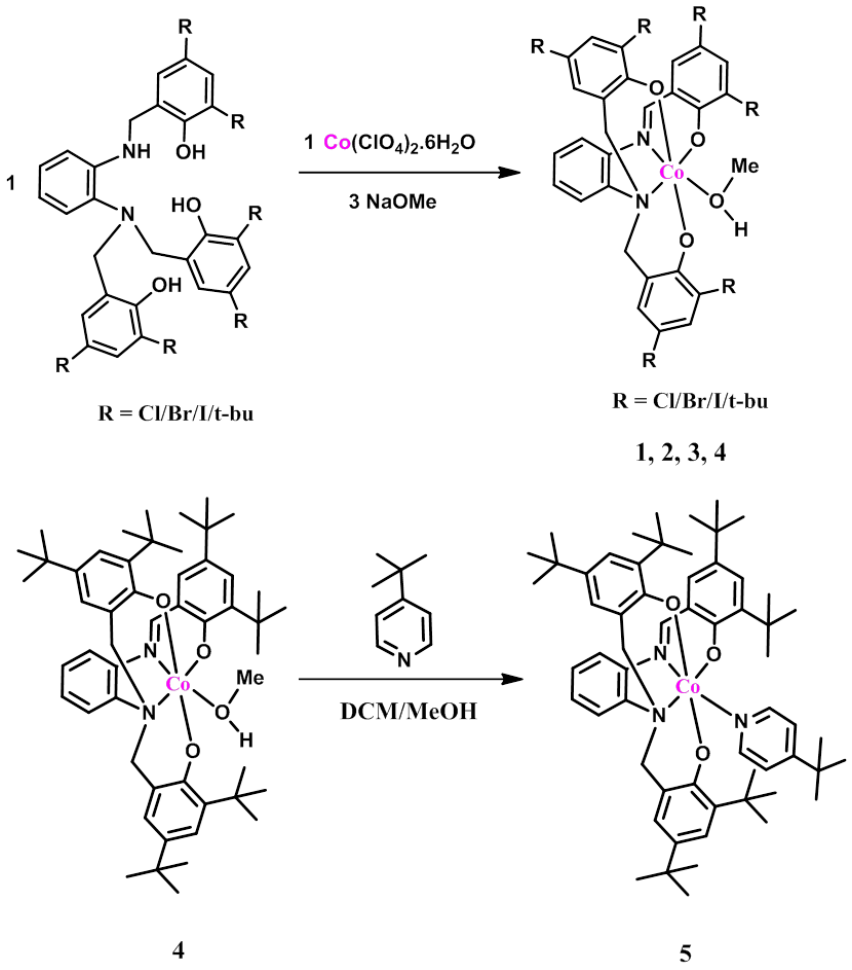

Figure 3.2. Synthesis of the cobalt(III) complexes **1**-**5**.

Compounds **1-5** were characterized by spectroscopic and spectrometric methods. The FTIR spectra for each complex confirms a C=N streaching around 1585 cm^{-1} resulting from ligand oxidation. The absence of peaks associated with the perchlorate anions confirms **1-5** as neutral Co(III) species, in excellent agreement with the resulting elemental analyses. High-resolution ESI mass spectra show the species $[M+H^+]^+$, $[M+Li^+]^+$, and $[M+Li^+]^+$, for **1-3**, respectively and

www.manaraa.com

$[M]^+$ for **5** (**Figure 3.3**). Experimental and simulated isotopic distributions are in agreement with the proposed molecular composition.

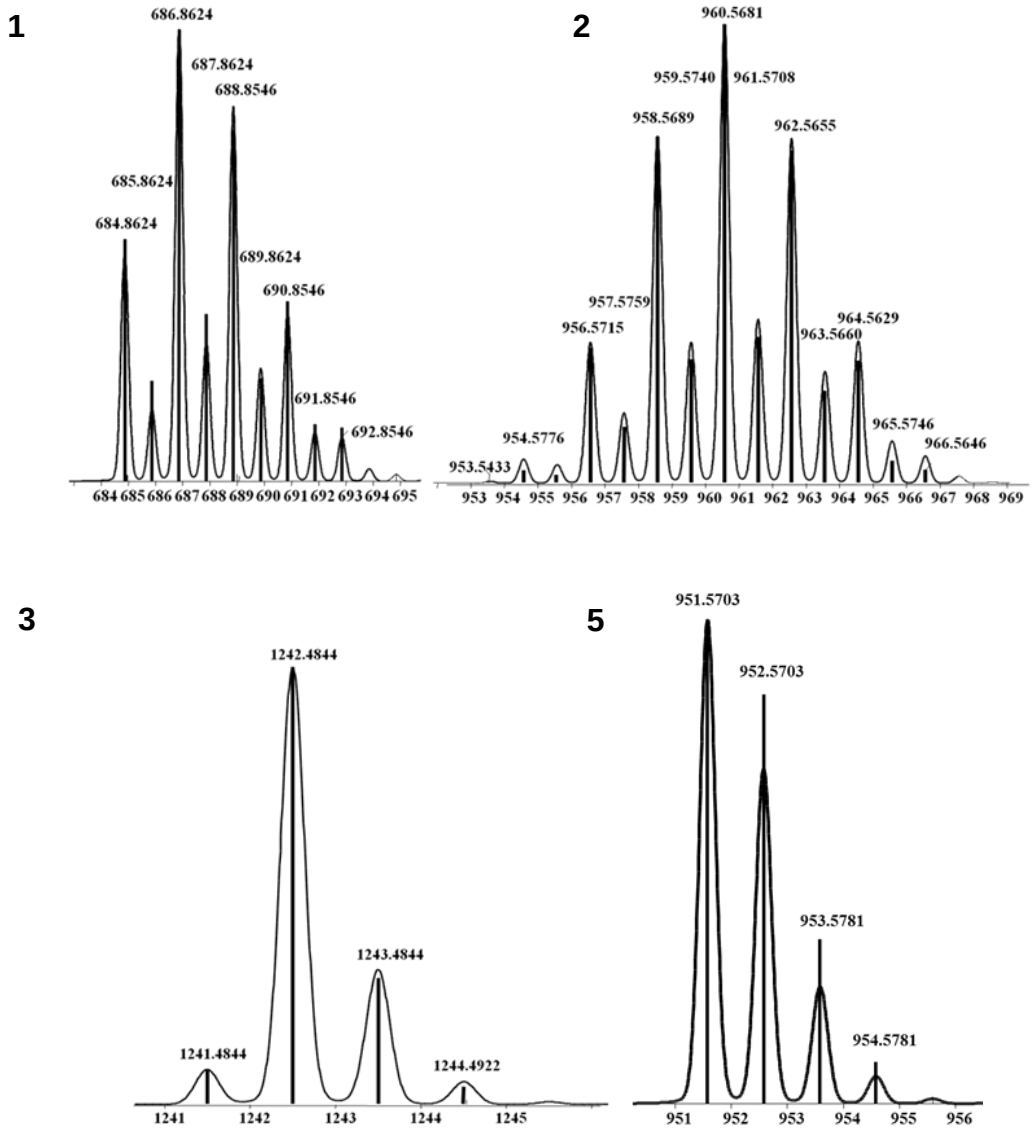

Figure 3.3. Experimental (bars) and simulated (line) isotopic distribution for the molecular ions of complexes **1**-**3** & **5**.

Due to the diamagnetic nature of the low spin cobalt(III) complexes the ^{1}H-NMR spectra for all the complexes were taken in d^6-DMSO. The spectra have shown appropriate line-splitting patterns for **1**-**4** with ten typical aromatic protons, the azomethine proton resonance (over the

www.manaraa.com

aromatic region), and four methylene hydrogens between 4.0 and 5.0 ppm. A methanol molecule bound to the sixth coordination position of the Co(III) center was assigned with a resonance line between 3.0 and 3.3 ppm for **1**-**4**. Species **4** shows intense peaks between 0 to 2 ppm due to the presence of *tert*-butyl substituents. Selected ^{1}H-NMR spectra for **1** and **4** are shown in **Figure 3.4**. Species **1**, **2** and **5** had their molecular structures solved by X-ray analysis, while complex **4** was described previously.[8]

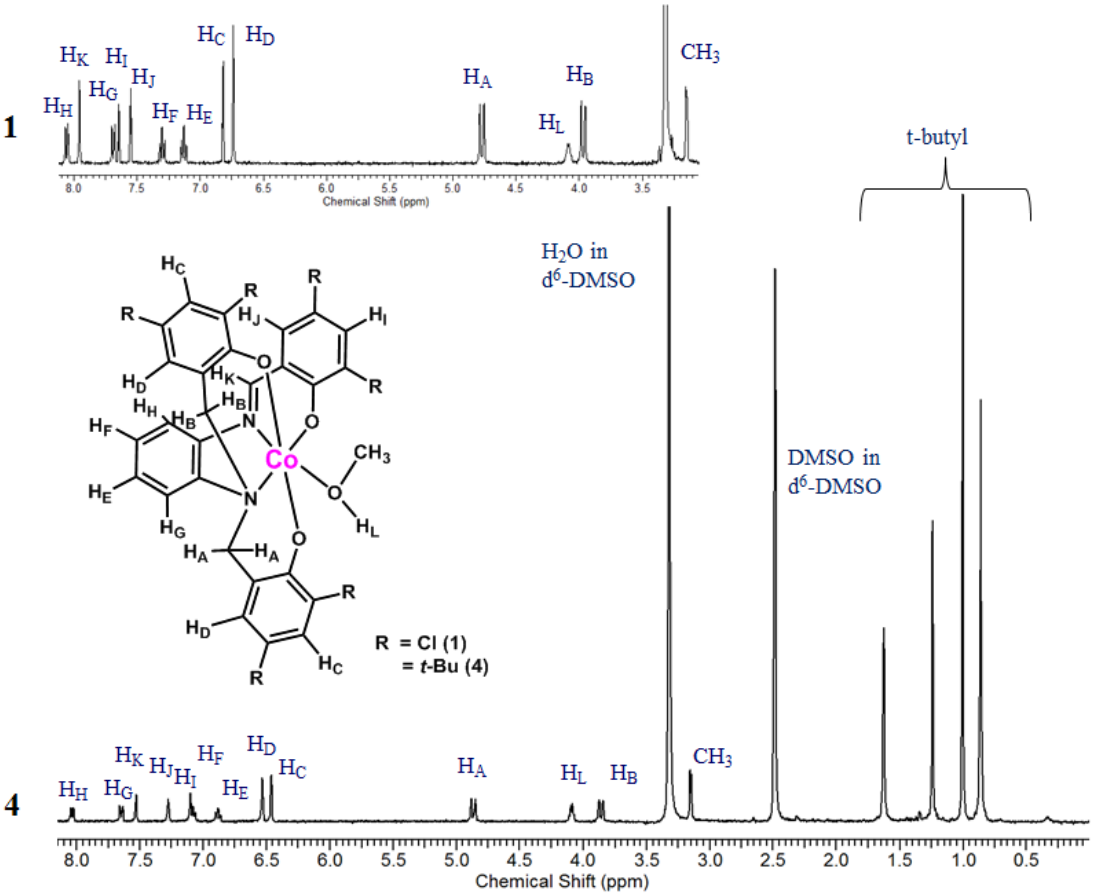

Figure 3.4. ^{1}H-NMR spectra for compounds **1** and **4** in d^{6}-DMSO.

www.manaraa.com

3.3.2. Molecular structures

Complexes **1**, **2** and **5** yielded well-formed brown crystals used for single crystal X-ray diffractometric analysis. The atomic labeling schemes of **1**, **2** and **5** are shown in **Figure 3.5.** while selected bond lengths and angles are shown in **Table 3.2.**

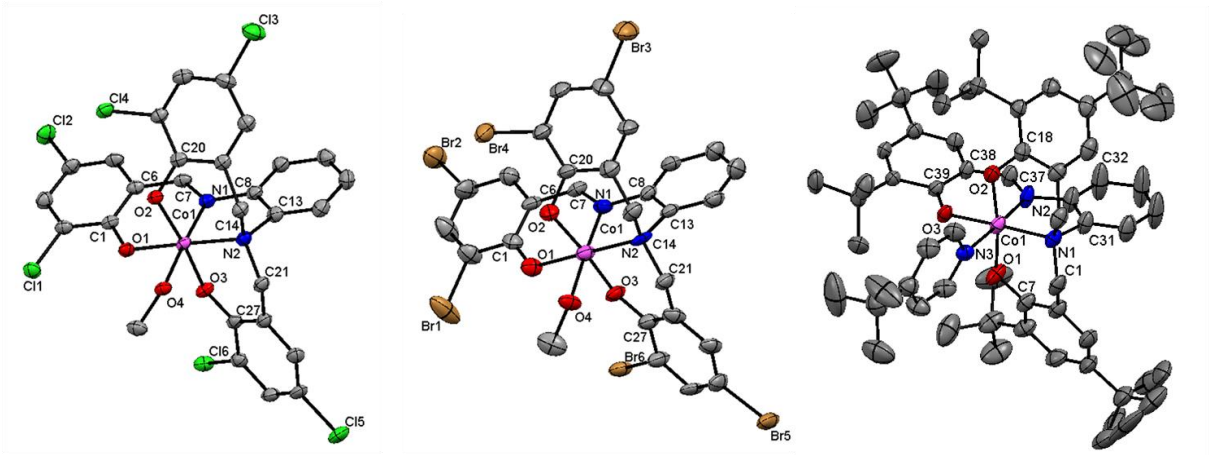

[$Co^{III}(L^{Cl})$MeOH] (1) **[$Co^{III}(L^{Br})$MeOH] (2)** **[$Co^{III}(L^{t\text{-}Bu})$4-t-bu-pyridine] (5)**

Figure 3.5. ORTEP[22] representations of **1**, **2** and **5** (left to right).

Complexes **1** and **2** belong to a C2/c monoclinic space group. Both crystal structures reveal a mononuclear $[Co^{III}L^{X}(MeOH)]$ neutral complex unit (X = Cl or Br) where each of the cobalt(III) centers is in an $[N_2O_4]$ coordination environment. A distorted octahedral geometry is imposed over the metallic ion by the three phenolate arms, the rigid azomethine, the amine moieties, and the coordinated methanol molecule, as summarized by the selected bond lengths and angles shown in **Table 3.2**. In all three structures the O1 oxygen atoms associated with the iminophenolates are coordinated to the Co1 center in a *trans* position to the N2 amine nitrogen atom, while the O2 and O3 aminophenolate oxygen atoms are *trans* to each other. The O4 oxygen atom of the weakly bound protonated molecule of methanol is *trans* to the N1 imine nitrogen atoms. This Co–O(4) is the longest, reaching 1.95 to 2.01 Å. The Co--$O_{phenolate}$ bonds

www.manaraa.com

vary between 1.87 and 1.92 Å, with the Co-O2 bonds being slightly longer than Co-O1 and Co-O3. The Co-N bonds show considerable length variability, with a short Co-N1 ≈ 1.87 Å associated with the C=N group (N1–C7 ≈ 1.29 Å) and longer Co-N2 ≈ 1.98 Å associated with the amine group. The average N1-C8 bond length at 1.41Å for **1** and **2** is slightly shorter than the equivalent N2-C13 (av. 1.47Å), thus suggesting electron delocalization along with the 1,2-diaminobenzene ring and the iminophenolate arm (**Figure 3.6**). Shorter O1-C1 (av. 1.30 Å) and C6-C7 (av. 1.42 Å) bonds reinforce the argument while the C6-C7-N1-C8 dihedral angles of 177.7(3)° for **1** and 174.3(8)° for **2** reveal planarity indicative of a conjugated π framework. The geometrical arrangement, as well as the bond lengths and angles are isostructural with the previously reported **4** and other species in similar [$N_2O_3O_{MeOH}$] environments.[8]

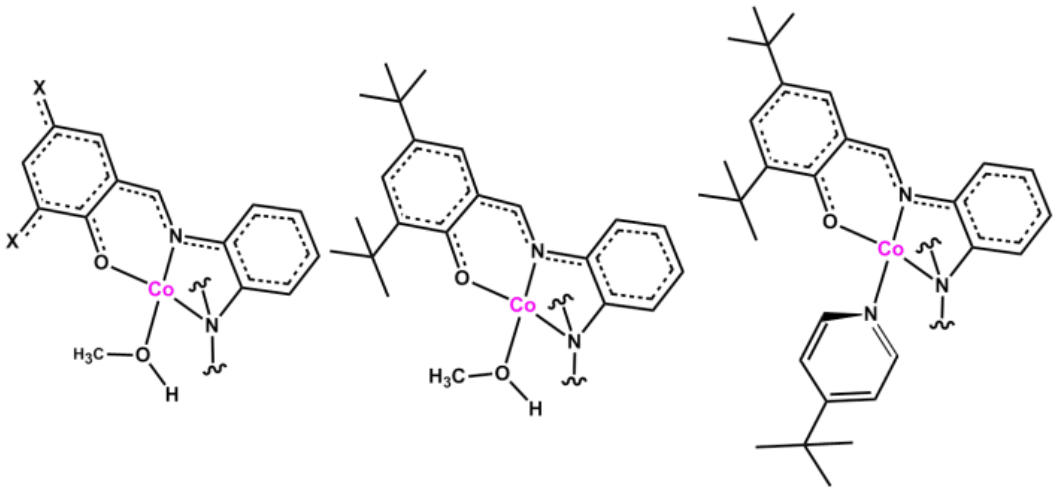

Where X = -Cl/-Br/-I; Partial structure used for simplicity

Figure 3.6. Fully conjugated structure of phelonate-imine-diamino aromatic ring system.

Complex **5** belongs to a C2/c monoclinic space group with similar pseudo-octahedral geometry imposed by the coordination sphere around the Co(III) ion. However, species **5** shows 4-*t*-butyl-pyridine replacing the methanol found in the sixth position of **1** and **2**. The Co1-N3 distance reaches 2.011 Å, while other chemical bonds are comparable to those previously

www.manaraa.com

described, including the 1,2-diaminobenzene/iminophenolate plane with a C38-C37-N2-C32 dihedral angle of 178.6(4)^{o}. The *t*-butyl-pyridine organizes itself perpendicular to that plane.

Table 3.2. Selected bond lengths and bond angles.

1		**2**		**5**	
Co1-N1	1.878(2)	Co1-N1	1.879(8)	Co1-N2	1.876(3)
Co1-N2	1.986(2)	Co1-N2	1.981(8)	Co1-N1	1.982(3)
Co1-O1	1.871(2)	Co1-O1	1.886(7)	Co1-O3	1.886(2)
Co1-O2	1.9077(19)	Co1-O2	1.925(7)	Co1-O2	1.902(2)
Co1-O3	1.8834(19)	Co1-O3	1.870(7)	Co1-O1	1.894(2)
Co1-O4	1.9627(19)	Co1-O4	1.955(7)	Co1-N3	2.011(3)
N1-C7	1.296(4)	N1-C7	1.305(12)	N2-C37	1.298(4)
N2-C14	1.517(4)	N2-C14	1.520(13)	N1-C16	1.507(4)
N2-C21	1.498(4)	N2-C21	1.501(11)	N1-C1	1.510(4)
N1-C8	1.426(4)	N1-C8	1.406(12)	N2-C32	1.416(5)
N2-C13	1.470(3)	N2-C13	1.473(14)	N1-C31	1.467(4)
O1-C1	1.297(3)	O1-C1	1.302(12)	O3-C39	1.302(4)
O2-C20	1.331(3)	O2-C20	1.357(11)	O2-C18	1.335(4)
O3-C27	1.316(3)	O3-C27	1.336(10)	O1-C7	1.336(4)
N1-Co1-O2	92.88(9)	N1-Co1-O2	92.6(3)	N2-Co1-O2	89.86(12)
O1-Co1-O2	85.41(9)	O1-Co1-O2	86.3(3)	O3-Co1-O2	86.43(10)
O2-Co1-O4	87.93(8)	O2-Co1-O4	89.4(3)	O2-Co1-N3	87.95(11)
O2-Co1-N2	94.81(9)	O2-Co1-N2	93.4(3)	O2-Co1-N1	95.10(11)
O1-Co1-N1	96.04(10)	O1-Co1-N1	95.4(3)	O3-Co1-N2	94.85(11)
O1-Co1-O3	87.58(9)	O1-Co1-O3	88.4(3)	O3-Co1-O1	85.44(10)
O1-Co1-O4	87.27(8)	O1-Co1-O4	86.5(3)	O3-Co1-N3	83.54(10)
N1-Co1-N2	85.65(10)	N1-Co1-N2	85.7(3)	N2-Co1-N1	85.95(12)
N1-Co1-O3	87.65(9)	N1-Co1-O3	87.8(3)	N2-Co1-O1	91.32(13)
O3-Co1-N2	92.21(9)	O3-Co1-N2	91.9(3)	O1-Co1-N1	93.02(11)
O4-Co1-N2	91.03(9)	O4-Co1-N2	92.5(3)	N3-Co1-N1	95.72(11)
O3-Co1-O4	91.95(8)	O3-Co1-O4	90.5(3)	O1-Co1-N3	90.64(11)

3.3.3. Electronic and electrochemical properties

3.3.3.1. Calculated electronic structures

Insight into the nature of the molecular orbitals of complexes **1**, **2**, **4**, and **5** were obtained by means of DFT calculations. Complexes **4** and **5** were modeled replacing the *t*-butyl groups of the phenolate rings by methyl groups (**4^{Me}**). In agreement with the ^{1}H-NMR data, the orbital

www.manaraa.com

occupancies are shown in **Figure 3.7** plotted as comparative molecular orbital ladders of diamagnetic closed shell singlets of $3d^6$ ^{LS}Co(III) complexes. The calculated bond lengths are consistent with experimental data. An energy difference of 0.6 eV (~14 kcal/mol) becomes evident when comparing the highest occupied molecular orbitals (HOMOs) of the electron-withdrawing chloro-substituted **1** with those of the electron-donating methyl-substituted **4**. The first four HOMOs, namely HOMO, HOMO-1, HOMO-2, and HOMO-3 are predominantly based on the phenolato groups, in good agreement with previous assignments.[7d-e,8,23,24] Species **1** and **2**, and species **4** and **5** are respectfully comparable to each other in MO occupancy and orbitals energies (**Figure 3.7** and **Figure 3.8**). A noticeable effect of halogen substitution on **1** and **2** is the energy lowering of the first three unoccupied orbitals LUMO, LUMO+1, and LUMO+2 which correspond to the empty π* orbital of the imine, and two empty Co-based orbitals, respectively.

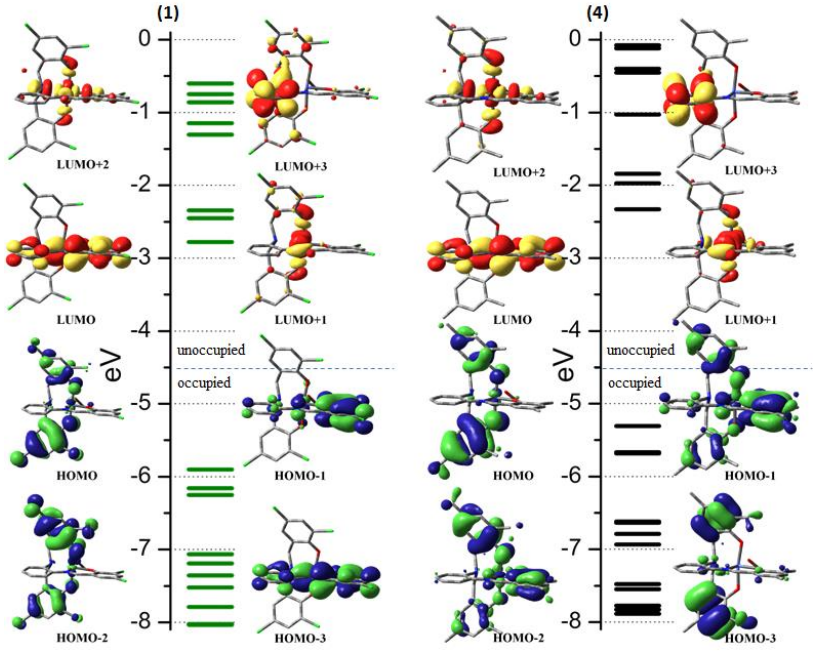

Figure 3.7. MO ladders and plots for **1** (left) and **4** (right).

www.manaraa.com

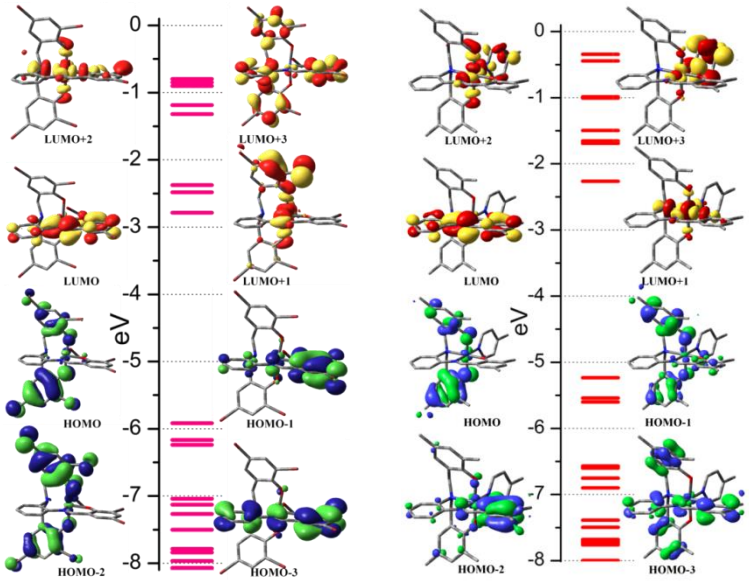

Figure 3.8. MO ladders and plots for **2** (left) and **5** (right).

3.3.3.2. Effect of ligand substitution and solvents in the electronic spectra

The electronic spectra of **1-5** were measured in acetonitrile and dichloromethane (**Figures 3.9, 3.10, 3.11**) and summarized in **Table 3.3**. UV-visible spectra were also measured in other coordinating solvents (**Figure 3.12**). The complexes show charge-transfer absorptions between 400 and 800 nm along with processes below 400 nm, typically associated with ligand-centered charge transfer.

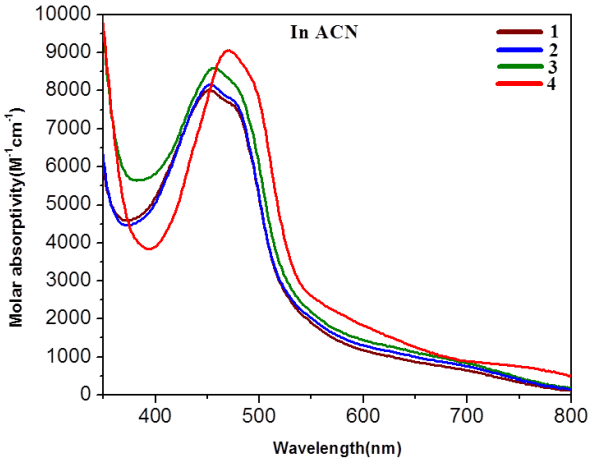

Figure 3.9. UV-Visible spectra of **1**– **4** (1.0×10^{-4} M; acetonitrile).

www.manaraa.com

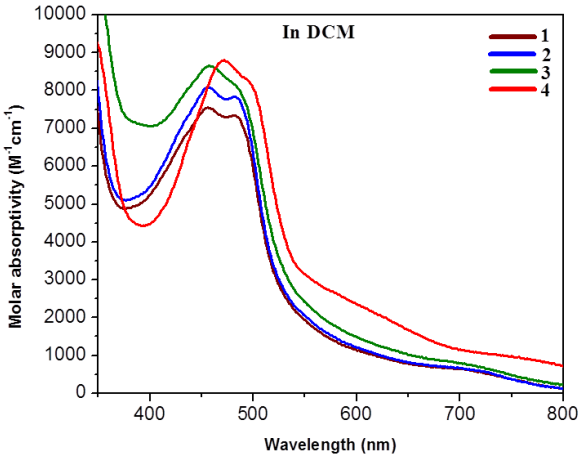

Figure 3.10. UV-visible spectra of **1-4** ([C] = 1.0×10^{-4} M) in dichloromethane.

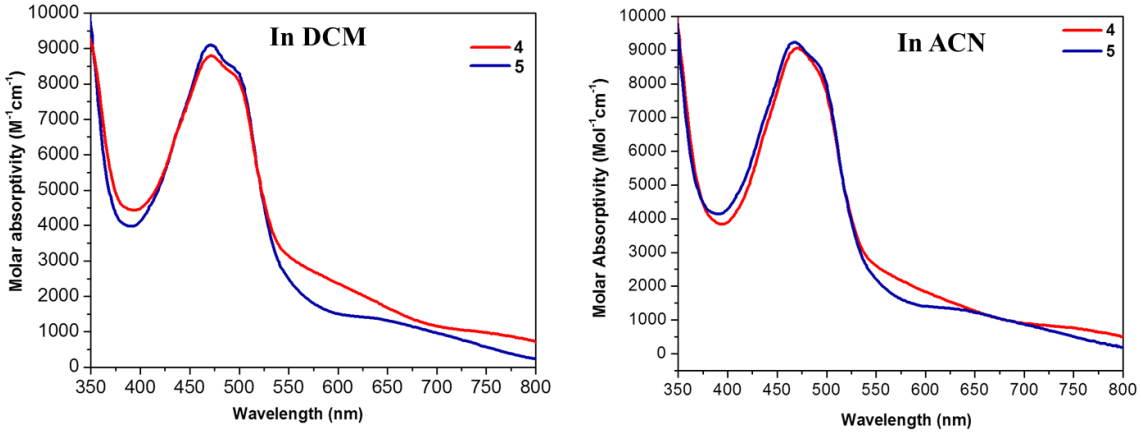

Figure 3.11. Comparative UV-visible spectra of complexes **4** and **5** in dichloromethane and acetonitrile.

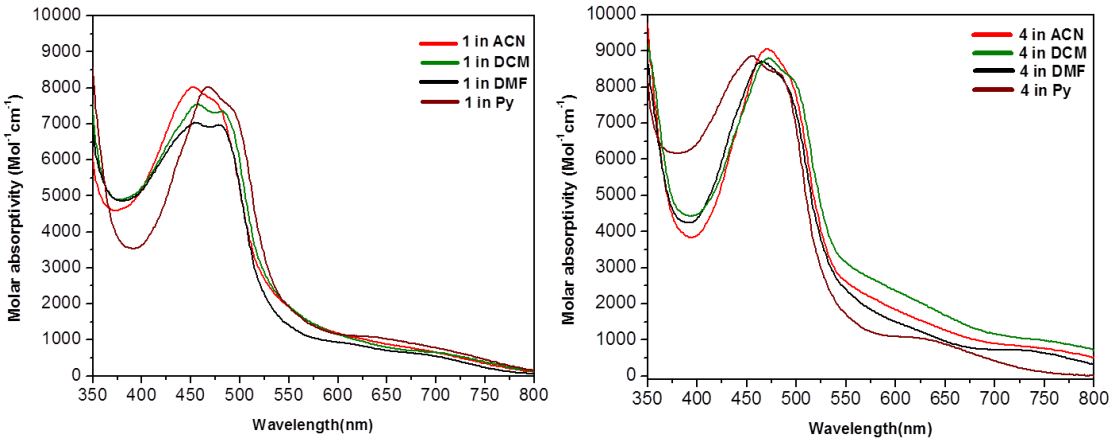

Figure 3.12. Comparison of UV-visible spectra for **1** and **4** in different solvents (acetonitrile, dichloromethane, dimethyl formamide and pyridine).

www.manaraa.com

The two strong but ill-solved bands between 400-500 nm are attributed to a phenolate-to-azomethine intraligand charge transfer (ILCT, 450 - 475 nm) and a ligand-to-metal charge transfer process (LMCT) involving an in-plane $p\pi_{phenolate} \rightarrow d\sigma^*_{Co(III)}$ transition[25] (475 - 500 nm). The shoulders seen at lower energy (550-800 nm) are attributed to out-of-plane $p\pi_{phenolate} \rightarrow d\sigma^*_{Co(III)}$[26] LMCT processes. A modest variation in the position of the ILCT and in-plane LMCT processes can be associated with the electron withdrawing or donating nature of the phenolate-installed substituents in the order **1** < **2** < **3** < **4**. Similarly, the LMCT bands for **1**-**3** in acetonitrile are hypsochromically shifted by 8-16 nm, when compared to dichloromethane, thus indicating that acetonitrile replaces the weakly bound methanol molecule in solution. Although changes are more subtle for **4** and **5**, the ability to replace methanol is relevant for proton-reduction catalysis.

Table 3.3. UV-Visible spectroscopic data for **1**-**5** in dichloromethane and acetonitrile.

Compound	**λ_{max}, nm / (ε, $M^{-1}.cm^{-1}$) in acetonitrile**	**λ_{max}, nm / (ε, $M^{-1}.cm^{-1}$) in dichloromethane**
1	451 (8034), 475 (7602), 697 (594)	455 (7431), 486 (7323), 712 (565)
2	453 (8160), 476 (7751), 696 (755)	456 (8077), 486 (7782), 712 (582)
3	456 (8592), 479 (8053), 697 (796)	457 (8684), 487 (8012), 712 (634)
4	468 (9011), 492 (8305), 757 (656)	471 (8798), 496 (8174), 759 (958)
5	466 (9253), 493 (8494), 658 (1167)	470 (9106), 497 (8357), 652 (1304)

Time-dependent DFT methods were used to model and assign the bands observed in acetonitrile spectra of **1**, **4**, and **5** (**Figure 3.13a, b, c**). The simulated spectrum of **1** indicates a lower energy band at 683 nm associated with an aminophenolate-to-Co(III) CT and in good agreement with the experimentally observed band at 697 nm. The main CT contribution at higher energy originates from amino/iminophenolate to phenyleneimine and amino/imino phenolate-to-

www.manaraa.com

Co(III) between 390 – 520 nm, in relatively good agreement with the experimentally observed processes at 451 to 475 nm. Calculated TD-DFT spectra for **4** and **5** also show similar behavior.

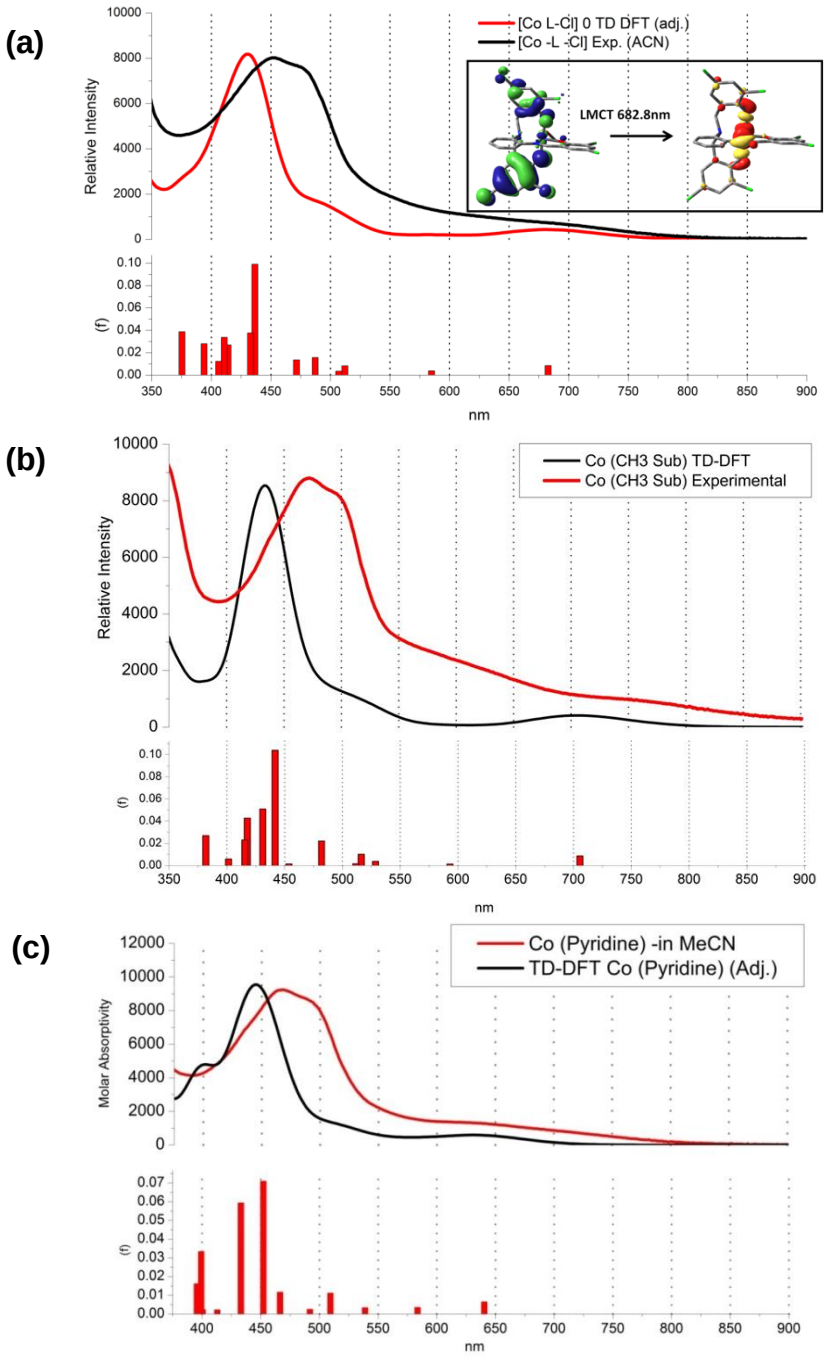

Figure 3.13. Absorption spectra for in CH_3CN.TD-DFT calculated spectra in CH_3CN as solvent model and experimental spectra in CH_3CN. The inset indicates the lowest energy transition. (a) Calculated vs experimental for **1** (B3PW91/ 6-311+g(d,p). (b) Calculated vs experimental for **4** (B3PW91/ 6-311+g(d,p) (c) Calculated vs experimental for **5** (B3PW91/6-311+g(d,p).

www.manaraa.com

3.3.3.3. Effect of ligand substitutients on the redox behavior

Cyclic voltammograms (CV) for **1**, **2**, **4** and **5** were recorded in acetonitrile using $TBAPF_6$ (0.1 M) as supporting electrolyte. Compound **3** was measured in *N*,*N*'-dimethylformamide due to solubility restrictions. Potentials were measured against Ag/AgCl and are reported *versus* the Fc/Fc^+ redox couple. **Table 3.4.** summarizes the electrochemical data and **Figure 3.14. (1**, **4**, and **5)** and **Figures 3.15 (2** and **3)** displays the results. Voltammograms taken in dichloromethane for **1, 4,** and **5** are displayed in **Figure 3.16** and data tabulated in **Table 3.5**, and show comparable behavior to those in acetonitrile (**Figure 3.17**).

Table 3.4. Cyclic voltammetric data for **1-5** in CH_3CN.

	3^{rd} $PhO^-/PhO^\bullet$ $E_{½}$, V (ΔE, V) $\lvert i_{pc}/i_{pa}\rvert$	2^{nd} $PhO^-/PhO^\bullet$ $E_{½}$, V (ΔE, V) $\lvert i_{pc}/i_{pa}\rvert$	1^{st} $PhO^-/PhO^\bullet$ $E_{½}$, V (ΔE, V) $\lvert i_{pc}/i_{pa}\rvert$	Co(III)/Co(II) $E_{½}$, [E_{pc}; E_{pa}], V (ΔE, V) $\lvert i_{pc}/i_{pa}\rvert$	$C{=}N/C^\bullet\text{-}N^-$ $E_{½}$, V (ΔE, V) $\lvert i_{pc}/i_{pa}\rvert$
1	+1.33 (0.13) |0.82|	+1.09 (0.08) |0.95|	+0.73 (0.08) |1.00|	-0.63 [-0.72; -0.52] (~0.20) |1.7| spike at E_{pa}= -0.15	-2.03 (0.06) |1.43|
2	+1.33 (0.05)	+1.06 (0.09) |0.53|	+0.70 (0.08) |0.30|	-0.68 [-0.80; -0.56] (0.22) |1.8|	-2.06 (0.11) |7.29| -2.20 (0.09) |2.53|
3	--	--	--	spike at E_{pa}= -0.16	E_{pc} = -2.07; E_{pc} = -2.25
4	+0.99 (0.16) |0.82|	+0.58 (0.07) |0.98|	+0.21 (0.07) |0.97|	-0.64 [-0.72; -0.56] (0.12) |1.06|	-2.55 (0.08) |1.09|
5	+1.01 (0.17) |0.84|	+0.65 (0.09) |1.04|	+0.27 (0.09) |0.80|	-1.33 [-1.46; -1.20] (0.26) |2.03| spike at E_{pa}= -0.55	-2.57 (0.11) |1.18|

3 in DMF

Compound **1** (**Figure 3.14, top**) shows three reversible phenolate/phenoxyl processes between 0.50 and 1.50 $V_{Fc/Fc+}$ while a reversible process at -2.03 $V_{Fc/Fc+}$ is attributed to the reduction of the phenylene-imine moiety.[27] The process attributed to the cobalt(III)/(II) couple is quasi-reversible with E_{pc} and E_{pa} respectively at -0.72 and *ca.* -0.52 $V_{Fc/Fc+}$, corresponding to $E_{1/2} \approx$ -0.63 $V_{Fc/Fc+}$ with $|i_{pc}/i_{pa}| = 1.7$.[7d,28] This process is obfuscated by a sharp spike at -0.15 $V_{Fc/Fc+}$ associated to an unidentified product. Compound **2**, (**Figure 3.15a**) shows a less reversible

www.manaraa.com

profile with three phenolate/phenoxyl processes between 0.70 and 1.50 $V_{Fc/Fc+}$, whereas the phenylene-imine process is split in two irreversible waves between -1.80 and -2.50 V. As the phenylene-imine moiety can accept 2 electrons, we infer that two electrons are transferred at slightly different potentials. We did not pursue this issue. The metal-centered process was quasi-reversible with E_{pc} = -0.80 and E_{pa}= -0.58 $V_{Fc/Fc+}$ and $E_{1/2} \approx$ -0.68 $V_{Fc/Fc+}$. The CV for **3** was taken in DMF is shown in **Figure 3.15b** over a narrower voltage window in the anodic region that prevents further discussion of the phenolate/phenoxyl processes. An irreversible cobalt(III)/(II) reduction was observed at $E_{p,c}$ = -1.04 $V_{Fc/Fc+}$, along with two irreversible processes attributed to the phenylene-imine observed with E_{pc} values of -2.07 and -2.25 $V_{Fc/Fc+}$. Complex **4** (**Figure 3.14, middle**) showed three reversible phenolate/phenoxyl processes between 0.10 and 1.25 $V_{Fc/Fc+}$ and one reversible phenylene-imine process at -2.55 $V_{Fc/Fc+}$. Additionally, contrary to the barely reversible behavior observed for **1-3** the Co(III)/Co(II) redox couple observed at -0.64 $V_{Fc/Fc+}$ exhibited excellent reversibility with ΔE = 0.12 and $|i_{pc}/i_{pa}|$ = 1.06.

www.manaraa.com

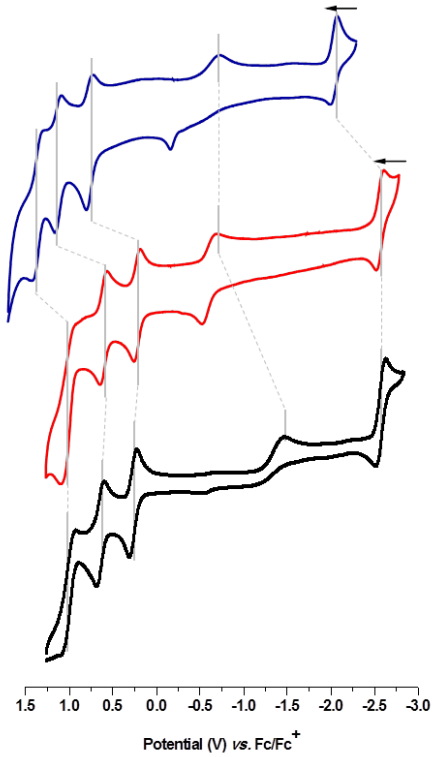

Figure 3.14. Cyclic voltammograms of **1** (top), **4** (middle), and **5** (bottom) in acetonitrile. Conditions: 0.1 M $TBAPF_6$ as supporting electrolyte; Glassy carbon (working), Pt wire (counter) and Ag/AgCl (reference); Scan rate: 100 mVs^{-1}**.**

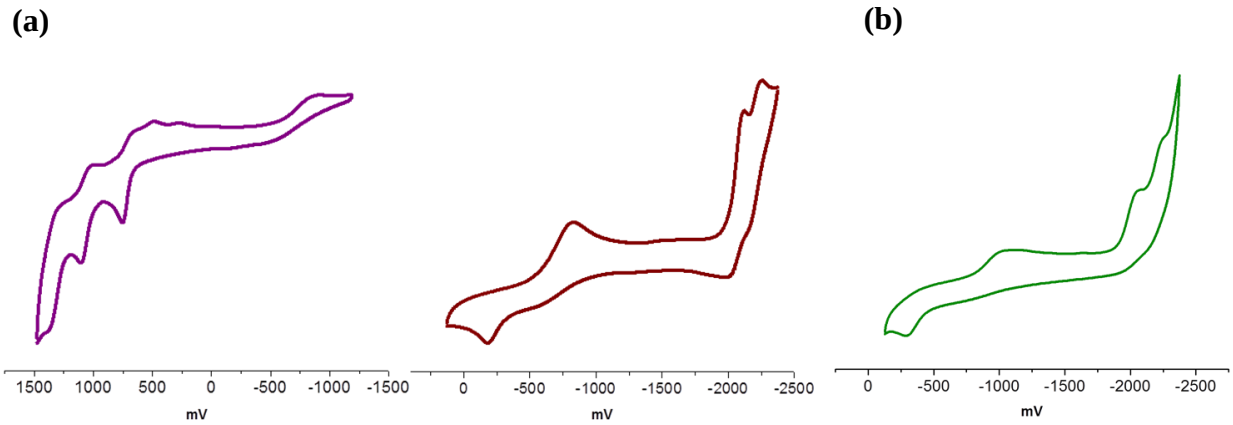

Figure 3.15. (a) Cyclic voltammograms of **2** in acetonitrile. (b) Cyclic voltammograms of **3** in dimethylformamide. Conditions: 0.1 M $TBAPF_6$ as supporting electrolyte; Glassy carbon (working), Pt wire (counter) and Ag/AgCl (reference); Scan rate: 100 mVs^{-1}**.**

www.manaraa.com

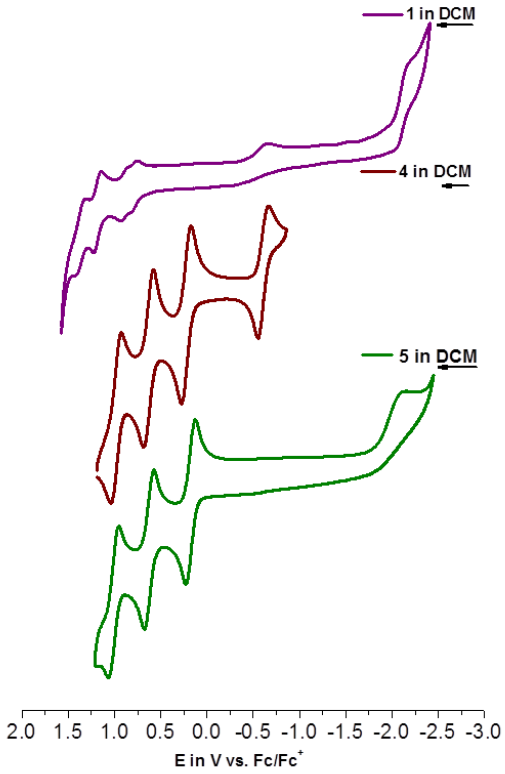

Figure 3.16. Cyclic voltammograms for **1** (top), **4** (middle), and **5** (bottom) in dichloromethane. Conditions: 0.1 M $TBAPF_6$ as supporting electrolyte; scan rate: 100 mVs^{-1}; Glassy carbon (working), platinum wire (counter) and Ag/AgCl (reference) in the three electrode cell.

Table 3.5. Cyclic voltammetric data for **1-5** in CH_2Cl_2.

	3rd $PhO^-/PhO^\bullet$ $E_{½}$, V (ΔE, V) $\lvert i_{pc}/i_{pa}\rvert$	**2nd $PhO^-/PhO^\bullet$** $E_{½}$, V (ΔE, V) $\lvert i_{pc}/i_{pa}\rvert$	**1st $PhO^-/PhO^\bullet$** $E_{½}$, V (ΔE, V) $\lvert i_{pc}/i_{pa}\rvert$	**Co(III)/Co(II)** $E_{½}$, [E_{pc}; E_{pa}], V (ΔE, V) $\lvert i_{pc}/i_{pa}\rvert$	**$C{=}N/C^\bullet\text{-}N^-$** $E_{½}$, V (ΔE, V) $\lvert i_{pc}/i_{pa}\rvert$
1	+1.34 (0.10) |0.85|	+1.16 (0.08) |0.81|	+0.75 (0.06) |0.87| +0.87 (0.07) |0.87|	-0.66 [-0.69; -0.64] (0.05) |1.16|	-2.12 (0.04) |1.03|
2	--	--	--	--	--
3	--	--	--	--	--
4	+0.96 (0.11) |1.04|	+0.61 (0.10) |1.08|	+0.21 (0.10) |1.10|	-0.63 [-0.68; -0.57] (0.11) |0.95|	-2.69 (0.03) |1.00|
5	+1.01(0.11) |0.65|	+0.63(0.10) |0.93|	+0.18(0.11) |0.94|	[E_{pc}: -2.08]	--

www.manaraa.com

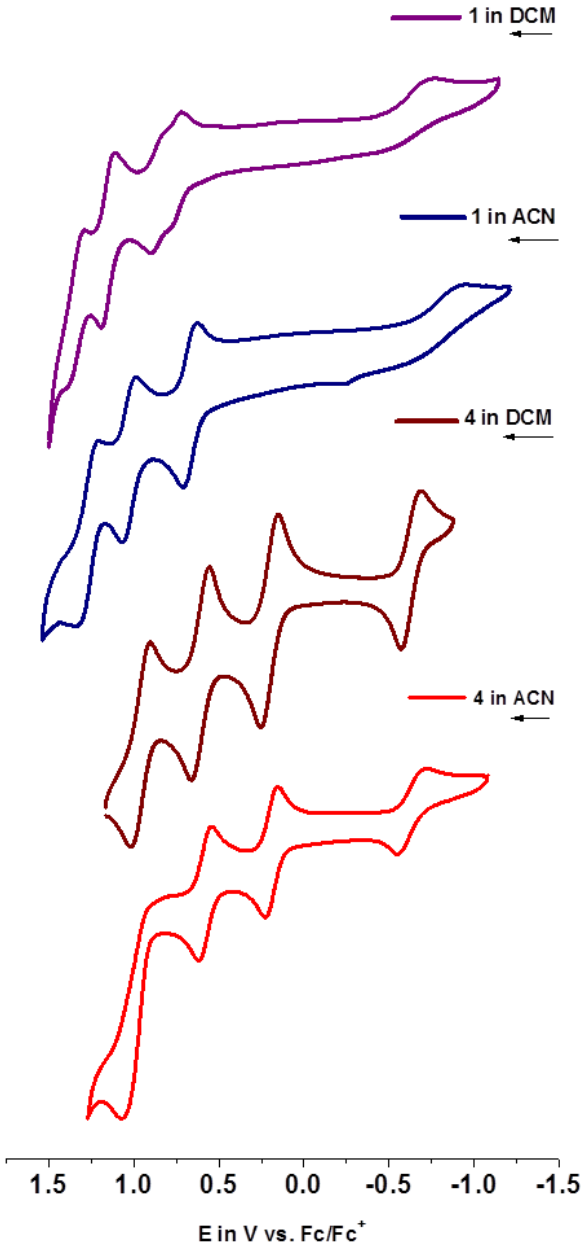

Figure 3.17. Cyclic voltammetry of **1** and **4** in CH_2Cl_2 and CH_3CN. Conditions: [C] = 1×10^{-4} M; 0.1 M $TBAPF_6$ as supporting electrolyte); Glassy carbon (working), Pt wire (counter) and Ag/AgCl (reference); Scan rate: 100 mVs^{-1}.

The quasi-reversible behavior observed for **1**-**3** is associated with the reorganizational energy barrier for the Co(II)/Co(III) couple.[29] The E_{pc} values for the Co(III)/(II) couple in **1** and **4** vary by ~0.72 V, whereas the imine based process (2^{nd} reduction) shifted to more negative

www.manaraa.com

potentials by 0.5 V. This variation is attributed to electronic effects of the different substituents attached to the imino-phenolate ring, and the more electronegative the substituent, the less electron density will be centered in the imine unit, resulting in less negative reduction potentials. For **1** —containing electron-withdrawing -Cl substituents— the lowest reduction potential for the imine process is observed. For the oxidative couples, the electrochemical potentials for the phenolates shifted to less positive values when substitution changes from the more electron-withdrawing chloro to the more donating *tert*-butyl group. Higher electron density upon the phenolate rings facilitates electrochemical oxidation and so, potentials tend to be less positive with a ~ 0.5 $V_{Fc/Fc+}$ shift from **1** to **4**. The pyridine-coordinated complex **5 (Figure 3.14, bottom)** showed the typical three phenolate-based processes in both dichloromethane and acetonitrile between 0.15 and 1.01 $V_{Fc/Fc+}$, thus closely resembling the potentials observed for **4**. On the other hand, a marked shift of the cobalt-based potential has been observed for **5**, when compared to **4**. The Co(III)/Co(II) potential shifted from -0.64 in **4** to -1.33 $V_{Fc/Fc+}$ in **5** in acetonitrile whereas in dichloromethane it shifted from -0.63 in **4** to -2.08 $V_{Fc/Fc+}$ in **5**, allowing us to postulate that reduction of the metal in **5** is considerably less favorable than in **4**. The potentials of **1**-**5** were recorded five times using different stock solutions to confirm reproducibility of the data.

Redox potentials were calculated via DFT methods and showed comparable values to the experimental data. In order to confirm the redox loci observed, we have evaluated the frontier molecular orbitals (MOs) for selected systems. These MOs are directly related to the reactivity of complexes and have proven useful in comparing the relevant redox sequences between species **1** and **4**. In order to make calculations more affordable, we modeled the *tert*-butyl substituents in **4** using methyl groups. All five electrochemical processes were probed and are summarized in

www.manaraa.com

Figure 3.18a. Spin density plots resulting from reduction, namely $[CoL]^{-}$, $[CoL]^{2-}$), as well as oxidation, namely [CoL], $[CoL]^{+}$ $[CoL]^{2+}$ and $[CoL]^{3+}$ were obtained. Interestingly, the second phenolate-based oxidation, $[CoL]^{2+}$, occurs at the amino-phenolate moiety for the $\mathbf{4^{CH3}}$ (**Figure 3.18b**), whereas for the chloro-substituted **1** this oxidation originates from the imino-phenolate **(Figure 3.18a**). An observed extended conjugation for **1** and other halogeno-substituted complexes is most likely the reason behind this phenomenon. The redox sequence for **5** is shown in **Figure 3.18c**.

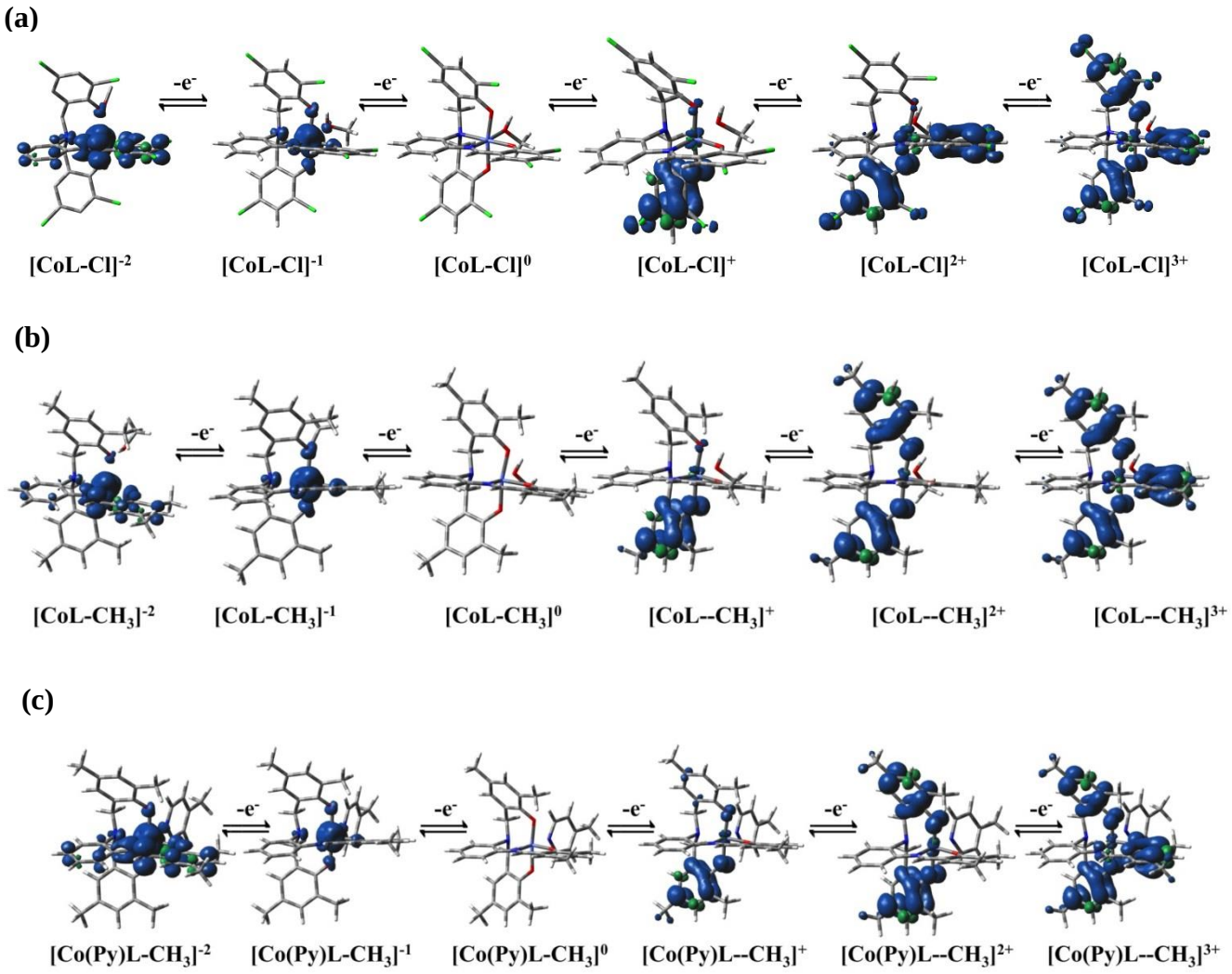

Figure 3.18. Spin density plots for redox processes in (a) **1**, (b) **4**, and (c) **5** (top to bottom).

www.manaraa.com

The first reduction yields spin density on the cobalt center, consistent with a high spin Co(II) while the second reduction is solely based on the imine moiety with most of the added electron being shared between the carbon and nitrogen atoms. Upon the addition of this second electron, we observed a significant bond length increase of 0.06 Å in the C=N bond. This is consistent with our previous assignment of this reduction as exclusively ligand-based. As reduction processes are relevant for proton reduction catalysis, usual attributions include the transformations Co(III) → Co(II) → Co(I). For species **1**-**5** we did not observe the Co(II)/Co(I) couple, instead we observed a ligand-based reduction that follows the Co(III)/Co(II) couple.

Better understanding of the redox processes observed for **1**-**4** was achieved via spectropotentiostatic experiments in acetonitrile (or dimethylformamide for **3**) using $TBAPF_6$ as supporting electrolyte. When the potential was fixed in -1.40 $V_{Fc/Fc+}$ spectral changes in the visible region were observed as shown in **Figure 3.19**. The LMCT absorption bands between 450 and 800 nm decrease, in agreement with the proposed Co(III)/Co(II) redox pair. Isosbestic points were observed at ca. 430 - 440 nm reflecting a decrease in the LMCT bands at 475 - 500 nm, while new absorption bands appeared at 420 - 440 nm for all complexes. The disappearance of the LMCT bands upon reduction suggests these new bands do not require the involvement of the metal center, thus supporting the TD-DFT assignment of intraligand charge transfer ($\pi_{phenolate} \rightarrow \pi^*_{imine}$).

www.manaraa.com

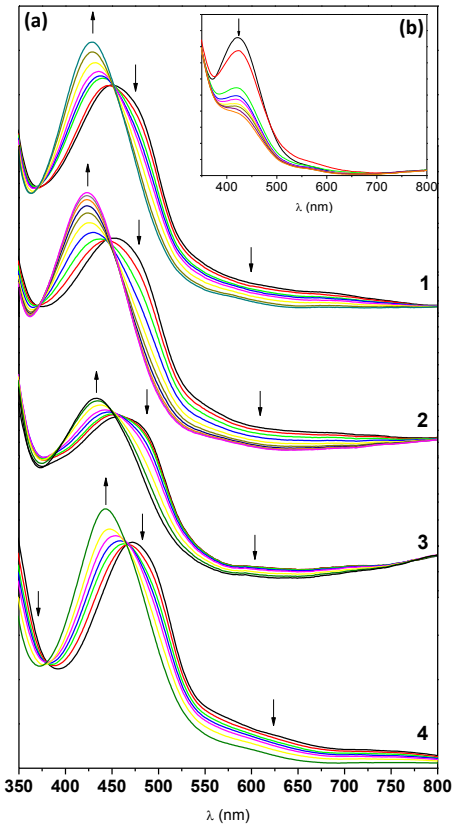

Figure 3.19. (a) Spectral changes upon electrochemical reduction of the Co(III)/Co(II) process in **1**, **2** and **4** in acetonitrile and **3** in DMF. The applied potential was –1.40 $V_{Fc/Fc+}$ over a period of 10 min.; (b) Spectral changes upon second reduction of **1** in acetonitrile. The applied potential was –2.40 $V_{Fc/Fc+}$ and the graph represents the behavior after 10 min. $TBAPF_6$ (0.1 M) was used as supporting electrolyte.

When a fixed potential was applied at -2.40 $V_{Fc/Fc+}$ (for **1** – **3**) targeting the azomethine process, the initial response within ca. 10 min was similar to that shown in **Figure 3.19a**. However after the full reduction of the cobalt(III) center, the ILCT absorption gradually starts to decrease **(Figure 3.19b, Figure 3.20**). This is indicative that the azomethine moiety becomes reduced.

www.manaraa.com

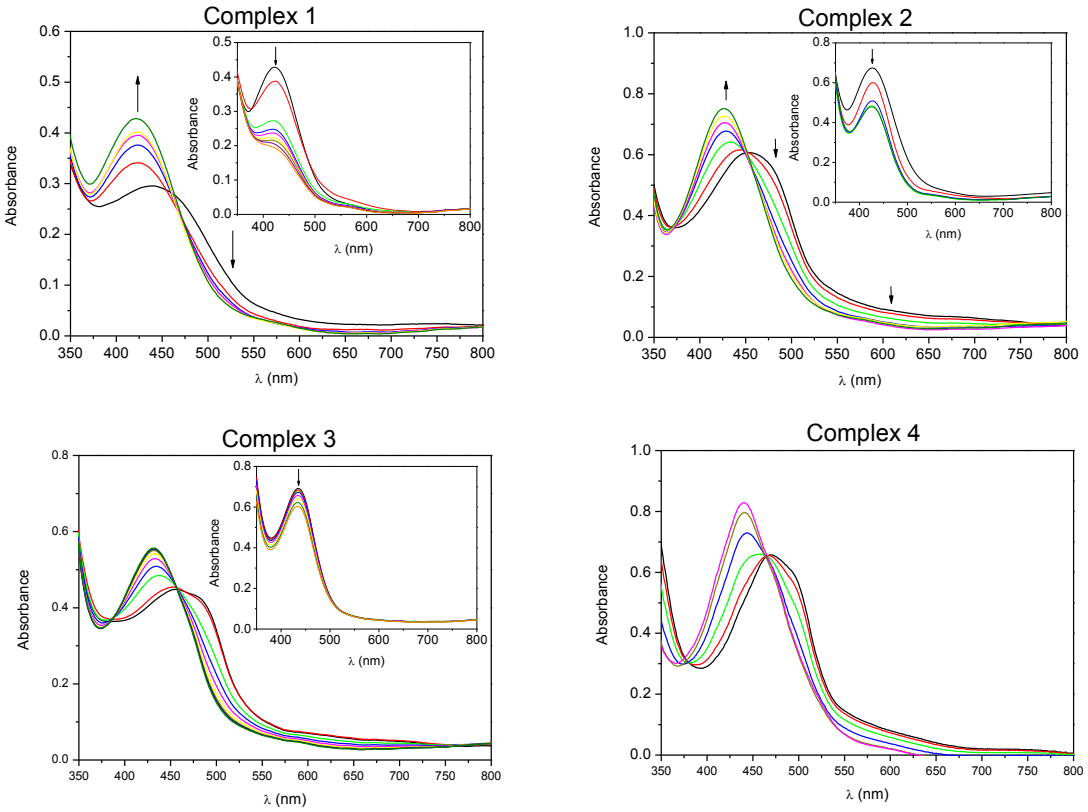

Figure 3.20. Spectral changes upon electrochemical reduction of complexes **1**, **2** and **4** in acetonitrile and **3** in *N*,*N*'-dimethylformamide. The applied potential was –2.40 V *vs*. Fc^{+}/Fc over a period of 10 minutes and after 10 minutes (inset – for **1** - **3**). $TBAPF_6$ (0.1 M) was used as supporting electrolyte.

As for oxidations, when the potential was fixed to 0.85 $V_{Fc/Fc+}$ for **1-3** (and 0.30 $V_{Fc/Fc+}$ for **4**) a band appeared around 1000 nm, which has been ascribed to a phenolate to phenoxyl ILCT process[12,30] (**Figure 3.21**). This is in good agreement with our previous observations in similar systems.[8]

www.manaraa.com

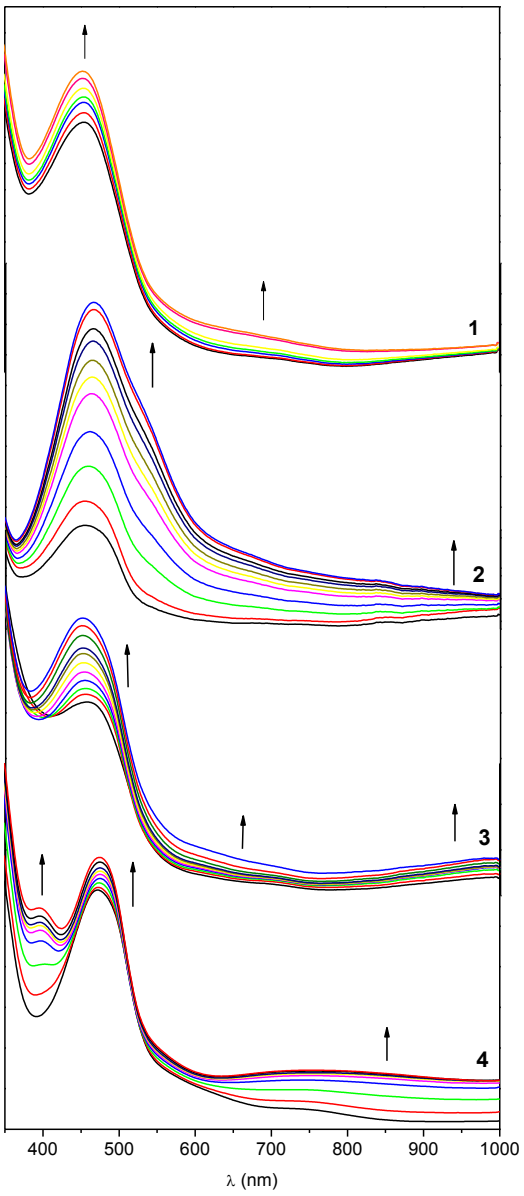

Figure 3.21. Spectral changes upon electrochemical oxidation of **1**, **2** and **4** in acetonitrile and **3** in *N*, *N'*-dimethylformamide. The applied potential was 0.85 V for **1-3** and 0.30 V for **4** *vs*. Fc^{+}/Fc over a period of 10 minutes. $TBAPF_6$ (0.1 M) was used as supporting electrolyte.

TD-DFT calculations were used to model the experimentally observed changes in the visible spectrum of **1**, both upon cobalt(III) reduction and phenolate oxidation (**Figure 3.22**, **3.23**). The first reduction results in disappearance of the LMCT process whereas the ILCT band remains intact. Similarly, oxidation results in a peak around 600-800 nm, along with another band at very

www.manaraa.com

low energy (~1500 nm). Both observations are in excellent agreement with the experimental findings.

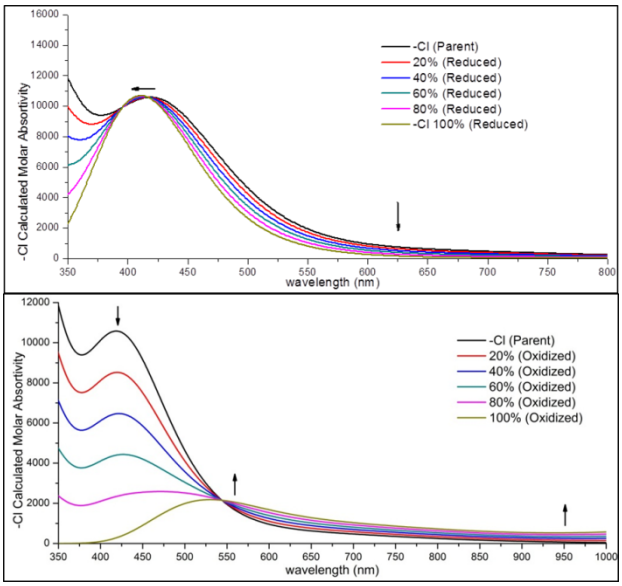

Figure 3.22. Computed electronic spectra for **1** in the parent state after 1st reduction (top) and after 1st oxidation (bottom).

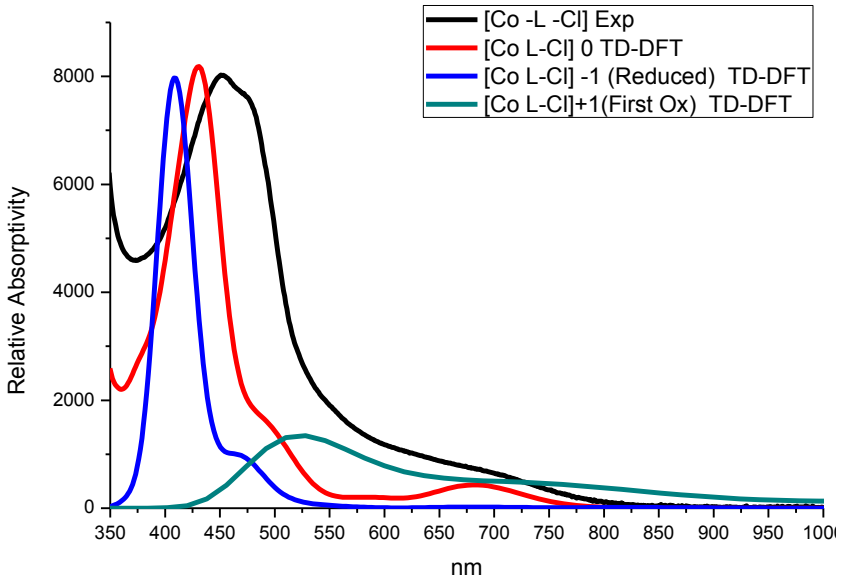

Figure 3.23. TD-DFT calculated UV-visible spectra for spectroelectrochemical changes.

www.manaraa.com

3.3.3.4. Effect of hydrogen bonding in the redox behavior

Analysis of the molecular structures suggests the presence of an H-bond interaction for **1**, **2**, and **4** between the coordinated methanol and its nearest phenolato oxygen atom at *ca.* 2.15 Å. This H-bond is not possible for the pyridine-coordinated complex **5 (Figure 3.24)** and likely contributes to stabilize the reduced Co(II) species in the former complexes.

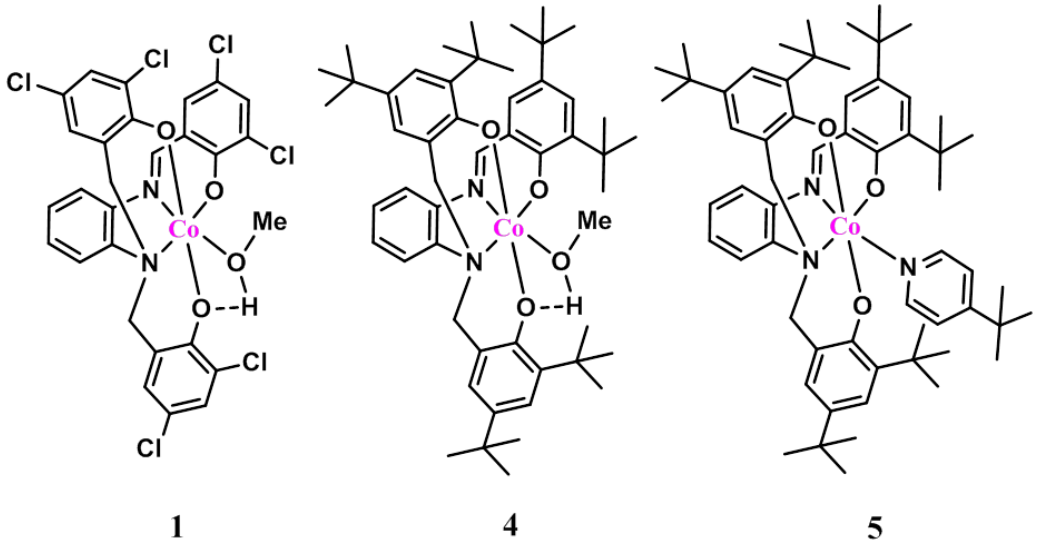

Figure 3.24. Presence (**1**, **4**) and absence (**5**) of H-bonding interactions in cobalt(III) complexes.

Therefore, we used DFT methods to interrogate how this H-bond can stabilize the Co(III)/Co(II) couple in **1**, **2**, and **4**, but not in **5** where the process potential is also significantly more negative. Our calculations favor a high-spin Co(II) species (S = 3/2) over its low-spin (S = 1/2) congener by 13.2 kcal/mol, implying that a high reorganizational barrier associated with the $^{LS}3d^6 \rightarrow {}^{HS}3d^7$ process must be overcome in order to attain redox reversibility. Similarly, the results for the reduced Co(II) species in **1** indicate that the methanol bond length elongates drastically from 2.01 to 3.60 Å, to the point where it is mainly H-bonded to the phenolate than coordinated to the cobalt center (**Figure 3.25**) whereas for **4** this bondlength reaches ~2.6 Å.

www.manaraa.com

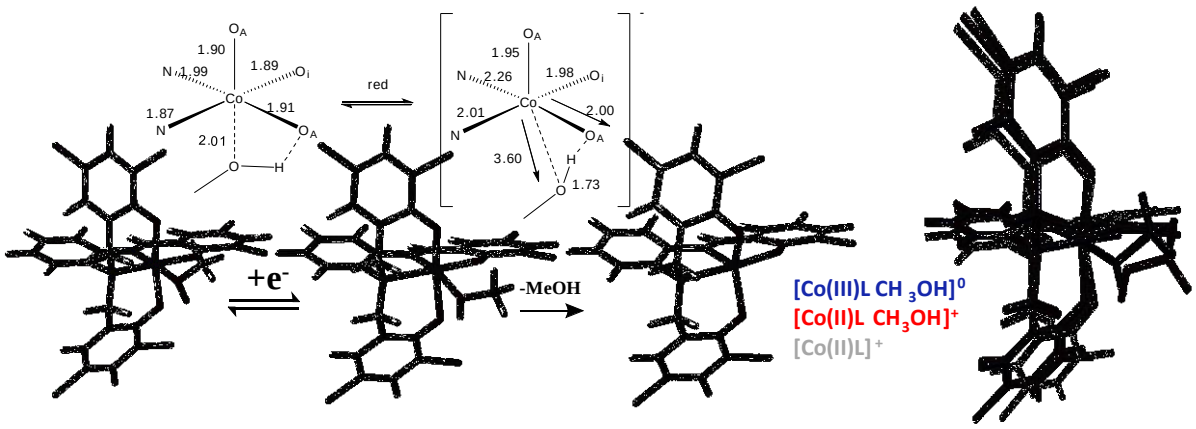

Figure 3.25. Geometrical changes upon reduction (left) and superimposition of various oxidation states for complex **1** (right).

This secondary interaction provides a pathway for the methanol to remain nearby the complex instead of freely roaming in solution. The H-bonded phenolate has its charge "shielded" by the H atom, resulting in a reduced *net* charge of less than 3-, that accommodates the ^{HS}Co(II) ion and contributes to the reversibility of the process, as seen that **4** is more reversible than **1**. To have a better insight, calculations were performed to evaluate the enthalpy change upon the dissociation of both methanol and pyridine for the divalent (reduced) complex.

$$[Co(II)LX]^- \rightarrow [Co(II)L]^- + X \quad (\Delta E) \quad \text{Eq.1.}$$

For complex **1** and **4** we calculate an enthalpy change of 0.05 and 4.0 kcal/mol respectably, whereas for **5** we observe a negative -1.8 kcal/mol. The numbers, even though small, show that the methanol interacts more strongly with **4** than for **1**. It is noteworthy that this enthalpy includes by definition, *all* possible interactions of the methanol, namely its interactions with the ligand and with the metal complex. It is expected that the stronger the H-bonding to the ligand, the harder it will be to completely remove the methanol. As previously mentioned, the presence (**1**, **4**) and absence (**5**) of H-bonding interactions play crucial role in determining the nature of redox behavior of cobalt center. Binding energy of methanol with cobalt(III) for **4** (t-butyl

www.manaraa.com

substituted) is much stronger than the binding energy for **1** (chloro substitued) (**Table 3.6**) which will have to lessen the reorganization of the coordination environment of **4** upon reduction with respect to **1**. Less environmental changes can lead to better reversibility such as in **4**. It has also been known that a di-*tert*-butyl phenol oxygen is more electron dense than a di-chloro-substitued phenol,[31] thus it results in a stronger H-bonding of di-*tert*-butyl phenol forming with the methanol hydrogen than the di-chloro-phenol which can help explain the binding energy and reversibility difference. As this effect is not available in **5**, the resulting Co(III)/Co(II) couple is irreversible and more difficult to reduce.

Table 3.6. Binding energy of methanol with cobalt(III) for **1** and **4** and of pyridine for **5**.

Co(II)	non-Vertical Enthalpy
(1) -Cl	0.05
(4) -CH_3	4.0
(5) -Py	-1.8
	(Kcal/mol, ub3pw91/6-311+g(d,p))

3.3.4. Reactivity studies

3.3.4.1. Behavior as electron acceptors

As phenolates stabilize the trivalent cobalt in complexes **1-4**, conversion of Co(III) into Co(II) is a fundamental step relevant for catalysis. In order to understand the electron acceptance ability of **1-4**, chemical reduction tests were carried out using excess ascorbic acid as the reductant. In contrary with electrochemical reduction which is slow and incomplete due to the operation for shorter time period, chemical reduction is generally more complete and quick. Spontaneous electron transfer reaction from ascorbic acid to **1-4** is assured by the electrochemical potentials observed for the Co(III)/Co(II) couple,[32] and the experiments were performed in CH_3CN/H_2O

www.manaraa.com

(90:10% v/v). Results were evaluated spectrophotometrically following the disappearance of the phenolate-to-cobalt(III) LMCT processes in the parent compounds at room temperature (**Figure 3.26a, Figure 3.27**). Plots of complex concentrations *versus* time were obtained and fitted using a first order exponential decaying equation (**Figure 3.28**) and linearized using a first order rate equation (**Figure 3.26b**). From the linearized data, the rate constants (k_{obs}) and half-life values ($t_{½}$) were obtained for the complexes **1** – **4** and are listed in **Table 3.7**.

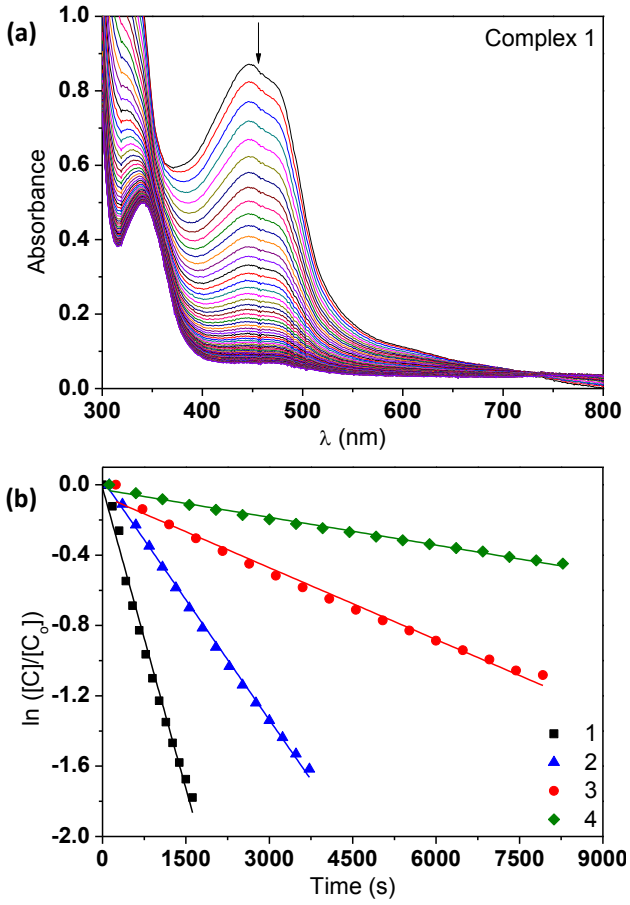

Figure 3.26. (a) Time-dependent UV-visible spectral changes in acetonitrile/water (90:10% v/v) for complex **1**; (b) Chemical reduction tests for **1** – **4** with the reducing agent ascorbic acid. Conditions: $[C]_{final} = 1.80 \times 10^{-4}$ M, $[AA] = 2.00 \times 10^{-2}$ M and pH ~ 3.0.

www.manaraa.com

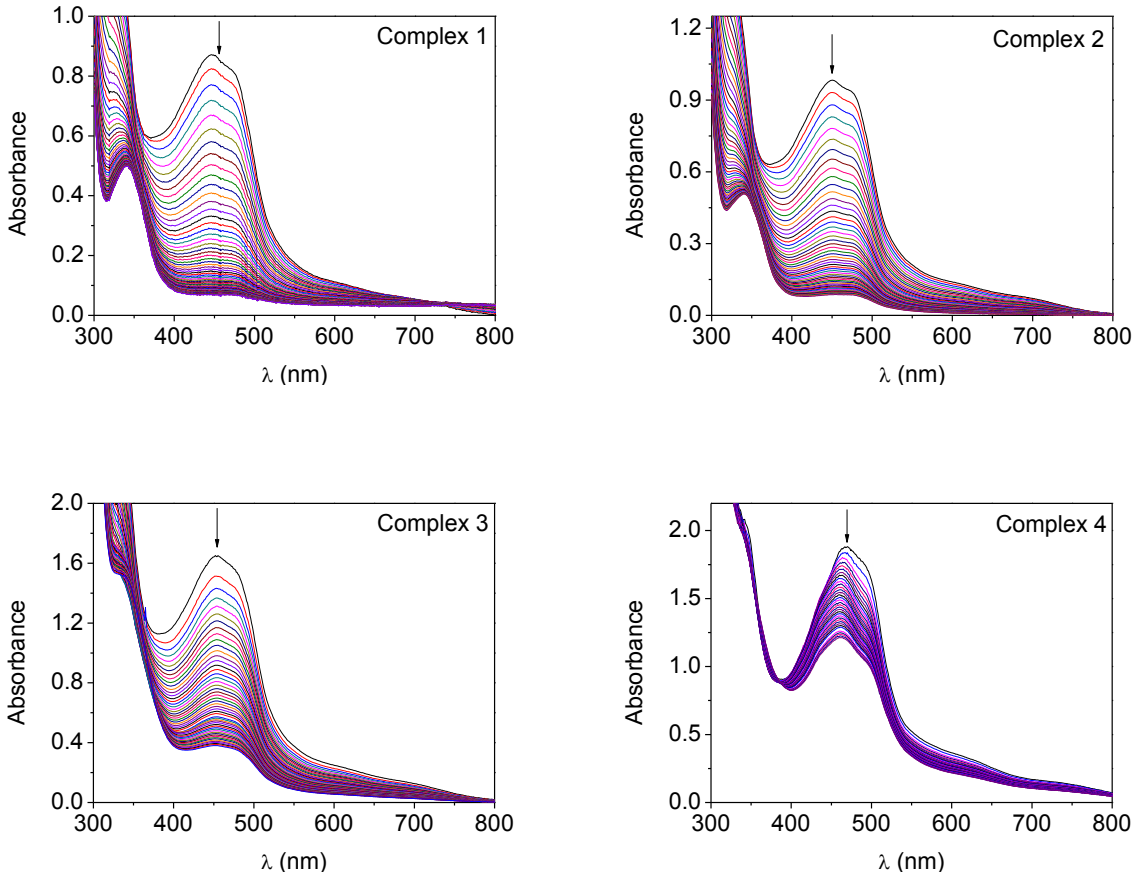

Figure 3.27. Time-tracked UV-visible spectral change in acetonitrile/water (90:10% v/v) for the complexes **1** – **4**. Conditions: $[C]_{final}$ = 1.80 × 10^{-4} M, [AA] = 2.00 × 10^{-2} M and pH ~ 3.0.

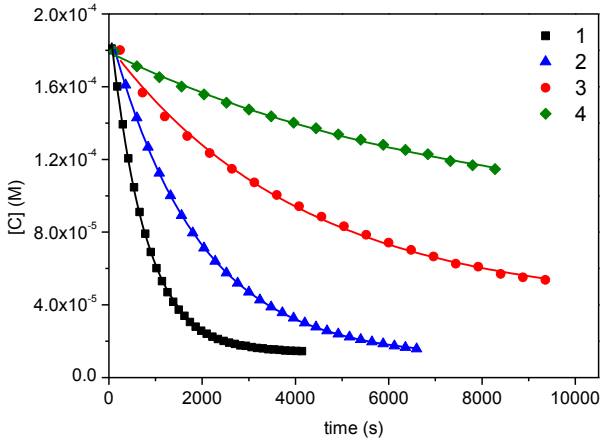

Figure 3.28. Chemical reduction tests for the complexes **1** – **4** towards the reductant (ascorbic acid). [Complex] (M) *versus* time (s) plot fitted as a first order exponential decaying equation.

www.manaraa.com

The electronic influence of the substituents present on the phenolate pendant arms was clearly observed on the kinetic parameters. Compound **1** presented a rate constant of 1.0 x 10^{-3} s^{-1} whereas compound **4** showed a considerably slower rate of 5.3 x 10^{-5} s^{-1}. Based on these results we conclude that the rate constants (k_{obs}) tend to decrease when electron-withdrawing groups such as chloro are replaced by electron-donating groups such as ^{t}butyl. Half-lives ($t_{½}$) for **1 - 4** were also calculated. For these electron transfer reactions, the $t_{½}$ values follow the same trend observed for the rate constants. The results show clearly the time-wise efficiency of the complex **1**, where in 12 minutes 50% of that species had been reduced to its Co(II) counterpart. For complex **4**, on the other hand, the $t_{½}$ value is approximately 20-fold lower. This behavior can be explained in terms of electron density over the metallic center: electron deficiency is triggered on the metal when electron-withdrawing groups are present, making the cobalt(III) centers more positive and electron acceptance easier. Overall, the trend can be summarized as follows: 1 (-Cl) > 2 (-Br) > 3 (-I) > 4 (^{t}Bu).

Table 3.7. Kinetic parameters obtained for the chemical reduction reaction between complexes **1 – 4** and ascorbic acid.

Parameter	Complexes			
	1	**2**	**3**	**4**
k_{obs} (s^{-1})	1.0×10^{-3}	4.4×10^{-4}	1.3×10^{-4}	5.3×10^{-5}
$t_{½}$ (min)	12	26	89	220

Acetonitrile/water (90:10% v/v); $[C]_{final}$ = 1.80×10^{-4} M, [AA] = 2.00×10^{-2} M, pH ~ 3.0 at room temperature.

3.3.4.2. Behavior as proton-reduction catalysts

We tested the activity of compounds **1-4** towards proton reduction in presence of weak acid such as acetic acid (HOAc). We focused our attention on complexes **1** and **4** due to their inherently different redox and electronic natures. We measured the catalytic activity in presence of the very weak acid HOAc, which shows the catalytic wave in close vicinity to the ligand-based imine

www.manaraa.com

process (**Figure 3.29a**). Overpotential was calculated to be 0.60 V and 0.90 V for **1** and **4**, respectively. The chloro-substituted **1** generated H_2 at lower overpotentials than those observed for the t-butyl substituted **4**. This is associated with the presence of the electron-withdrawing chloro substituents. Comparison of cyclic voltammogram between **1** with the blank in the presence of ten equivalent of acetic acid established the hydrogen generation in the presence of **1** at lower overpotential than the blank (**Figure 3.29b**). Hydrogen generation was confirmed from bulk-electrolysis measurements for **1** at an applied potential of -2.20 $V_{Fc/Fc+}$, and an associated turnover number (TON) of 10.8 was determined after three hours with a Faradaic efficiency of 85% using Hg-pool as working, Ag/AgCl as reference, and a platinum wire as the auxiliary electrode. Charge consumption over time is much higher with complex **1** than that with the blank solution (**Figure 3.29c**), validating **1** as the catalyst. Furthermore, the blank generates only 40 μmol of hydrogen in three hours during bulk-electrolysis at -2.2 $V_{Fc/Fc+}$, wheras the catalyst generates 472 μmol of hydrogen in three hours. Each set of experiments was repeated in triplicate using fresh solutions. During the controlled potential experiment, no deposition of any solids was observed on the electrode surface. Moreover, analysis of the solution after bulk electrolysis in the presence of HOAc suggested the presence of Co^{II}-species in similar ligand environment, as shown by the UV-visible spectra (**Figure 3.29d**), which is very similar to the Co(II) spectra obtained during spectroelectrochemistry. Similar bulk-electrolysis measurements were not possible for **4** due to its high overpotential. Appearance of the catalytic peak close to the imine-based process suggested the doubly reduced state as the catalytic species. On the other hand, protonation of the phenolates in these conditions was ruled out due to unchanged UV-visible spectra for either **1** or **4** upon addition of much stronger nitric acid to acetonitrile.

www.manaraa.com

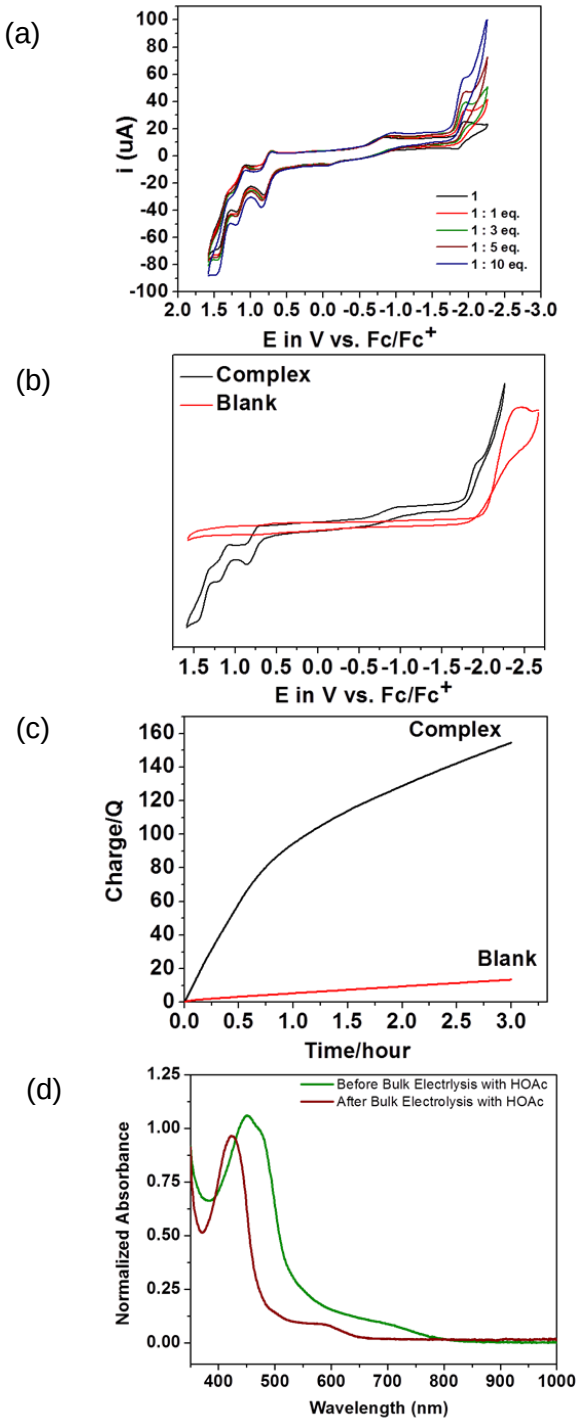

Figure 3.29. (a) Electrocatalytic activity of complex **1** towards proton reduction in presence of acetic acid. (b) Comparison of cyclic voltammogram between **1** and blank in the presence of 10 equivalents of acetic acid. For a and b: Glassy C: WE; Pt-wire: AE; Ag/AgCl: RE (c) Charge *versus* time plot over 3 h during bulk-electrolysis at -2.2 $V_{Fc/Fc+}$ of **1** *versus* blank in the presence of acetic acid. (d) UV-Visible spectra of the solution before and after bulk-electrolysis at -1.8 V *versus* Ag/AgCl in the presence of HOAc (For c, d: Hg-pool: WE; Pt-coil: AE; Ag/AgCl: RE).

www.manaraa.com

3.4. Conclusions

In this study we investigated the effect of phenolate substituents on the redox and electronic processes of a series of cobalt(III) complexes. These complexes showed the expected Co(III)/Co(II) couple along with multiple ligand-centered redox processes, and the nature of the substituent modulates the potentials by which ligand-based reduction takes place. The visible region of the spectrum dominated by phenolate-to-cobalt(III) and phenolate-to-phenyleneimine charge transfer bands. Upon reduction of the metal center, the LMCT disappears, evidencing the LLCT. We also showed that adventitious hydrogen-bonding enhanced the reversibility of the metal-based process. The chloro-substituted complex showed promising electron accepting ability. Kinetic plots for chemical reduction favored a relative order as -Cl > -Br > -I > -t-Bu. The chloro and t-butyl substituted species also showed potential as catalysts for proton reduction in acidic media. Again the chloro-substituted species yielded lower overpotentials than its t-Bu counterpart. These overpotentials are considerably negative, therefore, limiting practical use of this framework for efficient proton reduction. Nonetheless they support the notion that incorporation of strong electron-withdrawing groups to the ligand framework may lead to optimized catalytic properties. These efforts are currently under development in our labs.

www.manaraa.com

REFERENCES

1. Tran, P. D.; Artero, V.; Fontecave, M. *Energy Environ. Sci.* **2010,** *3,* 727. (b) Walter, M. G.; Warren, E. L.; McKone, J. R.; Boettcher, S. W.; Mi, Q.; Santori, E. A.; Lewis, N. S. *Chem. Rev.* **2010,** *110,* 6446. (c) Cook, T. R.; Dogutan, D. K.; Reece, S. Y.; Surendranath, Y.; Teets, T. S.; Nocera, D. G. *Chem. Rev.* **2010,** *110,* 6474. (d) Esswein, A. J.; Nocera, D. G. *Chem. Rev.* **2007,** *107,* 4022. (e) Lewis, N. S.; Nocera, D. G. *Proc. Natl. Acad. Sci. U.S.A.* **2006,** *103,* 15729. (f) Turner, J. A. *Science* **2004,** *305,* 972.
2. (a) McNamara, W. R.; Han, Z.; Yin, C. J.; Brennessel, W. W.; Holland, P. L.; Eisenberg, R. *Proc. Nat. Acad. Sci* **2012**, *109,* 15594.(b) Nguyen, M. T. D.; Charlot, M. F.; Aukauloo, A. *J. Phys. Chem. A* **2011,** *115,* 911. (c) Stubbert, B. D.; Peters, J. C.; Gray, H. B. *J. Am. Chem. Soc.* **2011,** *133,* 18070.
3. (a) Marinescu, S. C.; Winkler, J. R.; Gray, H. B. *Proc. Nat. Acad. Sci* **2012**, *109,* 15127. (b) Muckermann, J. T.; Fujita, E. *Chem. Comm.* **2011,** *47,* 12456. (c) Solis, B. H.; Hammes-Schiffer, S. *Inorg. Chem.* **2011,** *50,* 11252.
4. (a) McCrory, C. C.; Uyeda, L. C.; Peters, J. C. *J. Am. Chem. Soc.* **2012,** *134,* 3164. (b) Singh, W. M.; Baine, T.; Kudo, S.; Tian, S.; Ma, X. A. N.; Zhou, H.; DeYonker, N. J.; Pham, T. C.; Bollinger, J. C.; Baker, D. L.; Yan, B.; Webster, C. E.; Zhao, X. *Angew. Chem. Int. Ed.* **2012,** *51,* 5941. (c) McNamara, W. R.; Han, Z.; Yin, C. J.; Brennessel, W. W.; Holland, P. L.; Eisenberg, R. *Proc. Nat. Acad. Sci* **2012**, *109,* 15594. (d) Utschig, L. M.; Silver, S. C.; Mulfort, K. L.; Tiede, D. M. *J. Am. Chem. Soc.* **2011,** *133,* 16334. (e) McCormick, T. M. Han, Z.; Weinberg, D. J. Brennessel, W. W.; Holland, P.L.; Eisenberg, R. *Inorg. Chem.* **2011,** *50,* 10660. (f) Leung, C. F.; Chen, Y. Z.; Yu, H. Q.; Yiu, S. M.; Ko, C. C.; Lau, T. C. *Int. J. Hydro. Energy* **2011,** *36,* 11640. (g) Sun, Y.; Bigi, J. P.; Piro, N. A.;

www.manaraa.com

Tang, M. L.; Long, J. R.; Chang, C. J. *J. Am. Chem. Soc.* **2011,** *133,* 9212. (h) Probost, B.; Rodenberg, A.; Guttentag, M.; Hamm, P.; Alberto, R. *Inorg. Chem.* **2010,** *49,* 6453. (i) Jacques, P. A.; Artero, V.; Pecaut, J.; Fontecave *Proc. Nat. Acad. Sci.* **2009,** *106,* 20627. (j) Du, P.; Schneider, J.; Luo, G.; Brennessel, W. W.; Eisenberg, R. *Inorg. Chem.* **2009,** *48,* 4952. (k) Li, C.; Wang, M.; Pan, J.; Zhang, P.; Zhang, R.; Sun, L. *J. Organometal. Chem.* **2009,** *694,* 2814. (l) Fihri, A.; Artero, V.; Pereira, A.; Fontecave, M. *Dalton Trans.* **2008,** 5567. (m) C-F. Leung, S-M. Ng, C-C. Ko, W-L. Man, J. Wu, L. Chen, T-C. Lau, *Energy Environ. Sci.* 2012, **5**, 7903; (n) S. Varma, C. E. Castillo, T. Stoll, J. Fortage, A. G. Blackman, F. Moltan, A. Deronzier, M-N. Collomb, *Phys. Chem. Chem. Phys.* 2013, **15**, 17544; (o) L. Tong, R. Zong, R. P. Thummel, *J. Am. Chem. Soc.* 2014, **136**, 4881; (p) C. Bachmann, B. Probst, M. Guttentag, R. Alberto, *Chem. Commun.* 2014, **50**, 6737; (q) M. Natali, A. Luisa, E. Lengo, F. Scandola, *Chem. Commun.* 2014, **50**, 1842.

5. (a) Thomas, R. M.; Widger, P. C. B.; Ahmed, S. M.; Jeske, R. C.; Hirahata, W.; Lobkovsky, E. B. ; G. W. *J. Am. Chem. Soc.* **2010**, *132*, 16520. (b) Jacobsen, E. N. *Acc. Chem Res.* **2000**, *33*, 421.
6. (a) Chiang, L.; Allan, L. E. N.; Alcantara, J.; Wang, M. C. P.; Storr, T.; Shaver, M. P. *Dalton Trans* **2014**, *43*, 4295. (b) Solis, B.; Yu, Y.; Hammes-Schiffer, S. *Inorg. Chem.* **2013,** *52,* 6994. (c) Kochem, A.; Thomas, F.; Jarjayes, O.; Gellon, G.; Philouze, C.; Weyhermüller, T.; Neese, F.; van Gastel, M. *Inorg. Chem.* **2013,** *52,* 14428. (d) Kochem, A.; Kanso, H.; Baptiste, B.; Arora, H.; Philouze, C.; Jarjayes, O.; Vezin, H.; Luneau, D.; Orio, M.; Thomas, F. *Inorg. Chem.* **2012,** *51,* 10557.
7. (a) Lesh, F. D.; Lord, R. L.; Heeg, M. J.; Schlegel, H.B.; Verani, C. N. *Eur. J. Inorg. Chem.* **2012**, 463. (b) Tomco, D.; Xavier, F. R.; Allard, M. M.; Verani, C. N. *Inorg. Chim. Acta*

www.manaraa.com

2012, *393*, 269. (c) Tomco, D.; Schmitt, S.; Ksebati, B.; Heeg, M. J.; Dou. Q. P.; Verani. C. N. *J. Inorg. Biochem.* **2011,** *105*, 1759. (d) Shakya, R.; Hindo, S. S.; Wu, L.; Allard, M. M.; Heeg, M. J.; Hratchian, H. P.; McGarvey, B. R.; Rocha, S. R. P. D.; Verani, C. N. *Inorg. Chem.* **2007,** *46*, 9808. (e) Shakya, R.; Imbert, C.; Hratchian, H. P.; Lanznaster, M.; Heeg, M. J.; McGarvey, B. R.; Allard, M. M.; Schlegel, H. B.; Verani, C.N. *Dalton Trans.* **2006,** 2517.

8. Allard, M. M.; Xavier, F. R.; Heeg, M. J.; Schlegel, H. B.; Verani, C. N. *Eur. J. Inorg. Chem.* **2012,** 4622.
9. Elghachtouli, S.; Régis, G.; Dorlet, P.; Anxolabehere-Mallart, E.; Aukauloo, A. *Dalton Trans.* **2012,** *41*, 1675.
10. APEX II collection and processing programs are distributed by the manufacturer. Bruker AXS Inc., Madison WI, USA, **2009**.
11. Sheldrick, G. M. *Acta Cryst.* **2008,** *A64*, 112.
12. Spek, A. L. *J.Appl.Cryst.* **2003,** *36*, 7.
13. COSMO V1.61, Software for the CCD Detector Systems for Determining Data Collection Parameters. Bruker Analytical X-ray Systems, Madison, WI, USA, **2009**.
14. APEX2 V2010.11-3. Software for the CCD Detector System; Bruker Analytical X-ray Systems, Madison, WI, USA, **2010**.
15. SAINT V 7.68A Software for the Integration of CCD Detector System Bruker Analytical X-ray Systems, Madison, WI, USA, **2010**.
16. SADABS V2.008/2 Program for absorption corrections using Bruker-AXS CCD based on the method of Robert Blessing; Blessing, R.H. *Acta Cryst.* **1995,** *A51*, 33.
17. Frisch, M. J.; Trucks, G. W.; Schlegel, H. B.; Scuseria, G. E.; Robb, M. A.; Cheeseman, J.

www.manaraa.com

R.; Scalmani, G.; Barone, V.; Mennucci, B.; Petersson, G. A.; Nakatsuji, H.; Caricato, M.; Li, X.; Hratchian, H. P.; Izmaylov, A. F.; Bloino, J.; Zheng, G.; Sonnenberg, J. L.; Hada, M.; Ehara, M.; Toyota, K.; Fukuda, R.; Hasegawa, J.; Ishida, M.; Nakajima, T.; Honda, Y.; Kitao, O.; Nakai, H.; Vreven, T.; Montgomery, J. A.; Peralta, J. E.; Ogliaro, F.; Bearpark, M.; Heyd, J.; Brothers, J. E.; Kudin, K. N.; Staroverov, V. N.; Kobayashi, R.; Normand, J.; Raghavachari, K.; Rendell, A.; Burant, J. C.; Iyengar, S. S.; Tomasi, J.; Cossi, M.; Rega, N.; Millam, J. M.; Klene, M.; Knox, J. E.; Cross, J. B.; Bakken, V.; Adamo, C.; Jaramillo, J.; Gomperts, R.; Stratmann, R. E.; Yazyev, O.; Austin, A. J.; Cammi, R.; Pomelli, C.; Ochterski, J. W.; Martin, R. L.; Morokuma, K.; Zakrzewski, V. G.; Voth, G. A.; Salvador, P.; Dannenberg, J. J.; Dapprich, S.; Parandekar, P. V.; Mayhall, N. J.; Daniels, A. D.; Farkas, O.; Foresman, J. B.; Ortiz, J. V.; Cioslowski, J.; Fox, D. J. *Gaussian G09* Wallingford CT, **2009**.

18. (a) Becke, A. D. *J. Chem. Phys.* **1993**, *98*, 5648. (b) Perdew, J. P. *Phys. Rev. B* **1986**, *33*, 8822. (c) Perdew, J. P.; Burke, K.; Wang, Y. *Phys. Rev.* **1996**, *54*, 16533.
19. (a) Miertus, S.; Scrocco, E.; Tomasi, J. *Chem. Phys.* **1981,** *55*, 117. (b) Tomasi, J.; Mennucci, B.; Cammi, R. *Chem. Rev.* **2005**, *105*, 2999. (c) Scalmani, G.; Frisch, M. J.; Mennucci, B.; Tomasi, J.; Cammi, R.; Barone, V. *J. Chem. Phys.* **2006,** *124*, 9410. (d) Scalmani, G.; Frisch, M. J. *J. Chem. Phys.* **2010,** *132*, 114110. (e) Tomasi, J.; Mennucci, B.; Cammi, R. *Chem. Rev.* **2005**, *105*, 2999.
20. (a) Runge, E.; Gross, E. K. U. *Phys. Rev. Lett.* **1984,** 52. (b) Stratmann, R. E.; Scuseria, G. E.; Frisch, M. J. *J. Chem. Phys.* **1998,** *109*, 8218.
21. (a) V. Fourmond, P. A. Jacques, M. Fontecave, V. Artero, *Inorg. Chem.* 2010, **49**, 10338; (b) J. A. S. Roberts, R. M. Bullock, *Inorg. Chem.* 2013, **52**, 3823; (c) A. M. Appel, M. L. Helm,

www.manaraa.com

ACS Catal. 2014, **4**, 630.

22. (a) Farrugia, L. J. ORTEP for windows. *J. Appl. Cryst.* **1997,** *30,* 565. (b) Zsolnai, L. ZORTEP: an interactive ortep program. University of Heidelberg, Germany, **1997**.
23. Zats, G. M.; Arora, H.; Lavi, R.; Yufit, D.; Benisvy, L. *Dalton Trans.* **2011,** *40,* 10889.
24. Sokolowski, A.; Adam, B.; Weyhermuller, T.; Kikuchi, A.; Hildenbrand, K.; Schnepf, R.; Hildebrandt, P.; Bill, E.; Wieghardt, K. *Inorg. Chem.* **1997,** *36,* 3702.
25. (a) Khandar, A. A.; Shaabani, B.; Belaj, F.; Bakhtiari, A. *Inorg. Chim. Acta* **2007**, *360,* 3255. (b) Sarvestani, A. H.; Mohebbi, S. J. *Chem. Res.* **2006,** 257. (c) Shongwe, M. S.; Al-Hatmi, S. K. M.; Marques, H. M.; Smith, R.; Nukada, R.; Mikuriya, M. *J. Chem. Soc., Dalton Trans.* **2002,** 4064. (d) McCollum, D. G.; Yap, G. P. A.; Rheingold, A. L.; Bosnich, B. *J. Am. Chem. Soc.* **1996,** *118,* 1365.
26. Davis, M. I.; Orville, A. M.; Neese, F.; Zaleski, J. M.; Lipscomb, J. D.; Solomon, E. I. *J. Am. Chem. Soc.* **2002,** *124,* 602.
27. (a) Koyuncu, S.; Kaya, I.; Koyuncu, F. B.; Ozdemir, E. *Synth. Met.* **2009,** *159,* 1034. (b) Refaey, S. A. M.; Hassan, A. A.; Shehata, H. S. *Int. J. Electrochem. Sci.* **2008,** *3,* 325.
28. Bottcher, A.; Takeuchi, T.; Hardcastle, K. I.; Meade, T. J.; Gray, H. B.; Cwikel, D.; Kapon, M.; Dori, *Z. Inorg. Chem.* **1997,** *36,* 2498.
29. (a) Metelski, P. D.; Fu, Y.; Khan, K.; Swaddle, T. W. *Inorg. Chem.* **1999,** *38,* 3103. (b) Endicott, J. F.; Ramasami, T. *J. Phys. Chem.* **1986,** *90,* 3740.
30. Benisvy, L.; Bill, E.; Blake, A. J.; Collison, D.; Davies, E. S.; Garner, C. D.; Guindy, C. I.; McInnes, E. J. L.; McArdle, G.; McMaster, J.; Wilson, C.; Wolowska, J. *Dalton Trans.* **2004,** 3647.
31. (a) Liptak, M. D.; Gross, K. C.; Seybold, P. G.; Feldgus, S.; Shields, G. C. *J. Am. Chem.*

www.manaraa.com

Soc. **2002,** *124,* 6421. (b) Gross, K. C.; Seybold, P. G. *Int. J. Quantum Chem.* **2001,** *85,* 569.

32. Neves, A.; Herrmann, W.; Wieghardt, K. *Inorg. Chem.* **1984,** *23,* 3435.

www.manaraa.com

CHAPTER 4

EVALUATION OF THE MECHANISTIC AND CATALYTIC BEHAVIOR OF Co^{III}-OXIMES TOWARDS HYDROGEN GENERATION

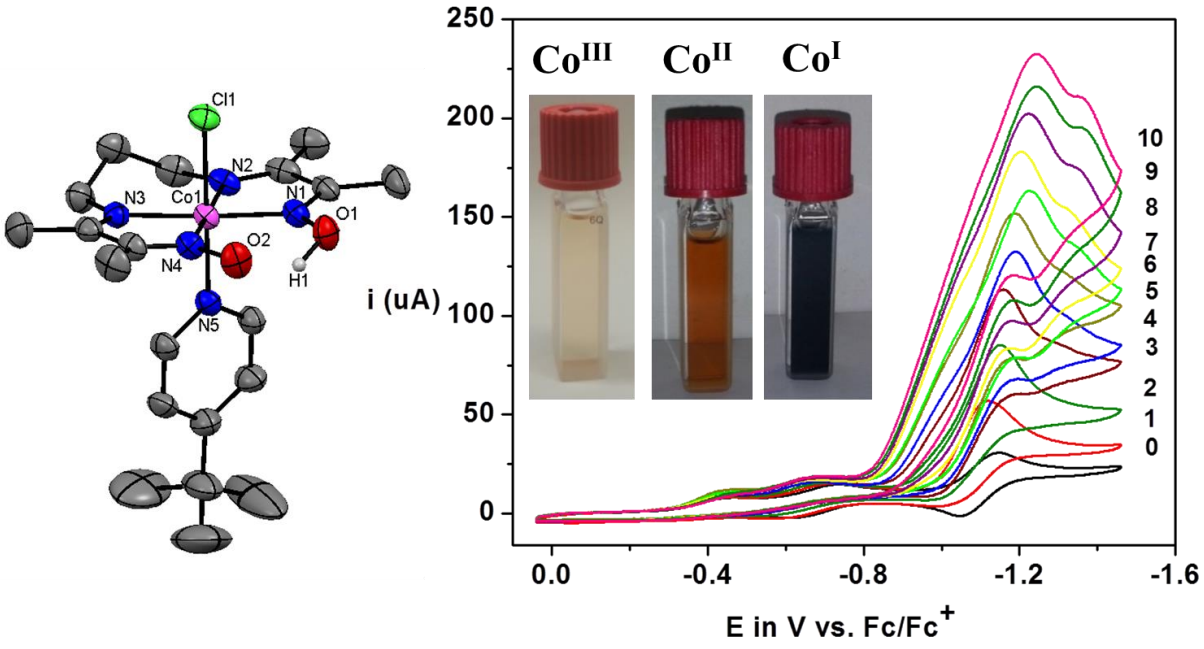

www.manaraa.com

CHAPTER 4

EVALUATION OF THE MECHANISTIC AND CATALYTIC BEHAVIOR OF Co^{III}-OXIMES TOWARDS HYDROGEN GENERATION

4.1. Introduction

We are interested in investigating a new series of complexes of polydentate ligands consisting of an acceptor moiety, in order to decrease the relatively high overpotential observed for the phenolato cobalt complexes described in the previous section. The advantage of using an acceptor moiety lies in its ability to stabilize a lower oxidation state of the metal which is otherwise absent in present of a π-donor ligand like phenolate.

We synthesized a tetradentate oxime ligand which can hold Co^{III} in the equatorial planes while allowing us to vary the axial ligands around it. First, we synthesized several complexes with homoaxial ligands. The axial ligands were systematically varied from negatively charged azide (**1**), thiocyanide (**2**) to neutral donor such as $^{4\text{-tBu}}$pyridine (**3**) (**Scheme 4.1a**). We investigated the successive redox, electronic, and catalytic behaviors of these complexes towards proton reduction. The parent Co^{III}-complex is expected to undergo two successive one-electron reduction processes to yield a catalytically active Co^{I}-intermediate able to take up a proton in acidic media, and subsequently generate the Co^{III}-hydride species. In order to enable increased effectiveness of the catalyst design, it is necessary to gain an accurate understanding of the coordination environment and electronic properties of the different redox species. Thus, furthering a collaboration on cobalt systems, we investigate three new heteroaxially substituted catalytic species $[Co^{III}(^{4\text{-tBu}}py)(HL^{oxime})(Cl)]PF_6$ (**4**), $[Co^{III}(^{4\text{-Pyr}}py)(HL^{oxime})(Cl)]PF_6$ (**5**), and $[Co^{III}(^{4\text{-Bz}}py)(HL^{oxime})(Cl)]PF_6$ (**6**) (**Scheme 4.1b**) based on oxime as the framework ligand with chloride and 4-substitued pyridine as the axial ligands. The main difference of these three species is the change of pyridine substituents in the axial position from mildly electron-donating t-butyl,

www.manaraa.com

to strongly donating pyrrolidine, to electron-withdrawing benzoyl. Using experimental and theoretical methods, we examined the successive structural, electronic, and redox variations of these species associated with proton reduction in acidic media. Catalytic mechanism for proton reduction was studied by means of experimental and theoretical tools.

We also describe the synthetic efforts towards designing photocatalytic assemblies containing the heterometallic [$Ru^{II}Co^{III}$] core, where Ru^{II} is the photosensitizer and Co^{III} is the catalytic site. The main motivation behind this work is to use the photosensitizer as an electron donor rather than an electrode. When the ruthenium center is excited with light of appropriate wavelength, one electron goes to the excited state, and can be transferred to the cobalt center.[1] Therefore, the cobalt center can be reduced and the active species will be generated *via* this electron transfer process.[1] The facility of using a heterometallic [$Ru^{II}Co^{III}$] complex rather than using two independent complexes of ruthenium and cobalt centers lies in the ease of intramolecular electron transfer rather than the intermolecular one.

In this study, we will describe synthetic, electronic, and catalytic implications of photocatalytic assemblies of [$Ru^{II}Co^{III}$] (Ru^{II} as photo-sensitizer and Co^{III} as catalytic site) for proton reduction. Generation of photocatalyst requires extensive investigation of (a) reactivity of photosensitizer, (b) excited state lifetime, (c) electron transfer, (d) reduction of the catalytic site, and (e) activity of active species towards proton, thus making the whole process fairly complicated.

These species were obtained using the oxime ligand which can act as a bridging unit, and can hold two metals in the close proximity. Therefore, we synthesized and tested proton reduction activity of water coordinated cobalt oxime complex (**7**), and a $[Ru(bpy)_2]^+$ unit was incorporated with this complex to generate a heterobimetallic [$Ru^{II}Co^{III}$] complex (**8**) (**Scheme 4.2**). To

www.manaraa.com

synthesize heterometallic complex [$Ru^{II}Co^{III}$] (**8**), a two-step synthetic procedure was executed, and has been thoroughly studied in terms of redox, electronic, catalytic, and electron-transfer behaviors.

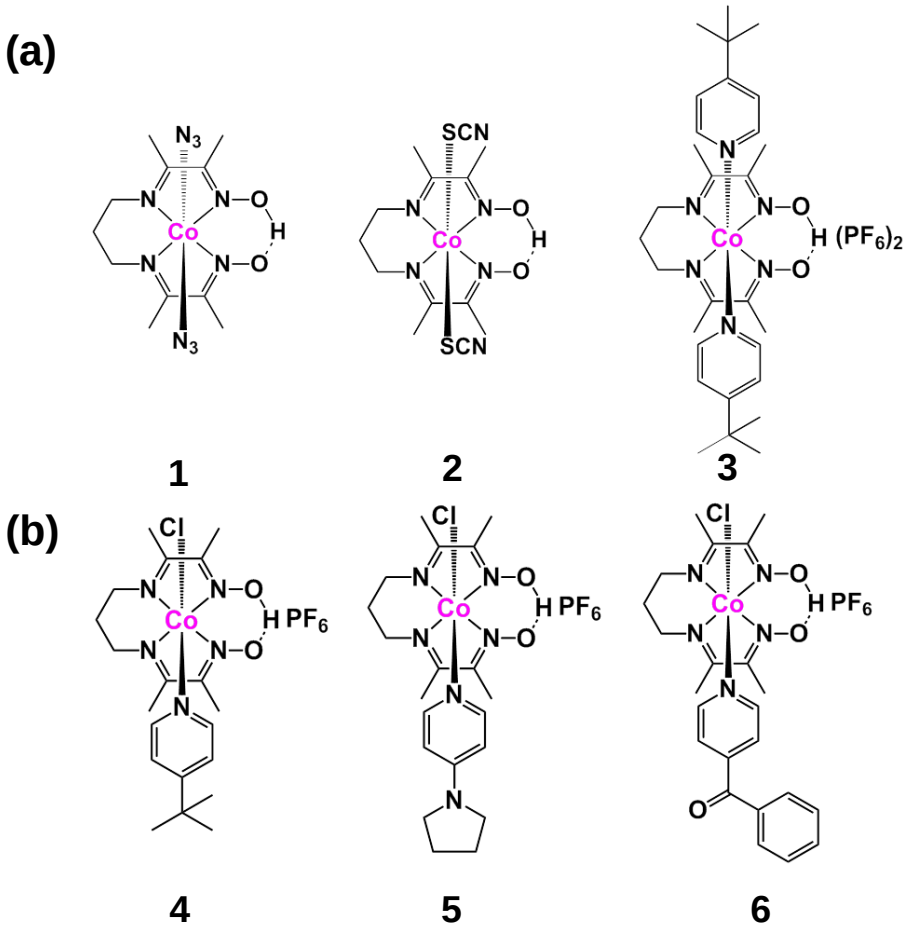

Scheme 4.1. (a) Homoaxially (**1-3**) and (b) heteroaxially (**4-6**) substituted Co(III) complexes.

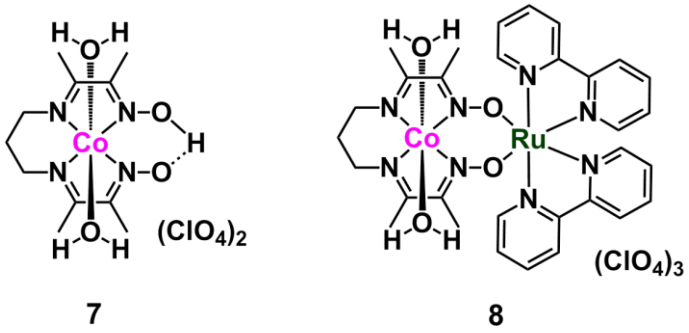

Scheme 4.2. Homoaxial water coordinated Co(III) complex and its [$Ru^{II}Co^{III}$] analog**.**

www.manaraa.com

4.2. Experimental

4.2.1. X-ray structural determination

For **2**, single crystals of $C_{13}H_{19}N_6O_2S_2Co$ was obtained *via* slow evaporation from methanol/water (2:1) mixture. A suitable crystal was selected and data was collected on a Bruker APEX-II Kappa geometry diffractometer with Mo radiation and a graphite monochromator using a Bruker CCD (charge coupled device) based diffractometer equipped with an Oxford Cryostream low-temperature apparatus. The data was measured at a temperature of 100 K. The structures were solved by the direct method using the SHELXS-97 program which is part of APEX II[2a] and refined by least squares method, SHELXL[2b], which is incorporated in OLEX2[2c] All hydrogen atoms were placed at calculated positions. The crystal structure of **2** includes one molecule in the unit cell with the SCN^- axial ligand being coordinated *via* the sulfur. The nitrogen N1 on one of the thiocyanide ligands was disordered as such it had to be refined isotropically and partial occupancy had to be assigned.

An orange single crystal for **3** was mounted. A Bruker CCD diffractometer was used to collect all the data. Phi and omega scans (0.5°/frame in the period of 20 s) were performed to measure the data. The program COSMO[2d] determined the sum of the images whereas completeness and redundancy was found to be 100% out to 0.83 Å and 4.0, respectively. APEX II software[2a] was used to determine all the parameters related to the unit cell and SAINT was used for refinement. SAINT software[2e] was used for the reduction of data. SADABS[2f] was used to perform absorption and scaling related adjustments. SHELXS-97 program was implemented to solve the crystal structures and further refined by the method of least squares on both F^2 and SHELXL- 97 (SHELXTL-PC V 6.10).[2g] This structure of **3** was measured and solved by Dr. Richard Staples from MSU and displayed $P2_1/n$ (# 14) space group. Anisotropic corrections for all atoms (non-

www.manaraa.com

hydrogen) were executed. Geometrical techniques were used to calculate hydrogen atom (except the Hs close to O1 and O2) and further refined by models based on riding method. No sign of decomposition was observed during the mounting, collection, and solving processes. All the structural representation was shown at an ellipsoidal probability of 50%.

An orange single crystal for **4** was mounted. A Bruker CCD diffractometer was used to collect all the data. Phi and omega scans (0.5°/frame in the period of 20 s) were performed to measure the data. The program COSMO[2h] determined the sum of the images whereas completeness and redundancy was found to be 100% out to 0.83 Å and 4.0, respectively. APEX II software[2i] was used to determine all the parameters related to the unit cell and SAINT was used for refinement. SAINT software[2j] was used for the reduction of the data. SADABS[2f] was used to perform absorption and scaling related adjustments. SHELXS-97 program was implemented to solve the crystal structures and further refined by the method of least squares on both F^2 and SHELXL- 97 (SHELXTL-PC V 6.10).[2g] This structure of **4** was measured and solved by Dr. Richard Staples from MSU and displayed $I\bar{4}$ (# 82) space group. Anisotropic corrections for all atoms (non-hydrogen) were executed. Geometrical techniques were used to calculate hydrogen atom and further refined by models based on riding method. The void lattice contains solvent octane which is most likely present due to crystallization. The remodeling of these solvents as dichloromethane did not generate a model which is chemically logical. The SQUEEZE[2k] function which is related to PLATON[2l] was employed to reduce or subtract any influence of the density of electron of void region from the data of intensity. 625 $Å^3$ was found to be the total volume of the solvent, with 80 electron count, which suggests the presence of CH_2Cl_2 (2 of those) in the cell. Some important parameters such as the density and F(000) and were gathered after considering two molecules of CH_2Cl_2/cell or one molecule of CH_2Cl_2/complex.

www.manaraa.com

The PLATON program was used to refine the new files with considering the presence of CH_2Cl_2. No sign of decomposition was observed during the mounting, collection, and solving processes. All the structural representation was shown at an ellipsoidal probability of 50%.

A yellow-plate single crystal for **6** was mounted. A Bruker CCD diffractometer was used to collect all the data. Phi and omega scans (0.5°/frame in the period of 20 s) were performed to measure the data. The program COSMO[2d] determined the sum of the images whereas completeness and redundancy was found to be 100% out to 0.83 Å and 4.0, respectively. APEX II software[2a] was used to determine all the parameters related to the unit cell and SAINT was used for refinement. SAINT software[2e] was used for the reduction of the data. SADABS[2f] was used to perform absorption and scaling related adjustments. SHELXS-97 program was implemented to solve the crystal structures and further refined by the method of least squares on both F^2 and SHELXL- 97 (SHELXTL-PC V 6.10)[2g] in combination with OLEX2.[2c] This structure of **6** was measured and solved by Dr. Richard Staples from MSU and displayed $P2_{1/c}$ (# 14) space group. Anisotropic corrections for all atoms (non-hydrogen) were executed. Geometrical techniques were used to calculate hydrogen atom and further refined by models based on riding method. No sign of decomposition was observed during the mounting, collection, and solving processes. All the structural representation was shown at an ellipsoidal probability of 50%.

www.manaraa.com

Table 4.1. Crystal data for complexes **2**, **3**, **4**, and **6**.

	2	**3**	**4**	**6**
Empirical formula	$C_{13}H_{19}CoN_6O_2S_2$	$C_{30}H_{49}CoF_{12}N_6O_3P_2$	$C_{21}H_{34}Cl_3CoF_6N_5O_2P$	$C_{23}H_{28}ClCoF_6N_5O_3P$
Formula weight	414.39	890.62	698.78	661.85
Temperature (K)	100.1	173(2)	173(2)	173.15
Wavelength (Å)	0.71073	0.71073	0.71073	0.71073
Crystal system, space group	Monoclinic, $P2_1/c$	Monoclinic, $P2_{1/n}$	Tetragonal, I -4	Monoclinic, $P2_{1/c}$
a (Å)	14.8641(9)	12.5242(14)	28.715(4)	6.9686(4)
b (Å)	7.2786(4)	16.7919(19)	28.715(4)	22.9724(13)
c (Å)	16.0779(9)	18.462(2)	7.0017(9)	17.7667(12)
α (º)	90.00	90.00	90	90
β (º)	94.887(3)	91.4660	90	96.4950(10)
γ (º)	90.00	90.00	90	90
Volume ($Å^3$)	1733.14(17)	3881.4(8)	5773.5(13)	2825.9(3)
Z	4	4	8	4
Calculated density (Mg/m^3)	1.588	1.524	1.608	1.556
Absorption coefficient (mm^{-1})	1.250	0.622	0.996	0.833
F (000)	856.0	1840	2864	1352
R(F) (%)	5.15	5.79	3.55	5.18
$R_w(F)$ *(%)*	7.00	8.27	3.85	7.88

4.2.2. Computational methods

All the calculations were performed with a development version of Gaussian,[3a] using B3PW91[3b-d] functional with double-zeta SDD basis set on cobalt and D95[3e-f] basis on the other atoms. All optimized structures were confirmed as minima by analyzing the harmonic vibrational frequencies. Solvation effects (in acetonitrile) were estimated using the IEF polarizable continuum model (PCM)[3g-j] and were included during structure optimization. Single-point energies were reevaluated with triple-zeta TZVP basis[3k] on the metal atom and 6-311++G(d,p)

www.manaraa.com

basis[3l] on the other atoms in presence of the continuum solvation model. The free energies were calculated using the triple-zeta SCF energy while the zero-point energy and thermal corrections were included from the double-zeta calculations. The standard states of 1 M concentration were considered for all the reactants and products for calculating the free energies of reactions. Low-spin configurations were found to be lower in energy for all the species. The wave functions of the optimized structures were tested for SCF stability.[3m-o] Isosurface plots were visualized using Gauss View.[3p] The calculation of the reduction potentials of the complexes included zero-point energy and thermal corrections and standard thermodynamic equation $\Delta G = -nFE$ was used. The calculated potentials were referenced to a value of $E_{1/2} = 4.678$ V for the ferrocene/ferrocenium couple calculated under our level of theory.

4.2.3. Catalytic activity

Proton reduction electrocatalysis was tested for **1-8** via cyclic voltammetry in presence of trifluoroacetic acid (TFA, pKa: 12.7 in CH_3CN) with tetra-butyl ammonium tetrafluoroborate ($TBABF_4$) as supporting electrolyte. For bulk electrolysis, the main chamber was filled with an electrolyte solution and proton source ($TBABF_4$: 1.317 g; TFA: 0.456 g [4 mmol], 20 mL acetonitrile) and the glass-fitted chamber was filled with another electrolyte solution ($TBABF_4$: 0.329 g; 5 mL acetonitrile). Bulk electrolysis was conducted with catalyst (0.04 mmol) in acetonitrile (CH_3CN) for 180 minutes at -1.0 $V_{Ag/AgCl}$ and the head space gas (100 µL) was injected into the GC to record the amount of dihydrogen produced. After the background subtraction, the turnover number was calculated as the ratio of the moles of dihydrogen produced over the moles of catalyst used. Faradaic efficiency was calculated from the gas chromatography measurements.

www.manaraa.com

4.2.4. Synthetic procedures

Synthesis of the ligand, H_2L^{oxime}: The tetradentate ligand, H_2L^{oxime}, was synthesized by following a standard literature procedure.[4]

Synthesis of the precursor complex $[Co^{III}(HL^{oxime})Cl_2]$: This synthesis was performed by following a literature procedure of the reaction of ligand, H_2L^{oxime}, with $CoCl_2.6H_2O$ in acetone/water (9:1) mixture.[5]

$[Co^{III}(HL^{oxime})(N_3)_2]$ (**1**). $[Co^{III}(HL^{oxime})(N_3)_2]$ was obtained by following a literature procedure.[6,7] Yield: 80 %. IR (KBr, cm^{-1}) 3436 (w) (OH); 2965 (w), 2935 (w), (aliphatic CH); 2021 (s), 2003 (s), 1941 (m) (N_3^-); 1620(m), 1528 (m) (C=N); 1430 (w) (C=C). ^{1}H-NMR [400MHz, CD_3CN, 300K] δ/ppm = 2.228 [m, 2H (CH_2)]; 2.522 [s, 6H (CH_3)]; 2.623 [s, 6H (CH_3)]; 3.928 [t, 4H (CH_2)]. ESI pos. in MeOH: m/z = 421.0668 for $[Co^{III}(HL^{oxime})(N_3)_2] + K^+$. Anal. Calcd for $C_{11}H_{19}CoN_{10}O_2$: C: 34.56; H: 5.01; N: 36.64; Found: C: 34.57; H: 4.96; N: 36.41.

$[Co^{III}(HL^{oxime})(SCN)_2]$ (**2**). $0.5H_2O$. $[Co^{III}(HL^{oxime})(SCN)_2]$ was obtained by following a literature procedure.[7] X-ray quality crystals were obtained after recrystalization from methanol/water (2:1) mixture. Yield: 85 %. IR (KBr, cm^{-1}) 3441 (w) (OH); 2958 (w), 2935 (w) (aliphatic CH); 2103 (s), 2013 (w) (SCN^-); 1621(m), 1511 (m) (C=N); 1427 (w) (C=C). ^{1}H-NMR [400MHz, CD_3CN, 300K] δ/ppm = 2.398 [m, 2H (CH_2)]; 2.530 [s, 6H (CH_3)]; 2.623 [s, 6H (CH_3)]; 3.970 [t, 4H (CH_2)]. ESI pos. in MeOH: m/z = 437.0234 for $[Co^{III}(HL^{oxime})(SCN)_2] + Na^+$. Anal. Calcd for $C_{13}H_{20}CoN_6O_{2.5}S_2$: C: 36.88; H: 4.76; N: 19.85; Found: C: 37.13; H: 4.47; N: 19.80.

www.manaraa.com

$[Co^{III}(HL^{oxime})(^{4\text{-}tBu}py)_2](PF_6)_2$ (**3**). $[Co^{III}(HL^{oxime})Br_2]$ was synthesized from $[Co^{III}(HL^{oxime})Cl_2]$ by following literature procedure.[7,8] $[Co^{III}(HL^{oxime})Br_2]$ (1 mmol, 0.458 g) was dissolved in 20 mL methanol. $AgNO_3$ (2 mmol, 0.34 g) in 10 mL of methanol was added to the methanol solution of $[Co^{III}(HL^{oxime})Br_2]$. The solution was stirred for 2 hours and the greyish white precipitate of AgBr was removed upon filtration. Then $^{4\text{-}tBu}$pyridine (2 mmol, 0.27 g) in 5 mL of methanol was added to the solution followed by KPF_6 (3.4 mmol, 0.6256 g) in 10 mL of water. The reaction mixture was stirred for 2 hours and then, rotary-evaporated to 10 mL. This solution was kept for 3-4 days and brownish-yellow precipitate was generated. X-ray quality crystals were obtained after recrystalization from methanol/water (2:1) mixture. Yield: 80 %. IR (KBr, cm^{-1}) 3671 (w) (OH); 3246 (w), 3149 (w), 3106 (w) (Aromatic-CH); 2971 (s), 2911 (m), 2875 (w) (t-butyl and other aliphatic CH); 1621 (s), 1508 (m) (C=N); 1436 (m) (C=C); 822 (s) (PF_6^-). ^{1}H-NMR [400MHz, CD_3CN, 300K] δ/ppm = 1.278 [s, 18H (t-butyl)]; 2.458 [m, 2H (CH_2)]; 2.556 [s, 6H (CH_3)]; 2.692 [s, 6H (CH_3)]; 4.262 [t, 4H (CH_2)]; 7.411 [s, 8H (aryl)]. ESI pos. in MeOH: m/z = 713.2578 for $[Co^{III}(HL^{oxime})(^{4\text{-}tBu}py)_2]$ + PF_6^-. Anal. Calcd for $C_{29}H_{45}CoF_{12}N_6O_2P_2$: C: 40.57; H: 5.28; N: 9.79; Found: C: 40.49; H: 5.19; N: 9.91.

$[Co^{III}(^{4\text{-}tBu}py)(HL^{oxime})(Cl)]PF_6$ (**4**). $[Co^{III}(HL^{oxime})Cl_2]$ (1mmol, 0.369 g) was dissolved in 20 mL methanol. KPF_6 (1.7 mmol, 0.3128 g) in 5 mL water was added to the solution followed by $^{4\text{-}tBu}$pyridine (1 mmol, 0.135 g) in 5 mL of methanol. The reaction mixture was stirred for 2 hours and then, rotary-evaporated to 10 mL. This solution was kept for 3-4 days and brownish-yellow crystals were generated. X-ray quality crystals were obtained after recrystalization from acetone/water (1:1) mixture. Yield: 75 %. IR (KBr, cm^{-1}) 3645 (w) (OH); 3234 (w) (Aromatic-CH); 2969 (s), 2907 (m), 2871 (m) (aliphatic CH); 1620 (s) (C=N); 1432 (m) (C=C); 847 (s) (PF_6^-). ^{1}H-NMR [400MHz, CD_3CN, 300K] δ/ppm =1.249 [s, 9H (t-butyl)]; 2.534 [s, 6H (CH_3)];

www.manaraa.com

2.631 [s, 6H (CH_3)]; 4.173 [m, 4H (CH_2)]; 7.358 [d, 2H(aryl)]; 7.526 [d, 2H (aryl)]. ESI pos. in MeOH: m/z = 468.1573 for $[Co^{III}(^{4\text{-}tBu}py)(HL^{oxime})(Cl)]^+$. Anal. Calcd for $C_{20}H_{32}ClCoF_6N_5O_2P$: C: 39.13; H:5.25; N: 11.41; Found: C: 39.05; H: 5.33; N: 11.37.

$[Co^{III}(^{4\text{-}Pyr}py)(HL^{oxime})(Cl)]PF_6$ (**5**). $[Co^{III}(HL^{oxime})Cl_2]$ (1mmol, 0.369 g) was dissolved in 20 mL methanol. KPF_6 (1.7 mmol, 0.3128 g) in 5 mL water was added to the solution followed by $^{4\text{-}Pyr}$pyridine (1 mmol, 0.148 g) in 5 mL of methanol. The reaction mixture was stirred for 2 hours and then, rotary-evaporated to 10 mL. This complex was extracted into dichloromethane (CH_2Cl_2) and this extraction process was repeated for 3-4 times. Petroleum ether was added to the CH_2Cl_2 layer until the solution turns turbid. After a few days, a reddish-brown precipitate was obtained. Yield: 60 %. IR (KBr, cm^{-1}) 3666 (w) (OH); 3115 (w) (Aromatic-CH); 2958 (w), 2872 (w) (aliphatic CH); 1623 (s) (C=N); 1461 (m) (C=C); 835 (s) (PF_6^-). ESI pos. in MeOH: m/z = 481.1563 for $[Co^{III}(^{4\text{-}Pyr}py)(HL^{oxime})(Cl)]^+$. Anal. Calcd for $C_{20}H_{31}ClCoF_6N_6O_2P$: C: 38.32; H:4.98; N: 13.41; Found: C: 38.25; H: 4.91; N: 13.36.

$[Co^{III}(^{4\text{-}Bz}py)(HL^{oxime})(Cl)]PF_6$ (**6**). $[Co^{III}(HL^{oxime})Cl_2]$ (1mmol, 0.369 g) was dissolved in 20 mL methanol. KPF_6 (1.7 mmol, 0.3128 g) in 5 mL water was added to the solution followed by $^{4\text{-}Bz}$pyridine (1 mmol, 0.183 g) in 5 mL of methanol. The reaction mixture was stirred for 2 hours and then, rotary-evaporated to 10 mL. This solution was kept for 3-4 days and brownish-yellow precipitate were generated. X-ray quality crystals were obtained after recrystalization from ethanol/acetone (1:1) mixture. Yield: 80 %. IR (KBr, cm^{-1}) 3509 (w) (OH); 3141 (w), 3090 (w) (Aromatic-CH); 2934 (w), 2850 (w) (aliphatic CH); 1674 (m) (C=O); 1613 (m), 1598 (m) (C=N); 1448 (m) (C=C); 840 (s) (PF_6^-). ESI pos. in MeOH: m/z = 516.1207 for $[Co^{III}(^{4\text{-}Bz}py)(HL^{oxime})(Cl)]^+$. Anal. Calcd for $C_{23}H_{28}ClCoF_6N_5O_3P$: C: 41.74; H:4.26; N: 10.58; Found: C: 41.60; H: 4.30; N: 10.16.

www.manaraa.com

$[Co^{III}(HL^{oxime})(H_2O)_2](ClO_4)_2$ (**7**): $[Co^{III}(HL^{oxime})Cl_2]$ (1 mmol, 0.369 g) was dissolved in 20 mL ethanol. $AgClO_4$ (2 mmol, 0.415 g) in 5 mL water was added to the solution. The reaction mixture was stirred for 2 hours and the greyish white precipitate of AgCl was removed upon filtration. The filtrate was rotary-evaporated to 10 mL. This solution was kept for 3-4 days and brownish-yellow precipitate was obtained. Yield: 90 %. IR (KBr, cm^{-1}) 3324 (m) (OH); 2934 (w), 2850 (w) (aliphatic CH); 1623 (w), 1526 (w) (C=N); 1436 (w) (C=C); 1122 (s) (ClO_4^-). ^{1}H-NMR [400MHz, CD_3CN, 300K] δ/ppm = 2.702 [m, 2H (CH_2)]; 2.801 [s, 6H (CH_3)]; 2.892 [s, 6H (CH_3)]; 4.242 [t, 4H (CH_2)]. ESI pos. in MeOH: m/z = 298.0827 for $[Co^{III}(HL^{oxime})]^+$. Anal. Calcd for $C_{11}H_{23}Cl_2CoN_4O_{12}$: C: 24.78; H: 4.35; N: 10.51; Found: C: 24.48; H: 4.38; N: 10.30.

$[Ru^{II}(bpy)_2Co^{III}(HL^{oxime})(H_2O)_2](ClO_4)_3$ (**8**). 2EtOH: 1 equivalent of $[Ru(bpy)_2Cl_2].2H_2O$ (1 mmol, 0.520 g) was treated with 2 equivalents of $AgClO_4$ (2 mmol, 0.415g) in 25 mL of $EtOH/H_2O$ (4:1) mixture at room temperature for 3 hours under argon atmosphere and the greyish white precipitate of AgCl was removed upon filtration. $[Co^{III}(HL^{oxime})(H_2O)_2](ClO_4)_2$ (**4**) (1 mmol, 0.533 g) in 20 mL of ethanol was subsequently added to the filtrate in the presence of triethylamine (1.7 mmol, 0.1717 g) as a base and stirred at refluxing condition for 48 hours under argon atmosphere to generate the desired complex. After the reaction, solvent was reduced to 5-10 mL and excess $NaClO_4$ in water was added to ensure precipitation. A brownish-black colored precipitate was obtained after keeping the solution in the fridge for 3-5 days. Yield: 70 %. IR (KBr, cm^{-1}) 3350 (m) (OH); 3250(w), 3150 (w) (aromatic CH); 2935(w), 2850 (w) (aliphatic CH); 1620 (s), 1520 (m) (C=N); 1463 (m) (C=C); 1088 (s) (ClO_4^-). Anal. Calcd for $C_{35}H_{50}Cl_3CoN_8O_{18}Ru$: C: 36.97; H: 4.43; N: 9.85; Found: C: 37.14; H: 4.48; N: 9.71.

www.manaraa.com

4.3. Results and discussions

4.3.1. Syntheses and characterizations

The tetradentate ligand H_2L^{oxime} was generated by following literature procedures. Complexes **1** – **3** were obtained by stepwise reaction of $CoCl_2.6H_2O$ with the ligand H_2L^{oxime} to obtain the dichloro complex which was further treated with sodium azide or potassium thiocyanide to produce **1**, and **2** respectively (**Figure 4.1a**). Complex **3** was generated by the stepwise formation of dibromo complex from the dichloro precursor followed by the addition of 4-substituted pyridines and KPF_6 as shown in **Figure 4.1b**.

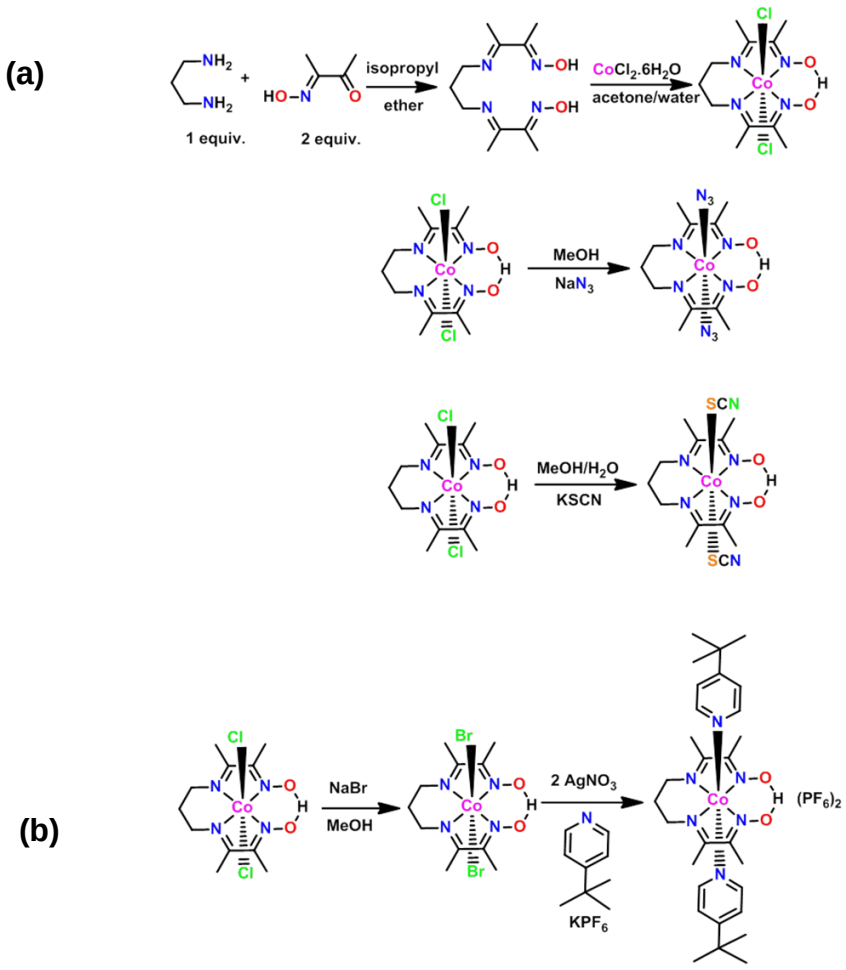

Figure 4.1. (a) Synthetic scheme for **1** and **2. (b)** Synthetic scheme for **3.**

www.manaraa.com

These complexes were designed to study the role of axial substituents on the electronic and catalytic properties of their corresponding Co^{III} complexes. Red (**1**) and yellow (**2**, and **3**) solids were obtained as the final products and characterized with multiple spectroscopic (FTIR and ^{1}H-NMR), spectrometric (ESI-MS) and combustion (C, H, N elemental analyses) techniques. The FTIR spectra for each complexes confirm two C=N peaks around 1500 and 1600 cm^{-1} characteristic of the imine and oxime moieties. For **3**, the presence of PF_6^- counterion was confirmed from the very strong and broad peak around 850 cm^{-1}, respectively. High-resolution ESI mass spectra display the species $[M + K^+]^+$, $[M + Na^+]^+$, $[M + PF_6^-]^+$ for **1-3**, respectively (**Figure 4.2**). Experimental and simulated isotopic distributions are in agreement with the proposed molecular composition.

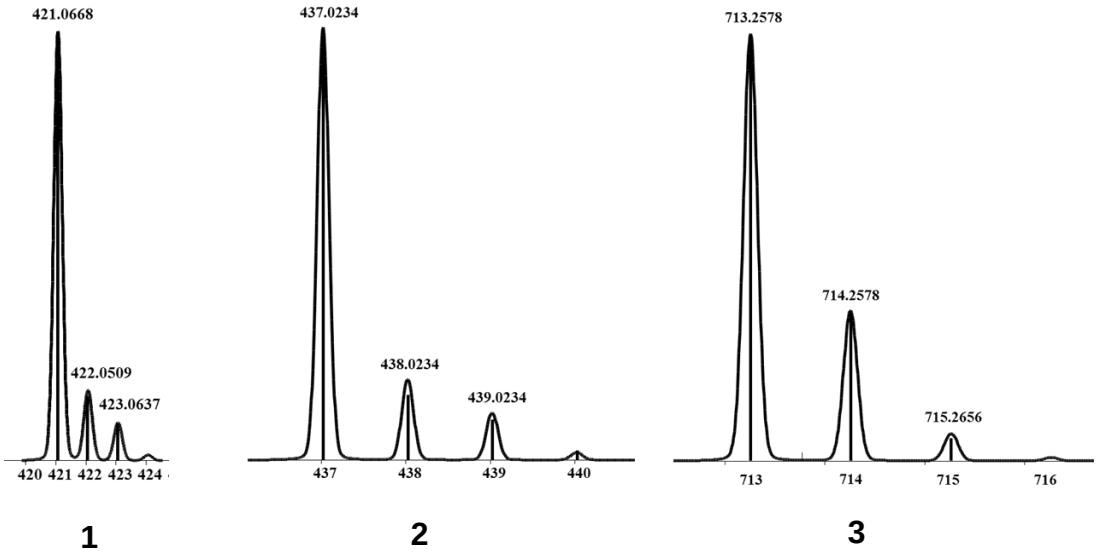

Figure 4.2. Experimental (bars) and simulated (line) isotopic distribution for the molecular ions of complexes **1-3**.

Due to the diamagnetic nature of the low spin Co^{III} configuration, the ^{1}H-NMR spectra were taken in CD_3CN for selected complexes and shown in **Figure 4.3**.

www.manaraa.com

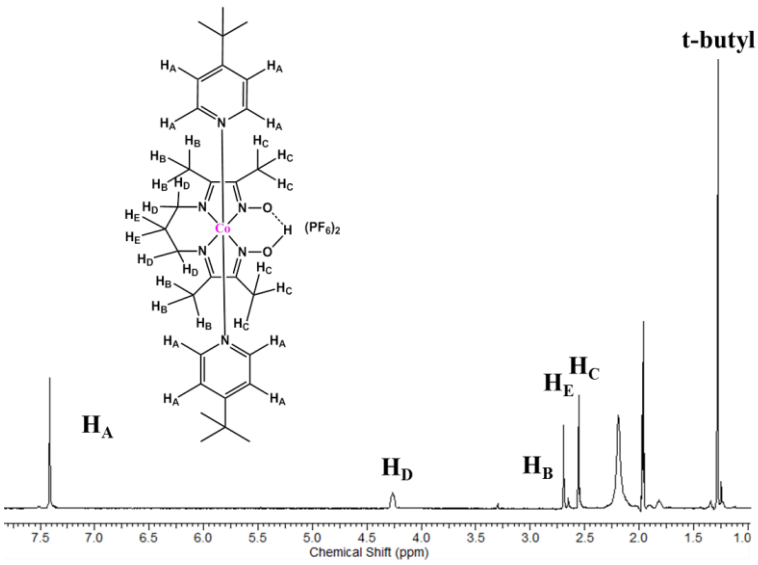

Figure 4.3. ^{1}H-NMR spectra of **3** in CD_3CN.

The hetero-axial complexes **4**, **5**, and **6** were generated by stepwise reaction of $CoCl_2.6H_2O$ with the ligand H_2L^{oxime} to obtain the dichloro complex which was further treated with 4-substituted pyridines and KPF_6 to get the desired complexes as shown in **Figure 4.4**. These new complexes were designed following the recent trends in the area of development of proton reduction catalysts. Yellow (**4** and **6**) and red (**2**) solids were obtained as the final products and characterized with spectroscopic (FTIR and ^{1}H-NMR), ESI-MS spectrometric and combustion (C, H, N elemental analyses) methods. The FTIR spectra for each complex confirm a C=N stretching around 1600 cm^{-1} characteristic of the oxime ligand and the presence of PF_6^- was confirmed from the broad peak around 850 cm^{-1}. High-resolution ESI mass spectra display the species $[M]^+$ for **4-6** (**Figure 4.5**). Experimental and simulated isotopic distributions are in agreement with the proposed molecular composition. Due to the diamagnetic nature of the low spin Co^{III}-configuration, the ^{1}H-NMR spectra were taken in CD_3CN and shown in **Figure 4.6**. The spectra have shown appropriate line-splitting patterns for **4** with four aromatic protons between 6-8 ppm originating from the pyridine moiety, one OH proton at 18.85 ppm, six

www.manaraa.com

methylene protons between 2.0-4.5 ppm and 12 methyl protons between 2.4-2.6 ppm. The intense peaks found around 1.3 ppm are from the protons (9H) of the t-butyl substituent.

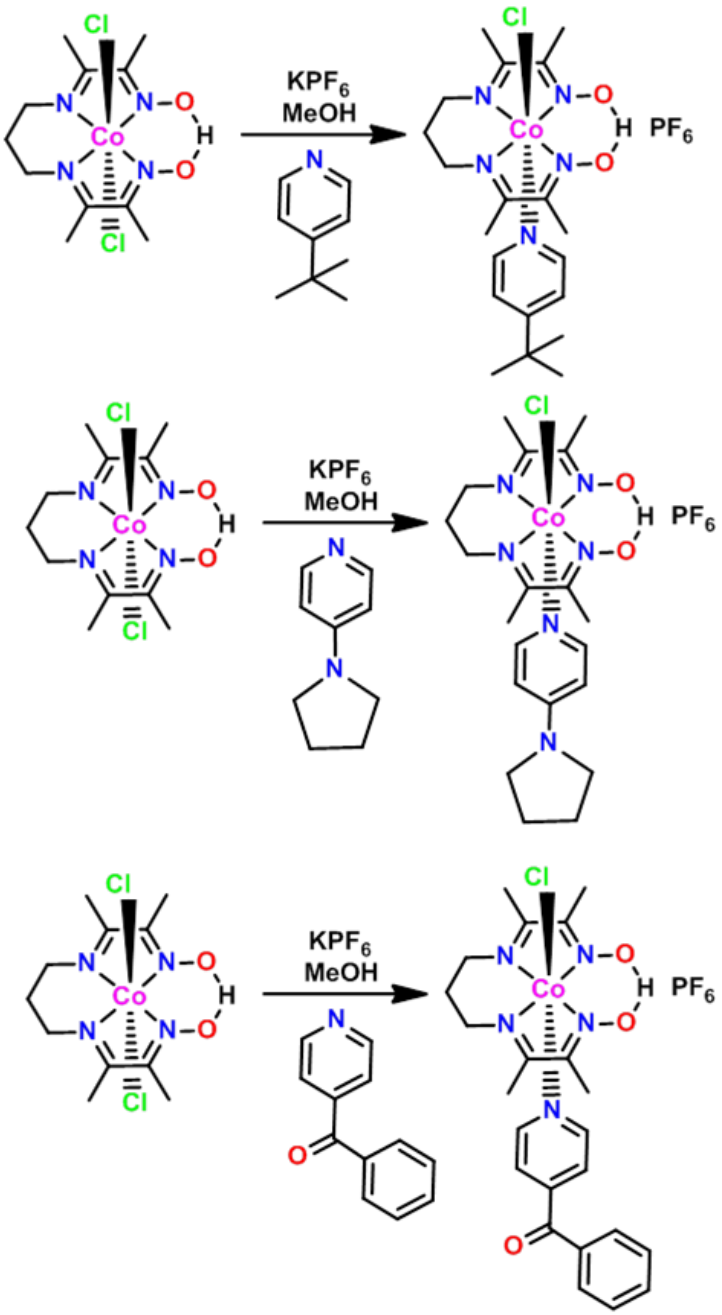

Figure 4.4. Synthetic schemes of complexes **4**, **5**, and **6**.

www.manaraa.com

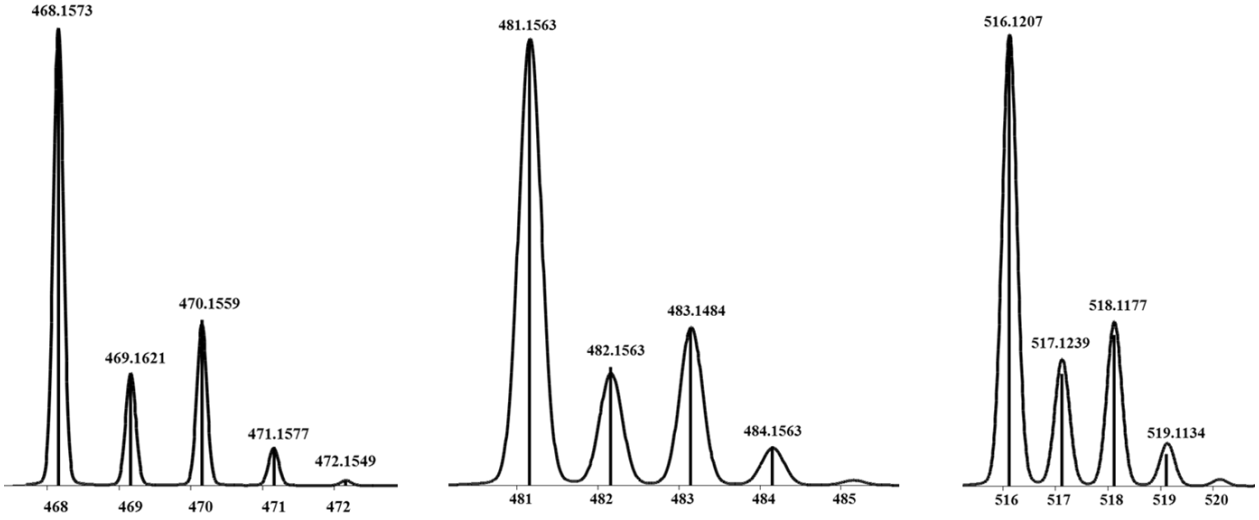

Figure 4.5. Experimental (bars) and simulated (line) isotopic distribution for the molecular ions of complexes **4**-**6** (left to right).

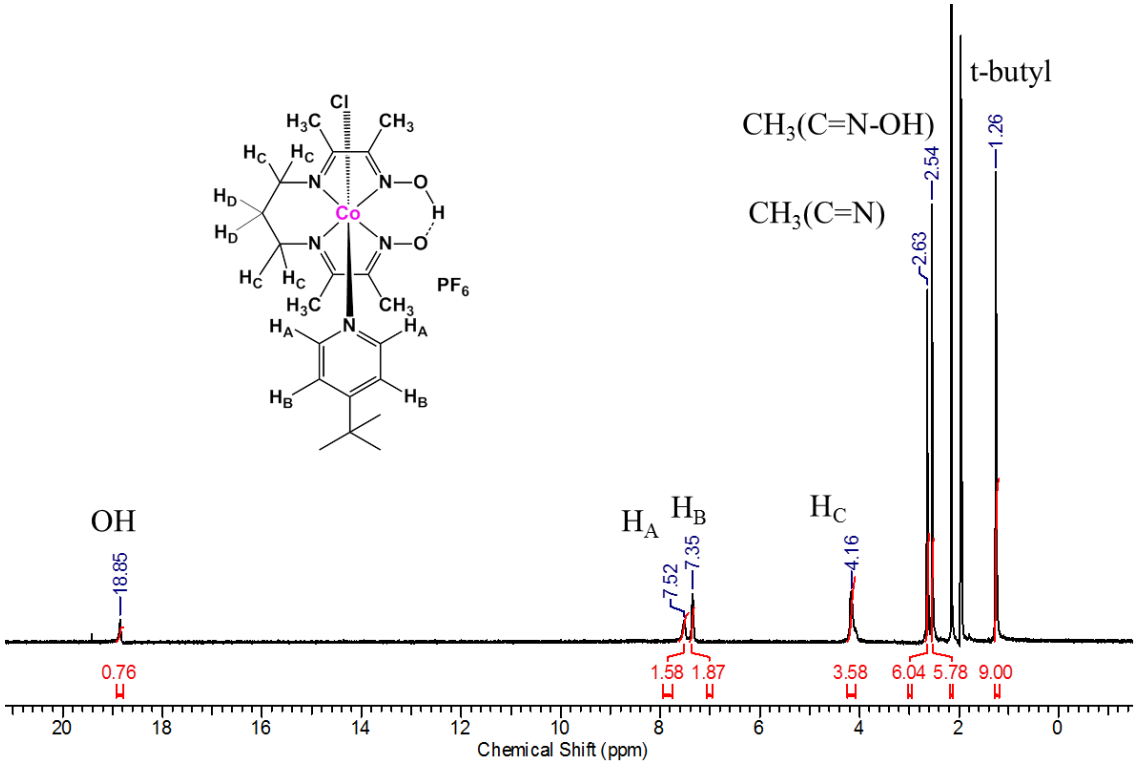

Figure 4.6. ^{1}H-NMR spectra of **4** in CD_3CN.

www.manaraa.com

The complex **7** was obtained upon reaction between the dichloro complex with $AgClO_4$ (**Figure 4.7**). To synthesize heterometallic complex [$Ru^{II}Co^{III}$] **8**, a two-step synthetic procedure was executed (**Figure 4.7**). During the first step, $Ru(bpy)_2Cl_2$ was treated with $AgClO_4$ in $EtOH/H_2O$ (9:1) mixture at room temperature for few hours to generate ethanol coordinated $Ru^{II}(bpy)_2$ complex which was further treated with complex **7** in presence of Et_3N to generate the [$Ru^{II}Co^{III}$] complex **8**. This complex was thoroughly characterized by multiple physico-chemical techniques.

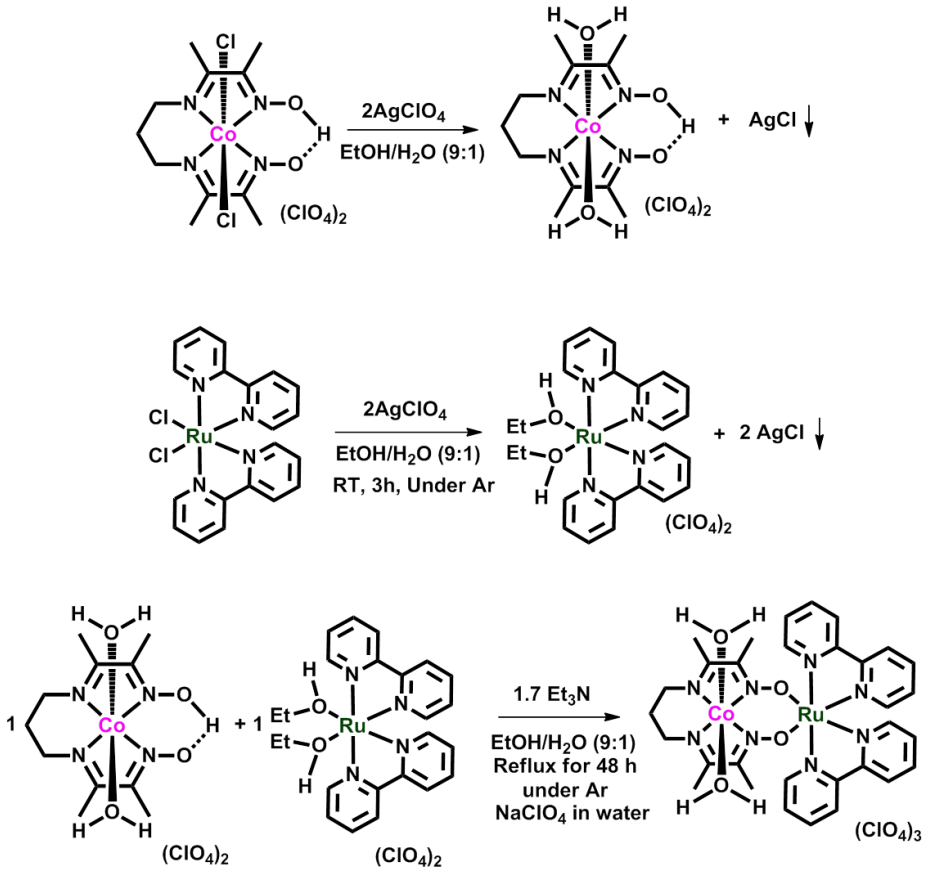

Figure 4.7. Synthetic Scheme for the formation of [Co^{III}] and heterometallic [$Ru^{II}Co^{III}$] complex.

These complexes were extensively characterized by FTIR, and ^{1}H-NMR spectroscopy, ESI mass spectrometry, and elemental analyses. The presence of a perchlorate counterion was confirmed from the very broad peak around 1100 cm^{-1} in the FTIR spectra.

www.manaraa.com

5.3.2. Molecular structures

Complexes **2** and **3** yielded diffraction-quality crystals. The molecular geometries obtained from the X-ray crystal structures of **2** and **3** are shown in **Figure 4.8.** It confirmed the octahedral geometry of the cobalt center with the oxime ligand occupying the equatorial plane whereas thiocyanide or $^{4\text{-tBu}}$pyridine coligands are in the axial positions. Furthermore, one of the oxime-oxygen atoms remains protonated while the other one is deprotonated forming an O-H---O hydrogen-bonding between them.

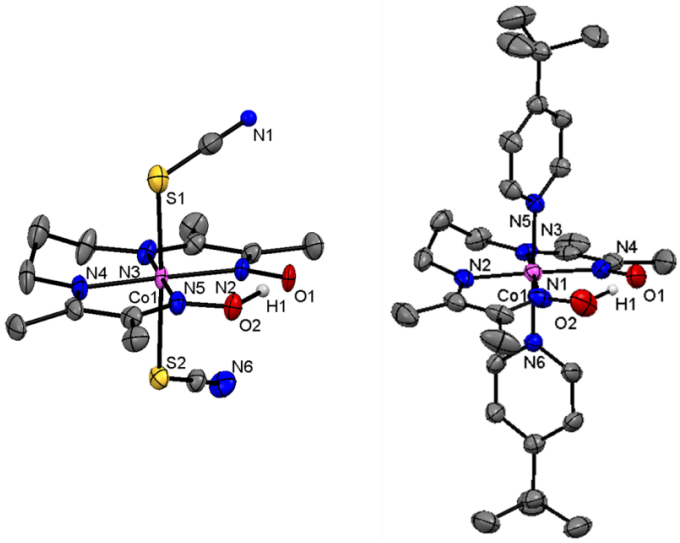

Figure 4.8. The ORTEP representation of the cations of **2** and **3** at 50% ellipsoid probability. Bond lengths are in Å: For 2: Co(1)-N(2): 1.880(2); Co(1)-N(3): 1.908(3); Co(1)-N(4): 1.921(2); Co(1)-N(5): 1.896(3); Co(1)-S(1): 2.2972(10); Co(1)-S(2): 2.3006(9). For 3: Co(1)-N(1): 1.901(3); Co(1)-N(2): 1.915(3); Co(1)-N(3): 1.912(3); Co(1)-N(4): 1.886(3); Co(1)-N(5): 1.973(3); Co(1)-N(6): 1.977(3).

Complexes **4** and **6** yielded diffraction-quality crystals. The molecular geometries obtained from the X-ray crystal structures of **4** and **6** are shown in **Figure 4.9.** It confirmed the octahedral geometry of the cobalt center with the oxime ligand occupying the equatorial plane whereas chloride and $^{4\text{-tBu}}$pyridine/$^{4\text{-Bz}}$pyridine coligands are in the axial positions. Furthermore, one of the oxime-oxygen atoms remains protonated while the other one is deprotonated forming an

www.manaraa.com

O-H---O hydrogen-bonding between them. Comparison of the Co–Cl bond length between **4** and **6** reveals slightly longer bond in **4** (2.2376Å) in comparison with **6** (2.2336Å). On the other hand, the bond length between Co and pyridine nitrogen atom (Co1–N5) becomes longer from 1.975Å in complex **4** to 1.990Å in **6**. Therefore, we can say that incorporation of the electron-withdrawing benzoyl substituent on the pyridine ring makes the Co–N5 (pyridine) bond weaker and the Co–Cl bond slightly stronger when compared with **4**.

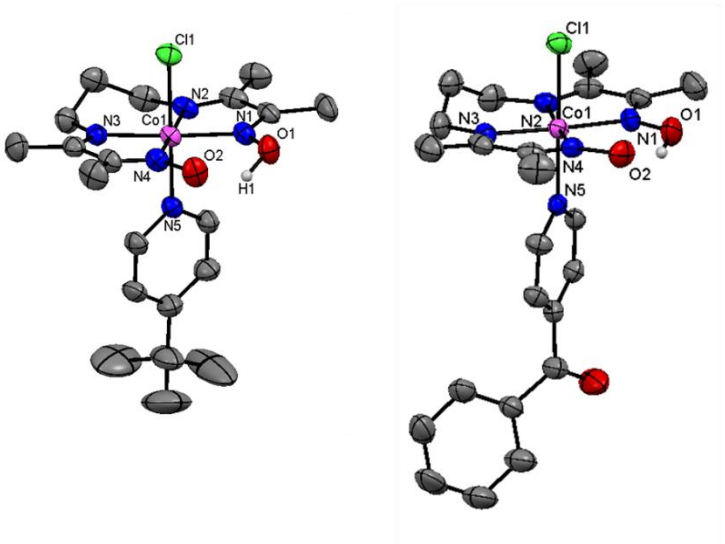

Figure 4.9. The ORTEP representation of the cations of **4** and **6** at 50% ellipsoid probability. Bond lengths are in Å: For **1**: Co(1)-N(1): 1.903(3); Co(1)-N(2): 1.917(2); Co(1)-N(3): 1.914(2); Co(1)-N(4): 1.898(2); Co(1)-N(5): 1.975(3); Co(1)-Cl(1): 2.237(8). For **3**: Co(1)-N(1): 1.891(3); Co(1)-N(2): 1.934(3); Co(1)-N(3): 1.923(3); Co(1)-N(4): 1.893(3); Co(1)-N(5): 1.990(3); Co(1)-Cl(1): 2.2336(11).

4.3.3. Oxidation states and coordination preferences of the complexes generated in the electrochemical pathway towards proton reduction

The reduced analogs of **1-6**, generated in the electrochemical pathway, play important role in proton reduction catalysis. Therefore, a detailed analysis of their coordination environments, spin states and electronic structures is of the utmost importance. We employed multiple methodologies, namely, cyclic voltammetry, ^{1}H-NMR, UV-visible, EPR spectroscopy and

www.manaraa.com

density functional theory (DFT) to characterize the nature of those species.

4.3.3.1. Redox Properties

Cyclic voltammetry was performed for **1**-**3** in CH_3CN to elucidate the nature of the redox species present in the solution (**Figure 4.10**).

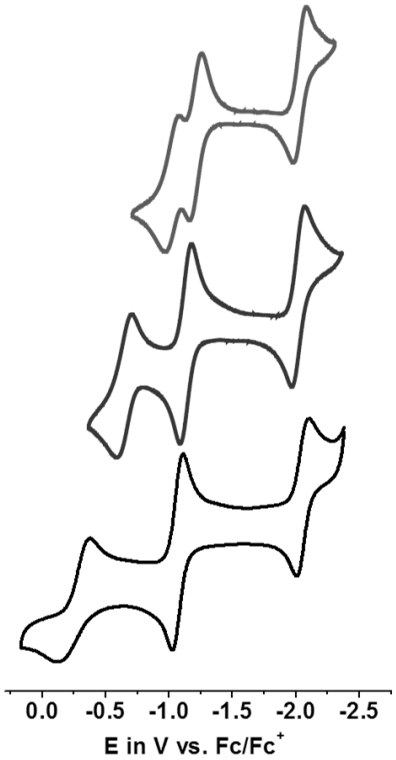

Figure 4.10. Cyclic voltammograms of **1**, **2**, and **3** in CH_3CN (Supporting electrolyte: $TBAPF_6$; Scan rate: 100 mV/s; Glassy C: working electrode; Pt-wire: auxillary electrode; Ag/AgCl: reference electrode).

All of these complexes displayed three reversible redox processes which can be tentatively assigned to Co^{III}/Co^{II}, Co^{II}/Co^{I} and a ligand based. Co^{III}/Co^{II} process was varied significantly upon changing the axial ligands whereas the Co^{II}/Co^{I} couple (around -1.1 $V_{Fc/Fc+}$) was altered slightly. The Co^{III}/Co^{II} redox potential was found to be less negative for neutral donors like $^{4\text{-tBu}}$pyridine, whereas the negatively charged ligand showed more negative potential (azide coordinated complex displays more negative potential than the thiocyanide coordinated one).

www.manaraa.com

The corresponding $E_{1/2}$ of Co^{III}/Co^{II} potentials for complex **1-3** are -1.01, -0.65, and -0.25 $V_{Fc/Fc+}$, respectively. On the other hand, Co^{II}/Co^{I} process remained between -1.05 to -1.2 $V_{Fc/Fc+}$ for all these complexes. The azide coordinated complex (**1**) exhibited the most negative shift of Co^{II}/Co^{I} potential at -1.20 $V_{Fc/Fc+}$ whereas the least negative Co^{II}/Co^{I} process was observed for $^{4\text{-}tBu}$pyridine substituted complex (**3**). The Co^{I}-complex generated is known to be catalytically active towards proton reduction and generation of dihydrogen via a Co^{III}–H and/or Co^{II}–H intermediate. The ligand-based processes observed around -2.00 $V_{Fc/Fc+}$ may be attributed to the redox non-innocence of imine-oxime moieties.

Table 4.2. Cyclic voltammetric parameters for **1-3** in CH_3CN. The potentials are reported *versus* Fc/Fc^+.

	Co^{III}/Co^{II} $E_{½}$, [E_{pc}; E_{pa}], V (ΔE, V) $\lvert i_{pc}/i_{pa}\rvert$	**Co^{II}/Co^{I}** $E_{½}$, V (ΔE, V) $\lvert i_{pc}/i_{pa}\rvert$	**C=N/$C^{\bullet}$-N^{-}** $E_{½}$, V (ΔE, V) $\lvert i_{pc}/i_{pa}\rvert$
1	-1.01 (0.11) |1.59|	-1.20 (0.10) |0.70|	-2.03 (0.11) |1.37|
2	-0.65 (0.12) |0.88|	-1.14 (0.09) |0.99|	-2.02 (0.10) |1.26|
3	-0.25 (0.25) |N/A|	-1.07 (0.09) |1.09|	-2.05 (0.10) |1.13|

Similarly, the electrochemical properties were also investigated for heteroaxially substituted cobalt complexes. Cyclic voltammetry (CV) study of **4** in CH_3CN (**Figure 4.11**) revealed two events associated with the Co^{III}/Co^{II} couple at -0.49V ($E_{p,c}$) and -0.70V ($E_{1/2}$) [ΔE = 0.10V; $|i_{pc}/i_{pa}|$ = 0.91], whereas the Co^{II}/Co^{I} process appears at -1.09V ($E_{1/2}$) [ΔE = 0.11V; $|i_{pc}/i_{pa}|$ = 0.99] *versus* the ferrocene/ferrocenium (Fc/Fc^+) couple. One additional reduction process found at -2.11$V_{Fc/Fc+}$ [ΔE = 0.23V; $|i_{pc}/i_{pa}|$ = 2.23] is attributed to the oxime ligand. A similar CV profile was observed for complex **6** with the potentials listed in **Table 4.3.** A significantly different behavior was observed for complex **5** with only one Co^{III}/Co^{II} event (**Figure 4.11** and **Table 4.3**) appearing.

www.manaraa.com

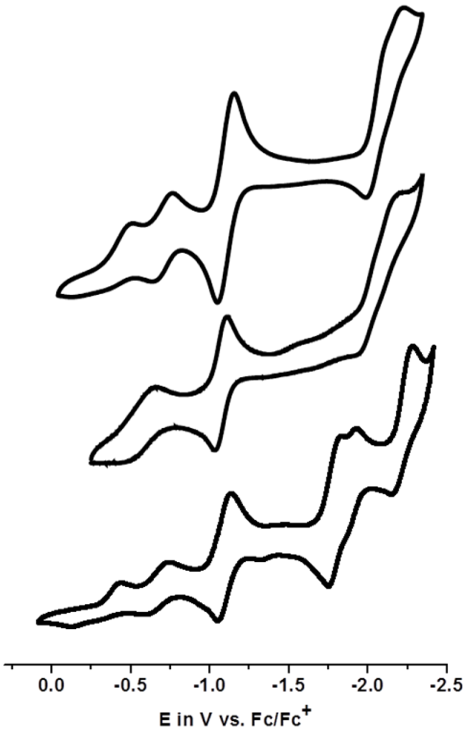

Figure 4.11. Cyclic voltammograms of **4, 5,** and **6** in CH_3CN (Supporting electrolyte: $TBAPF_6$; Scan rate: 100 mV/s; Glassy C: working electrode; Pt-wire: auxillary electrode; Ag/AgCl: reference electrode).

The first Co^{III}/Co^{II} event is irreversible for both **4** and **6** and the $E_{p,c}$ shifts from -0.49 V to -0.43 $V_{Fc/Fc+}$ (**Table 4.3**). The second Co^{III}/Co^{II} process appears at around -0.70 V indicating that it is most likely originated from the same species. Complex **5** shows only one Co^{III}/Co^{II} event at -0.59 V. Moreover, the potential for the Co^{II}/Co^{I} event remains constant (~ -1.1 V) for all the three complexes. The Co^{I}-complex generated is known to be catalytically active towards proton reduction and generation of dihydrogen via a Co^{III}–H and/or Co^{II}–H intermediate. The ligand-based processes observed between -1.79 to -2.22 V may be attributed to the redox non-innocence of imine-oxime (in case of **4-6**) and benzoyl moieties (for complex **6**).

www.manaraa.com

Table 4.3. Cyclic voltammetric parameters for **4**-**6** in CH_3CN. The potentials are reported *versus* Fc/Fc^+.

	Co^{III}/Co^{II} $E_{½}$, [E_{pc}; E_{pa}], V (ΔE, V) $\lvert i_{pc}/i_{pa}\rvert$	**Co^{II}/Co^{I}** $E_{½}$, V (ΔE, V) $\lvert i_{pc}/i_{pa}\rvert$	**$C{=}N/C^{\bullet}\text{-}N^{-}$** $E_{½}$, V (ΔE, V) $\lvert i_{pc}/i_{pa}\rvert$	**Other ligand based events** $E_{½}$, V (ΔE, V) $\lvert i_{pc}/i_{pa}\rvert$
1	$E_{p,c}$: -0.49; $E_{p,a}$: -0.19 -0.70 (0.10) |0.91|	-1.09 (0.11) |0.99|	-2.11 (0.23) |2.23|	
2	-0.59 (0.12) |0.45|	-1.07 (0.08) |1.09|	-2.07 (0.23) |N/A|	
3	$E_{p,c}$: -0.43; $E_{p,a}$: -0.13 -0.68 (0.11) |1.41|	-1.09 (0.08) |1.19|	-2.22 (0.12) |5.99|	-1.79 (0.08) |N/A| -1.91 (0.03)|1.03|

To check for involvement of a solvent CH_3CN molecule in the second Co^{III}/Co^{II} redox events for **4** and **6**, the cyclic voltammetry experiment of **4** was repeated in a non-coordinating solvent, CH_2Cl_2 (**Figure 4.12**). Appearance of two Co^{III}/Co^{II} events in presence of CH_2Cl_2 allows us to dismiss the possibility of interference of CH_3CN in the second Co^{III}/Co^{II} event. The origin of this second Co^{III}/Co^{II} process will be discussed in a later section.

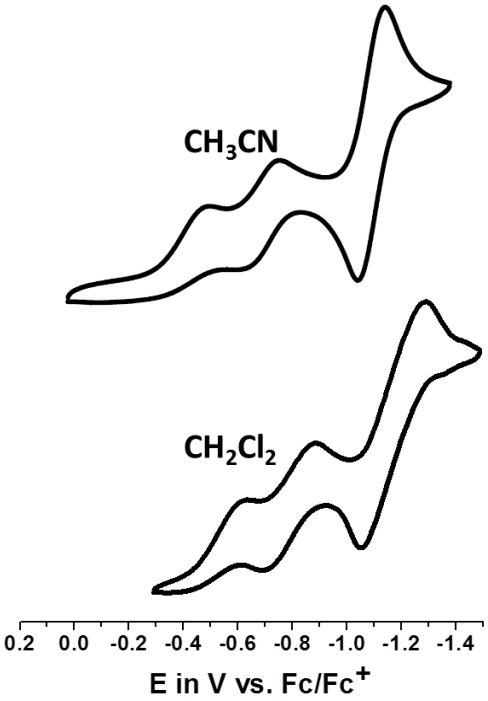

Figure 4.12. Cyclic voltammograms of **4** in coordinating (CH_3CN) *versus* in a non-coordinating (CH_2Cl_2) solvent. The redox processes undergo cathodic shift in CH_2Cl_2.

www.manaraa.com

To understand the electrochemical processes, cyclic voltammetry has been performed in CH_3CN for **7** and **8** (**Figure 4.13**). The complex **7** exhibits Co^{III}/Co^{II}, Co^{II}/Co^{I}, and ligand based processes. The bimetallic [$Ru^{II}Co^{III}$] (**8**) complex shows four reversible processes at $E_{1/2}$ = 0.46 $V^{Fc/Fc+}$ due to Ru^{II}/Ru^{III} couple, -1.27 $V_{Fc/Fc+}$ due to Co^{II}/Co^{I} redox couple, -1.89 $V_{Fc/Fc+}$ and -2.11 $V_{Fc/Fc+}$ due to the bipyridine and imine based processes and one irreversible process at E_{pa} = 1.20 $V_{Fc/Fc+}$ due to the ligand centered oxidation in CH_3CN. The shifting of potential for Ru^{II}/Ru^{III} couple from 0 V as in [$Ru(bpy)_2Cl_2$] to 0.46 V for the [$Ru^{II}Co^{III}$] (**8**) complex further confirms the coordination of oxygen on ruthenium. All the cyclic voltammetric parameters are shown in **Table 4.4**.

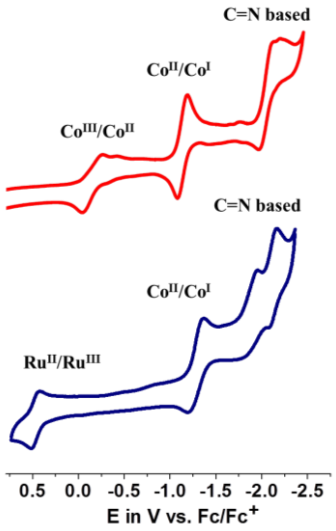

Figure 4.13. Electrochemistry of **7** and **8** in CH_3CN.

Table 4.4. Electrochemical parameters in CH_3CN.

	Ru^{II}/Ru^{III} $E_{½}$, V (ΔE, V) $\lvert i_{pc}/i_{pa}\rvert$	**Co^{III}/Co^{II}** $E_{½}$, V (ΔE, V) $\lvert i_{pc}/i_{pa}\rvert$	**Co^{II}/Co^{I}** $E_{½}$, V (ΔE, V) $\lvert i_{pc}/i_{pa}\rvert$	**$C{=}N/C^{\bullet}\text{-}N^{-}$** $E_{½}$, V (ΔE, V) $\lvert i_{pc}/i_{pa}\rvert$
7		-0.14 (0.21) |1.01|	-1.13 (0.11) |1.16|	-2.03 (0.15) |N/A|
8	+0.47 (0.09) |0.53|		-1.28 (0.17) |1.12|	-1.88 (0.14) |N/A| -2.12 (0.07) |N/A|

www.manaraa.com

4.3.3.2. Electronic properties

In the visible region, complexes **1-3** showed relatively transparent spectra which are characteristics of the Co^{III}-parent state (**Figure 4.14**).

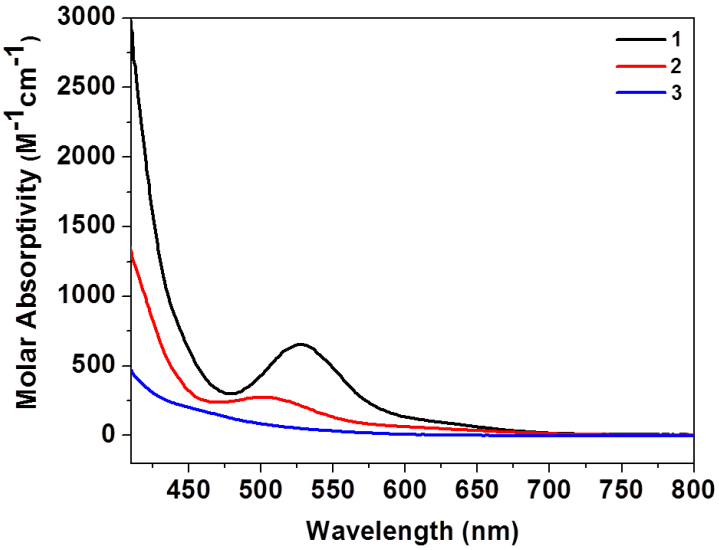

Figure 4.14. UV-visible spectra of **1-3** ([C] = 1.0×10^{-3} M) in acetonitrile.

Co^{II}- and Co^{I}-complexes of **2** were isolated in CH_3CN by bulk electrolysis at -0.46$V_{Ag/AgCl}$ and -0.95$V_{Ag/AgCl}$, respectively. Distinctive electronic behaviors of **2**, and its Co^{II}- and Co^{I}-analogs were observed in the UV-visible region as illustrated in **Figure 4.15**. The spectrum of **2** does not show any charge-transfer (CT) band and it is a characteristic of a low-spin $3d^6$ Co^{III}-center with a strong-field π-acceptor ligand framework. This complex displays a faint yellow color. The Co^{II}-species shows a shoulder at around 435 nm (ε = 2742 $M^{-1}cm^{-1}$) and is orange in color which can be attributed to a metal-to-ligand charge transfer (MLCT) transition originating from the Co^{II}-center to the oxime ligand framework. The Co^{I}-complex is tentatively associated with both intra-ligand charge transfer (ILCT) and MLCT bands at 606 and 672 nm (ε = 3668 and 3562 $M^{-1}cm^{-1}$) accounting for the characteristic blue color of the complex.

www.manaraa.com

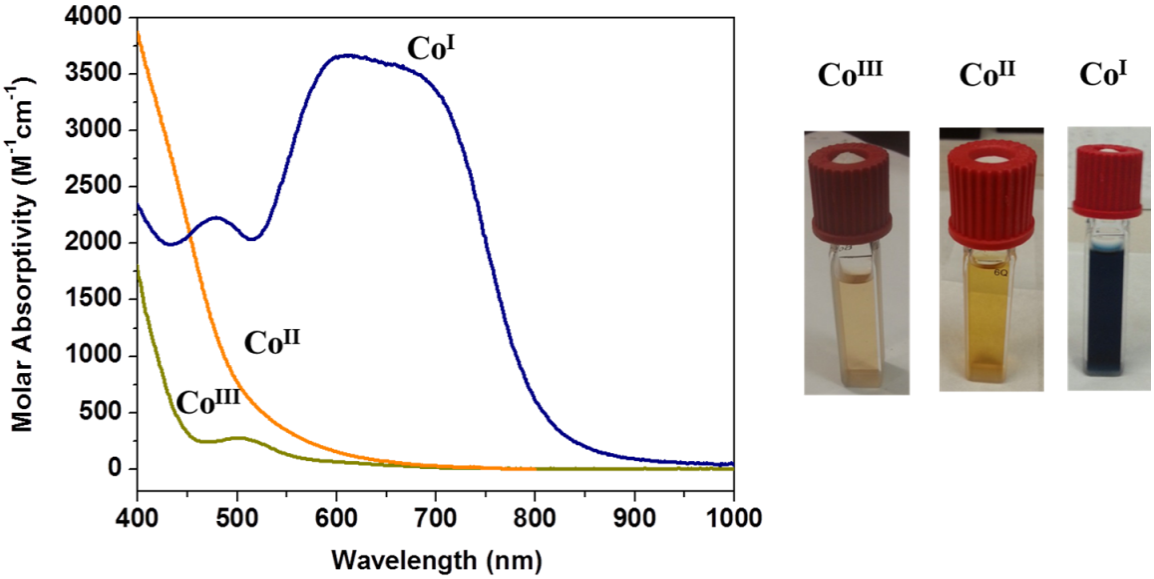

Figure 4.15. (a) UV-absorption spectra of complex **2** [$Co^{III}(HL^{oxime})(SCN)_2$] and its reduced analogues, Co^{II}- [λ = 435 nm (ε = 2742 $M^{-1}cm^{-1}$)] and Co^{I}-species [λ = 606 nm (ε = 3668 $M^{-1}cm^{-1}$); λ = 672 nm (ε= 3562 $M^{-1}cm^{-1}$)]. (b) Colors of complex **2** in different oxidation states of cobalt.

Similarly, in the visible region, complexes **4-6** showed relatively transparent spectra which are characteristics of the Co^{III}-parent state (**Figure 4.16**).

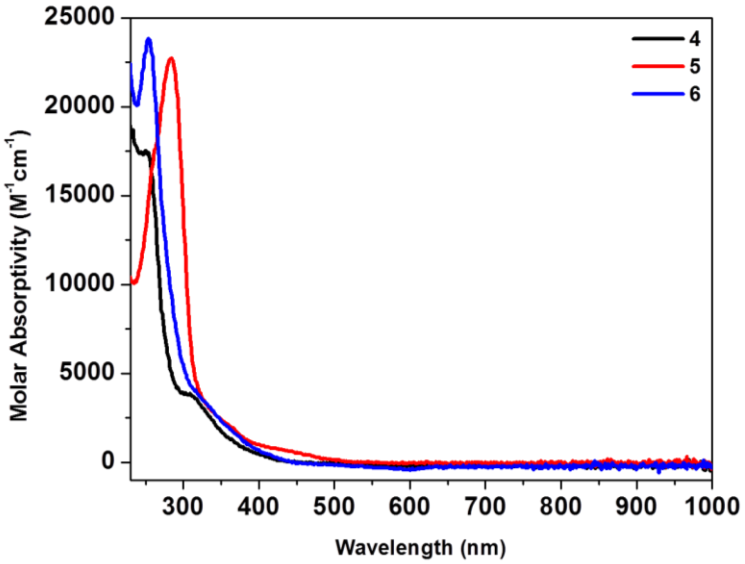

Figure 4.16. UV-visible spectra of **4-6** ([C] = 1.0 × 10^{-5} M) in acetonitrile.

www.manaraa.com

Co^{II}- and Co^{I}-complexes of **4** were isolated in CH_3CN by bulk electrolysis at -0.46$V_{Ag/AgCl}$ and -0.95$V_{Ag/AgCl}$, respectively. Distinctive electronic behaviors of **4**, and its Co^{II}- and Co^{I}-analogs were observed in the UV-visible region as illustrated in **Figure 4.17**. The spectrum of **4** does not show any charge-transfer band and it is a characteristic of a low-spin $3d^6$ Co^{III}-center with a strong-field π-acceptor ligand framework.[5] This complex displays a faint yellow color. The Co^{II}-species shows a distinct peak at 480 nm (ε = 2288 $M^{-1}cm^{-1}$) and is orange in color which can be attributed to a MLCT transition originating from the Co^{II}-center to the oxime ligand framework. The Co^{I}-complex is tentatively associated with both ILCT and MLCT bands at 572 and 685 nm (ε = 1738 and 1570 $M^{-1}cm^{-1}$) accounting for the characteristic blue color of the complex.

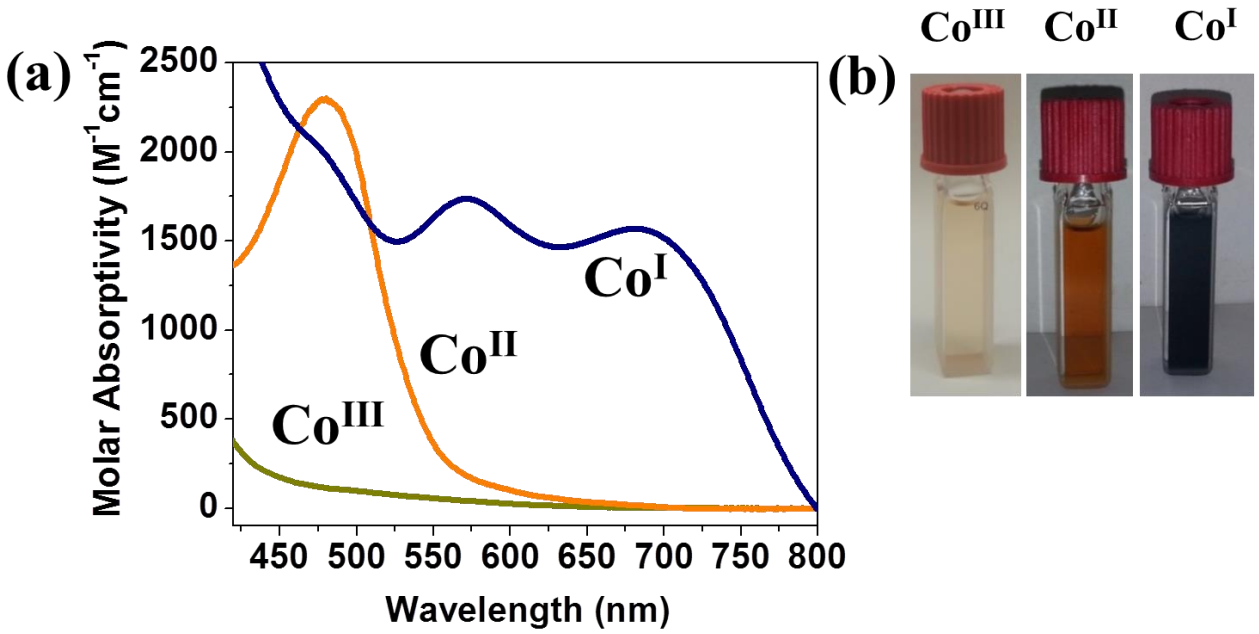

Figure 4.17. (a) UV-absorption spectra of complex **4** [Co^{III}($^{4\text{-tBu}}$py)(HL^{oxime})(Cl)]PF_6 and its reduced analogues, Co^{II}- [λ = 480 nm (ε = 2288 $M^{-1}cm^{-1}$)] and Co^{I}-species [λ = 572 nm (ε = 1738 $M^{-1}cm^{-1}$); λ = 685 nm (ε= 1570 $M^{-1}cm^{-1}$)]. (b) Colors of complex **1** in different oxidation states of cobalt.

UV-visible spectra were taken in CH_3CN to understand the electronic properties of the

www.manaraa.com

heterometallic complex (**Figure 4.18**). This complex exhibited brown color and the visible region spectra are occupied by strong metal to ligand charge transfer (MLCT) bands at 440-500 nm from Ru^{II} to bipyridine moieties. We compared the spectra of [RuCo] complexes with its precursor cobalt and ruthenium complexes (**Figure 4.18**).

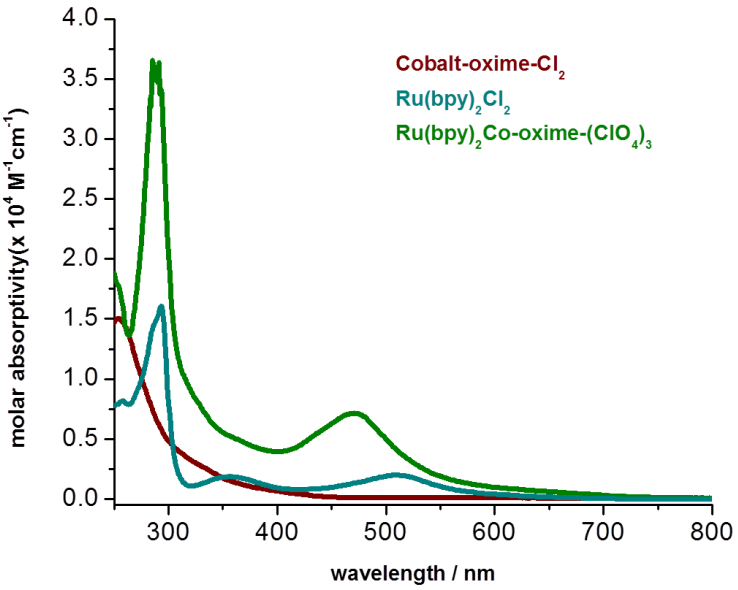

Figure 4.18. UV-visible spectra for **2** in CH_3CN in comparison with $Co(oxime)Cl_2$ and $Ru(bpy)_2Cl_2$.

We are interested to study the coordination environments of various redox species generated from heteroaxially substitued cobalt complexes due to the complicated nature of the redox behavior.

5.3.3.3. Coordination environments of the Co^{III}-species

Crystal structures combined with ^{1}H-NMR spectra provided the strongest evidence to elucidate the coordination environment for Co^{III} in the parent state. Crystal structure of complex **4** (**Figure 4.8**) suggested hexa-coordinated geometry with oxime as the planar ligand, and chloride and 4-substituted pyridines as axial ligands in the solid state. The ^{1}H-NMR spectra (**Figure 4.6**)

www.manaraa.com

confirmed the presence of 4-substituted pyridines in the Co^{III} state in solution even in the presence of coordinating solvent such as CD_3CN.

In the study to elucidate the second Co^{III}-species present in the solution of complex **4** during the cyclic voltammetry experiment, possibilities of formation of $[Co^{III}(HL^{oxime})Cl_2]$ and/or $[Co^{III}(^{4\text{-}tBu}py)_2(HL^{oxime})](PF_6)_2$ complexes were considered. Cyclic voltammetry experiments were performed separately with those two complexes synthesized independently. **Figure 4.19** illustrates the comparison of the cyclic voltammogram of complex **4** with those of its dichloro and di$^{4\text{-}tBu}$pyridine analogs. The anodic potential ($E_{p,a}$, -0.19V) of the first Co^{III}/Co^{II} process of **4** nearly matches to that (-0.12V) of the Co^{III}/Co^{II} process of the di$^{4\text{-}tBu}$pyridine complex, suggesting the formation of the same Co^{II}-species during the oxidation back to Co^{III} for both the complexes. Moreover, the half-wave potential ($E_{1/2}$, -0.70V) of the second Co^{III}/Co^{II} process of **4** is identical to that of the Co^{III}/Co^{II} process for the dichloro analog suggesting the possibility of formation of this dichloro species during the CV experiment of complex **4**. In addition, the appearance of this second Co^{III}/Co^{II} process at the very same potentials for **4** and **6** suggests the formation of the same dichloro species in both cases.

www.manaraa.com

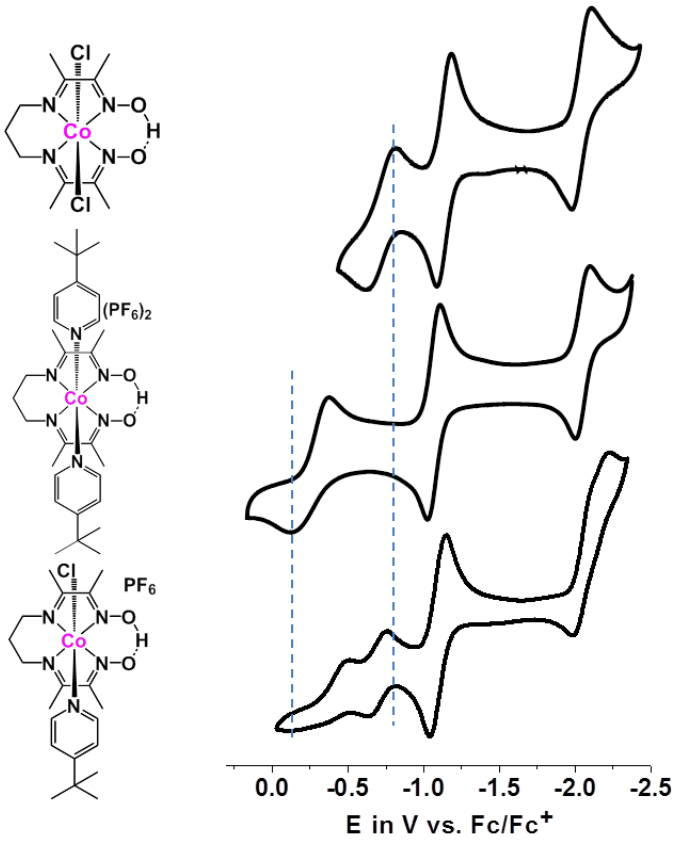

Figure 4.19. Comparison of the cyclic voltammograms of $[Co^{III}(HL^{oxime})Cl_2]$, $[Co^{III}(^{4\text{-}tBu}py)_2(HL^{oxime})](PF_6)_2$, and **4** in CH_3CN. The second Co^{III}/Co^{II} event appears at the same potentials for **4** and its dichloro analog, $[Co^{III}(HL^{oxime})Cl_2]$ suggesting the formation of the later species during the electrochemistry of **4**.

To determine the lability of the axial ligands in complex **4**, ^{1}H-NMR experiments were performed with **4** in presence of the external chloride and $^{4\text{-}tBu}$pyridine sources, added separately. The acidic nature of the oxime-OH hydrogen was evaluated as well since it can contribute to the cyclic voltammogram. We added one equivalent of $^{4\text{-}tBu}$pyridine, tetraethyl ammonium chloride (Et_4NCl), and triethyl amine (Et_3N) independently, to the CD_3CN solution of **4** and compared their ^{1}H-NMR spectra with those of complex **4** and free $^{4\text{-}tBu}$pyridine (**Figure 4.20**)

www.manaraa.com

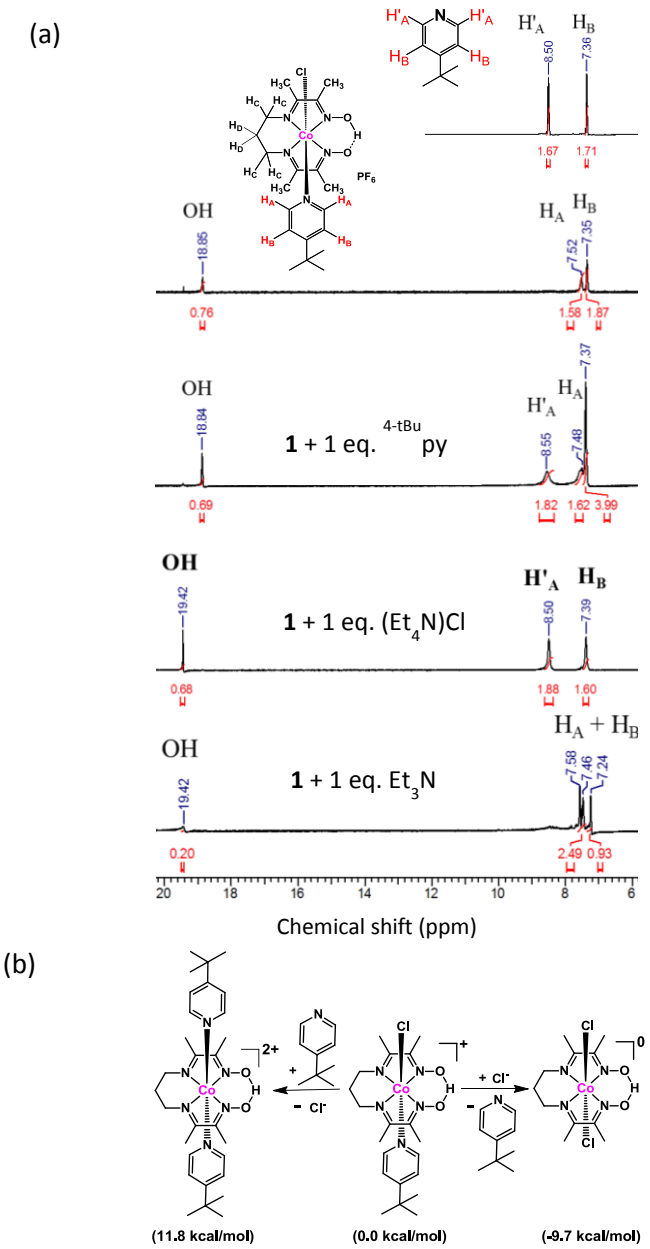

Figure 4.20. (a) ^{1}H-NMR experiments in CD_3CN of **4** upon addition of 1 equivalent of $^{4\text{-tBu}}$pyridine, Et_4NCl, and Et_3N. (b) Energetics of substitution of the axial ligands in complex **4**. As demonstrated by the ^{1}H-NMR spectra and DFT calculations, chloride can replace the $^{4\text{-tBu}}$pyridine ligand in **4** but the $^{4\text{-tBu}}$pyridine ligand cannot substitute the chloride.

Uncoordinated $^{4\text{-tBu}}$pyridine exhibited two sets of ^{1}H-NMR peaks at 7.36 (H_B) and 8.50 (H'_A) ppm whereas the coordinated $^{4\text{-tBu}}$pyridine in complex **4** displayed peaks at 7.35 (H_B) and 7.52 (H_A) ppm. The H_B protons retain the same chemical shift but the H'_A protons shifted from 8.50 to

www.manaraa.com

7.52 ppm on coordinating $^{4\text{-tBu}}$pyridine to the metal center. After one equivalent of $^{4\text{-tBu}}$pyridine was added to the CD_3CN solution of **4**, appearance of the signals from the uncoordinated $^{4\text{-tBu}}$pyridine protons at 8.55 ppm (2H) was observed and an increase of the intensity of the peak at 7.37 ppm (2H + 2H) was found whereas the proton count at 7.48 ppm (associated with the coordinated $^{4\text{-tBu}}$pyridine) did not change in intensity suggesting no coordination of the external $^{4\text{-tBu}}$pyridine ligand by replacing the chloride on cobalt. Furthermore, no deprotonation, i.e. no change of the proton count or shift of the oxime-OH hydrogen at 18.84 ppm was found upon addition of $^{4\text{-tBu}}$pyridine. On the contrary, when 1 equivalent of Et_3N was added to the solution of **4** in CD_3CN, we observed a considerable decrease of the oxime-OH peak intensity and slight shift of the position of the signal from the OH suggesting that Et_3N can deprotonate the OH. When external chloride source was added in the form of Et_4NCl (one equivalent) to the CD_3CN solution of **4**, peaks at 7.39 (2H) and 8.50 ppm (2H) were found which are characteristics of the uncoordinated $^{4\text{-tBu}}$pyridine ligand that can be obtained via a substitution process where the $^{4\text{-tBu}}$pyridine ligand in complex **4** gets replaced by the external chloride. These ^{1}H-NMR experiments suggest that external $^{4\text{-tBu}}$pyridine can neither replace chloride nor deprotonate the oxime-OH in the Co^{III}-complex whereas an external chloride can substitute the $^{4\text{-tBu}}$pyridine ligand in **4**.

In order to confirm these substitution processes, DFT calculations were used to obtain the energetics of different chemical events, i.e. substitution and loss of the axial ligands. All the calculated reaction energies reported are free energy changes in kcal/mol unless otherwise mentioned. The low spin states were found to be energetically favorable for all the calculated complexes which is confirmed by EPR as well.

As depicted in **Figure 4.20b**, the substitution of the $^{4\text{-tBu}}$pyridine ligand in complex **4** by an

www.manaraa.com

external chloride is calculated to be energetically favorable by 9.7 kcal/mol while an external $^{4\text{-tBu}}$pyridine replacing the chloride ligand in **4** is found to be unlikely as the substitution process is energetically uphill by about 12 kcal/mol. Moreover, the loss of chloride from the positively charged complex **4** should have a significant coulomb barrier. Therefore, the calculated results are in consistent with the experimental observation of substitution of the $^{4\text{-tBu}}$pyridine ligand in complex **4** by an external chloride giving rise to the dichloro complex $[Co^{III}(HL^{oxime})(Cl)_2]$. **Table 4.4** shows the energetics of the substitution of the pyridine ligands by external chloride for **4**-**6**. The mechanism of this substitution process is expected to involve a coordinatively unsaturated five-coordinate Co^{III}-intermediate from the loss of the axial pyridine ligand and this event is supposed to be uphill in energy. This first step is the limiting step and it requires about 14 kcal/mol energy for complexes **4** and **6**. The addition of an external chloride to the five-coordinate intermediate is favored by 23 kcal/mol and drives the overall substitution process forward for complexes **4** and **6** and these complexes have a large preference for the substitution mechanism as they favor the overall process by about 9-10 kcal/mol. Complex **5**, on the other hand, has the first step most energy-demanding (20 kcal/mol) among the three complexes and shows little (as the total energy of the substitution process is only -3.2 kcal/mol) preference for the substitution of the axial pyridine ligand by an external chloride. As shown in **Figure 4.11**, absence of the second Co^{III}/Co^{II} process for complex **5** implies the nonexistence of $[Co^{III}(HL^{oxime})(Cl)_2]$ species during the CV experiment. The Co–N(py) bond distances found in the optimized geometries of **4**, **5**, and **6** are 1.988, 1.972 and 1.986 Å, respectively. Complex **5** with the electron-donating pyrrolidine ligand, has the strongest Co–N(py) bond among the three complexes and hence, the Co–N($^{4\text{-Pyr}}$py) bond will be least susceptible towards substitution by chloride. These structural data support the trend of the substitution reaction energies [(A+B) in

www.manaraa.com

Table 4.5] calculated for **4**-**6** and we conclude that the axial pyridine ligand substitution will be more difficult in complex **5**, compared to **4** and **6**, and is unlikely to happen.

Table 4.5. Energetics of the substitution of pyridine with external chloride in complexes **4**, **5**, **6**.

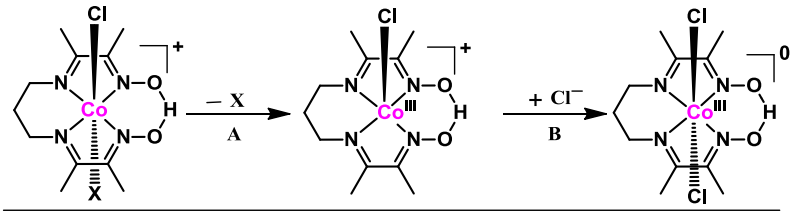

X	A[a]	B[a]	(A + B)[a]
$^{4\text{-tBu}}$py	13.5	-23.2	-9.7
$^{4\text{-Pyr}}$py	20.0	-23.2	-3.2
$^{4\text{-Bz}}$py	14.1	-23.2	-9.1

[a]Values are in kcal/mol.

To determine the spin-states of the Co^{III}-complexes, we performed the EPR experiments in CH_3CN (**Figure 4.21**). The silent signal in the EPR spectrum confirmed the diamagnetic low-spin nature of Co^{III} with $3d^6$ configuration and 0 unpaired electrons.

Thus, from the above discussions, we conclude the followings, a) the second Co^{III}/Co^{II} events observed for complexes **4** and **6** are due to the formation of a Co^{III}-species, $[Co^{III}(HL^{oxime})Cl_2]$. The later complex is obtained by the substitution of the pyridine ligand on the cobalt center in **4** and **6** by an external chloride and b) this substitution is unlikely to happen in case of complex **5** because of its strongest Co–N($^{4\text{-Pyr}}$py) bond when compared among all three complexes **4**-**6**. As a result, complex **5** does not show the second Co^{III}/Co^{II} process in the CV experiment.

5.3.3.4. Coordination environments of the Co^{II}-species

To elucidate the spin states of the Co^{II}-complexes generated after the first and second Co^{III}/Co^{II} events for complex **4**, EPR measurement were performed on the first and second Co^{II}-species

www.manaraa.com

obtained following the bulk electrolysis at appropriate potentials of -0.20 $V_{Ag/AgCl}$ and -0.46 $V_{Ag/AgCl}$, respectively. These potentials were selected after careful observation of the cyclic voltammetric profile of complex **4**. **Figure 4.21** displays the EPR spectra recorded. The first Co^{II}-species shows a peak corresponds to a low-spin (S = ½) $3d^7$ Co^{II} center and the presence of the super-hyperfine structure in the EPR spectrum suggests axial interaction of cobalt with a nitrogen donor. This suggests the presence of a possible N_5 environment around the cobalt center implying that the $^{4\text{-tBu}}$pyridine moiety is retained on the metal center after the first Co^{III}/Co^{II} reduction of complex **4**. The EPR spectrum of the second Co^{II}-species supports the low-spin configuration (S = 1/2) of the metal but it lacks the super-hyperfine signature proposing a N_4 environment around the metal center with the possibility of the presence of the chloride axial ligand(s).

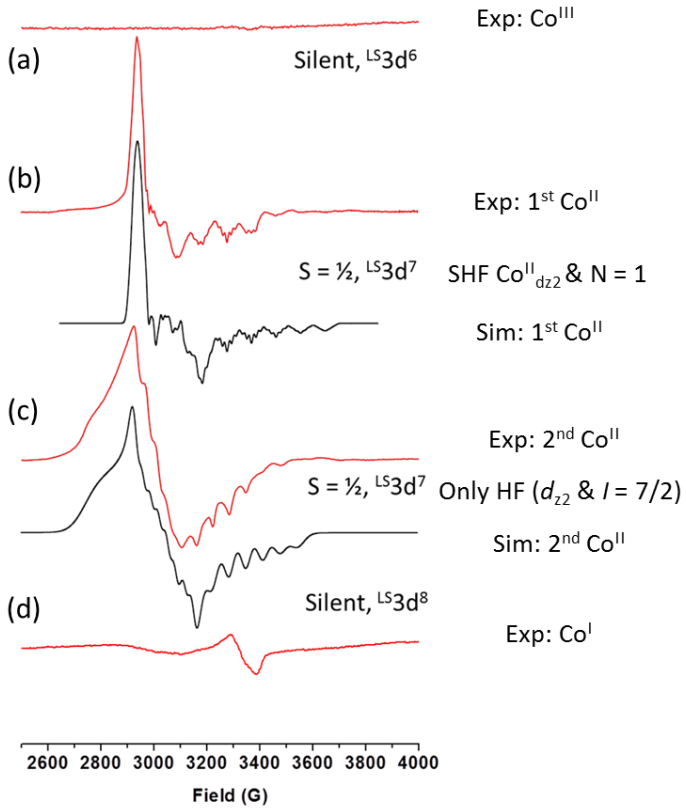

Figure 4.21. EPR experiments to identify the spin-states and coordination environments of the complexes (Co^{III}, Co^{II}, and Co^{I}) generated during the electrochemistry of **4** in CH_3CN.

www.manaraa.com

Titration experiments were carried out with **4** to evaluate the effects of the external chloride and $^{4\text{-tBu}}$pyridine ligands added separately during the electrochemistry measurement on **4** (**Figure 4.22a**). In the presence of increasing amounts of Et_4NCl, the first Co^{III}/Co^{II} process started decreasing while the second Co^{III}/Co^{II} process started increasing in intensity. After adding about 0.6 equivalents of Et_4NCl, the first process disappeared completely.

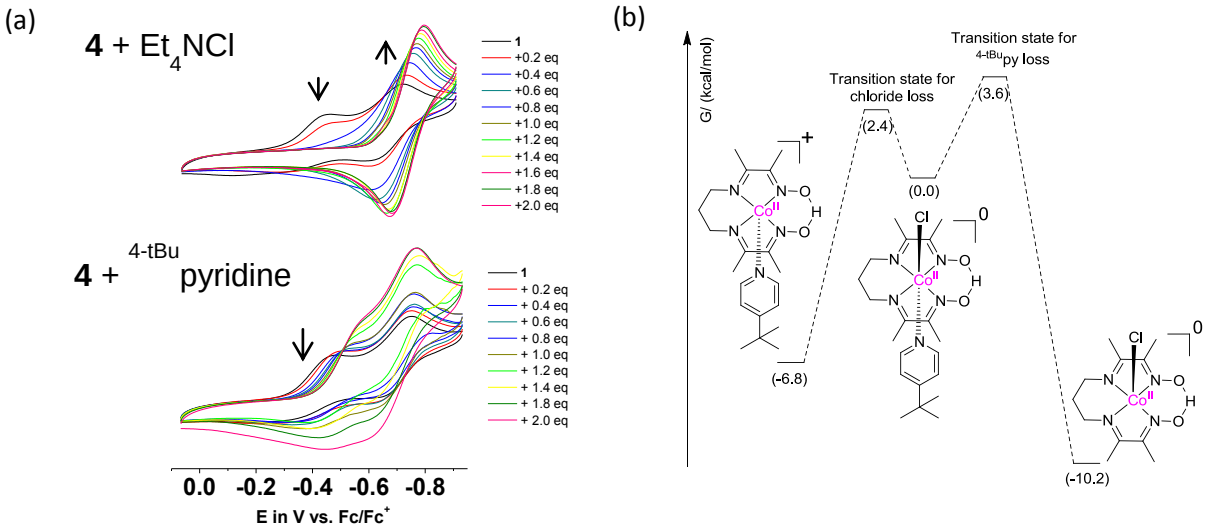

Figure 4.22. (a) Changes of the cyclic voltammograms of **4** upon addition of Et_4NCl and $^{4\text{-tBu}}$pyridine in CH_3CN. The first Co^{III}/Co^{II} event disappears with increase of the amount of the external chloride source added whereas $^{4\text{-tBu}}$pyridine has no effect on the CV profile. (b) Calculated activation barriers showing that the dissociation of chloride ligand is more favorable than the dissociation of the $^{4\text{-tBu}}$pyridine ligand from $[Co^{II}(^{4\text{-tBu}}py)(HL^{oxime})(Cl)]$ giving rise to $[Co^{II}(^{4\text{-tBu}}py)(HL^{oxime})]^{+}$.

On the other hand, addition of $^{4\text{-tBu}}$pyridine ligand showed very little cathodic shift for both the Co^{III}/Co^{II} processes. Cyclic voltammogram (**Figure 4.23**) of a solution prepared independently from addition of equal amounts of Et_4NCl and **4**, confirmed the disappearance of the first Co^{III}/Co^{II} process and an increase in intensity of the second Co^{III}/Co^{II} event. A solution prepared similarly from addition of equal amounts of $^{4\text{-tBu}}$pyridine and **4**, failed to show any effect as both the Co^{III}/Co^{II} processes retained their intensities (**Figure 4.23**). These results confirm the CV

www.manaraa.com

experiments in **Figure 4.22a** and suggest that the chloride ion is involved in both the Co^{III}/Co^{II} reduction events of complex **4**. On the other hand, $^{4\text{-tBu}}$pyridine has little or no involvement towards the Co^{III}/Co^{II} reduction.

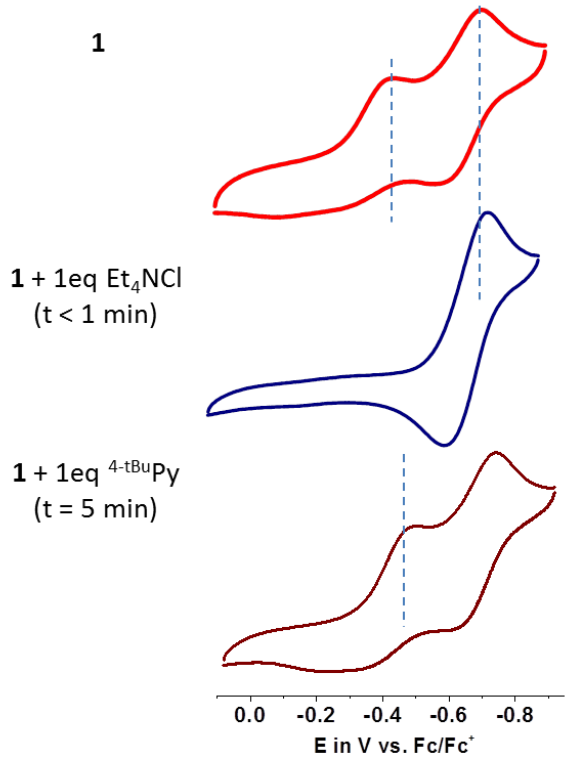

Figure 4.23. Change of Cyclic voltammogram of **4** upon addition of 1 equivalent of Et_4NCl and $^{4\text{-tBu}}$pyridine in CH_3CN.

DFT calculations found that the loss of chloride from complex $[Co^{II}(^{4\text{-tBu}}py)(HL^{oxime})(Cl)]$, obtained after the first Co^{III}/Co^{II} reduction of **4**, is thermodynamically favorable by 6.8 kcal/mol giving rise to the five-coordinate $[Co^{II}(^{4\text{-tBu}}py)(HL^{oxime})]^{+}$. Alternatively, dissociation of the $^{4\text{-tBu}}$pyridine ligand is calculated to be downhill by 10.2 kcal/mol. These results demonstrate that there is a greater thermodynamic preference of $[Co^{II}(^{4\text{-tBu}}py)(HL^{oxime})(Cl)]$ to release $^{4\text{-tBu}}$pyridine rather than chloride giving rise to $[Co^{II}(HL^{oxime})(Cl)]$. However, calculations of the transition states of the axial ligand dissociation find that the loss of the chloride is associated with a larger kinetic barrier than that of the dissociation of the $^{4\text{-tBu}}$pyridine ligand (**Figure 4.22b**). The

www.manaraa.com

difference between the activation energies is 1.2 kcal/mol. The Arrhenius model, $k= A*e^{(-E/RT)}$, estimates that the rate constant k of a chemical reaction increases by 10 times with a decrease of the activation energy E by 1.36 kcal/mol at 298.15K. Therefore, we propose that the dissociation of the axial ligands from $[Co^{II}(^{4\text{-}tBu}py)(HL^{oxime})(Cl)]$ is kinetically controlled favoring the pathway that leads to the formation of $[Co^{II}(^{4\text{-}tBu}py)(HL^{oxime})]^{+}$ and this is confirmed by the identification of the later species by EPR (**Figure 4.21**).

Table 4.6 shows the metal–ligand bond distances of complex **4** from the X-ray crystal and the DFT-calculated structures. We also evaluated the metal-ligand bond distances of the one-electron reduced analog of **4** by DFT calculation. The Co^{III}/Co^{II} reduction is associated with the addition of an electron into the $3d_{z2}$ orbital of the metal which being antibonding in nature increases the metal–axial ligand bond distances in the Co^{II}-complex and the axial ligands become prone to dissociation. This is illustrated in **Table 4.6** and the increase of the Co–Cl bond length being 0.441Å is considerably greater than the increase (0.300Å) of the Co–N($^{4\text{-}tBu}$py) bond length. Therefore, the Co–Cl bond gets significantly more labile than the Co–N($^{4\text{-}tBu}$py) bond in $[Co^{II}(^{4\text{-}tBu}py)(HL^{oxime})(Cl)]$ and the loss of the chloride ligand is invoked with the reduction of complex **4**. The dichloro complex of Co^{II}, $[Co^{II}(HL^{oxime})(Cl)_2]^{-}$, obtained from the reduction of $[Co^{III}(HL^{oxime})(Cl)_2]$, is negatively charged and therefore, the loss of chloride is expected to be favorable from it. This ligand loss is calculated to be downhill by 9.7 kcal/mol giving rise to the five-coordinate neutral $[Co^{II}(HL^{oxime})(Cl)]$ complex. The later complex can substitute the remaining chloride ligand with a $^{4\text{-}tBu}$pyridine and/or a solvent acetonitrile molecule to give rise to $[Co^{II}(^{4\text{-}tBu}py)(HL^{oxime})]^{+}$ and/or $[Co^{II}(CH_3CN)(HL^{oxime})]^{+}$ complex, respectively. Absence of the hyperfine structure in the EPR spectrum (**Figure 4.18**) of the Co^{II}-species, obtained after the second Co^{III}/Co^{II} reduction of complex **4**, suggests that these substitution processes are slow.

www.manaraa.com

Table 4.6. Co–ligand bond lengths[a] of complex **4** from the X-ray crystal and the DFT-optimized structures. Metal–ligand bond distances[a] of the one-electron reduced (Co^{II}) analog of **4** are also reported.

		Co–N_1	Co–N_2	Co–N_3	Co–N_4	Co–N_5	Co–Cl
X-ray:	$[Co^{III}(^{4\text{-tBu}}py)(HL^{oxime})(Cl)]^+$	1.903	1.917	1.914	1.898	1.975	2.237
DFT:	$[Co^{III}(^{4\text{-tBu}}py)(HL^{oxime})(Cl)]^+$	1.907	1.925	1.928	1.905	1.988	2.304
DFT:	$[Co^{II}(^{4\text{-tBu}}py)(HL^{oxime})(Cl)]$	1.904	1.927	1.928	1.904	2.288	2.745

[a]Values are in Å.

Thus, we can conclude that 5-cordinate geometry was exhibited by Co^{II} species after 1st reduction with $^{4\text{-tBu}}$pyridine as the axial ligand. The 2nd reduction generates the Co^{II} species with two chloride axial ligands which subsequently get replaced by $^{4\text{-tBu}}$pyridine/CH_3CN to produce 5-coordinated Co^{II}-species. All these species have shown low-spin $3d^7$ configuration.

4.3.3.5. Coordination environments of the Co^{I}-species

The EPR results following bulk electrolysis of complex **4** at the potential of -0.95$V_{Ag/AgCl}$ in CH_3CN showed that the Co^{I}-complex, generated after the Co^{II}/Co^{I} reduction, is a low-spin singlet $3d^8$ species. A silent EPR spectrum was recorded for the Co^{I}-species as shown in **Figure 4.21**. We propose this species to be five-coordinate with $^{4\text{-tBu}}$pyridine ligand attached to the metal center. Calculations found that the oxime ligand may show some degree of redox non-innocence during the reduction event but the electrons on the ligand and the metal centers are strongly antiferromagnetically coupled giving rise to an overall singlet (S=0) state of the reduced species (**Figure 4.24**).

www.manaraa.com

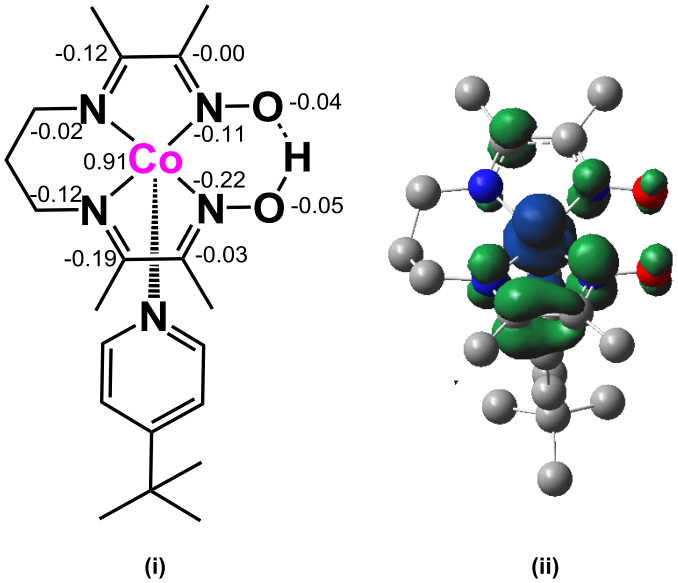

(i) (ii)

Figure 4.24. Redox non-innocence of the oxime ligand during the reduction of $[Co^{II}(^{4\text{-}tBu}py)(HL^{oxime})]^{+}$. Mulliken spin density analysis **i** and spin density plot **ii** for the complex. The hydrogen atoms are omitted for clarity in the spin density plot **ii**.

Calculations found that the reduction of $[Co^{II}(^{4\text{-}tBu}py)(HL^{oxime})]^{+}$ complex may have significant degree of redox non-innocence character displayed by the oxime ligand as the resulting metal-reduced, closed-shell (S=0), $3d^8$ Co^{I}-complex, $[Co^{I}(^{4\text{-}tBu}py)(HL^{oxime})]$, is 3.8 kcal/mol higher in energy than the ligand-reduced, open-shell (S=0), $3d^7$ Co^{II}-complex, $[Co^{II}(^{4\text{-}tBu}py)(HL^{oxime\bullet})]$. As illustrated in **Figure 4.24**, spin density analysis of $[Co^{II}(^{4\text{-}tBu}py)(HL^{oxime\bullet})]$ complex shows that the total spin on the cobalt center is +0.91 while it is -0.90 on the imine-oxime ligand framework confirming the electronic state of the complex as open-shell $[Co^{II}(^{4\text{-}tBu}py)(HL^{oxime\bullet})]$. The two unpaired electrons on the cobalt center and imine-oxime ligand HL are antiferromagnetically coupled as shown by the spin density plot (blue and green) in **Figure 4.24ii** giving rise to an overall singlet (S=0) state. However, the EPR experiment (**Figure 4.21**) demonstrated a silent spectrum that is characteristic of an overall singlet state (S=0) and failed to distinguish between the closed-shell and open-shell configurations of the species obtained from the reduction of $[Co^{II}(^{4\text{-}tBu}py)(HL^{oxime})]^{+}$. When we reevaluated the energy difference of these two configurations

www.manaraa.com

with different functionals, we found that the energy difference between the two electronic states is dependent on the functional used and hybrid functionals favor the open-shell configuration while the pure functionals predict the two configurations to be isoenergetic.

To gain insights about the coordination environment of the Co^{I}-species, this complex was independently synthesized using a known chemical reduction method[9]. The Co^{III}-parent complex **4** in dry methanol was treated in presence of a methanol solution of sodium hydroxide (NaOH) and sodium borohydride ($NaBH_4$) in a schlenk flask under airtight conditions in argon atmosphere. The resulting dark-blue suspension was vigorously stirred and dried under vacuum followed by addition of acetonitrile to solubilize the Co^{I}-complex. Rapid filtration followed by vaccum drying generates the blue-colored Co^{I}-complex which was stored in a glove-box. The ^{1}H-NMR spectra of this complex are shown in **Figure 4.25**. The well-defined peaks of the spectra assured the low-spin nature of the species and the appearance of the signals from the aromatic protons and t-butyl substituent confirmed the presence of $^{4\text{-tBu}}$pyridine ligand on the metal center. In addition, formation of five-coordinate Co^{I}-complexes with axial ligands like pyridine and boron-capped dimethylglyoxime in the equatorial positions is well-known in CH_3CN solvent.[10]

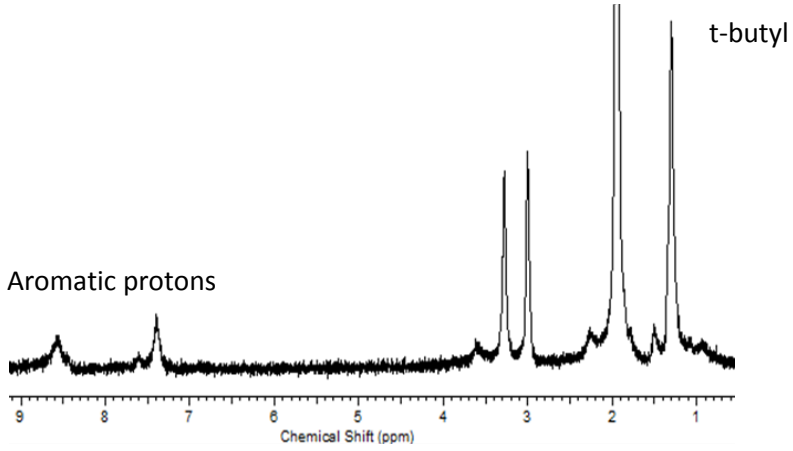

Figure 4.25. ^{1}H-NMR spectra of the Co^{I}-complex, [Co^{I}($^{4\text{-tBu}}$py)(HL^{oxime})], in CD_3CN.

www.manaraa.com

Figure 4.26 summarizes our proposed electrochemical pathway starting from the parent complex **4**.

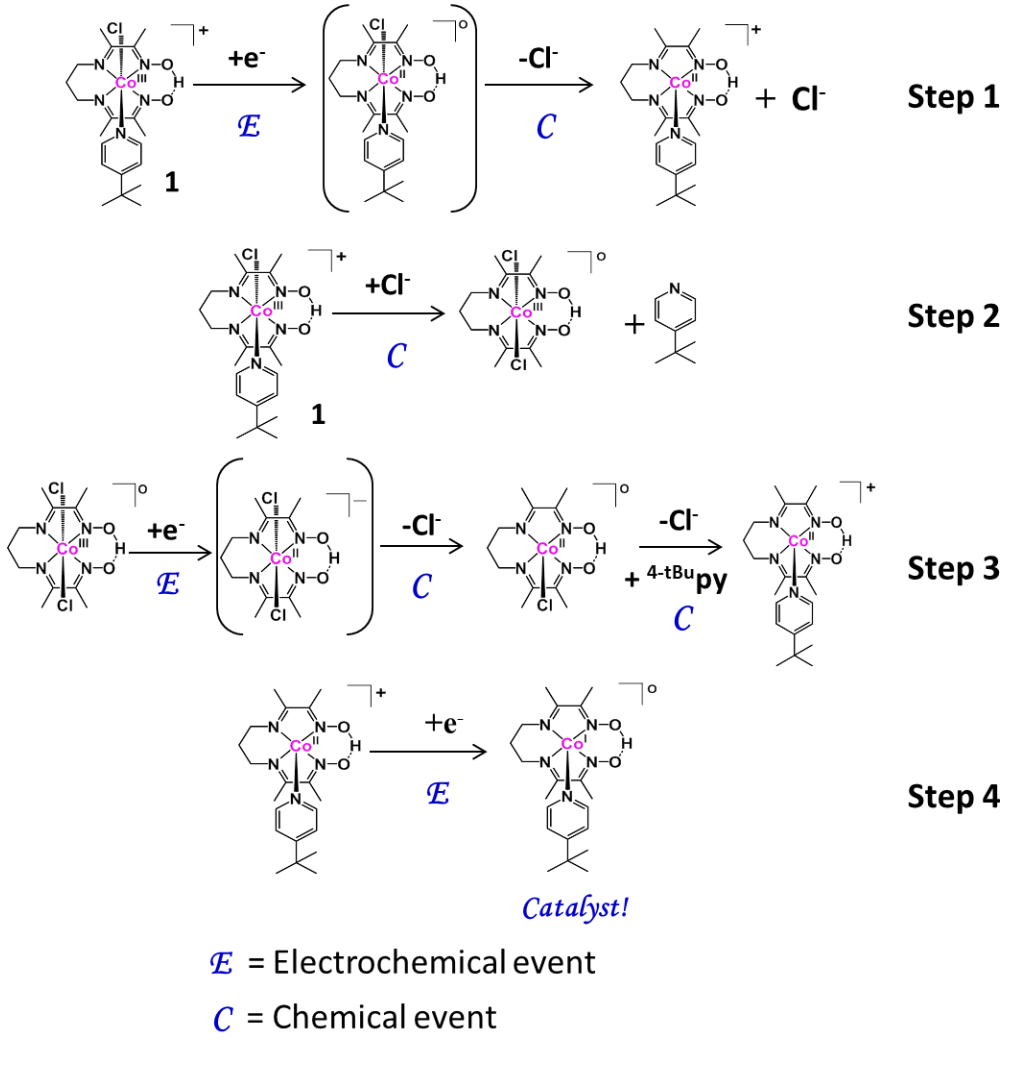

Figure 4.26. Proposed electrochemical pathway starting from complex **4**. The chloride released after the first Co^{III}/Co^{II} reduction can replace the $^{4\text{-tBu}}$py ligand in **4** giving rise to the second Co^{III}-species, $[Co^{III}(HL^{oxime})(Cl)_2]$. Reduction of the later species followed by substitution of the chloride ligands with $^{4\text{-tBu}}$py give rise to $[Co^{II}(^{4\text{-tBu}}py)(HL^{oxime})]^+$ which gets further reduced to $[Co^{I}(^{4\text{-tBu}}py)(HL^{oxime})]^+$, the active form of the catalyst. The substitution event in **step 3** does not preclude the involvement of solvent CH_3CN.

The first Co^{III}/Co^{II} reduction followed by loss of a chloride ligand converts complex **4**, $[Co^{III}(^{4\text{-}tBu}py)(Cl)(HL^{oxime})]^+$, into the five-coordinate Co^{II}-species $[Co^{II}(^{4\text{-tBu}}py)(HL^{oxime})]^+$ (**step 1**). The

www.manaraa.com

chloride released can replace the $^{4\text{-tBu}}$py ligand in the remaining $[Co^{III}(^{4\text{-tBu}}py)(Cl)(HL^{oxime})]^{+}$ complex giving rise to a second Co^{III}-species, $[Co^{III}(HL^{oxime})(Cl)_2]$, and free $^{4\text{-tBu}}$pyridine molecule (**step 2**). The second Co^{III}/Co^{II} reduction is $[Co^{III}(HL^{oxime})Cl_2]$ complex transforming into $[Co^{II}(HL^{oxime})Cl_2]^{-}$ and the later species can replace the chloride ligands with one $^{4\text{-tBu}}$pyridine molecule from the solution and can convert into $[Co^{II}(^{4\text{-tBu}}py)(HL^{oxime})]^{+}$ complex (**step 3**) that undergoes Co^{II}/Co^{I} reduction and transforms into five-coordinate $[Co^{I}(^{4\text{-tBu}}py)(HL^{oxime})]$ (**step 4**) which is the active species for proton reduction catalysis. Here it is important to mention that in a previous study[11] with a similar cobalt oxime complex, generation of a Co^{II}–Cl species was proposed in **step 1**. It was further concluded that an outer sphere electron transfer mechanism (involving the Co^{II}–Cl and the parent Co^{III}-complexes) and transfer of the chloride ligand from one metal center to another can give rise to a Co^{III}-dichloro species. The present study with the cobalt oxime complex **4** is not in agreement with those proposals.

4.3.4. Catalytic Yields and Mechanism

Rational design of enhanced proton-reducing catalysts requires a detailed understanding of the plausible catalytic mechanisms and study of the catalytic parameters, e.g. overpotential (η), turn-over number (TON), and Faradaic efficiency are absolutely crucial in this regard.

4.3.4.1. Catalytic Profiles and Yields

These complexes (**1-8**) were treated with mild acid, such as TFA to evaluate their catalytic activity towards proton reduction.

First, we treated the homoaxial complexes **1-3** with TFA. The cyclic voltammetry experiment was performed for all of these complexes to probe catalytic activity. A catalytic peak appeared close to the Co^{II}/Co^{I} process for all the cases whereas the Co^{III}/Co^{II} process remains unchanged.

www.manaraa.com

The catalytic CV plots were shown in **Figure 4.27**. The overpotentials for these complexes were altered from 0.41, 0.34, and 0.32 V for **1-3** respectively, measured including the homoconjugation effect of the acid.[12] A redox process appears slightly negative to the Co^{III}/Co^{II} couple which can be assigned as the Co^{III}-H/Co^{II}-H process. Controlled potential electrolysis was performed to confirm the generation of hydrogen. A fixed potential of -1.0 $V_{Ag/AgCl}$ was applied in CH_3CN solution of **1-3** in presence of TFA. The turnover numbers for these complexes were found to be 12, 19.5, and 17.5 after three hours for **1-3** respectively, where the corresponding Faradaic efficiency was calculated to be 50%, 75%, and 70%.

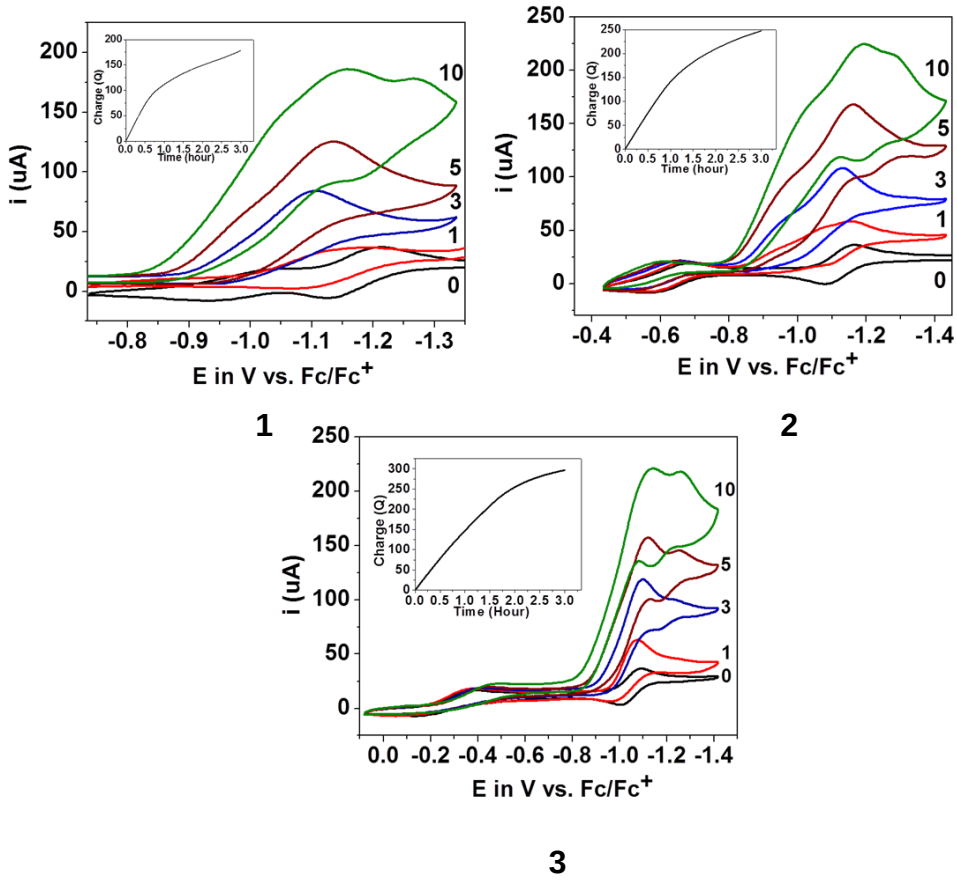

Figure 4.27. Cyclic voltammetry experiments showing the electrocatalytic behavior of **1-3** towards H_2 generation in the presence of TFA in CH_3CN solution. The numbers 0-10 indicate the equivalents of TFA used in comparison to **1-3** (Inset: Plot of charge consumed against time during the bulk-electrolysis experiment for dihydrogen generation by complex **1-3** in about three hours).

www.manaraa.com

We performed the catalytic and mechanistic studies for heteroaxial complexes in great detail. We investigated the electrocatalytic behavior of **4** in presence of trifluoroacetic acid (TFA with pK_a = 12.7 in CH_3CN) and the cyclic voltammetry data revealed a catalytic peak appearing near the reduction potential of the Co^{II}/Co^{I} couple upon addition of various equivalents (0 – 10) of TFA (**Figure 4.28**) suggesting the Co^{I}-species to be catalytically active. Generation of H_2 happens at a low overpotential of 0.35V, measured including the homoconjugation effect of the acid.[12] The CV profile of the Co^{III}/Co^{II} couple did not change with increasing amount of acid ruling out the possibility of the involvement of this couple towards proton reduction. We also observed a new process appearing at a potential slightly negative to that of the catalytic peak in presence of ≥ 5 equivalents of TFA which may be attributed to the Co^{III}-H/Co^{II}-H couple.

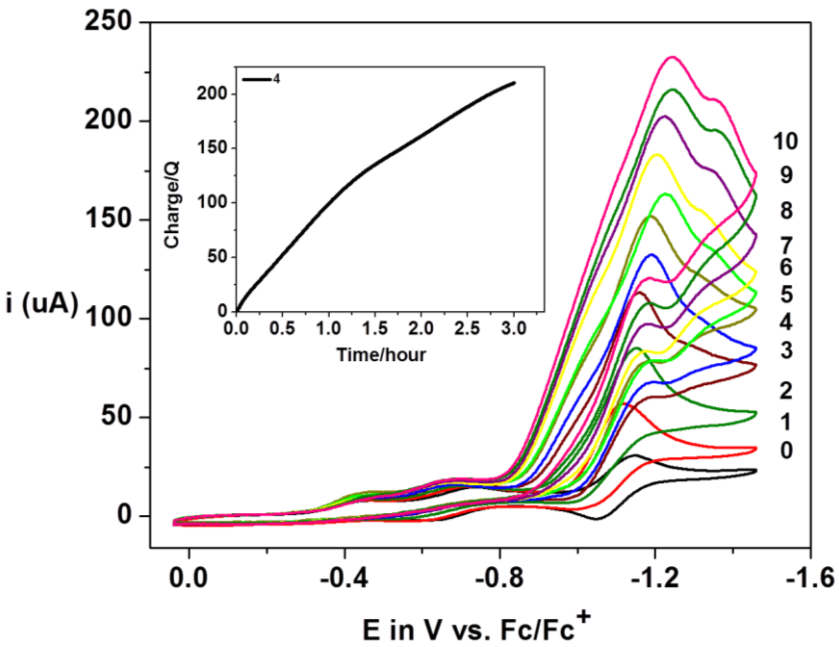

Figure 4.28. Cyclic voltammetry experiments showing the electrocatalytic behavior of **4** towards H_2 generation in the presence of TFA in CH_3CN solution. The numbers 0-10 indicate the equivalents of TFA used in comparison to **4** (Inset: Plot of charge consumed against time during the bulk-electrolysis experiment for dihydrogen generation by complex **4** in about three hours).

The reduced analog for **4** was generated *via* controlled potential electrolysis at -1.0 $V_{Ag/AgCl}$ in

www.manaraa.com

the presence of TFA and TON was determined by gas-chromatography. A TON of 18.7 within three hours was observed in CH_3CN in presence of 4.0 x 10^{-5} mol of catalyst **4** and one hundred equivalents of TFA. The solution in the main chamber displayed a color change from faint yellow to dark green during the controlled potential electrolysis experiment. The Faradaic efficiency for the catalysis was calculated to be 77% for **4**. As shown in **Figure 4.28** inset, complex **4** consumed around 200 Coulombs of charge in three hours validating that the complex **4** is catalytically active.

Electrocatalytic dihydrogen generation was confirmed with complexes **5** and **6** as well (**Figures 4.29**) following the same method described above. Overpotential and rate of H_2 generation (k_{obs}) for **4**-**6** were calculated from the CV experiments whereas TON and Faradaic efficiency were measured from the controlled potential electrolysis experiments and all of these catalytic parameters are reported in **Table 4.7**.

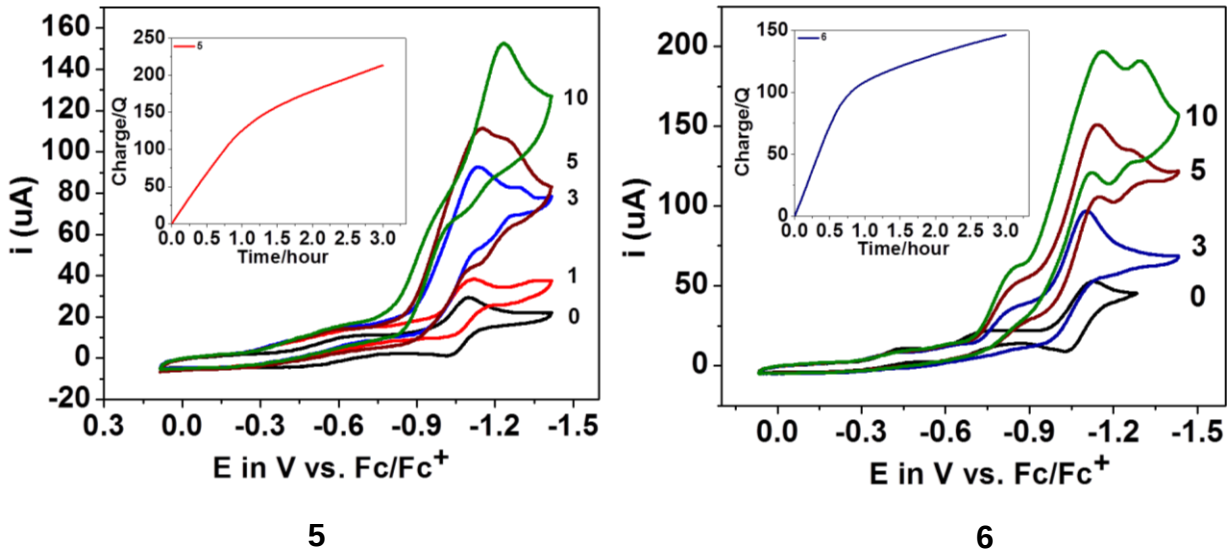

Figure 4.29. Cyclic voltammetry experiments showing the electrocatalytic behavior of **5** and **6** towards H_2 generation in the presence of TFA in CH_3CN solution. The numbers 0-10 indicate the equivalents of TFA used in comparison to **5** or **6** (Inset: Plot of charge consumed against time during the bulk-electrolysis experiment for dihydrogen generation by complex **5** or **6** in about three hours).

www.manaraa.com

Table 4.7. Catalytic parameters for **4-6** in CH_3CN in presence of TFA ([catalyst] : [acid] = 1: 100).

Catalytic parameters	4	5	6
E (H^+/H_2) (V) *vs.* Fc/Fc^+	-1.03	-1.04	-1.03
Overpotential (V) (10eq TFA)	0.35	0.36	0.35
K_{obs} (s^{-1}) (10eq TFA)	3.02	5.18	2.66
TON/3h (4.0 X 10^{-5} mol)	18.7	13.8	13.8
Faradaic efficiency (%)	77	84	75

As depicted in **Table 4.7**, variation of the substituent on the pyridine ligand has little or no effect on the overpotential of complexes **4-6**. Although overpotential did not vary, k_{obs} increased by a factor of 1.95 on changing the substituent on the pyridine moiety from electron-withdrawing benzoyl in **6** to electron-donating pyrrolidine in **5**. It is expected that in the later complex, the Co^I center becomes more nucleophilic than that in complex **6** and hence, the metal center in **5** can react faster with a proton. The TON varies from 18.7 to 13.8 when compared between complexes **4-6** with **4** displaying the highest TON. The Faradaic efficiency for proton reduction was calculated to be around 80%. Complexes **4-6** exhibited low overpotential and higher catalytic current with respect to the blank in the presence of TFA. Moreover, these complexes consumed much more charges (**Figures 4.29 inset**) than those consumed by the blank solutions validating that all these three complexes are catalytically active.

Because the Co^{II}/Co^I process was maintained in the cyclic voltammogram, we performed proton reduction catalysis with complex **7** and **8** in the presence of TFA. The overpotential was calculated to be 0.34 and 0.37 V, respectively for **7** and **8** in the presence of 10 equivalents of TFA, after considering the homoconjugation effect. To confirm the release of hydrogen, bulk electrolysis experiment was performed at -1.0 $V_{Ag/AgCl}$. **Figure 4.30** shows the plot of charge *versus* time for the monometallic Co^{III} complex **7** and the heterolytic [$Ru^{II}Co^{III}$] complex **8**

www.manaraa.com

during the controlled potential experiment. The TON of complex **7** was calculated to be 7.2 with a Faradaic efficiency of 75% in one hour, whereas the TON and Faradaic efficiency for complex **8** was calculated to be 7.0 in one hour and 75%, respectively.

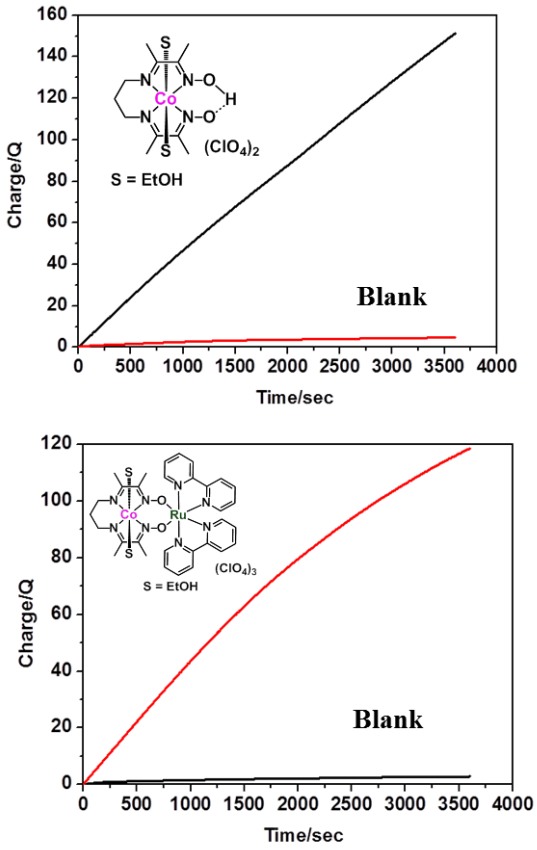

Figure 4.30. Change of charge *versus* time during bulk-electrolysis for cobalt-module (**7**) and $[Ru^{II}Co^{III}]$ (**8**) complex in presence of TFA at -1.0 $V_{Ag/AgCl}$ applied potential.

4.3.4.2. Analysis of the catalytic pathways for H_2 evolution

Experimentally, complexes **4, 5,** and **6** displayed the electrocatalytic waves in presence of TFA at potentials very close to the reduction potentials of Co^{II}/Co^{I}. $E_{(H+/H2)}$ are found to be -1.03, -1.04 and -1.03V *versus* the Fc/Fc^{+} couple in presence of 10 equivalents of TFA for complexes **4**, **5** and **6**, respectively, (**Table 4.8**) and the Co^{II}/Co^{I} reduction potentials are measured to be -1.09, -1.07 and -1.09V *versus* the Fc/Fc^{+} couple for **4**, **5**, and **6**, respectively. Electrocatalytic H_2

www.manaraa.com

evolution by cobalt oximes is known to occur by either heterolytic (monometallic) or homolytic (bimetallic) pathways. It is known[13] that the pathways of H_2 evolution by cobalt oximes are dependent on the strength of the acid present in the medium and proton-coupled electron transfer (PCET) process may be relevant in sufficiently acidic systems. Theoretical studies[14a-c] have shown that the most likely mechanism involves the formation of a Co^{III}–H intermediate from protonation of the Co^{I}-complex. One-electron reduction of the Co^{III}–H species generates the Co^{II}–H intermediate which reacts heterolytically with a proton to produce H_2. Protonation at the oxime bridge (O–H---O) is known[14b] to be possible in the Co^{II}-complex in presence of a sufficiently strong acid (pKa $\leq$ 10.7 in acetonitrile). The resulting ligand-protonated Co^{II}-complex undergoes one-electron reduction followed by a protonation on the metal center giving rise to a ligand-protonated Co^{III}–H complex which is an important species involved in the production of H_2. In presence of a strong acid, *p*-cyanoanilinium (pKa = 7.6 in acetonitrile), the electrocatalytic wave of a cobalt oxime complex was observed at a potential of 320 mV more positive than that required for the Co^{II}/Co^{I} reduction.[14d] A pathway involving the protonation of the oxime bridge was proposed by Artero *et al.*[14d] to be mechanistically relevant and could explain the observed potential shift. Support for the bimetallic mechanism for cobalt oximes has also been reported but without the presence of kinetic evidence. Evidence for the formation of a transient Co^{III}–H complex has been reported[14e] from the protonation of a Co^{I}-triphos species and both the heterolytic and homolytic pathways were invoked for H_2 generation. **Scheme 4.3** summarizes various pathways of proton reduction by cobalt oximes. Although the thermodynamics of these pathways are well-studied, there is little emphasis on the free energy barriers for the proton transfer and H_2 production steps which are equally important in evaluating the likeliness of various mechanisms.

www.manaraa.com

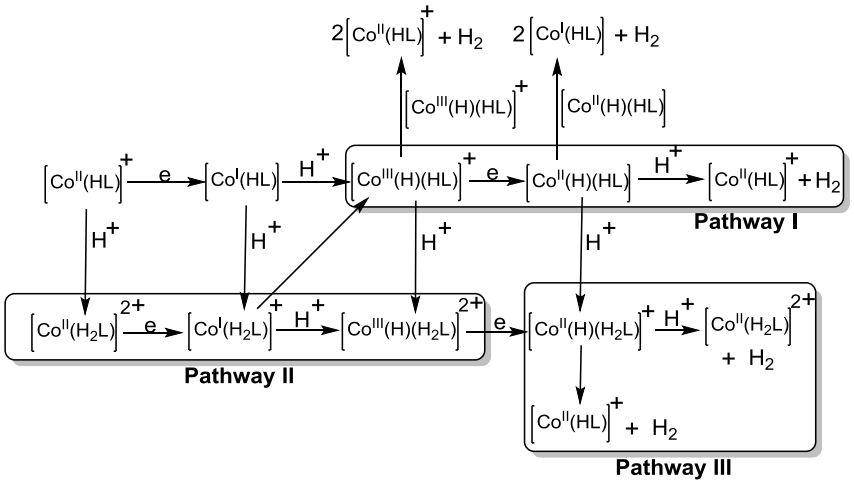

Scheme 4.3. Pathways for H_2 evolution by cobalt oxime catalysts. Complexes of pathway I are reported to be mechanistically important.[11a,c] The ligand-protonated pathways (II and III) have been demonstrated to be relevant in sufficiently acidic medium.[11b,d]

The potential calculated for the Co^{II}/Co^{I} reduction for complex **4** is -1.25V *versus* the Fc/Fc^{+} couple and the protonation of the oxime bridge in $[Co^{II}(^{4\text{-}tBu}py)(HL^{oxime})]^{+}$ species is found to be energetically unfavorable by 19.0 kcal/mol. This is consistent with a previous study[14b] of a cobalt oxime catalyst where it was concluded that a weak acid like TFA cannot protonate the oxime moiety. The catalytic pathways proved for complex **4** are shown in **Figure 4.31**. The species obtained after the Co^{II}/Co^{I} reduction, $[Co^{I}(^{4\text{-}tBu}py)(HL^{oxime})]$, is a neutral complex and hence, can easily take up a proton by reacting with the acid, TFA. As the calculation shows, the protonation on the metal site is energetically favorable by 4.6 kcal/mol giving rise to $[Co^{III}(H)(^{4\text{-}tBu}py)(HL^{oxime})]^{+}$. This is expected since Co^{I} is a closed-shell $3d^8$ center and can behave as a good Lewis base. A PCET event is not invoked for the conversion of the Co^{II}-complex to the Co^{III}–H species as the electrocatalytic wave did not show any anodic shift with the decrease of the pH when compared to the reduction potential of the Co^{II}/Co^{I} couple (**Figure 4.29**). The pK_a of the $[Co^{III}(H)(^{4\text{-}tBu}py)(HL^{oxime})]^{+}$ species is calculated to be 6.7 from the acid dissociation reaction, $[Co^{III}(H)(^{4\text{-}tBu}py)(HL^{oxime})]^{+} \rightarrow [Co^{I}(^{4\text{-}tBu}py)(HL^{oxime})] + H^{+}$, and the Co^{III}–H complex should be

www.manaraa.com

stable provided that pH < pK_a (6.7). **Figure 4.31a** shows the catalytic pathway without considering the loss of the $^{4\text{-tBu}}$pyridine ligand. The reduction potential of the Co^{III}–H/Co^{II}–H couple is calculated to be more negative, -1.43V, than that of the Co^{II}/Co^{I} couple while the PCET for the Co^{I}/Co^{II}–H couple is calculated to be -1.23V which is almost equal to the potential of the Co^{II}/Co^{I} couple and hence, is more likely to occur than the Co^{III}–H/Co^{II}–H event. Protonation of the resulting [Co^{II}(H)($^{4\text{-tBu}}$py)(HL^{oxime})] complex by TFA is significantly downhill by 31.4 kcal/mol giving rise to the H_2-adduct complex, [Co^{II}(H_2)($^{4\text{-tBu}}$py)(HL^{oxime})]$^+$. Release of the dihydrogen is favorable by 8.7 kcal/mol and the resulting five-coordinate [Co^{II}($^{4\text{-tBu}}$py)(HL^{oxime})]$^+$ can reenter the cycle.

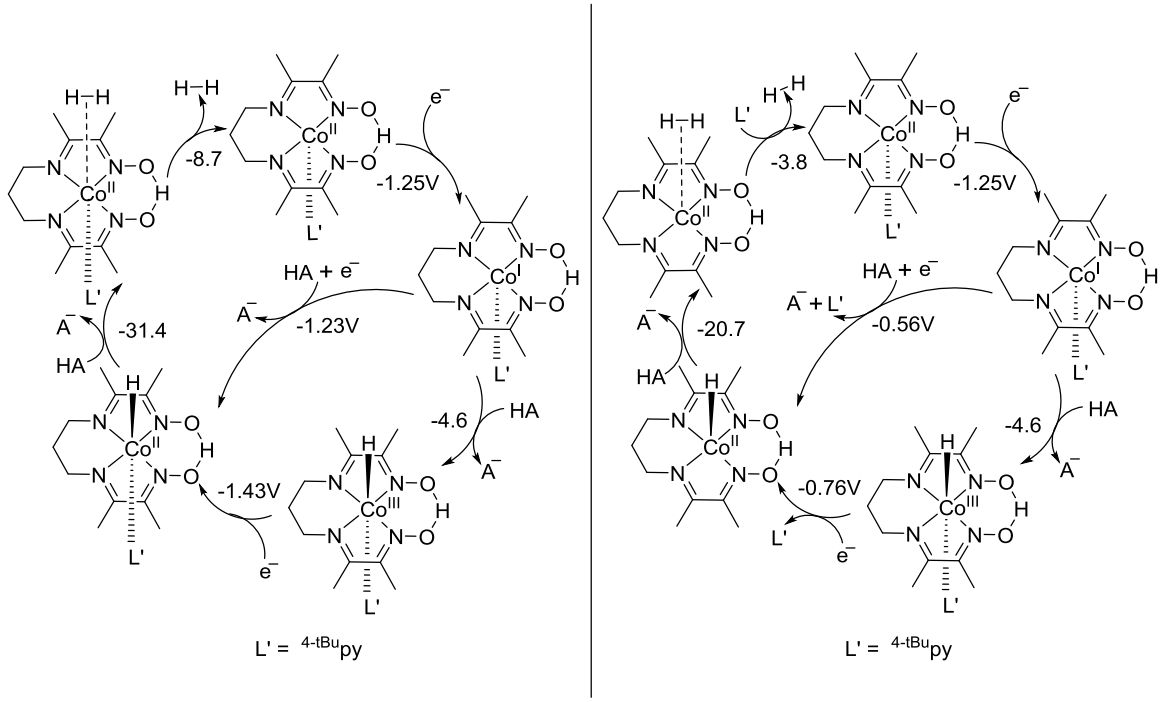

Figure 4.31. Various pathways considered for the evolution of H_2 by complex **4** in presence of TFA (HA) in acetonitrile. **a**) The catalytic mechanism without considering the loss of the $^{4\text{-tBu}}$pyridine ligand, **b**) the catalytic cycle invoking the ligand loss in the Co^{II}–H complex. The pathways in cycle **b** are more likely than that in cycle **a**. The energetics of the chemical events are in kcal/mol calculated by B3PW91//TZVP/6-311++G(d,p) level of theory.

The [Co^{II}(H)($^{4\text{-tBu}}$py)(HL^{oxime})] complex is a 19-electron species and can loose the $^{4\text{-tBu}}$pyridine

www.manaraa.com

ligand giving rise to the five-coordinate, 17-electron [Co^{II}(H)(HL^{oxime})] intermediate. The loss of the ligand is favored by 15.5 kcal/mol. The catalytic pathway shown in **Figure 4.31b** considers that the reduction of [Co^{III}(H)($^{4\text{-tBu}}$py)(HL^{oxime})]$^{+}$ complex to [Co^{II}(H)($^{4\text{-tBu}}$py)(HL^{oxime})] is coupled with the loss of the $^{4\text{-tBu}}$pyridine ligand and the calculated potential for this event is -0.76V. The PCET for the Co^{I}/Co^{II}–H event, when coupled with the loss of the ligand from the Co^{II}–H species, is found to be -0.56V. Both of these calculated potentials are more positive compared to the calculated value (-1.25V) of the Co^{II}/Co^{I} potential and hence, both of these processes can contribute to the mechanism. Generation of the H_2-adduct complex, [Co^{II}(H_2)(HL^{oxime})]$^{+}$, via the protonation of [Co^{II}(H)(HL^{oxime})] species by TFA is energetically favorable by 20.7 kcal/mol. It requires a $^{4\text{-tBu}}$pyridine ligand to replace the dihydrogen from [Co^{II}(H_2)(HL^{oxime})]$^{+}$ to obtain [Co^{II}($^{4\text{-tBu}}$py)(HL^{oxime})]$^{+}$ species to restart the catalytic cycle. This substitution event is calculated to be favored by 3.8 kcal/mol. In order to map the kinetic barriers of the proton addition pathways to [Co^{II}(H)($^{4\text{-tBu}}$py)(HL^{oxime})] and [Co^{II}(H)(HL^{oxime})] complexes, we performed a relaxed scan for each complex where an external proton was approached to the hydride on the metal center from a distance of 3.0Å. Simulation of these pathways showed no barrier on the electronic energy surface for the formation of the H_2-adduct complexes from [Co^{II}(H)($^{4\text{-tBu}}$py)(HL^{oxime})] and [Co^{II}(H)(HL^{oxime})] species and these results are in agreement with a previous study[14c] on bis(dialkylglyoximate)-cobalt complexes. However, these proton addition events are disfavored by entropy and are expected to have kinetic barriers when free energies are considered. The activation energies will have an upper bound of 10 kcal/mol which results from the estimated loss of the translational entropy for a bimolecular reaction. Considering these low-energy barriers and presence of excess of TFA in the medium, evolution of H_2 from the reaction of the Co^{II}–H complexes with the acid is very likely. However, considering the fact that the loss

www.manaraa.com

of the axial ligand L' from the six-coordinate [Co^{II}(H)(L')(HL^{oxime})] complex is a favorable process, the catalytic pathways shown in Figure **4.31b** are more likely than the pathway in **Figure 4.31a**. The bimetallic pathway of H_2 generation by the combination of two neutral [Co^{II}(H)(HL^{oxime})] complexes is not likely because of presence of excess of protons compared to the Co-complex and low-energy barriers for the reactions of proton from TFA with [Co^{II}(H)($^{4\text{-}tBu}$py)(HL^{oxime})] and [Co^{II}(H)(HL^{oxime})] complexes. The bimetallic pathway requires two Co-complexes to approach with the hydrides of the Co–H moieties facing each other and hence, is expected to have a moderate kinetic barrier.[14c]

4.4. **Conclusions**

A series of homo- and heteroaxial complexes of Co^{III} in a oxime ligand framework were synthesized and characterized by multiple physico-chemical techniques. All of these complexes (**1 - 6**) exhibited excellent catalytic properties towards proton reduction (TFA as the proton source) with a low overpotentials and good turnover numbers. Variations of axial ligands affect both the overpotential and TONs, whereas the pyridine substitution does not affect the overpotentials but the TONs and k_{obs} were greatly affected. Electrochemistry of heteroaxially substituted complexes exhibited complicated behavior with two Co^{III}/Co^{II} and one Co^{II}/Co^{I} processes, the origin of which has been identified with multiple methods like CV, ^{1}H-NMR, UV-vis, EPR and DFT calculations. A detailed understanding of the electrochemical path with coordination preferences was revealed in CH_3CN. The coordination environment of the active species for the catalysis was found to be five-coordinate with $^{4\text{-}tBu}$pyridine as the fifth ligand. Detailed catalytic mechanism of proton reduction was investigated for complex **4**. Complexes **4-6** favor the mechanism of hydrogen generation by heterolytic reaction of proton with Co^{II}–H. We were also able to synthesize homoaxially substituted water-coordinated cobalt-oxime complex

www.manaraa.com

(**7**) and its corresponding ruthenium analog (**8**). These two complexes were successfully characterized by various physico-chemical techniques. Both of these complexes were able to stabilize atleast doubly reduced species during electrochemical scan, and thus tested towards proton reduction activity in the presence of mild acid TFA with overpotential close to 0.35 V after three hours of experiment. Hydrogen generation was confirmed from bulk electrolysis experiment, and the corresponding TON and Faradaic efficiency was found close to 7.0 and 75% respectively, after one hour. Therefore, the heterometallic [$Ru^{II}Co^{III}$] complex retains the electrocatalytic activity in comparison with its cobalt module. The complex **8** exhibited brown color and absorbs between 400-500 nm in the visible region due to the strong MLCT transition from ruthenium center to bipyridine moieties.

To study electron transfer from the excited state of ruthenium to the acceptor cobalt, transient absorption (TA) spectroscopy was performed in CH_3CN and CH_3OH by exciting the complex at 500 nm. Excited state was found to be quenched by Co^{III} upon irradiation on Ru^{II}. Future studies are aimed at the investigation of the photocatalytic proton reduction with complex **8**. The photocatalytic activity of this complex towards hydrogen production is under investigation in the collaboration with Dr. Karen Mulfort at Argonne National Laboratory.

www.manaraa.com

REFERENCES

1. (a) Fihri, A.; Artero, V.; Razavet, M.; Baffert, C.; Leibl, W.; Fontecave, M. *Angew. Chem. Int. Ed.* **2008**, *47*, 564. (b) Fihri, A.; Artero, V.; Pereira, A.; Fontecave, M. *Dalton Trans.* **2008**, 5567. (c) Li, C.; Wang, M.; Pan, J.; Zhang, P.; Zhang, R.; Sun, L. *J. Organometal. Chem.* **2009**, *694*, 2814. (d) Mulfort, K. L.; Mukherjee, A.; Kokhan, O.; Du, P.; Tiede, D. M. *Chem. Soc. Rev.* **2013**, *42*, 2215. (e) Mulfort, K. L.; Tiede, D. M. *J. Phys. Chem. B* **2010**, *114*, 14572. (f) Mukherjee, A.; Kokhan, O.; Huang, J.; Niklas, J.; Chen, L. X.; Tiede, D. M.; Mulfort, K. L. *Phys. Chem. Chem. Phys.* **2013**, *15*, 21070.

2. (a) APEX2 V2010.11-3. Software *for the CCD Detector System*; Bruker Analytical X-ray Systems, Madison, WI, **2010** (b) SHELXS-97 (Sheldrick, 2008) Sheldrick, G.M. *Acta Cryst.* **2008**, *A64*, 112. (c) Dolomanov, O. V.; Bourhis, L. J.; Gildea, R. J.; Howard, J. A. K.; Puschmann, H. OLEX2: a complete structure solution, refinement and analysis program. *J. Appl. Cryst.* **2009**, *42*, 339. (d) COSMO V1.61, *Software for the CCD Detector Systems for Determining Data Collection Parameters.* Bruker Analytical X-ray Systems, Madison, WI, **2009**. (e) SAINT V 7.68A Software *for the Integration of CCD Detector System* Bruker Analytical X-ray Systems, Madison, WI, **2010**. (f) SADABS V2.008/2 Program for absorption corrections using Bruker-AXS CCD based on the method of Robert Blessing; Blessing, R.H. *Acta Cryst.* **1995**, *A51*, 33. (g) Sheldrick, G.M. "A short history of SHELX". *Acta Cryst*. **2008**, *A64*, 112. (h) COSMO V1.58, *Software for the CCD Detector Systems for Determining Data Collection Parameters.* Bruker Analytical X-ray Systems, Madison, WI, **2008**. (i) APEX2 V2008.5-0 Software *for the CCD Detector System*; Bruker Analytical X-ray Systems, Madison, WI, **2008**. (j) SAINT V 7.34 Software *for the Integration of CCD Detector System* Bruker Analytical X-ray Systems, Madison, WI, **2008**. (k) Sluis, P. V. D.; Spex, A.L. *Acta Cryst*. **1990**,

www.manaraa.com

A46, 194. (l) Spex, A. L. *J. Apply. Cryst*. **2003**, *36*, 7.[a] Obtained with graphite monochromated Mo Kα (*l* = 0.71073 Å) radiation. [b]$R1 = \sum||F_o|-|F_c||/\sum|F_o|$. [c]$wR_2 = \{\sum[w(F_o^2-F_c^2)^2/\{\sum[w(F_o^2)^2]\}^{1/2}$.

3. (a) Frisch, M. J.; Trucks, G. W.; Schlegel, H. B. *et al. Gaussian Development Version; Revision H.35 ed.; Gaussian, Inc.: Wallingford, CT* **2010.** (b) Becke, A. D. *J. Chem. Phys.* **1993,** *98*, 5648. (c) Perdew, J. P. *Phys. Rev. B* **1986,** *33*, 8822. (d) Perdew, J. P.; Burke, K.; Wang, Y. *Phys. Rev*. **1996,** *54*, 16533. (e) Dunning, T. H. Jr.; Hay, P. J. *In Modern Theoretical Chemistry, Ed. H. F. Schaefer III, Vol. 3 (Plenum: New York*, **1977**) 1-28. (f) Dolg, M.; Wedig, H.; Preuss, H. *J. Chem. Phys.* **1987,** *86*, 866. (g) Miertus, S.; Scrocco, E.; Tomasi, J. *Chem. Phys.* **1981,** *55*, 117. (h) Scalmani, G.; Frisch, M. J. *J. Chem. Phys.* **2010,** *132*, 114110. (i) Scalmani, G.; Frisch, M. J.; Mennucci, B.; Tomasi, J.; Cammi, R.; Barone, V. *J. Chem. Phys.* **2006,** *124*, 9410. (j) Tomasi, J.; Mennucci, B.; Cammi, R. *Chem. Rev.* **2005**, *105*, 2999. (k) Schaefer, A.; Huber, C.; Ahlrichs, R. *J. Chem. Phys.* **1994,** *100*, 5829. (l) Krishnan, R.; Binkley, J.S.; Seeger, R.; Pople, J. A. *J. Chem. Phys.* **1980,** *72*, 650. (m) Seeger, R.; Pople, J. A. *J. Chem. Phys.* **1977,** *66*, 3045. (n) Schlegel, H. B.; McDouall, J. J. *In Computational Advances in Organic Chemistry;* Ögretir, C., Csizmadia, I. G., Eds.; Kluwer Academic: Amsterdam, The Netherlands, **1991**. (o) Bauernschmitt, R.; Ahlrichs, R. *J. Chem. Phys.* **1996**, *104*, 9047. (p) Pennington, R.; Keith, T.; Millam, J. M.; GaussView V. 5.0, Semichem, Inc.: Shawnee Mission, KS, **2009**.

4. Uhlig, E.; Friedrich, M. *Z. Anorg. Allg. Chem.* **1966**, *343*, 299.

5. Costa, G.; Mestroni, G.; Savorgnani, E. D. *Inorg. Chim. Acta* **1969,** 323.

6. Cavichiolo, L. J.; Horner, M.; Gigilo, V. F.; Nunes, F. *Spectrochim. Acta Part A* **2009**, *73*, 154.

7. Hay, R.; Bradshaw, R. *Trans. Met. Chem.* **1996**, *21*, 64.

www.manaraa.com

8. Jacques, P-A.; Artero, V.; Pecaut, J.; Fontecave, M. *Proc. Natl. Acad. Sci.* **2009**, *106*, 20627.

9. Bhattacharjee, A.; Chavarot-Kerlidou, M.; Andreiadis, E. S.; Fontecave, M.; Field, M. J.; Artero, V. *Inorg. Chem.* **2012,** *51,* 7087.

10. (a) Shi, S.; Daniels, L. M.; Espenson, J. H. *Inorg. Chem.* **1991,** *30*, 3407. (b) Hu, X.; Brunschwig, B. S.; Peters, J. C. *J. Am. Chem. Soc.* **2007,** *129*, 8988. (c) Weakley, T. J. R.; Marks, J.; Finke, R. G. *Acta Cryst. C* **1994,** *C50,* 1690.

11. Gerli, A.; Marzilli, L. G. *Inorg. Chem.* **1992**, *31*, 1152.

12. Fourmond, V.; Jacques, P. A.; Fontecave, M.; Artero, V. *Inorg. Chem.* **2010,** *49,* 10338.

13. Baffert C.; Artero, V.; Fontecave, M. *Inorg. Chem*. **2007**, *46,* 1817.

14. (a) Solis, B. H.; Hammes-Schiffer, S. *Inorg. Chem.* **2011,** *50,* 11252. (b) Solis, B.; Yu, Y.; Hammes-Schiffer, S. *Inorg. Chem.* **2013,** *52,* 6994. (c) Muckermann, J. T.; Fujita, E. *Chem. Comm.* **2011,** *47,* 12456. (d) Bhattacharjee, A.; Andreiadis, E. S.; Kerlidou, M. C.; Fontecave, M.; Field, M. J.; Artero, V. *Chem. Eur. J.* **2013,** *19,* 15166. (e) Marinescu, S. C.; Winkler, J. R.; Gray, H. B. *Proc. Nat. Acad. Sci* **2012**, *109,* 15127.

www.manaraa.com

CHAPTER 5

DISTINCT PROTON AND WATER REDUCTION BEHAVIOR WITH A COBALT(III) ELECTROCATALYST BASED ON PENTADENTATE OXIMES

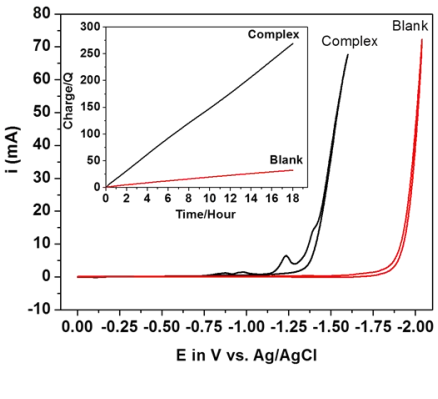

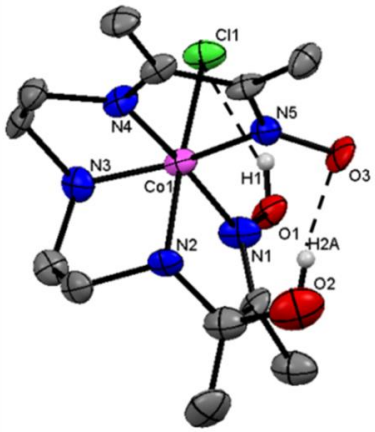

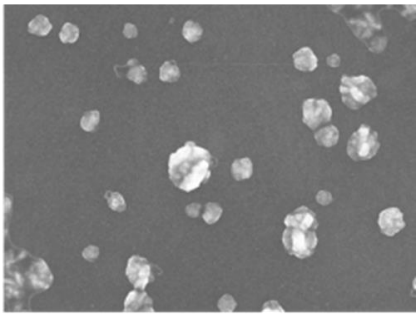

www.manaraa.com

CHAPTER 5

DISTINCT PROTON AND WATER REDUCTION BEHAVIOR WITH A COBALT(III) ELECTROCATALYST BASED ON PENTADENTATE OXIMES

Portions of the text in this chapter were reprinted or adapted with permission from: Basu, D.; Mazumder, S.; Shi, X.; Staples, R.; Schlegel, H. B.*; Verani, C. N.* *Angew. Chem. Int. Ed.* **2015**, *54*, DOI: 10.1002/anie.201501410. All rights to the work are retained by the authors and any reuse requires permission of the authors.

5.1. Introduction

Glyoxime-based Espenson catalysts have been investigated in great detail (**chapter 4**), and the catalytic Co^{I} state seems to favor a five-coordinate environment originated by axial coordination that stabilizes a low-spin $3d^8$ configuration required for nucleophillic attack on the proton. However important this five-coordinate species is, current catalyst designs are limited by the fact that the untethered axial ligand can dissociate easily contributing to sluggish electro and photocatalytic use and degradation of the molecular catalyst. Ergo, we hypothesize that rational ligand design should include pentadentate oxime species for the investigation of new catalyst frameworks. Moreover, such ligand design can be useful to address other relevant issues of glyoxime-based systems, namely, (i) the mechanisms of catalyst degradation in acidic media, and (ii) the quest for water-soluble systems. Conversion of the molecular catalyst into cobalt oxide nanoparticulates at the surface of the electrode has been reported for boron-capped cobalt glyoximes[1] and pyridyloximes[2], whereas the most studied systems capable of generating H_2 from water include bivalent and trivalent cobalt complexes of tetrapyridines,[3] pentapyridines,[3] bis-bipyridines,[3] and imino-pyridines.[3] Our groups have shown that pentadentate $[N_2O_3]$ ligands originally used with Fe^{III} in current rectification,[4] can support cobalt complexes in catalytic proton reduction.[5]

www.manaraa.com

Here we report on a pentadentate nitrogen-rich oxime ligand H_2L^1, its coordination to Co^{II} and water incorporation through one of the imine double bonds to form the water soluble catalytic species $[Co^{III}(HL^{1\cdot})Cl]PF_6$ (1), shown in **Scheme 5.1**. Catalyst **1** presents distinct mechanisms of H_2 generation in acidic organic media and in water. The results follow.

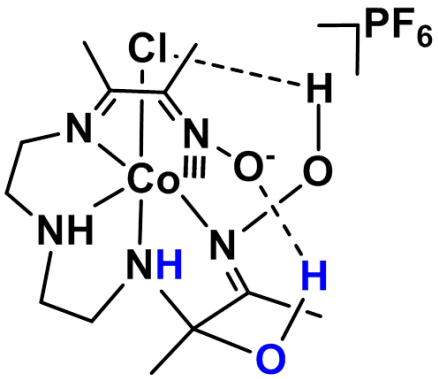

1

Scheme 5.1. Cobalt(III) complex.

5.2. Experimental

5.2.1. X-ray structural determination

An orange chunk crystal for **1** with dimensions 0.20 x 0.10 x 0.08 mm was mounted on a Nylon loop using very small amount of paratone oil.

Data were collected using a Bruker CCD (charge coupled device) based diffractometer equipped with an Oxford Cryostream low-temperature apparatus operating at 173 K. Data were measured using omega and phi scans of 1.0° per frame for 30 s. The total number of images was based on results from the program COSMO[6a] where redundancy was expected to be 4.0 and completeness to 0.83 Å to 100%. Cell parameters were retrieved using APEX II software[6b] and refined using SAINT on all observed reflections. Data reduction was performed using the SAINT software[6c] which corrects for Lp. Scaling and absorption corrections were applied using SADABS[6d] multi-

www.manaraa.com

scan technique, supplied by George Sheldrick. The structures are solved by the direct method using the SHELXS-97 program and refined by least squares method on F[3], SHELXL-97[6e], which are incorporated in OLEX2.[6f]

The structure was solved in the space group $P2_1/c$ (# 14). All non-hydrogen atoms are refined anisotropically. Hydrogens were calculated by geometrical methods and refined as a riding model. All drawings are done at 50% ellipsoids.

Table 5.1. Crystal Data for the complex **1**.

	1
Empirical formula	$C_{12}H_{24}ClCoF_6N_5O_3P$
Formula weight	525.71
Temperature (K)	173.01
Wavelength (Å)	0.71073
Crystal system, space group	Monoclinic, $P2_1/c$
a (Å)	14.9473(15)
b (Å)	11.7925(12)
c (Å)	11.1994(12)
α (°)	90.00
β (°)	90.00
γ (°)	90.00
Volume ($Å^3$)	1974.1(4)
Z	4
Calculated density (Mg/m^3)	1.769
Absorption coefficient (mm^{-1})	9.600
F (000)	1072.0
R(F) (%)	6.99
R_w(F) (%)	17.11

www.manaraa.com

5.2.2. Computational methods

All the calculations were performed using Density Functional Theory (DFT)[7a] with a development version of Gaussian,[7b] B3PW91 functional[7c-e] with SDD basis set[7f] on cobalt and 6-31G(d,p)[7g,h] basis on the other atoms. Solvation effects (in acetonitrile and acetone) were accounted for using the IEF polarizable continuum model (PCM)[7i-l] solvation model and were included during structure optimization. Low spin states were found to be lower in energy for the metal complexes.

5.2.3. Catalytic activity

Proton reduction electrocatalysis was tested for **1** via cyclic voltammetry in presence of acetic acid (HOAc, pKa: 22.3 in CH_3CN) with tetra-butyl ammonium tetrafluoroborate ($TBABF_4$) as supporting electrolyte. For bulk electrolysis, the main chamber was filled with an electrolyte solution and proton source ($TBABF_4$: 1.317 g; HOAc: 0.024 g [0.4 mmol], 20 mL acetonitrile) and the glass-fitted chamber was filled with another electrolyte solution ($TBABF_4$: 0.329 g; 5 mL acetonitrile). Bulk electrolysis was conducted with catalyst (0.004 mmol) in acetonitrile (CH_3CN) for 180 minutes at -1.7 $V_{Ag/AgCl}$ and the head space gas (100 µL) was injected into the GC to record the amount of dihydrogen produced. After the background subtraction, the turnover number was calculated as the ratio of the moles of dihydrogen produced over the moles of catalyst used. Faradaic efficiency was calculated from the gas chromatography measurements. For water reduction, similar procedure has been followed. For controlled potential experiment, the main chamber was filled with 20 mL of phosphate buffer solution whereas the glass-fitted chamber was filled with 5 mL of solution. Bulk electrolysis at -1.7 $V_{Ag/AgCl}$ was applied for complex **1** to generate H_2. The typical concentration of catalyst for water reduction experiment is 0.0002 mmol.

www.manaraa.com

5.2.4. Synthetic procedures

The ligand H_2L^1 (1 mmol, 0.269 g) was dissolved in 36 mL acetone. $CoCl_2.6H_2O$ (1 mmol, 0.238 g) in water (2 mL) was added slowly to the acetone solution of the ligand. KPF_6 (1.7 mmol, 0.3128 g) in 2 mL water was added to the solution after 10 minutes. It was stirred at room temperature for 2-3 hours to ensure the completion of the reaction. After the reaction, the solution is rotary evaporated to 5 mL and poured into a crystallization flask. A yellowish-orange crystalline precipitate was obtained after 7-10 days. X-ray quality crystals were obtained from recrystallization with MeOH/H_2O (2:1) mixture. Yield: 75 %. IR (KBr, cm^{-1}) 3646 (w) (OH); 3244 (m), 3127 (m) (NH); 2954 (w), 2921 (w) (aliphatic CH); 1621 (w) (C=N); 1453 (m) (C=C); 832 (s) (PF_6^-). ESI pos. in MeOH: m/z = 380.0900 for $[Co^{III}(^{H2O}HL^1)(Cl)]^+$. Anal. Calcd for $M.H_2O$: $C_{12}H_{26}ClCoF_6N_5O_4P$: C: 26.51; H: 4.82; N: 12.88; Found: C: 26.41; H: 4.39; N: 12.84.

5.3. Results and discussions

5.3.1. Syntheses and characterizations

The ligand H_2L^1 was prepared by literature methods[8] and contains one secondary amine along with two imine and two oxime nitrogen donor atoms. The redox-active and π-accepting nature of the imine and oxime moieties stabilize the monovalent cobalt responsible for catalytic activity. Moreover, the pentadentate and macrocyclic nature of H_2L^1 is expected to inhibit the lability of the N donor atoms. Reaction of the ligand with $CoCl_2.6H_2O$ in acetone/water (9:1) yields complex **1** where a chloride occupies the sixth position (**Figure 5.1**) and water incorporation was observed through one of the imine bond.

www.manaraa.com

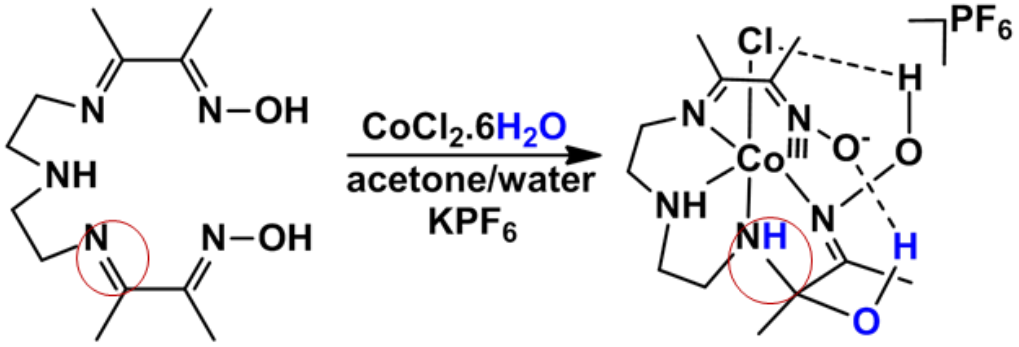

Figure 5.1. Synthesis of the cobalt(III) complex.

Complex **1** was characterized by multiple spectroscopic and spectrometric methods, and by elemental analyses. The presence of a PF_6^- counterion was confirmed with the observation of a broad peak in the FTIR spectra at 832 cm^{-1}. The diamagnetic nature of the $^{LS}3d^6$ **1** was confirmed by the presence of sharp peaks in the ^{1}H-NMR spectra. ESI-MS analysis confirmed the presence of the molecular ion species $[Co^{III}(HL^{1'})Cl]^+$ with m/z = 380.9000 in methanol (**Figure 5.2**).

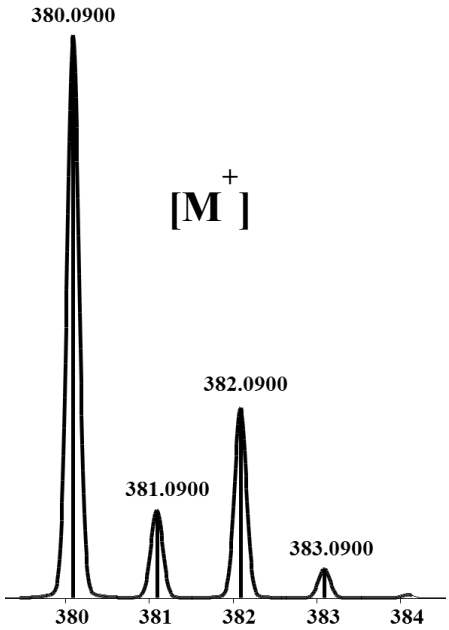

Figure 5.2. Experimental (bars) and simulated (line) isotopic distribution for the molecular ion of the complex **1** in CH_3OH.

Comparison between the pentadentate H_2L^1 and the tetradentate glyoxime analog (**Figure 5.3**) confirmed the former as susceptible to water addition; while water incorporation in the $[N_4]$

www.manaraa.com

oxime is detrimental to the conjugated planar ligand framework and unfavorable by *ca.* 11 kcal/mol. The decreased electronic communication between the imine moieties in H_2L^1 together with the formation of a strong OH---O hydrogen bonding of 1.727Å in the resulting aqua complex make this incorporation favorable by *ca.* 4 kcal/mol.

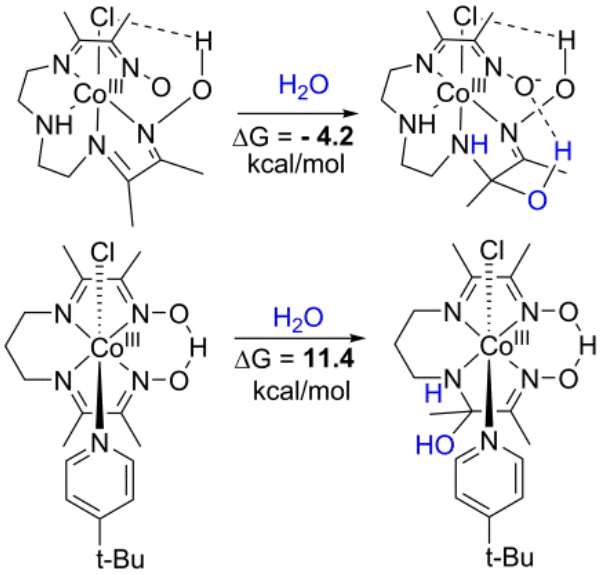

Figure 5.3. DFT-calculated energetics of water addition to one of the imine moieties in tetradentate *vs.* pentadentate oxime complexes.

5.3.2. Molecular structures

Molecular structural information was gathered from X-ray quality crystals obtained by recrystallization from CH_3OH/H_2O (2:1). The structure of **1**, shown in **Figure 5.4**, confirmed the distorted octahedral nature of the complex with a chlorido ligand occupying the sixth position. Incorporation of H_2O is diagnostic of the newly formed C-O(H) and the lengthening of the C=N bond to C-N from *ca.* 1.30 to 1.48 Å. Bond-lengths and angles, along with crystallographic parameters are given in **Tables 5.1**. Two H-bonding interactions seem to be operative in the stabilization of the molecular structure. The newly incorporated OH forms an H-bond with the

www.manaraa.com

formally deprotonated oxime O(3) atom, whereas the second H-bond is formed between the oxime O(1)H and the chloride ligand.

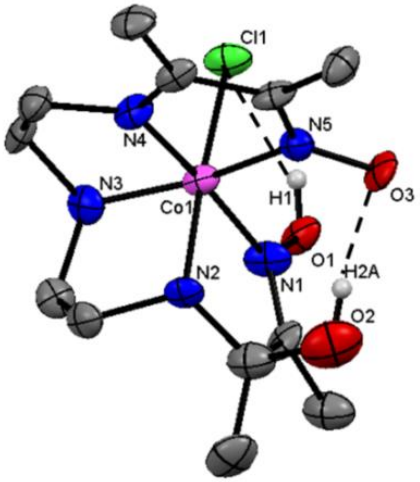

Figure 5.4. The ORTEP representation of the cation of mononuclear $[Co^{III}(^{H_2O}HL^{oxime})(Cl)]PF_6$ complex (**1**) at 50% ellipsoid probability. Bond lengths in Å: Co(1)-N(1): 1.925(7); Co(1)-N(2): 1.949(6); Co(1)-N(3): 1.947(8); Co(1)-N(4): 1.865(6); Co(1)-N(5): 1.894(7); Co(1)-Cl(1): 2.248(2); O(1)-N(1): 1.375(8); O(3)-N(5): 1.304(9).

This particular orientation of atoms is the most stable thermodynamic configuration, as confirmed by DFT methods (**Figure 5.5**).

.

www.manaraa.com

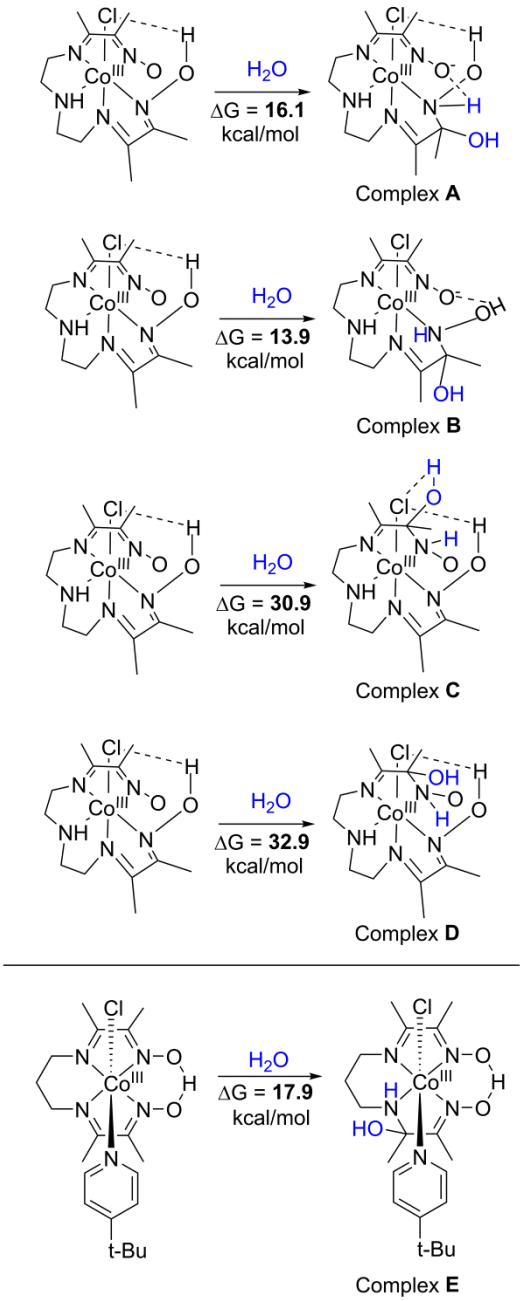

Figure 5.5. Water addition probed to the different imine bonds in the pentadentate and tetradentate oxime complexes. All the water addition events to the pentadentate oxime complex shown in this figure are found to be higher in energy than that in **Figure 5.3**. In case of the tetradentate oxime, complex **E** is obtained by the addition of one water molecule to the imine function from a face opposite to the one probed in **Figure 5.3** and species **E** is calculated to be higher in energy than the corresponding complex in **Figure 5.3**.

www.manaraa.com

5.3.3. Electronic, electrochemical, and electrocatalytic properties

5.3.3.1. Electronic properties

Electronic spectroscopic studies were performed in CH_3CN for the parent $[Co^{III}(HL^{1'})Cl]^+$ **(1)** species. The yellowish $^{LS}3d^6$ parent species **1** shows an absorption band in the visible region at 441 nm (ε = 627 $M^{-1}cm^{-1}$) originating from a d-d transition tentatively associated with the $^1T_{2g}(I) \leftarrow {}^1A_{1g}(D)$ process of an ideal octahedral field (**Figure 5.6**, **Table 5.2**).

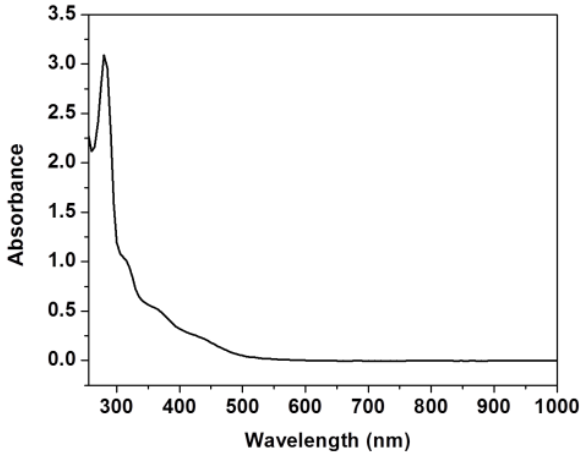

Figure 5.6. UV-visible spectra for **1** (left to right as 10^{-3} M and 10^{-5} M) in CH_3CN.

Table 5.2. UV-visible parameters in CH_3CN.

	λ (nm) |ε ($M^{-1}cm^{-1}$)|	λ (nm) |ε ($M^{-1}cm^{-1}$)|	λ (nm) |ε ($M^{-1}cm^{-1}$)|	λ (nm) |ε ($M^{-1}cm^{-1}$)|
1	363 |1411|	441 |627|		
1^-		472|1030|	583 |72|	671 |77|
1^{2-}		466|1623|		

5.3.3.2. Electrochemical and electrocatalytic properties

Cyclic voltammetry (CV) was performed in CH_3CN (**Figure 5.7**). Three quasi-reversible processes are observed at -0.75 $V_{Fc/Fc+}$ (ΔE = 0.12 V; i_{pc}/i_{pa} = 1.29), -1.68 $V_{Fc/Fc+}$ (ΔE = 0.10 V; i_{pc}/i_{pa} = 1.5), and -1.86 $V_{Fc/Fc+}$ (ΔE = 0.10 V; i_{pc}/i_{pa} = 1.4). The potentials of **1** were recorded in a

www.manaraa.com

total of five different stock solutions and confirmed reproducibility of the data.

Catalytic proton reduction studies were performed in CH_3CN by CV experiments in presence of various sources that included weak acids triethyl ammonium chloride (Et_3NHCl, pKa = 18.7 in CH_3CN) (**Figure 5.7**) and acetic acid (HOAc, pKa = 22.3 in CH_3CN) (**Figure 5.8**). The H^+/H_2 catalytic peak was observed close to the second reduction process for the weak acids Et_3NHCl and HOAc. Due to our interest in water reduction we focused our attention on the catalytic activity of **1** in presence of 0-5 equivalents of the weakest acid, HOAc. The catalytic peak becomes evident at potentials close to -1.50 V peaking at 5 equivalents of the acid, with clear formation of a gaseous product. The catalytic current reaches 130 μA after addition of 5 equiv. of acid, and an overpotential of 0.24 V was observed after considering the homoconjugation effect.[9]

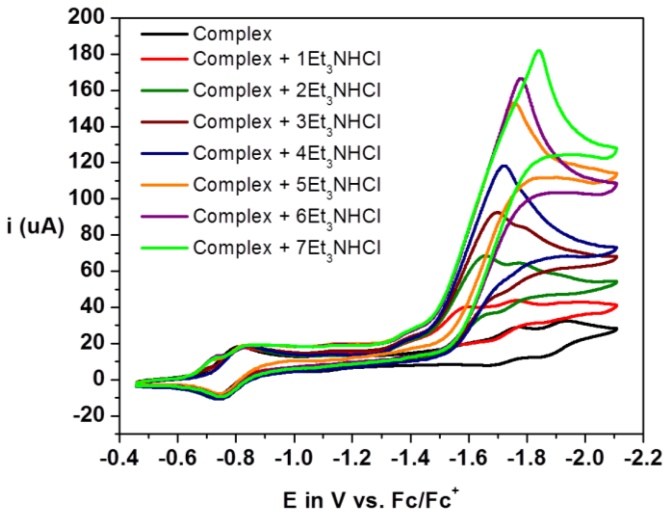

Figure 5.7. Cyclic voltammetric experiment for hydrogen generation for **1** in the presence of triethyl ammonium chloride (Et_3NHCl) in CH_3CN (Glassy carbon (WE); Ag/AgCl (RE); Pt wire (AE); $TBABF_4$ (SE)).

www.manaraa.com

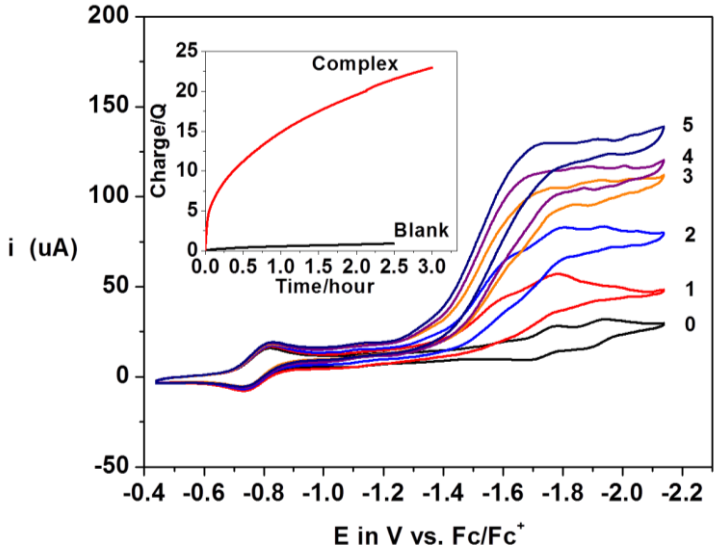

Figure 5.8. CV experiments for dihydrogen generation. The numbers 0-5 indicate the number of HOAc equivalents used in comparison to **1.** Inset: Charge *vs.* time plot for **1** in comparison with an HOAc blank for 3 h during bulk-electrolysis.

The fact that a lower overpotential is observed in presence of **1** with an associated higher catalytic current than that of the blank (**Figure 5.9**) validates the complex as the catalyst.

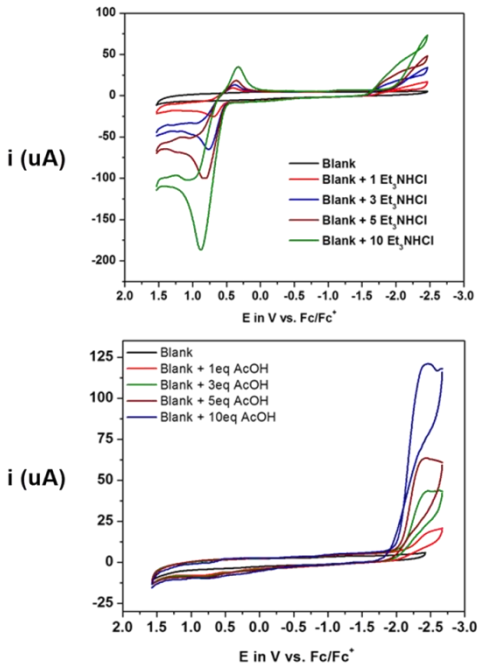

Figure 5.9. Cyclic voltammetric experiment for hydrogen generation for blank in the presence of various acids in CH_3CN.

www.manaraa.com

Controlled potential electrolysis was performed at -1.7 $V_{Ag/AgCl}$ to confirm the identity of the gaseous product as dihydrogen. Complex **1** consumes more charge than the blank during the bulk-electrolysis experiment (**Figure 5.8 inset**), supporting the complex as being responsible for catalysis. The turnover number (TON) in CH_3CN for **1** was calculated at 14.7 after 3 h with Faradaic efficiency of 75% in presence of 100 equivalents of acid. The color of the solution remains unaltered and the corresponding post-catalysis UV-Visible spectrum under anaerobic conditions reveals peaks at 265 and 325 nm (**Figure 5.10**) in excellent agreement with the reduced $3d^7$ Co^{II} species (**Figure 5.11**) thus suggesting that the molecular catalyst is preserved and no nanoparticulate species are formed.

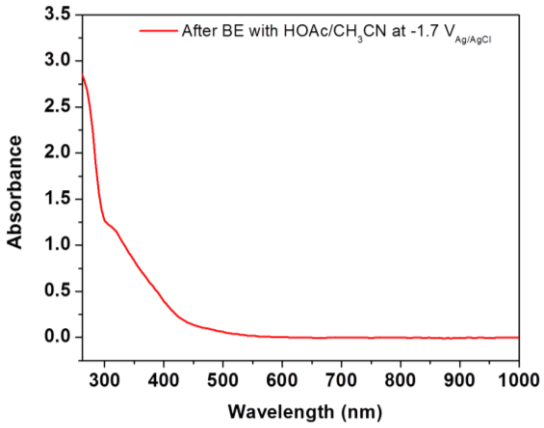

Figure 5.10. UV-Visible spectra after electrocatalysis of **1** in the presence of HOAc in CH_3CN at -1.7 $V_{Ag/AgCl}$.

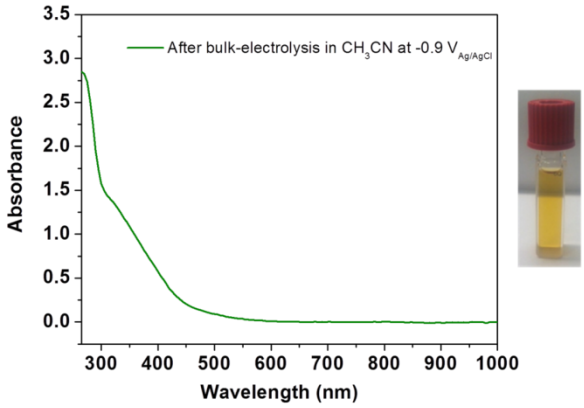

Figure 5.11. UV-Visible spectra of the Co^{II}-species after bulk-electrolysis of **1** in CH_3CN at -0.9 $V_{Ag/AgCl}$.

www.manaraa.com

The DFT optimized geometries for **1** and its relevant reduced species is summarized in **Figure 5.12**. The parent Co^{III}-complex displays a pseudo-octahedral geometry with two hydrogen bonds, OH····O and OH····Cl. A $1e^-$ reduction yields a $^{LS}3d^7$, Co^{II}-complex, in which occupation of an antibonding e_{g*}-like, Co-based $3d_{z2}$ orbital weakens the metal–ligand interactions along the z-axis fostering an increase in the Co–Cl and Co–N bond distances from 2.28 to 2.82 and 1.96 to 2.20 Å, respectively. The OH····Cl interaction becomes stronger as the hydrogen bonding distance decreases from 2.09 in **1** to 1.98 Å in the Co^{II} species. Loss of chloride from the later complex requires *ca.* 6 kcal/mol. Further reduction of the Co^{II} complex affords the Co^{I} species, which is a five-coordinate complex with the metal center in a distorted square pyramidal environment. At nearly 4 Å from the metal center, the chloride is no longer part of the coordination sphere.

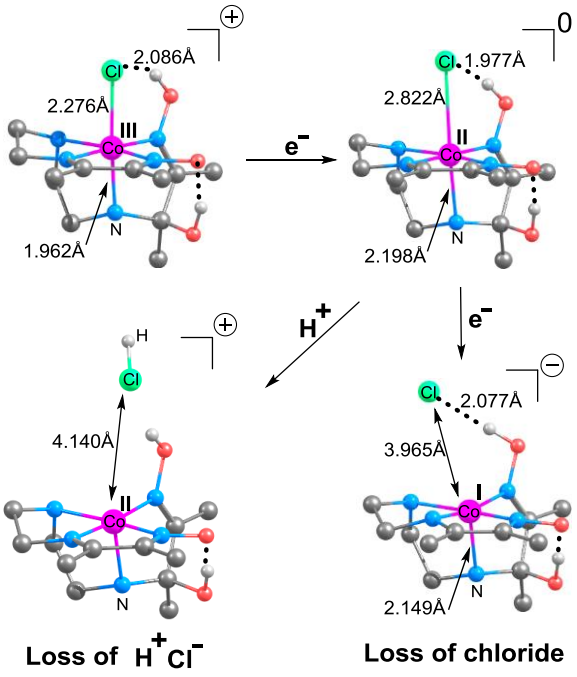

Figure 5.12. DFT-calculated structures of the redox species generated in the electrochemical pathway in CH_3CN.

.

www.manaraa.com

As seen in **Figure 5.8**, an anodic shift of about 180 mV was observed upon addition of acid to **1** in CH_3CN and the electrocatalytic peak was found at potentials close to -1.50 $V_{Fc/Fc+}$ whereas the Co^{II}/Co^{I} process is observed at -1.68 $V_{Fc/Fc+}$ in absence of acid. DFT-calculations find that in presence of acid the addition of a proton on the Co^{II}-species results in the loss of chloride as H^+Cl^- giving rise to the five-coordiante cationic Co^{II}-complex (**Figure 5.12**). The later species can subsequently get reduced to the corresponding Co^{I}-complex. The reduction potentials of the $[Co^{II}(HL^{1'})]^+/[Co^{I}(HL^{1'})]$ and $[Co^{II}(HL^{1'})Cl]/[Co^{I}(HL^{1'})Cl]^-$ couples are calculated to be -1.65 $V_{Fc/Fc+}$ and -1.89 $V_{Fc/Fc+}$, respectively. Alternatively, a proton-coupled electron transfer (PCET) mechanism from $[Co^{II}(HL^{1'})Cl]$ to Co^{III}–hydride $[Co^{III}(H)(HL^{1'})]$ was considered without invoking chloride loss from the Co^{II}-complex. The redox potential for the PCET Co^{II}/Co^{III}–H couple is calculated[10] to be -1.55V, see supporting information for details. The anodic shift calculated by invoking chloride loss from the Co^{II}-complex is 240 mV and is in better agreement with the experimental measurement of 180 mV while the shift in the potential calculated from the PCET mechanism is 340 mV and differs by 160 mV from the experiment. Moreover, a Co^{II}/Co^{I} process is found in water at -1.25 $V_{Ag/AgCl}$ (**Figure 5.14)** that supports the formation of a Co^{I}-species and hence, a PCET mechanism does not seem viable under the conditions of our study. The DFT-calculated catalytic mechanism of H_2 generation by complex **1** in presence of acid in CH_3CN is shown in **Figure 5.13**. The Co^{III}–H complex can be reduced to a more reactive Co^{II}–H species at a potential of -1.43 $V_{Fc/Fc+}$. Uptake of another proton and generation of H_2 by this Co^{II}–H complex is favorable by *ca.* 46 kcal/mol, regenerating the five-coordinate Co^{II}-complex to restart the catalytic cycle. The reaction of the proton with the Co^{II}–H species is expected to be activationless.[10] Homolytic coupling of the two Co^{II}–H species is calculated to be unfavorable compared to the heterolytic mechanism by *ca.* 32 kcal/mol.

www.manaraa.com

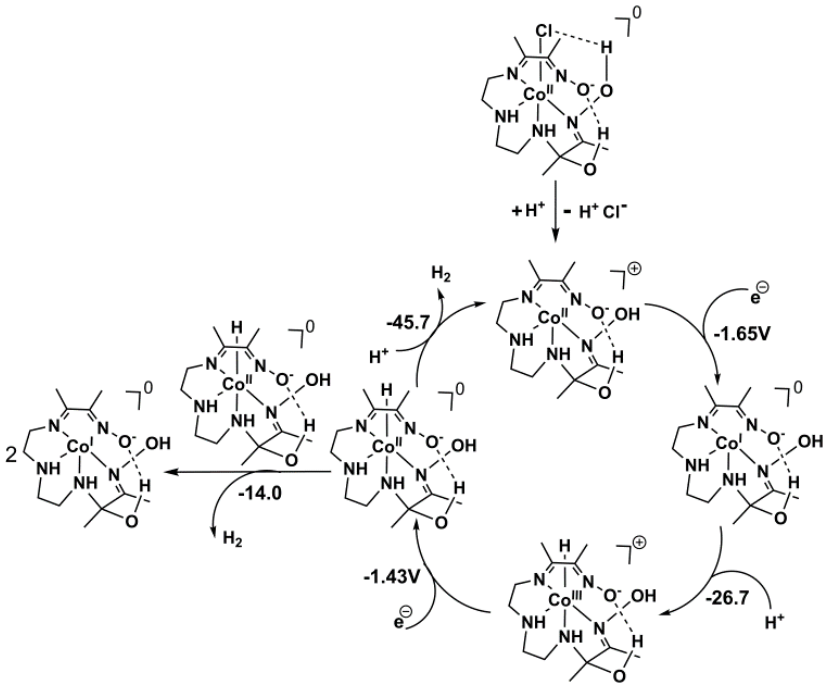

Figure 5.13. Catalytic mechanism of H_2 generation by complex **1** in CH_3CN. Energetics reported as free energy changes in kcal/mol.

Complex **1** is water soluble due to the presence of various polar groups such as —NH and —OH. Thus, cyclic voltammetric experiments were performed to study the viability of **1** as electrocatalyst for neutral water (pH = 7) reduction in presence of phosphate buffer using a mercury pool electrocell. We observed a peak at -1.25 $V_{Ag/AgCl}$, which corresponds to the Co^{II}/Co^{I} process, followed by a sharp increase of current from -1.30 $V_{Ag/AgCl}$. This sharp peak is assigned to the catalytic peak for H_2 evolution, and an onset overpotential of 0.65 V was calculated for this system. This result is relevant when compared to the blank experiment in absence of **1** where dihydrogen is generated at -1.90 $V_{Ag/AgCl}$, ergo, at a much more negative potential (**Figure 5.14**). This result validates **1** as water reduction catalyst with an observed low onset overpotential similar to other documented water reduction catalysts. Bulk electrolysis was performed at -1.7 $V_{Ag/AgCl}$ during 3 h in order to confirm the presence of dihydrogen. A TON of 950 was calculated after 3 h with Faradaic efficiency of 95%. The activity of the catalyst was

www.manaraa.com

assessed by performing an extended controlled potential experiment for 18 h at -1.7 $V_{Ag/AgCl}$ and pH 7. As indicated in **Figure 5.14 inset** a linear charge buildup indicative of continued catalysis was observed over time associated with 5680 TONs and Faradaic efficiency of 95%. All the catalytic parameters are summarized in **Table 5.3**.

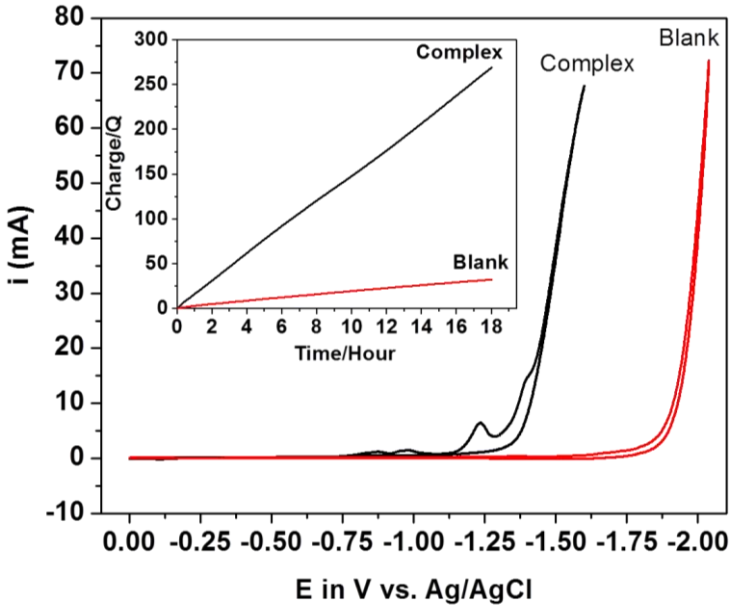

Figure 5.14. CV experiments for H_2 generation in water/phosphate buffer (pH: 7): Blank *vs.* **1** (Inset: Plot of charge *vs.* time in the bulk electrolysis experiment for 1 at -1.7 V vs. Ag/AgCl for 18 h).

Table 5.3. Catalytic parameters in HOAc and water for **1** (bulk electrolysis (BE): Applied potential (AP): -1.7 $V_{Ag/AgCl}$ with HOAc; AP: -1.7 $V_{Ag/AgCl}$ with water/phosphate buffer (pH: 7).

Parameters	**(HOAc)**	**(H_2O)**
Overpotential (V) (10 eq. HOAc) Overpotential (H_2O) (10 mL 1M buffer)	0.24	0.65
TON/3h (4.0 X 10^{-6} mol) (100 eq HOAc) TON/3h (2.0 X 10^{-7} mol) (H_2O, 20 mL 1M buffer)	14.7	950
Faradaic efficiency	75	95

www.manaraa.com

The actual overpotential of this complex was determined by controlled potential electrolysis at different potentials using mercury pool as the working electrode in water with pH 7 phosphate buffers. The overpotentials were applied over a period of 60 s and altered from 450 to 950 mV to determine the rate of H_2 production. The total consumption of charge was negligible below 550 mV (**Figure 5.15**), whereas at more negative potentials the charge increased linearly over time. Moreover, the charge *vs.* overpotential plot (**Figure 5.15 inset**) clearly indicates the consumption of charge started increasing consistently after an overpotential of 650 mV concomitant with the generation of bubbles. Therefore, the onset and actual overpotentials resides at close proximity. Interestingly, this overpotential is very close the electrochemical potential involved with the Co^{II}/Co^{I} process.

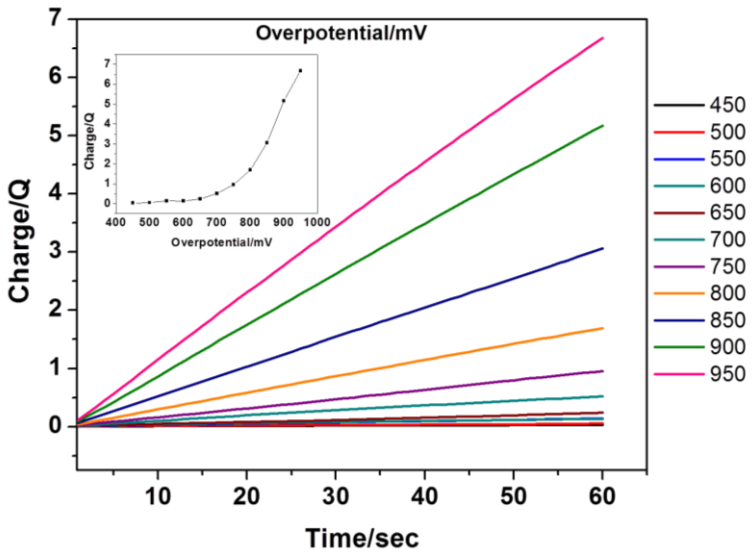

Figure 5.15. Charge vs. time plot during controlled potential experiments at different overpotentials (inset: charge at 60 s vs. overpotential plot).

During the extended bulk-electrolysis shown in **Figure 5.14 in**set an approximate tenfold more charge (270 vs. 25 μA) was consumed than in the blank experiment, thus leading to the indication that 1 is responsible for catalysis. However, the UV-visible spectra of the post-

www.manaraa.com

catalysis solution was measured after bulk-electrolysis at -1.25, -1.40, and -1.70 $V_{Ag/AgCl}$ (**Figure 5.16**) as a means to probe the resilience of the catalyst. As we observed spectral changes, the nature of the catalytic events was thoroughly investigated. Electrolysis for 1 h at -1.25 $V_{Ag/AgCl}$ resulted in some degree of color change from deep to pale yellow with the corresponding intensities of the UV-visible peaks being reduced by *ca*. 40% (**Figure 5.16a**). The near-complete disappearance of the UV-visible bands at *ca.* 95% was observed after 1 h electrolysis at -1.40 and -1.70 $V_{Ag/AgCl}$ (**Figures 5.16b,c**). As the catalytic activity was maintained, this was suggestive of possible formation of nanoparticulates.[1]

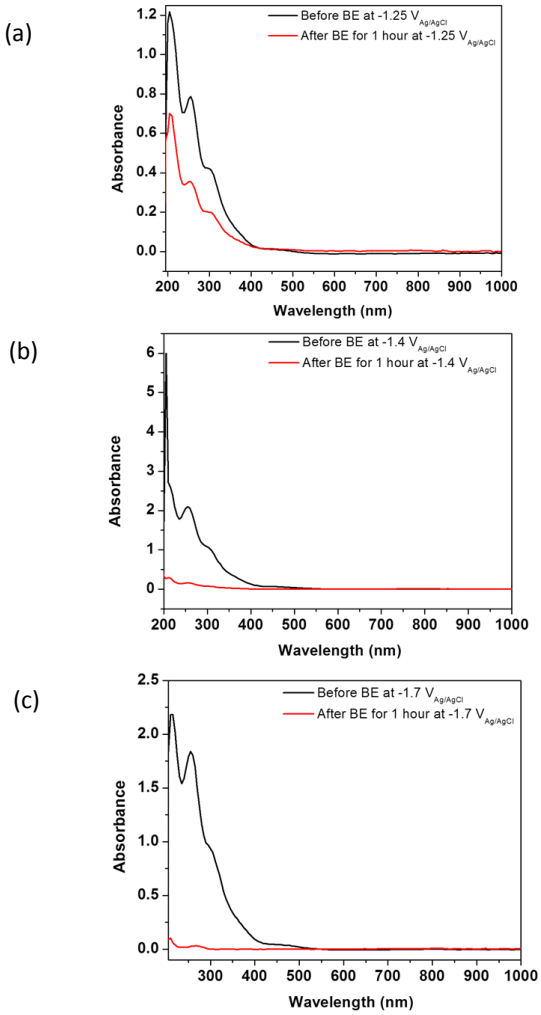

Figure 5.16. UV-Visible spectra of **1** before and after electrocatalysis for one hour in the presence of water/phosphate buffer (pH: 7) at (a) -1.25, (b) -1.4, and (c) -1.7 $V_{Ag/AgCl}$.

www.manaraa.com

Moreover, the charge consumption increased upon application of more negative potentials (**Figure 5.17**).

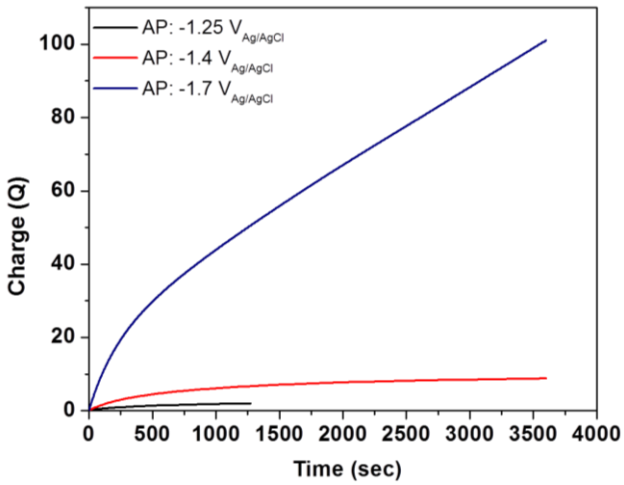

Figure 5.17. Charge *versus* time plot for **1** in the presence of water/phosphate buffer (pH: 7) at -1.25, -1.4, and -1.7 $V_{Ag/AgCl}$.

Nanoparticle formation was further probed by performing a "rinse" experiment in water at pH 7: A glassy carbon electrode was used in water in the presence of **1** and scanned to -1.7 $V_{Ag/AgCl}$ followed by extensive rinsing and dipping into a freshly prepared solution with no complex. A catalytic peak appeared around -1.15 $V_{Ag/AgCl}$, thus before the potential peak observed for the bare electrode (**Figure 5.18**), and implying that nanoparticle deposition on the surface of the electrode enables water reduction.

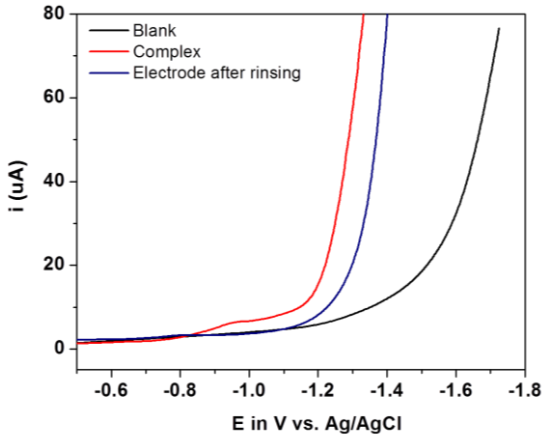

Figure 5.18. CV experiment to assess nanoparticle formation.

www.manaraa.com

Further confirmation of nanoparticle formation was obtained *via* scanning electron microscopy (SEM) analyses of a graphoil working electrode before and after bulk-electrolysis in water at -1.45 and -1.70 $V_{Ag/AgCl}$. The SEM images shown in **Figure 5.19** clearly indicate the formation of cobalt-based nanoparticle with a size distribution between 80-300 nm. Similar observations were described in recent studies with cobalt and nickel-based oxime complexes.[1,2,11] Although the composition of these nanoparticles is unknown, the ligand architecture was proposed to be crucial in the nanoparticle activity.[12]

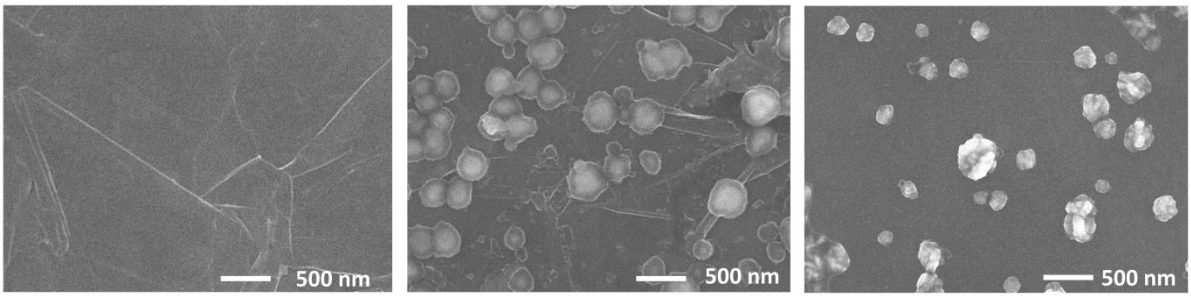

Figure 5.19. SEM images of the graphoil electrode: (a) bare, before electrolysis; with deposited particles after bulk electrolysis at (b) -1.45 $V_{Ag/AgCl}$ and (c) -1.70 $V_{Ag/AgCl}$.

In order to gain more insight into the catalyst decomposition process in water, we have considered the hydrolysis of the imine bonds in the Co^{II}- and Co^{I}-complexes. The later species is found to be more susceptible to water incorporation.[1] Addition of a water molecule to the Co^{I}-complex is found to be energetically uphill by only 6 kcal/mol (**Figure 5.20**) and is feasible in presence of a large excess of water. Moreover, the acid strength of the C=N(OH) function is expected to be greater in more polar aqueous solvent than in acetonitrile and as a result, a greater fraction of the deprotonated form $C=N(O^{-})$ is present in water than in acetonitrile (**Figure 5.21**). Incorporation of a water molecule into the imine bond of this deprotonated ligand backbone is significantly favorable by about 21 kcal/mol (**Figure 5.20**). These results indicate a number of

www.manaraa.com

plausible pathways that can lead to catalyst decomposition and subsequent nanoparticle formation in water and are in agreement with a recent study[1,2,11] of formation of Co-nanoparticle H_2 evolution catalyst by the use of inorganic cobalt salt in neutral water. A detailed study of the mechanism of catalyst decomposition and nanoparticle formation is currently underway.

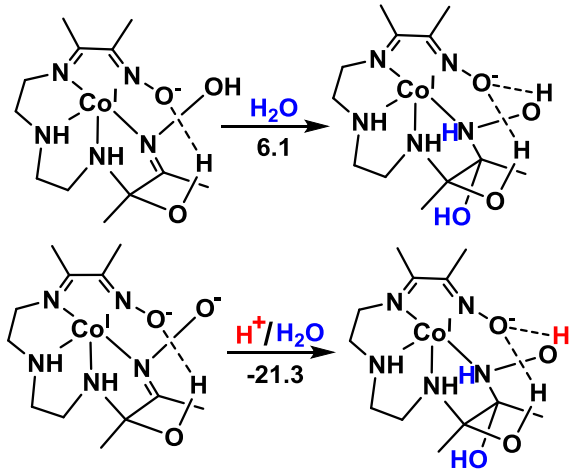

Figure 5.20. Plausible pathways for the decomposition of the catalyst in water: hydrolysis of the imine bond on the oxime ligand of the Co^{I}-complex. The energetics is reported as free energy changes in kcal/mol.

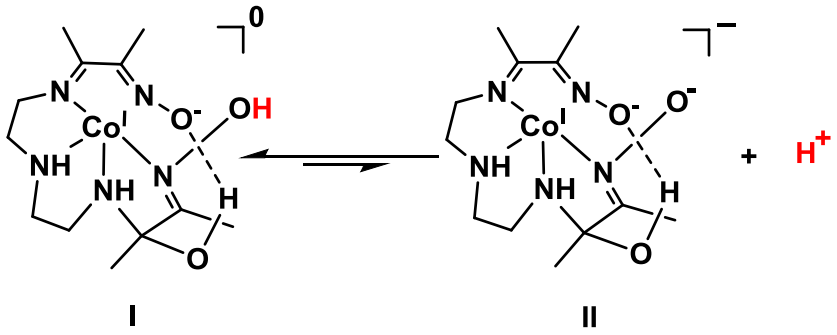

Figure 5.21. The acid-base equilibrium considered for the Co^{I}-complex.

www.manaraa.com

5.4. Conclusions

In conclusion, a new proton reduction catalyst, a Co^{III} complex with pentadentate oxime, was synthesized and thoroughly characterized by multiple physico-chemical techniques. Thermodynamically favorable water incorporation was observed through one of the imine bonds, whereas two OH$^{\cdots}$O and OH$^{\cdots}$Cl hydrogen bonding interactions seem to stabilize the resulting molecular structure. This water-compatible complex exhibited excellent catalytic activity towards weak acids such as acetic acid in CH_3CN with TON of 14.7 in 3 h and overpotential of 0.24 V. The calculated catalytic mechanism suggests a heterolytic pathway for H_2 evolution from the protonation of the Co^{II}–H intermediate generated *in situ*. Protonation on the chloride of $[Co^{II}(HL^{1'})Cl]$ leads to the formation of a cationic $[Co^{II}(HL^{1'})]^+$ complex that undergoes reduction at a potential 240 mV more positive compared to its neutral counterpart, $[Co^{II}(HL^{1'})Cl]$. This phenomenon is consistent with the anodic shift observed experimentally for **1** in presence of acid. The result suggests that the use of pentadentate oxime ligands precludes nanoparticule formation observed for glyoxime-based catalysts in acidic media and Co-hydride formation is favored. Excellent catalytic activity was observed in water with a TON of 5680 after 18 h and overpotential of 0.65 V. This activity is, however, attributed to the formation of cobalt-based nanoparticles resulting from the decomposition of **1** due to the plausible incorporation of water molecule into the imine bond of the ligand.

www.manaraa.com

REFERENCES

1. Anxolabéhère-Mallart, E.; Costentin, C.; Fournier, M.; Nowak, S.; Robert, M.; Savéant, J-M. *J. Am. Chem. Soc.* **2012**, *134*, 6104.
2. Ghachtouli, S. E.; Guillot, R.; Brisset, F.; Aukauloo, A. *Chem. Sus. Chem.* **2013**, *6*, 2226.
3. (a) Bigi, J. P.; Hanna, T. E.; Harman, W. H.; Chang, A.; Chang, C. J. *Chem. Commun.* **2010**, *46*, 958. (b) Sun, Y.; Bigi, J. P.; Piro, N. A.; Tang, M. L.; Long, J. R.; Chang, C. J. *J. Am. Chem. Soc.* **2011**, *133*, 9212. (c) King, A. E.; Surendranath, Y.; Piro, N. A.; Bigi, J. P.; Long, J. R.; Chang, C. J. *Chem. Sci.* **2013**, *4*, 1578. (c) Nippe, M.; Khnayzer, R. S.; Panetier, J. A.; Zee, D. Z.; Olaiya, B. S.; Head-Gordon, M.; Chang, C. J.; Castellano, F. N.; Long, J. R. *Chem. Sci.* **2013**, *4*, 3934. (d) Stubbert, B. D.; Peters, J. C.; Gray, H. B.; *J. Am.Chem.Soc.* **2011**, *133*, 18070. (e) Leung, C. F.; Chen, Y. Z.; Yu, H. Q.; Yiu, S. M.; Ko, C. C.; Lau, T. C. *Int. J. Hydro. Energy* **2011**, *36*, 11640.
4. (a) Lanznaster, M.; Hratchian, H. P.; Heeg, M. J.; Hryhorczuk, L. M.; McGarvey, B. R.; Schlegel, H. B.; Verani, C. N. *Inorg. Chem.* **2006**, *45*, 955. (b) Lanznaster, M.; Heeg, M. J.; Yee, G. T.; McGarvey, B. R.; Verani, C. N. *Inorg. Chem.* **2007,** *46*, 72. (c) Allard, M. M.; Sonk, J. A.; Heeg, M. J.; McGarvey, B. R.; Schlegel, H. B.; Verani, C. N. *Angew. Chem. Int. Ed.* **2012,** *51*, 3178. (d) Wickramasinghe, L. D.; Perera, M. M.; Li, L.; Mao, G.; Zhou, Z.; Verani, C. N. *Angew. Chem. Int. Ed*. **2013**, *52*, 13346. (e) Wickramasinghe, L. D.; Mazumder, S.; Gonawala, S.; Perera, M. M.; Baydoun, H.; Thapa, B.; Li, L.; Xie, L.; Mao, G.; Zhou, Z.; Schlegel, H. B.; Verani, C. N. *Angew. Chem. Int. Ed*. **2014**, *53*, 14462.
5. (a) Allard, M. M.; Xavier, F. R.; Heeg, M. J.; Schlegel, H. B.; Verani, C. N. *Eur. J. Inorg. Chem.* **2012**, 4622. (b) Basu, D.; Allard, M. M.; Xavier, F. R.; Heeg, M. J.; Schlegel, H.

www.manaraa.com

B.; Verani, C. N. *Dalton Trans*. **2015**, *44*, 3454.

6. (a) COSMO V1.61, *Software for the CCD Detector Systems for Determining Data Collection Parameters. Bruker Analytical X-ray Systems, Madison, WI,* **2009**. (b) APEX2 V**2010**.11-3. *Software for the CCD Detector System; Bruker Analytical X-ray Systems, Madison, WI,* **2010**). (c) SAINT V 7.68A *Software for the Integration of CCD Detector System Bruker Analytical X-ray Systems, Madison, WI,* **2010**. (d) SADABS V2008/2 *Program for absorption corrections using Bruker-AXS CCD based on the method of Robert Blessing*; Blessing, R.H. *Acta Cryst.* **1995**, *A51*, 33. (e) Sheldrick, G.M. "A short history of SHELX". *Acta Cryst.* **200**8, *A64*, 112. (f) Dolomanov, O. V.; Bourhis, L. J.; Gildea, R. J.; Howard, J. A. K.; Puschmann, H. OLEX2: *a complete structure solution, refinement and analysis program*. *J. Appl. Cryst.* **2009**, *42*, 339.
7. (a) Parr, R. G.; Yang, W. in *Density-functional theory of atoms and molecules; Oxford University Press: New York*, **1989**. (b) Frisch, M. J.; Trucks, G. W.; Schlegel, H. B. *et al. Gaussian Development Version; Revision H.31ed.; Gaussian, Inc.: Wallingford, CT* **2010.** (c) Perdew, J. P. *Phys. Rev. B* **1986,** *33,* 8822. (d) Becke, A. D. *J. Chem. Phys.* **1993,** *98,* 5648. (e) Perdew, J. P.; Burke, K.; Wang, Y. *Phys. Rev.* **1996,** *54,* 16533. (f) Dolg, M.; Wedig, U.; Stoll, H.; Preuss, H. *J. Chem. Phys*. **1987**, *86*, 866. (g) Francl, M. M.; Petro, W. J.; Hehre, W. J.; Binkley, J. S.; Gordon, M. S.; DeFrees, D. J.; Pople, J. A. *J. Chem. Phys.* **1982**,*77*, 3654. (h) Hariharan, P. C.; Pople, J. A. *Theor.Chim.Acta* **1973**, *28*, 213. (i) Miertus, S.; Scrocco, E.; Tomasi, J. *Chem. Phys.* **1981,** *55,* 117. (j) Scalmani, G.; Frisch, M. J. *J. Chem. Phys.* **2010,** *132,* 114110. (k) Scalmani, G.; Frisch, M. J.; Mennucci, B.; Tomasi, J.; Cammi, R.; Barone, V. *J. Chem. Phys.* **2006,** *124,* 9410. (l) Tomasi, J.; Mennucci, B.; Cammi, R. *Chem. Rev.* **2005**, *105*, 2999.

www.manaraa.com

8. (a) Serbest, K.; Karabokek, S.; Degirmencioglu, I.; Guner, S.; Kormali, F. *Trans. Met. Chem.* **2001**, *26*, 375. (b) Megyes, T.; May, Z.; Schubert, G.; Grosz, T.; Simandi, L. I.; Radnai, T. *Inorg. Chim. Acta* **2006,** *359*, 2329. (c) Szigyarto, I. C.; Simandi, L. I.; Parkanyi, L.**;** Korecz**,** L.; Schlosser, G. *Inorg. Chem.* **2005**, *45*, 7480.
9. Fourmond, V.; Jacques, P. A.; Fontecave, M.; Artero, V. *Inorg. Chem.* **2010**, *49*, 10338.
10. Muckermann, J. T.; Fujita, E. *Chem. Comm.* **2011**, *47*, 12456.
11. Cherdo, S.; Ghachtouli, S. E.; Sircoglou, M.; Brisset, F.; Oriob, M.; Aukauloo, A. *Chem. Commun.* **2014**, *50*, 13514.
12. Hong, D.; Jung, J.; Park, J.; Yamada, Y.; Suenobu, T.; Lee, Y-M.; Nam, W.; Fukuzumi, S. *Energy Environ. Sci.* **2012**, *5*, 7606.

www.manaraa.com

CHAPTER 6

LIGAND TRANSFORMATIONS AND EFFICIENT PROTON/WATER REDUCTION WITH COBALT CATALYSTS BASED ON PENTADENTATE PYRIDINE-RICH ENVIRONMENTS

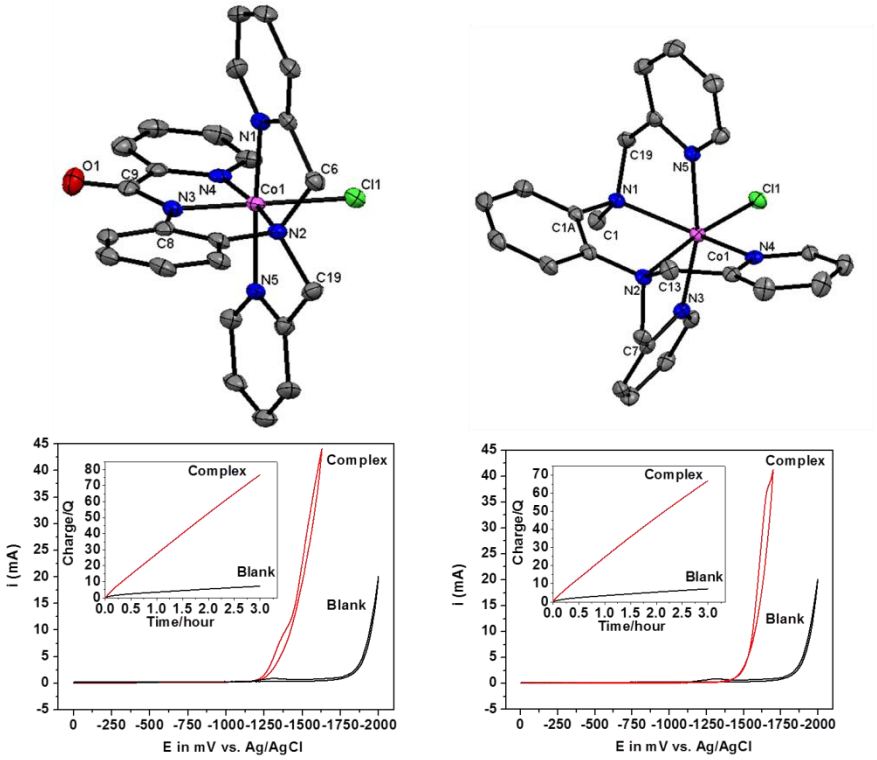

www.manaraa.com

CHAPTER 6

LIGAND TRANSFORMATIONS AND EFFICIENT PROTON/WATER REDUCTION WITH COBALT CATALYSTS BASED ON PENTADENTATE PYRIDINE-RICH ENVIRONMENTS

Portions of the text in this chapter were reprinted or adapted with permission from: Basu, D.; Mazumder, S.; Shi, X.; Baydoun, H.; Niklas, J.; Poluektov, O.; Schlegel, H. B.*; Verani, C. N.* *Angew. Chem. Int. Ed.* **2015**, *54*, 2105. All rights to the work are retained by the authors and any reuse requires permission of the authors.

6.1. Introduction

Pentadenate nitrogen-rich ligands are known to stabilize lower oxidation state of the cobalt, which can act as proton/water reduction catalysts.[1] Recent results point out the importance of cobalt complexes of pyridine-containing ligands in proton reduction, where complexes of imino-, di-, tetra- and pentapyridine ligands have been investigated.[1] Several of these systems are also water-soluble, and therefore relevant for direct water reduction.

The Verani group has a long-standing interest in redox-active phenylenediamine-bridged pentadentate [N_2O_3] ligands capable of forming stable first-row transition metal complexes.[2] Thus far we emphasized phenolate-rich environments, and observed a facile conversion from the secondary amine to imine. While Fe^{III} species with this ligand environment have been used in current rectifying devices,[2e,f] Co^{III} complexes of this nature are electrocatalysts for proton reduction in trifluoroacetic acid/MeCN.[2g] However, these species have intrinsic negative overpotentials, and we hypothesized that similar [$N_2N^{py}_3$] pentadentate pyridine-rich environments would yield affordable catalysis and water solubility. Such systems allow the proton to bind to the sixth position of the metal in a framework that is potentially redox-active and π-acceptor, thus contributing to the stabilization of the Co^{I} state.

www.manaraa.com

Thus, we synthesized a series of Co(III)/Co(II) complexes based on pentadentate phenylenediamine bridged tris-pyridine [$N_2N^{py}_3$] type ligands (**Scheme 6.1**), and their respective redox, electronic, catalytic, and mechanistic properties were thoroughly investigated towards proton reduction. A ligand centered reactivity was observed in the ligand framework for the N-H containing ligand (HL^1). Therefore, a methyl group was incorporated in the ligand framework (MeL^2) to inhibit this kind of insertion. There are a few complexes in this series which are both robust and water soluble, and have been tested towards water reduction activity.

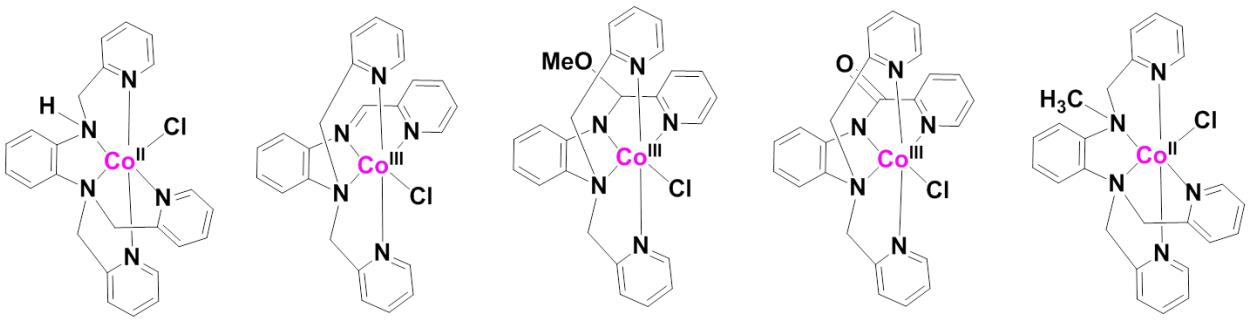

1 2 3 4 5

Scheme 6.1. Cobalt complexes of pyridine-rich ligands.

6.2. Experimental

6.2.1. X-ray structural determination

All the data were collected on a Bruker APEX-II Kappa geometry diffractometer with Mo radiation and a graphite monochromator using a Bruker CCD (charge coupled device) based diffractometer equipped with an Oxford Cryostream low-temperature apparatus. The data was measured at a temperature of 100 K. The structures were solved by the direct method using the SHELXS-97 program which is part of APEX II[3a] and refined by least squares method on F^3, SHELXL-97,[3b] which is incorporated in OLEX2.[3c] All hydrogen atoms were placed at calculated positions.

www.manaraa.com

Single crystals of **2**: one molecule of **2**, two perchlorate counter ion, one water molecule, and one methanol molecule were found in the asymmetric unit. The structure was solved with a resolution of 0.74 Å in space group $P2_1$. All non-hydrogen atoms were refined anisotropically.

Single crystals of **3**: one molecule of **3**, one perchlorate counter ion, and one methanol molecule were found in the asymmetric unit. The structure was solved with a resolution of 0.85 Å in space group P-1. All non-hydrogen atoms were refined anisotropically. Carbon C25 of the methanol molecule was at the corner of the asymmetric unit cell, therefore it was not possible to place hydrogen atoms at calculated positions for that atom.

Single crystals of **4**: one molecule of **4** and one perchlorate counter ion were found in the assymetric unit. The structure was solved with a resolution of 0.82 Å in space group $Pna2_1$. All non-hydrogen atoms were refined anisotropically, however the perchlorate counter ion was found to be disordered, as such partial occupancies for O3 and O4 had to be assigned.

Single crystals of **5**: Two molecules of **5** and two perchlorate counter ions were found in the asymmetric unit. The structure was solved with a resolution of 0.76 Å in space group $P2_1/C$. All non-hydrogen atoms were refined anisotropically.

Table 6.1. Important bond lengths for **2** – **5**.

2		**3**		**4**		**5**	
Co1-N2	1.947(7)	Co1-N2	1.945(3)	Co1-N1	1.949(3)	Co1-N1	2.2027(16)
Co1-N3	1.898(7)	Co1-N3	1.941(3)	Co1-N2	1.949(2)	Co1-N2	2.1862(15)
Co1-N4	1.943(7)	Co1-N4	1.924(3)	Co1-N3	1.883(2)	Co1-N3	2.1429(16)
Co1-N5	1.948(7)	Co1-N5	1.884(3)	Co1-N4	1.944(2)	Co1-N4	2.1000(16)
Co1-N20	1.927(6)	Co1-N6	1.923(3)	Co1-N5	1.942(2)	Co1-N5	2.2094(16)
Co1-Cl1	2.253(3)	Co1-Cl2	2.2827(10)	Co1-Cl1	2.2589(8)	Co1-Cl1	2.3307(5)
N3-C5	1.280(11)	N5-C26	1.416(5)	N3-C9	1.350(4)	N1-C19	1.483(2)
N4-C8	1.517(10)	N2-C11	1.501(5)	N2-C6	1.502(4)	N2-C7	1.488(2)
N4-C17	1.521(10)	N2-C5	1.496(5)	N2-C19	1.502(4)	N2-C13	1.485(2)
				C9-O1	1.233(3)		

www.manaraa.com

Table 6.2. Important crystallographic parameters for **2 – 5**.

	2	**3**	**4**	**5**
Empirical formula	$C_{25}H_{27}Cl_3CoN_5O_{10}$	$C_{25.5}H_{25}Cl_2CoN_5O_6$	$C_{24}H_{20}Cl_2CoN_5O_5$	$C_{50}H_{50}Cl_4Co_2N_{10}O_8$
Formula weight	722.80	627.35	589.29	1178.66
Temperature (K)	100	100.1	100.1	100.1
Wavelength (Å)	0.71073	0.71073	0.71073	0.71073
Crystal system, space group	Monoclinic, $P2_1$	Triclinic, P-1	Orthorhombic, $Pna2_1$	Monoclinic, $P2_1/c$
a (Å)	10.014(10)	8.8179(7)	18.9149(14)	22.1651(12)
b (Å)	15.255(18)	9.8101(7)	14.3671(11)	13.9135(6)
c (Å)	10.462(10)	15.1228(12)	8.8288(6)	16.2600(9)
α (°)	90	101.482(4)	90	90
β (°)	115.626(14)	94.105(4)	90	90.159(2)
γ (°)	90	90.908(4)	90	90
Volume ($Å^3$)	1441(3)	1278.11(17)	2399.2(3)	5014.5(4)
Z	2	2	4	4
Calculated density (Mg/m^3)	1.666	1.630	1.631	1.561
Absorption coefficient (mm^{-1})	0.940	0.934	0.986	0.941
F (000)	740	645.6	1204.0	2424.0
R(F) (%)	7.06	5.24	3.38	3.30
R_w(F) (%)	12.93	6.26	3.95	4.81

6.2.2. Computational methods

All the calculations were performed using Density Functional Theory (DFT)[4a] with a development version of Gaussian,[4b] using B3LYP[4c,d] functional with SDD basis set[4e] on cobalt and 6-31G(d,p)[4f,g] basis on the other atoms. All the optimized structures were confirmed as minima by analyzing the harmonic vibrational frequencies. Solvation effects (in acetonitrile and methanol) were accounted for using the implicit SMD[4h] continuum solvation model and were included during structure optimization. Wave functions were tested for self-consistent field stability.[4i-k] Isosurface plots of spin densities were visualized using GaussView.[4l] The literature value[4m] of -266.5 kcal/mol is used for the free energy of proton in acetonitrile solution. The calculation of the reduction potentials of the complexes included zero-point energy and thermal corrections and standard thermodynamic equation $\Delta G = -nFE$ was used. The calculated

www.manaraa.com

potentials were referenced to a calculated value of $E_{1/2}$ = 4.043 V for the ferrocene/ferrocenium couple under our level of theory.

6.2.3. Electron paramagnetic resonance (EPR) spectra measurement

All samples were prepared under a nitrogen atmosphere. A 10^{-3} M solution of complex **5** was filled in suprasil quartz capillaries with 4 mm outer diameter and frozen in liquid nitrogen. Continuous wave (cw) X-band (9-10 GHz) EPR experiments were carried out with a Bruker ELEXSYS E580 EPR spectrometer (Bruker Biospin, Rheinstetten, Germany), equipped with a Bruker ER 4102ST resonator or a Bruker ER 4122SHQ resonator. The temperature was controlled using a helium gas-flow cryostat (ICE Oxford, UK) and an ITC (Oxford Instruments, UK). Data processing was done using Xepr (Bruker BioSpin, Rheinstetten) and Matlab 7.11.2 (The MathWorks, Inc., Natick) environment. Simulations were performed using the EasySpin software package (version 4.5.5).[5]

6.2.4. Catalytic activity

Proton reduction electrocatalysis was tested for **4** and **5** via cyclic voltammetry in presence of acetic acid (HOAc, pKa: 22.3 in CH_3CN) with tetra-butyl ammonium hexafluorophosphate ($TBAPF_6$) as supporting electrolyte. For bulk electrolysis, the main chamber was filled with an electrolyte solution and proton source ($TBAPF_6$: 1.56 g; HOAc: 0.024 g [0.4 mmol], 20 mL acetonitrile) and the glass-fitted chamber was filled with another electrolyte solution ($TBABF_4$: 0.39 g; 5 mL acetonitrile). Bulk electrolysis was conducted with catalyst (0.004 mmol) in acetonitrile (CH_3CN) for 180 minutes at -1.7 $V_{Ag/AgCl}$ and the head space gas (100 µL) was injected into the GC to record the amount of dihydrogen produced. After the background subtraction, the turnover number was calculated as the ratio of the moles of dihydrogen produced over the moles of catalyst used. Faradaic efficiency was calculated from the gas chromatography

www.manaraa.com

measurements. For water reduction, similar procedure has been followed. For controlled potential experiment, the main chamber was filled with 20 mL of phosphate buffer solution whereas the glass-fitted chamber was filled with 5 mL of solution. Bulk electrolysis at -1.7 $V_{Ag/AgCl}$ was applied for complex **1** to generate H_2. The typical concentration of catalyst for water reduction experiment is 0.0002 mmol.

6.2.5. Synthetic procedures

Syntheses: Ligand HL^1 was synthesized as per literature procedure.[6]

MeL^2 was synthesized by following the same procedure however using N-methyl-1,2-phenylene diamine (3 mmol, 0.366 g) instead of 1,2-phenylenediamine. The final product was extracted to dichloromethane layer from water followed by column chromatography with neutral alumina in the presence of dichloromethane (CH_2Cl_2): ethyl acetate (EtOAc) (1:1) mixture. The 2nd fraction obtained after column was rotary evaporated to dryness and dried under vaccum.

Yield: 40 %. IR (KBr, cm^{-1}) 3052 (w), 3007 (w) (Aromatic-CH); 2992 (w), 2954 (w), 2878 (w), 2839 (w) (aliphatic CH); 1589 (s) (C=N); 1432 (s) (C=C). ^{1}H-NMR [400MHz, $CDCl_3$, 300K] δ/ppm = 2.863 [s, 3H (CH_3)]; 4.665 [s, 4H (CH_2)]; 4.737 [s, 2H (CH_2)]; 6.884 [d, 1H (aryl)]; 6.948 [q, 2H (aryl)]; 7.018 [d, 1H (aryl)]; 7.115 [t, 3H (aryl)]; 7.199 [d, 3H (aryl)]; 7.511 [t, 3H (aryl)]; 8.5 [d, 2H (aryl)]; 8.552 [d, 1H (aryl)]. ESI pos. in MeOH: m/z = 396.2 for $[MeL^2 + H^+]^+$.

Complex syntheses (**1** - **4**): Method (a) HL^1 (1 mmol, 0.381 g) was dissolved in 20 mL methanol. $CoCl_2.6H_2O$ (1 mmol, 0.238 g) in 5 mL methanol was added dropwise to the solution. The solution turns pinkish (Complex (**1**)) and was stirred for 2-3 hours, where the solution then turns greenish. Dry oxygen gas was purged through the solution for 30 minutes. Anhydrous $NaClO_4$ (4 mmol, 0.488 g) in 5 mL methanol was added to the solution and stirred for 1-2 hours. After the reaction, the volume of solution was reduced to 5 mL. A mixture of orange (**2**) and green (**3**)

www.manaraa.com

crystals were obtained after 2-3 days. Brownish yellow crystals of complex (**4**) was formed after 5-7 days if we keep the crystals a long time in solution or recrystallize it from EtOH/acetone (1:1) or CH_3CN/diethyl ether (1:1) mixture.

Method (b) HL^1 (1 mmol, 0.381 g) was dissolved in 20 mL acetone. $CoCl_2.6H_2O$ (1 mmol, 0.238 g) in 7 mL acetone was added dropwise to the solution. The solution turns pink (Complex (**1**)) and was stirred for 2-3 hours. The solution turns greenish brown. Dry oxygen gas purged through the solution for 30 minutes. Anhydrous $NaClO_4$ (4 mmol, 0.488 g) in water (3 mL) was added to the solution and further stirred for 1-2 hours. After the reaction, the volume of solution was reduced to 5 mL. Brownish yellow crystals of (**4**) were obtained after few days.

Complex (**1**): Yield: 75 %. IR (KBr, cm^{-1}) 3154 (w) (NH); 3105 (w) (Aromatic-CH); 2922 (w) (aliphatic CH); 1607 (m) (C=N); 1435 (m) (C=C); 1094 (s) (ClO_4^-). Anal. Calcd for **1**.H_2O: $C_{24}H_{25}Cl_2CoN_5O_5$: C: 48.58; H: 4.25; N: 11.80; Found: C: 48.76; H: 4.12; N: 11.32.

Complex (**2**): X-ray quality crystals were obtained from MeOH. It was further recrystallized from EtOH to generate purified product in one day. Yield: 45 %. IR (KBr, cm^{-1}) 3099 (w), 3033 (w) (Aromatic-CH); 2934 (w) (aliphatic CH); 1607 (m) (C=N); 1444 (m) (C=C); 1092 (s) (ClO_4^-). ^{1}H-NMR [400MHz, CD_3CN, 300K] δ/ppm = 5.230 [d, 2H (CH_2)]; 5.885 [d, 2H (CH_2)]; 6.881 [d, 2H (aryl)]; 7.337 [t, 2H (aryl)]; 7.536 [d, 2H (aryl)]; 7.628 [t, 1H (aryl)]; 7.874 [t, 2H (aryl)]; 7.976 [t, 2H (aryl)]; 8.282 [t, 1H (aryl)]; 8.374 [d, 1H (aryl)]; 8.679 [d, 1H (aryl)]; 8.745 [t, 1H (aryl)]; 9.041 [s, 1H (N=CH)]; 9,665 [d, 1H (aryl)]. ESI pos. in MeOH: m/z = 473.0818 for $[Co^{III}(L'^1)(Cl)]^+$. Anal. Calcd for **2**.CH_3CH_2OH: $C_{26}H_{27}Cl_3CoN_5O_9$: C: 43.44; H: 3.79; N: 9.74; Found: C: 43.94; H: 3.74; N: 9.44.

Complex (**3**): X-ray quality crystals were obtained from MeOH. Yield: 45 %. IR (KBr, cm^{-1}) 3077 (w) (Aromatic-CH); 2976 (w), 2940 (w), 2819 (w) (aliphatic CH); 1615 (m) (C=N); 1435

www.manaraa.com

(w) (C=C); 1092 (s) (ClO_4^-). ESI pos. in MeOH: m/z = 504.1004 for $[Co^{III}(^{OMe}L'^{1})(Cl)]^+$. Anal. Calcd for **3**.$H_2O$: $C_{25}H_{26}Cl_2CoN_5O_6$: C: 48.25; H: 4.21; N: 11.25; Found: C: 48.22; H: 4.19; N: 11.50.

Complex (**4**): X-ray quality crystals were obtained from CH_3CN/diethyl ether (1:1). Yield: 70 %. IR (KBr, cm^{-1}) 3119 (w), 3084 (w), 3041 (w) (Aromatic-CH); 2940 (w) (aliphatic CH); 1650 (s) (C=O); 1600 (s) (C=N); 1450 (m) (C=C); 1092 (s) (ClO_4^-). ^{1}H-NMR [400MHz, CD_3CN, 300K] δ/ppm = 5.150 [d, 2H (CH_2)]; 5.882 [d, 2H (CH_2)]; 6.837 [d, 2H (aryl)]; 7.254 [t, 4H (aryl)]; 7.444 [d, 2H (aryl)]; 7.880 [t, 2H (aryl)]; 8.032 [t, 1H (aryl)]; 8.110 [t, 1H (aryl)]; 8.840 [d, 1H (aryl)]; 8.574 [t, 1H (aryl)]; 8.653 [m, 1H (aryl)]; 9.822 [d, 1H (aryl)]. ESI pos. in MeOH: m/z = 488.0688 for $[Co^{III}(^{C=O}L'1)(Cl)]^+$. Anal. Calcd for **4**.$2H_2O$: $C_{24}H_{24}Cl_2CoN_5O_7$: C: 46.17; H: 3.87; N: 11.22; Found: C: 45.77; H: 3.46; N: 10.91.

Complex (**5**): MeL^2 (1 mmol, 0.395 g) was dissolved in 20 mL methanol. $CoCl_2.6H_2O$ (1 mmol, 0.238 g) in 5 mL methanol was added dropwise to the solution. The solution turns pinkish and was stirred for 2-3 hours. Dry oxygen gas purged through the solution for 30 minutes. Anhydrous $NaClO_4$ (4 mmol, 0.488 g) in 5 mL methanol was added to the solution and further stirred for 1-2 hours. After the reaction, the volume of solution was reduced to 5 mL. A pinkish colored X-ray quality crystals were obtained after few days. Yield: 90 %. IR (KBr, cm^{-1}) 3069 (w); 3034 (w) (Aromatic-CH); 3004 (w), 2970 (w), 2941 (w) (aliphatic CH); 1607 (s) (C=N); 1450 (s) (C=C); 1098 (s) (ClO_4^-). ESI pos. in MeOH: m/z = 489.1130 for $[Co^{II}(MeL^2)(Cl)]^+$. Anal. Calcd for **5**.H_2O: $C_{25}H_{27}Cl_2CoN_5O_5$: C: 49.44; H: 4.48; N: 11.53; Found: C: 49.76; H: 4.19; N: 11.56.

www.manaraa.com

6.3. Results and discussions

6.3.1. Syntheses and characterizations

The $[N_2N^{py}_3]$ ligand L^{1H} was obtained by treatment of phenylenediamine with picolyl chloride in water and in the presence of sodium hydroxide and hexadecyl trimethyl ammonium chloride.[6] The purified ligand was treated with $CoCl_2.6H_2O$ in methanol under aerobic conditions for 3 h and followed by counterion exchange with $NaClO_4$. An initial pink solution containing $[Co^{II}(L^{1H})Cl]^{2+}$ turned greenish within minutes and yielded a crystalline mixture of an orange $[Co^{III}(L^{1C=N})Cl](ClO_4)_2$ (**2**) and a green $[Co^{III}(L^{1OMe})Cl]$ ClO_4 (**3**) species after 2 days (**Scheme 6.2**). When the mother liquor was allowed to stand for 5-7 days, light-orange crystals of $[Co^{III}(L^{1C=O})Cl]ClO_4$ (**4**) were obtained. Identeical results were obtained by recrystallizing the mixture of **2** and **3** from either MeCN/diethyl ether (1:1) or ethanol/acetone (1:1). Furthermore, species **4** can be generated directly upon complexation of L^{1H} and $CoCl_2.6H_2O$ in acetone/water (1:1) at RT after 5-7 days under aerobic condition.

www.manaraa.com

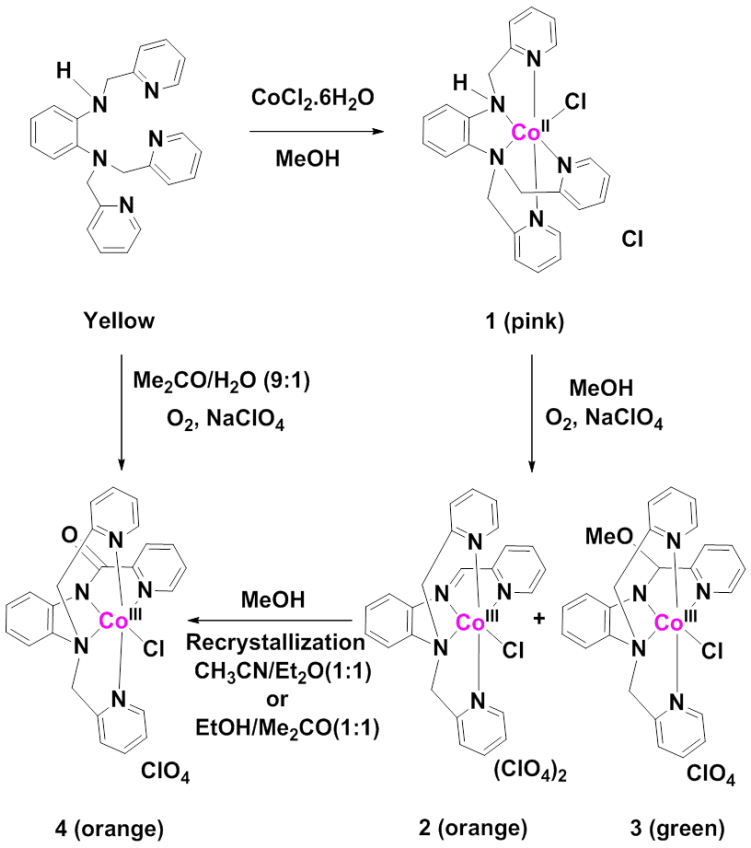

Scheme 6.2. Synthetic scheme of cobalt complexes **1**, **2**, **3**, and **4**.

Complexes **1**-**4** have been characterized spectroscopically by FT-infrared, and ^{1}H-NMR methods (for **2**-**4**) as well as by ESI mass spectrometry and elemental analyses. The presence of perchlorate counterion was confirmed for **2**-**4** from the very broad peak in the FTIR spectra at 1090 cm^{-1}. Well-defined and sharp peaks in the ^{1}H-NMR spectra in CD_3CN confirm the diamagnetic nature ($3d^6$ $^{LS}Co^{III}$) of these complexes (**2**-**4**). The ^{1}H-NMR spectra of selected complexes are shown in **Figure 6.1**. ESI-Mass spectra exhibited molecular ion peaks for complexes **2**-**4** in methanol (**Figure 6.2**)

www.manaraa.com

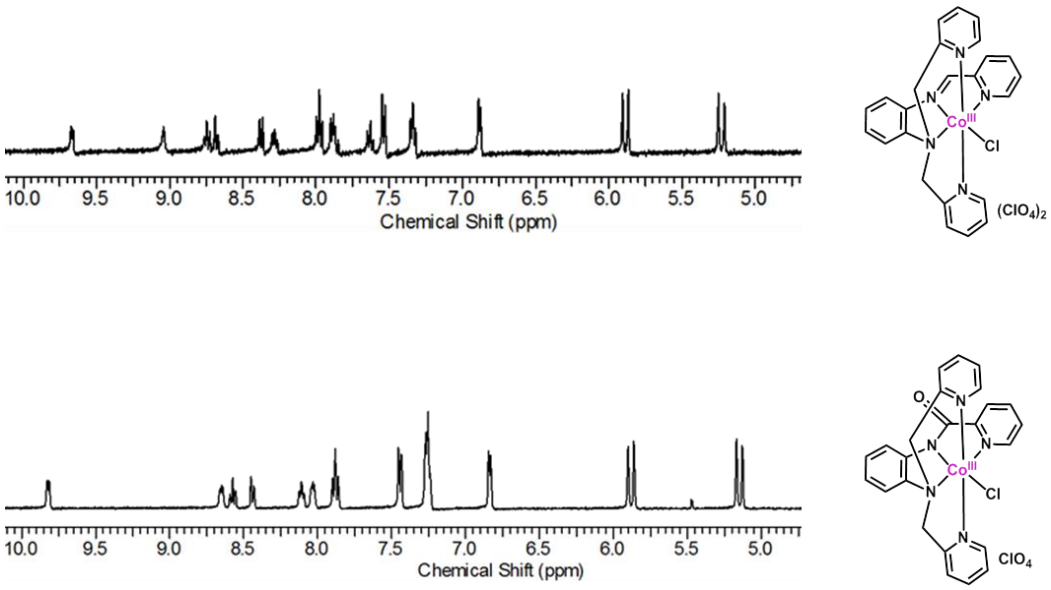

Figure 6.1. ^{1}H-NMR spectra of **2** and **4** (top to bottom) in CD_3CN.

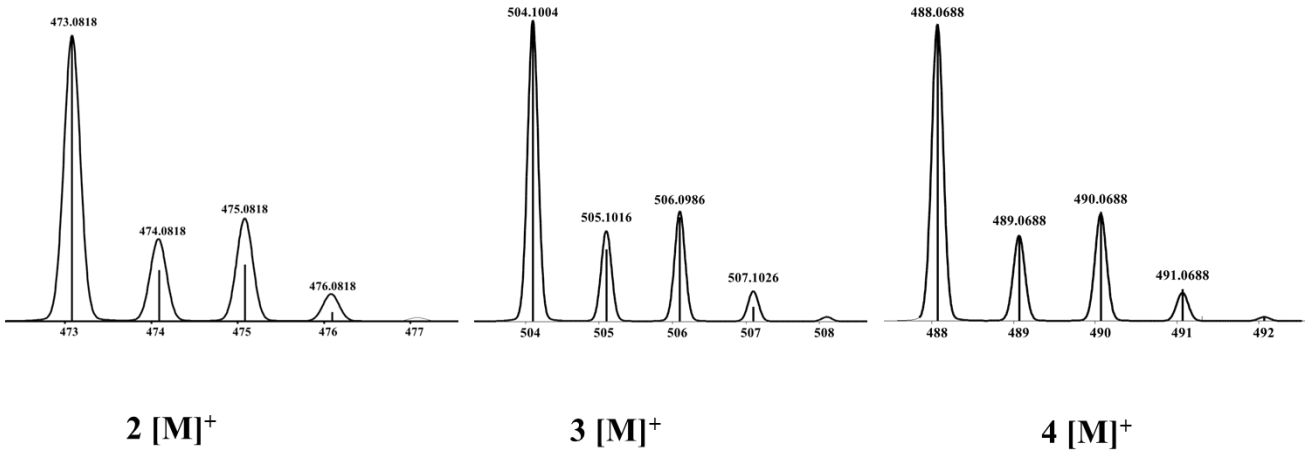

Figure 6.2. Experimental (bars) and simulated (line) isotopic distribution for the molecular ions of the complexes **2** ($[Co^{III}(L'^{1})(Cl)]^{+}$), **3** ($[Co^{III}(^{OMe}L'^{1})(Cl)]^{+}$), and **4** ($[Co^{III}(^{C=O}L'1)(Cl)]^{+}$) (left to right) in CH_3OH.

www.manaraa.com

In order to prevent the initial oxidation of L^{1H} into its imine counterpart, an N-methylamine derivative ligand L^2 was designed. Synthesis of the ligand was performed by the reaction of N-methyl phenylenediamine with picolyl chloride in the presence of NaOH and hexadecyl trimethyl ammonium chloride (**Figure 6.3**). The corresponding ^{1}H-NMR spectra of the ligand in $CDCl_3$ is shown in **Figure 6.3**.

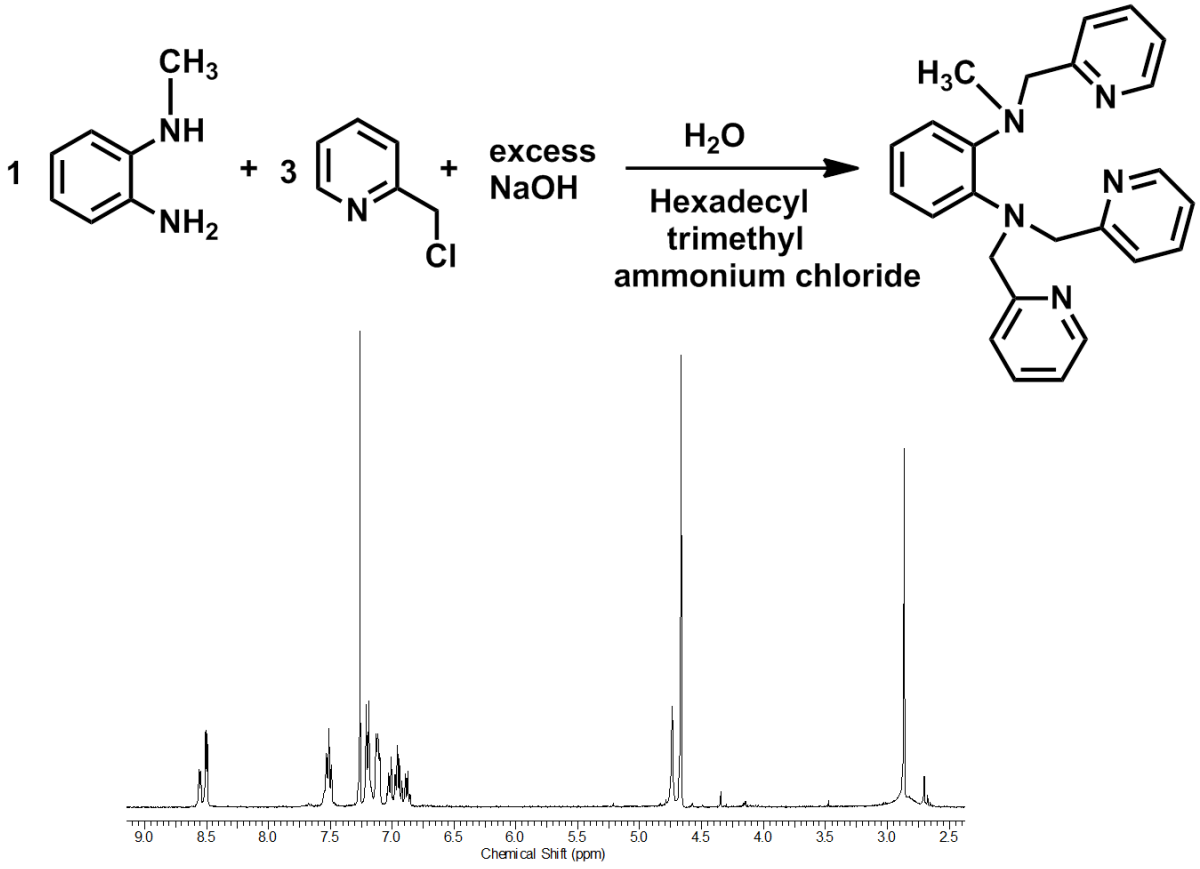

Figure 6.3. Synthesis of the ligand MeL^2 and its ^{1}H-NMR spectra in $CDCl_3$.

This new ligand allowed for the complexation of a $3d^7$ Co^{II} from $CoCl_2.6H_2O$ in methanol under aerobic conditions without the previously observed oxidation to imine. The pinkish colored $[Co^{II}(L^2)Cl]ClO_4$ (**5**) was isolated by counterion exchange with $NaClO_4$ after 2 h (**Figure 6.4**).

www.manaraa.com

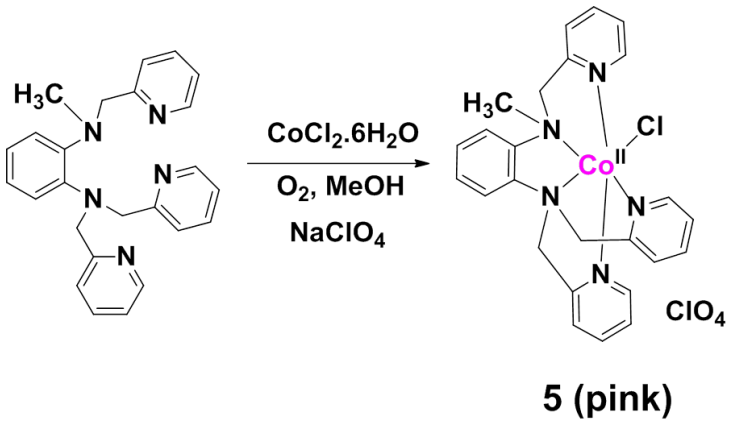

Figure 6.4. Synthetic Scheme for Co^{II} complex **5** and its ORTEP representation at 50% ellipsoid probability.

The complex was also characterized by FTIR, ESI-MS, and elemental analysis. FTIR spectra exhibited broad peak at 1098 cm^{-1} due to the presence of ClO_4^- counterion. ESI mass spectra revealed the molecular ion peak in methanol (**Figure 6.5**). DFT calculations predict that the high-spin (S = 3/2) configuration is more stable than the low-spin (S = 1/2) one by 13.7 kcal/mol. Indeed, use of ^{1}H-NMR yielded broad and shifted peaks indicating a paramagnetic nature for the complex.

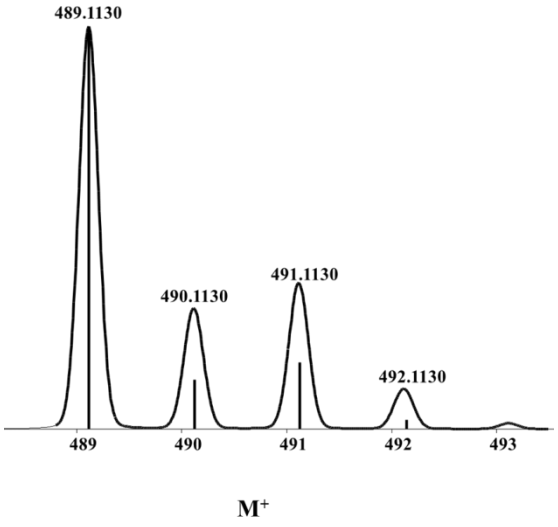

Figure 6.5. Experimental (bars) and simulated (line) isotopic distribution for the molecular ion of the complex **5** ($[Co^{II}(MeL^2)(Cl)]^+$) in CH_3OH.

www.manaraa.com

6.3.2. Molecular structures

Figure 6.6 shows the ORTEP representations of crystals for **2**, **3** and **4,** and relevant bond lengths and crystallographic parameters are summarized in **Tables 6.1** and **6.2**. These complexes are pseudo-octahedral in which two N_{amine}, one N_{py}, and one Cl define the basal plane and two N_{py} atoms occupy the axial positions. The amine moiety of the ligand framework is oxidized to imine in **2**, as observed by a shorter 1.28 Å C(5)-N(3) bond than a regular C–N bond length (~1.5 Å). Species **3** is obtained *via* addition of a methoxide to C(26) from the solvent methanol. The C(26)–N(5) bond increases from 1.28 Å in **2** to 1.42 Å and N(5) becomes formally negative. Both the imine and methoxy functionalities in **2** and **3** are converted into an amide moiety in **4.** The N(3) amide atom is also negatively charged, and coordinated to Co(III) at 1.88 Å is the strongest among all the Co–N bonds of the species. The C(9)=O(1) moiety is 1.23 Å long and the C(9)–N(3) distance at 1.35 Å is shorter than a regular C–N bond, suggestive of significant π-conjugation in the ligand framework.

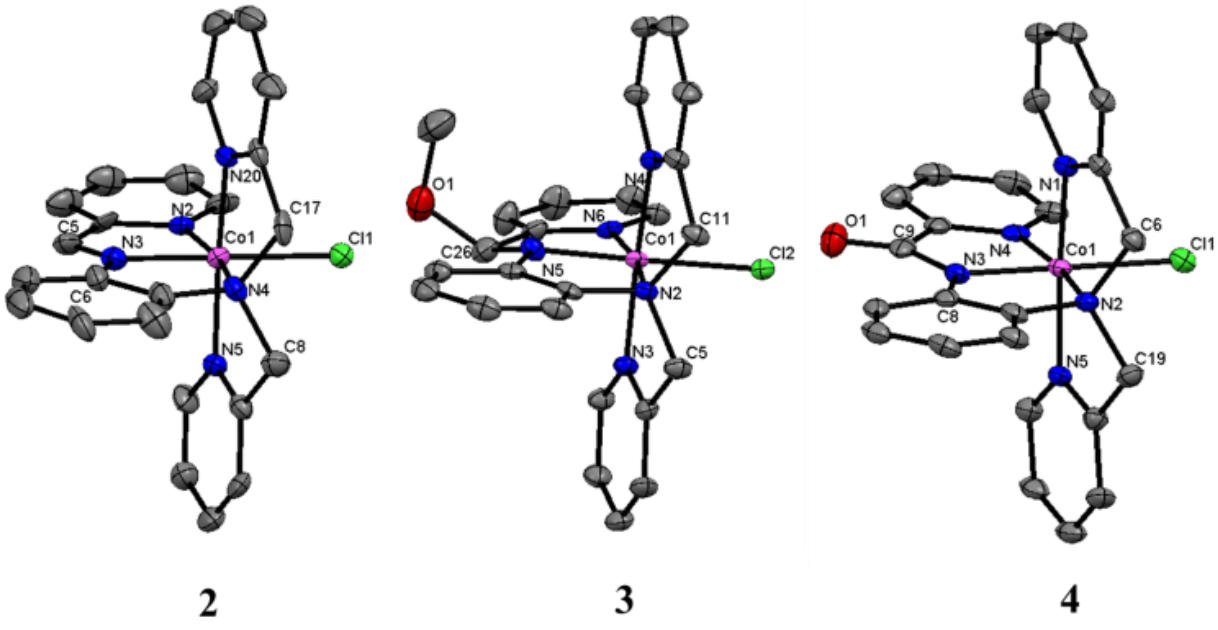

2 **3** **4**

Figure 6.6. ORTEP representations of **2-4** at 50% probability.

www.manaraa.com

The X-ray structure of **5** (**Figure 6.7**) is also pseudo-octahedral, and shows the Co–Cl bond at 2.33 Å, thus longer than those found in **2-4.**

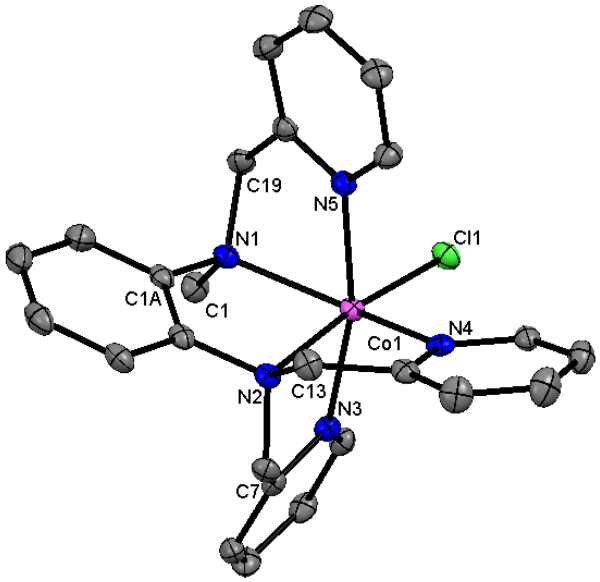

Figure 6.7. The ORTEP representation of complex **5** at 50% ellipsoid probability.

Inspection of the geometries of the Co^{III} **2** and the Co^{II} **5** complexes reveals a change in the conformation of the ligand framework. This reversal of the conformational stability is imposed by the change of the ligand from imine to N-methylamine, rather than by the change of the oxidation state from Co^{III} to Co^{II} (**Figure 6.8, 6.9**). Inspection of the geometries of complexes **2** and **5** reveals a change in the conformation of the ligand framework and a reversal of the conformational stability (**2**(**i**) to **5**(**ii**)) is found as illustrated in **Figure 6.8**. Complexes **2** and **5** have different functionalities (imine *vs.* N-methylamine) in the ligand framework and different oxidation states (Co^{III} *vs.* Co^{II}) of the metal center. In order to evaluate the contribution of the oxidation state and ligand functionality towards the reversal of the conformational stability, conformational isomers were studied for four species, Co^{III}-imine, Co^{III}-amine, Co^{III}-N-methylamine and Co^{II}-N-methylamine (**Figure 6.8**). Species **2** with a planar, conjugated and rigid imine ligand framework prefers conformer **i** as the other conformer **ii** requires the imine

www.manaraa.com

bond to be twisted and it deviates from the planarity. Saturating the rigid imine backbone to more flexible amine reduces the strain in conformer **ii** while decreases the stability of conformer **i** because of loss of the conjugation. As a result, the energy difference between the two conformers decreases from 31.9 in **2** to 2.7 kcal/mol in **6**. Introducing a N-methyl moiety makes conformer **i** sterically more crowded than **ii** as the former has three phenyl moieties (**A**, **B** and **C**) close to the methyl function while the later has only two (**A** and **D**). Consequently, **ii** becomes more stable than **i** for **7** and the change of the oxidation state of cobalt cannot affect this stability order as **5(ii)** is found to be lower in energy than **5(i)**. Therefore, the reversal of the conformational stability from **2(i)** to **5(ii)** is a result from the contribution of the ligand functionality rather than the oxidation state of cobalt center.

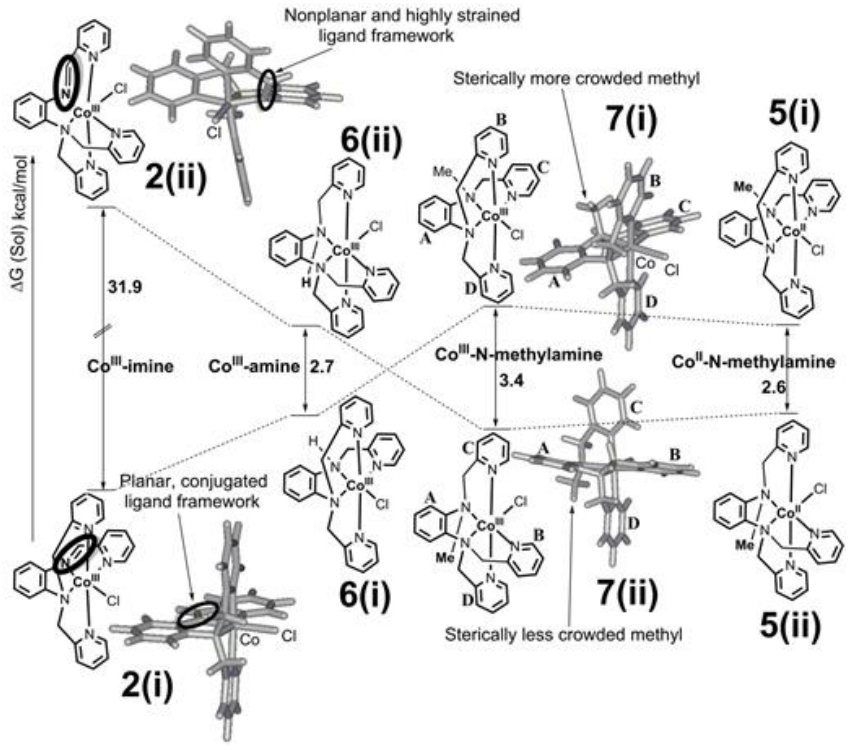

Figure 6.8. Relative energetics of the conformational isomers of Co^{III}-imine, Co^{III}-amine, Co^{III}-N-methylamine and Co^{II}-N-methylamine complexes in MeOH. Reversal of the conformational stability (i to ii) from Co^{III}-imine to Co^{II}-N-methylamine species is imposed by the change of the ligand from imine to N-methylamine rather than by the change of the oxidation state of the metal center from Co^{III} to Co^{II}.

www.manaraa.com

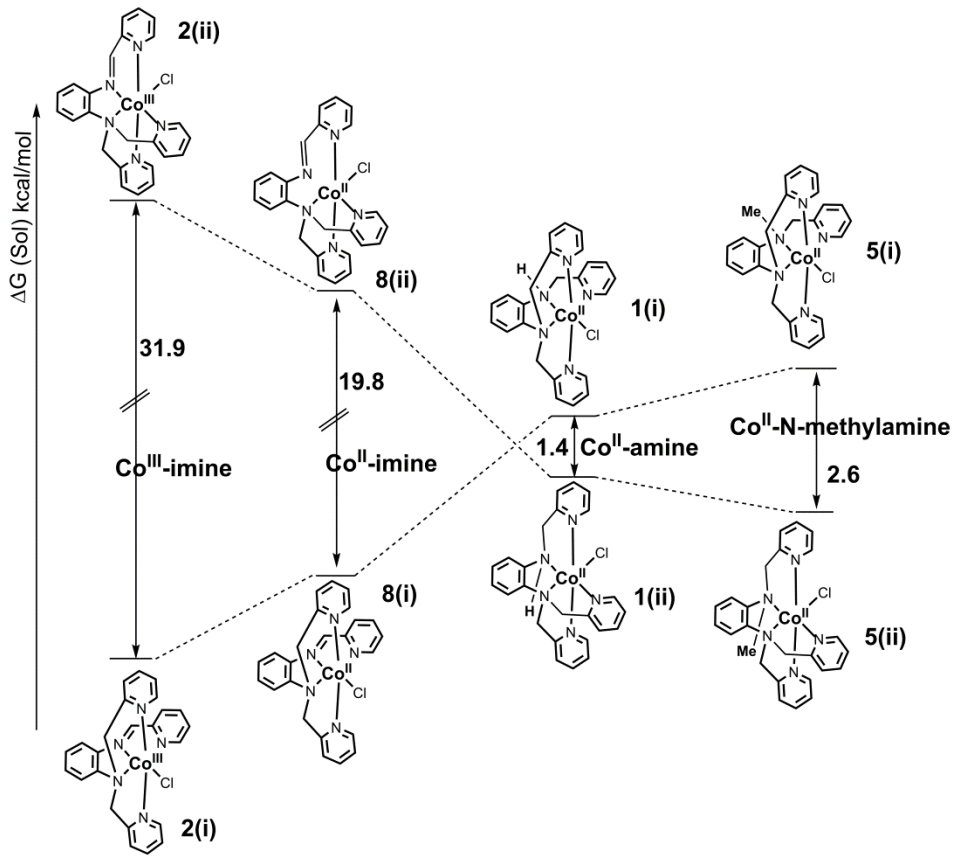

Figure 6.9. Relative energetics of the conformational isomers of Co^{III}-imine, Co^{II}-imine, Co^{II}-amine and Co^{II}-N-methylamine complexes in MeOH. Reversal of the conformational stability (**i** to **ii**) from Co^{III}-imine to Co^{II}-N-methylamine species is imposed by the change of the ligand from imine to amine rather than by the change of the oxidation state of the metal center from Co^{III} to Co^{II}.

6.3.3. Reactivity studies towards amide formation

Isolation of the methoxy species **3** demonstrates the susceptibility of the imine function in **2** to undergo facile nucleophilic attack from the solvent. Similarly, in order to explain the amide conversion from **2** to **4**, a hydroxy intermediate must be invoked by addition of adventitious water present in the solvent to the imine moiety of **2**. This step has been documented.[7] A detailed density functional theory (DFT)[8] study was also performed to evaluate details of the hydroxyl to amide conversion mechanism (**Figure 6.10**). Calculations indicate that the transformation

www.manaraa.com

requires atmospheric $^3O_2$ to react with the C–H function of the intermediate hydroxyl complex. The C–H hydrogen abstraction event is rate-limiting and nearly isoenergetic as the resulting intermediate (**I**) is about 2 kcal/mol higher than the starting hydroxyl complex. In species **I** the hydroperoxo radical (·OOH) is weakly bonded to the hydroxyl and the unpaired electron generated on the ligand is transferred to the metal center reducing it to Co^{II}. Thus, the metal center helps stabilize the radical intermediate (**I**) and makes the C–H hydrogen removal event nearly isoenergetic.[7] An intersystem crossing (triplet to singlet surface) from species (**I**) followed by the removal of the hydroxyl hydrogen by the hydroperoxo radical gives rise to the amide complex **4** and the overall process is favored by about 38 kcal/mol. Geometry optimization of intermediate (**I**) on the singlet surface results in the transfer of the hydroxyl hydrogen from the metal complex to the hydroperoxo radical giving rise to **4**.

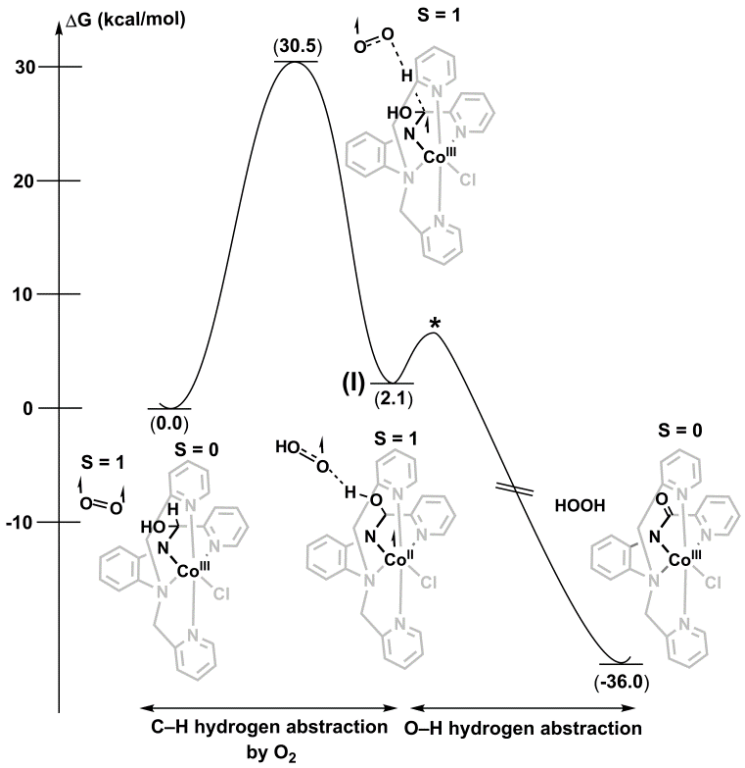

Figure 6.10. Reaction energy profile for the hydroxyl to amide conversion in MeCN. The transition state * is not explicitly located.

www.manaraa.com

Other mechanistic possibilities considered for the formation of Co^{III}-amide (**4**) from Co^{III}-hydroxide can be found in **Figure 6.11-6.13**.

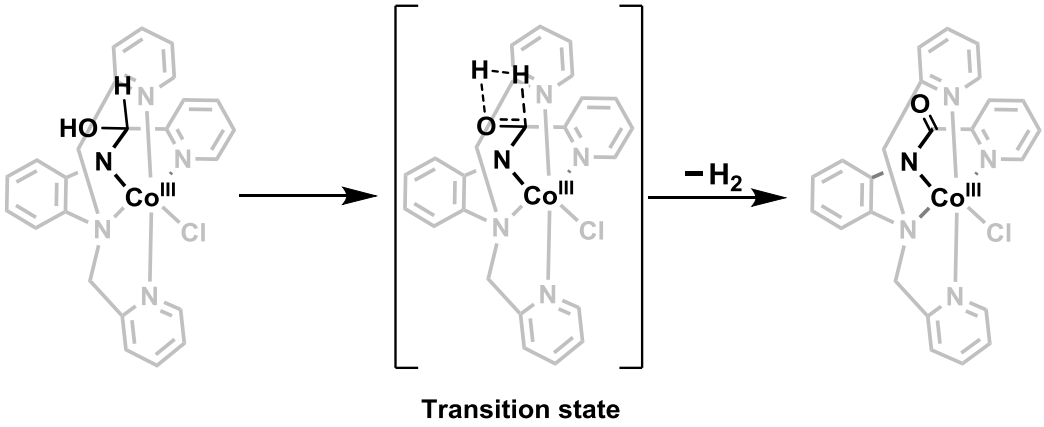

Figure 6.11. The pathway for the conversion of the hydroxyl complex to amide via direct H_2 elimination.

The pathway in **Figure 6.11** involves a strained four-membered fragment in the transition state. A linear scan (DFT calculations) in CH_3CN was performed from the hydroxyl complex bringing two reacting hydrogen centers closer to each other. As expected, the scan showed that the energy required for the conversion is too high (> 50 kcal/mol) invalidating the possibility of this pathway.

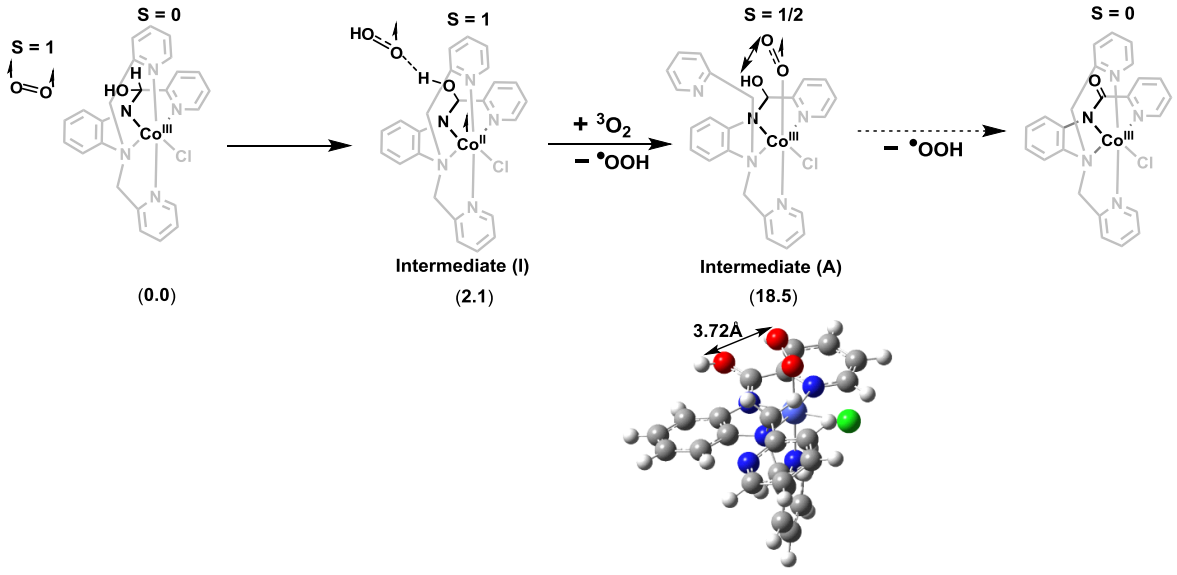

Figure 6.12. An alternative pathway for the conversion of intermediate (**I**) into the amide complex in CH_3CN.

www.manaraa.com

The pathway in **Figure 6.12** involves opening of one of the coordination sites on cobalt in intermediate (**I**) when one of the pyridine rings dissociates. One $^3O_2$ molecule can coordinate on the Co^{II} center and an internal electron transfer from metal to O_2 gives rise to Co^{III}–$O2^{(\cdot)}$ fragment as shown in intermediate (**A**). Abstraction of the hydroxyl hydrogen by this activated $O2^{(\cdot)}$ fragment can potentially give rise to the amide product. However, DFT calculations find that the transformation of intermediate (**I**) to (**A**) is energy-requiring by 16.4 kcal/mol. Moreover, the optimized geometry of intermediate (**A**) demonstrates that the hydroxyl hydrogen and the oxygen atom of $O2^{(\cdot)}$ fragment are too far away (3.72Å) to combine with each other.

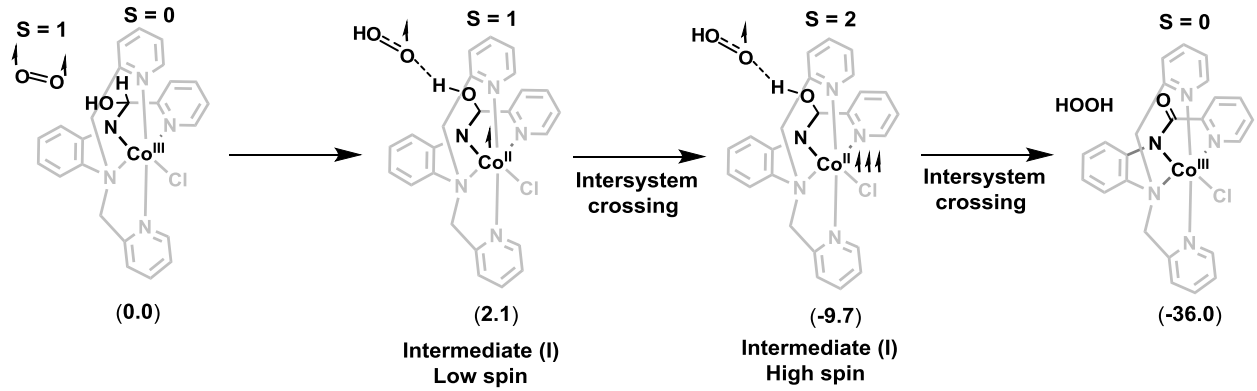

Figure 6.13. An alternative pathway for the conversion into the amide complex in CH_3CN.

The high-spin (S=2) configuration of intermediate (**I**) is found to be lower in energy than its low-spin (S=1) state by about 12 kcal/mol in CH_3CN. Therefore, we propose that, in addition to the low-spin (S=1) state giving rise to the amide product as described in **Figure 6.13**, the high-spin (S=2) configuration can also potentially give rise to the singlet amide complex via intersystem crossing.

Experimental results revealed that the conversion of **2** and **3** into the amide **4** does not take place in the absence of oxygen (**Figure 6.14**). After keeping the mixture of imino (**2**) and methoxy (**3**)

www.manaraa.com

pyridine under argon for few hours, no transformation to amide was observed in anaerobic condition (no oxygen).

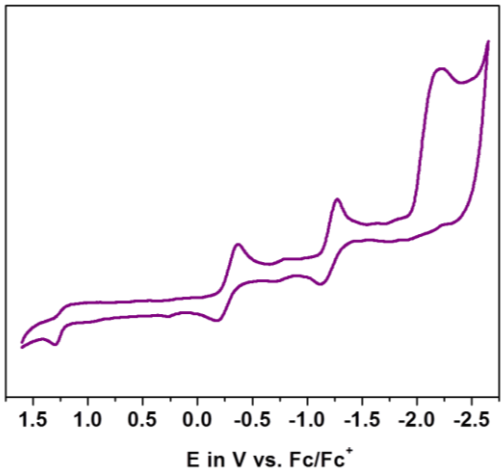

Figure 6.14. Electrochemical experiment to the mixture of **2** and **3** after few days in anaerobic condition (CV of the final solution containing Imine (**2**) + methoxy (**3**) in CH_3CN in air-tight condition after 24 hours).

Inspection of the optimized geometry of **3** reveals that a direct S_N2 attack on the carbon atom bearing the methoxy function by a water molecule is also not feasible because of steric crowding imposed by one of the pyridine rings (**Figure 6.15**). As a result, conversion of **3** into **4** must proceed *via* the regeneration of **2** that then undergoes water addition followed by oxidation with O_2 (**Figure 6.15**).

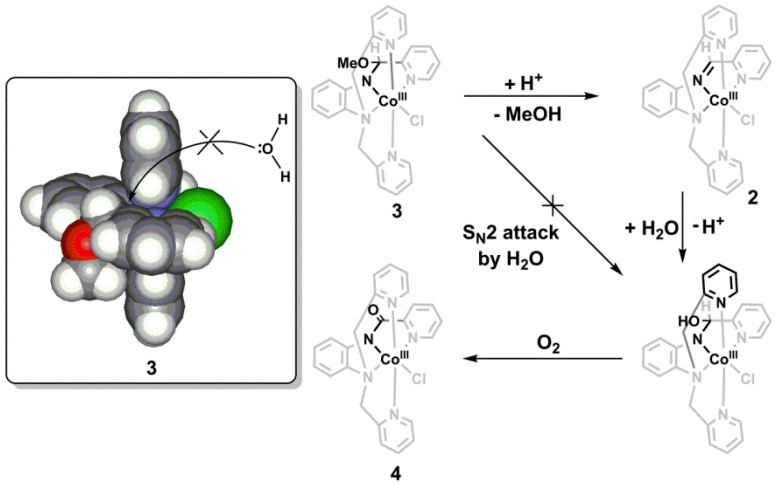

Figure 6.15. Conversion of complex **3** to **4.**

www.manaraa.com

As shown by the CPK model of the optimized structure of complex **3** (inset: **Figure 6.15**), nucleophilic attack by a water molecule on the carbon atom bearing the methoxy moiety is not feasible as the S_N2 approach of the water is sterically blocked by a pyridine moiety attached on the cobalt center. Alternatively, addition of a proton to the methoxy function from water results in the loss of a MeOH molecule from complex **3** and can give rise to complex **2**. Addition of water to the imine function in **2** can produce the hydroxyl complex which eventually gets oxidized with atmospheric O_2 to convert into the amide complex **4**.

6.3.4. Magnetic properties

Well-defined and sharp peaks in the ^{1}H-NMR spectra in CD_3CN confirm the diamagnetic nature ($3d^6$ $^{LS}Co^{III}$) of complexes **2**-**4**. On the other hand, for complex **5**, DFT calculations predict that the high-spin (S = 3/2) configuration is more stable than the low-spin (S = 1/2) one by 13.7 kcal/mol. Indeed, use of ^{1}H-NMR yielded broad and shifted peaks indicating a paramagnetic nature for the complex.

The electron paramagnetic resonance (EPR) spectrum of **5** in MeCN was taken at 4 K and confirms the species as $^{HS}Co^{II}$ in a pseudo-octahedral environment (**Figure 6.16a**). The observed peaks are interpreted as transitions between $\Delta m_s = \pm 1/2$ sublevels and can be simulated with the parameters $g_1 = 6.34$, $g_2 = 3.47$, $g_3 = 1.96$ and $A_1 = 474$, $A_2 = 130$, and $A_3 = 170$ MHz. As a rule, the EPR lines for $\Delta m_s = \pm 3/2$ are not observed in non-crystalline $3d^7$ systems due to their strong orientation dependence. Comparisons of the crystal structure with the calculated high-spin (**Figure 6.16b**) and low-spin (**Figure 6.16c**) configurations also find a much better agreement with the HS species, showing deviations in the metal–ligand bond distances between 0.03-0.08 Å, while the same deviation for an LS species varies from 0.03-0.34 Å (**Figure 6.17**). As shown in the **Figure 6.17**, calculated bond lengths of the high-spin (S=3/2) configuration match

www.manaraa.com

satisfactorily with those of the crystal structure while the calculated bond lengths of the low-spin (S=1/2) complex deviate significantly. These results support for the high-spin state of complex **5** which is confirmed by its EPR measurement.

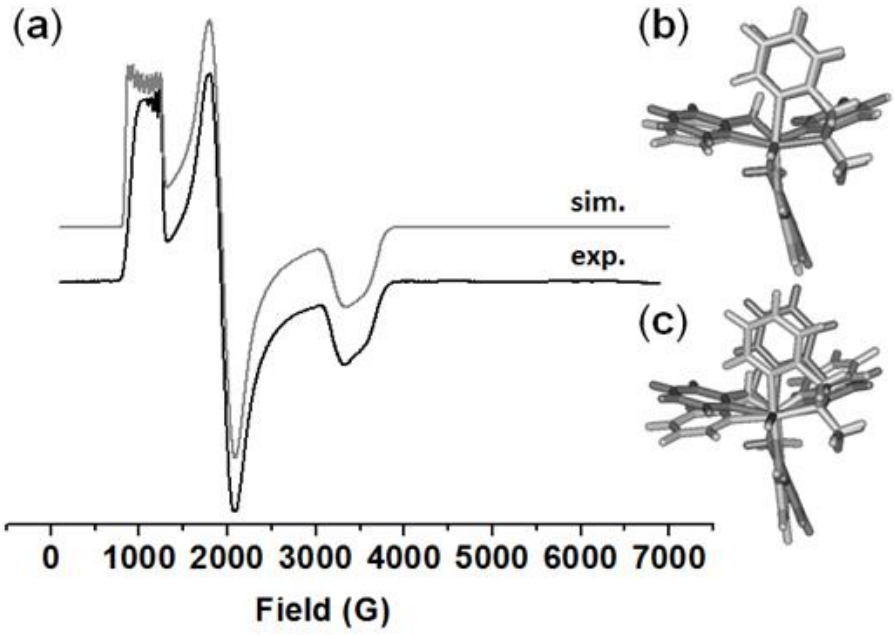

Figure 6.16. (a) EPR spectrum in MeCN for ^{HS}**5** (S = 3/2). Comparisons of the crystal structure with the calculated HS (b) and LS (c) species.

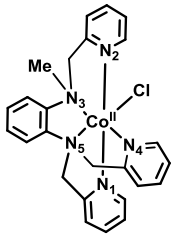

5

Differences of bond distances (Å) between the crystal and calculated structures

	Calculated (High spin, S= 3/2)	Calculated (Low spin, S=1/2)
Co-N_1	0.03	0.13
Co-N_2	0.04	0.20
Co-N_3	0.06	0.12
Co-N_4	0.06	0.09
Co-N_5	0.07	0.03
Co-Cl	0.08	0.34

Figure 6.17. Differences of the metal-ligand bond distances (Å) between the crystal and DFT-optimized structures of complex **5** in MeOH.

www.manaraa.com

6.3.5. Electronic properties

The UV-visible spectra of the Co^{III} complexes **2-4** in MeCN are shown in **Figure 6.18** and **Table 6.3**. They are dominated by intense intraligand UV processes along with faint visible processes associated with d-d transitions. The imine **2** and amide **4** show absorptions at 490 nm (20,400 cm^{-1}, $\varepsilon = 240\ M^{-1}cm^{-1}$) and 488 nm (20,500 cm^{-1}, $\varepsilon = 320\ M^{-1}cm^{-1}$), respectively, associated with the $^1T_{2g}(I) \leftarrow {}^1A_{1g}(D)$ transition of an ideal octahedral field.[9] These species absorb in the blue region and are characterized by a faint orange color. The methoxy species **3** shows a lower energy absorption at 667 nm (15,000 cm^{-1}, $\varepsilon = 410\ M^{-1}cm^{-1}$) associated with $^1T_{2g}(I) \leftarrow {}^1A_{1g}(D)$. It absorbs in the red region and is green colored. On the other hand, the pinkish color observed for the $^{HS}Co^{II}$ species **5** is the result of an absorption in the green region at 504 nm (19,800 cm^{-1}, $\varepsilon = 46\ M^{-1}cm^{-1}$) associated with an idealized $^4T_{1g}(P) \leftarrow {}^4T_{1g}(F)$ process.[9]

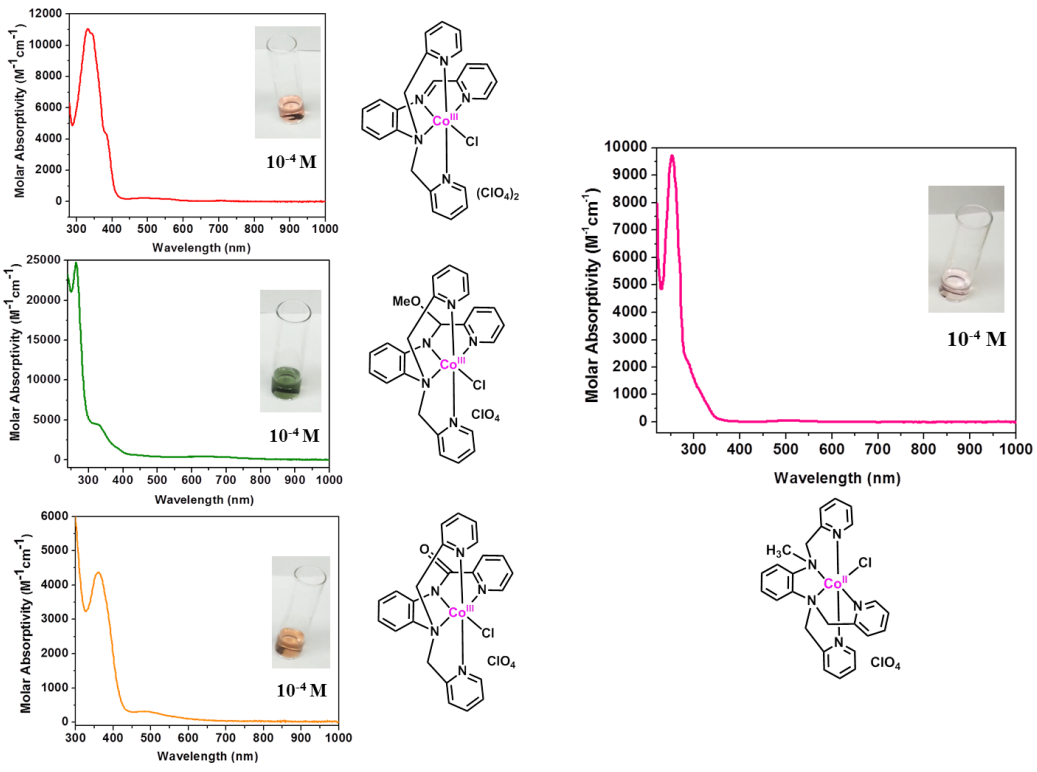

Figure 6.18. UV-visible Spectra of **2-5** ([C] = 1.0×10^{-4} M) in acetonitrile.

www.manaraa.com

Table 6.3. UV-visible parameters for **2-5** in CH_3CN.

	λ (nm) |ε ($M^{-1}cm^{-1}$)|	λ (nm) |ε ($M^{-1}cm^{-1}$)|	λ (nm) |ε ($M^{-1}cm^{-1}$)|	λ (nm) |ε ($M^{-1}cm^{-1}$)|
2	331 |11041|	346 |10706|	384 |4255|	490 |239|
3	263 |24624|		332 |4406|	667 |410|
4			360 |4384|	488 |320|
5	252 |9717|			504 |46|

6.3.6. Electrochemical properties

Cyclic voltammetry was performed for complexes which are more robust and well-behaved. The cyclic voltammetry (CV) profile for **2** in dry MeCN shows two reversible and two quasi-reversible processes at -0.27, -1.16, -2.01, and -2.12 $V_{Fc/Fc+}$. Complex **4** shows two reversible and one irreversible process at -0.69, -1.99, and -2.41 $V_{Fc/Fc+}$ while two reversible and one quasi-reversible process were found at -0.02, -1.92, and -2.39 $V_{Fc/Fc+}$ for species **5** (**Figure 6.19**).

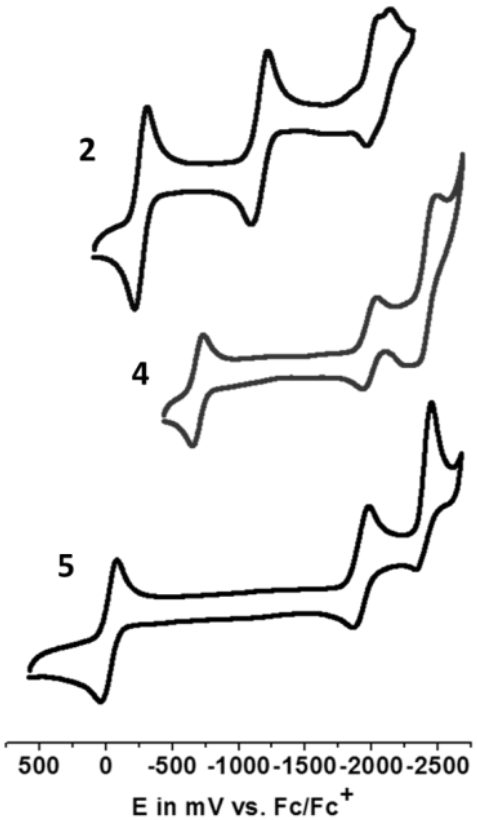

Figure 6.19. Cyclic voltammetry profiles of **2**, **4**, and **5** in dry MeCN**.**

www.manaraa.com

The reduced species generated at affordable potentials for the chemically robust species **4** and **5** are of immense interest to proton and water reduction, and a detailed electronic characterization is offered here. Important CV parameters for the reduced analogs of **2-5** are presented in **Table 6.4** and electronic and energetic analyses are shown in **Figure 6.20**. Mulliken spin density analysis finds the first reduction event associated to the Co^{III}/Co^{II} couple for **4** yielding a $3d^7$ $^{HS}Co^{II}$ center. Occupation of the antibonding metal-based and idealized e_g* MOs increases the metal–ligand bond distances in the Co^{II}-species and leads to rapid loss of the chloro ligand in the newly formed six-coordinate Co^{II}-complex. This loss is energetically favorable by 5.5 kcal/mol and results in a five-coordinate $^{HS}Co^{II}$ species. Because of the presence of a planar and conjugated amide framework, some degree of redox non-innocence behavior is shown by the ligand during the second reduction event (**Figure 6.20**). Complex **5** undergoes oxidation at -0.02 V (Co^{II} to Co^{III}) while the first reduction event happens at -1.92 V. Calculations suggest that this reduction event is metal-based and results into a $3d^8$ Co^{I} center. Loss of the chloro ligand from Co^{I} complex is favored by 5.4 kcal/mol. On the other hand, chloride elimination from the six-coordinate Co^{II} analog is unfavorable by 4.9 kcal/mol.

Table 6.4. CV parameters for **2, 4,** and **5** in CH_3CN.

	Co^{III}/Co^{II} $E_{½}$, [E_{pc}; E_{pa}], V (ΔE, V) $\lvert i_{pc}/i_{pa}\rvert$	**Co^{II}/Co^{I}** $E_{½}$, V (ΔE, V) $\lvert i_{pc}/i_{pa}\rvert$	**C=N/$C^{\bullet}$-N^{-}** $E_{½}$, V (ΔE, V) $\lvert i_{pc}/i_{pa}\rvert$
2	-0.27 (0.09) |0.96|	-1.16 (0.12) |1.20|	-2.00 (0.08) |N/A|
			-2.12 (0.06) |N/A|
4	-0.69 (0.09) |1.03|	-1.99 (0.10) |1.59|	-2.41 (0.14) |2.20|
5	-0.02 (0.12) |1.01|	-1.92 (0.11) |1.38|	-2.39 (0.11) |3.00|

www.manaraa.com

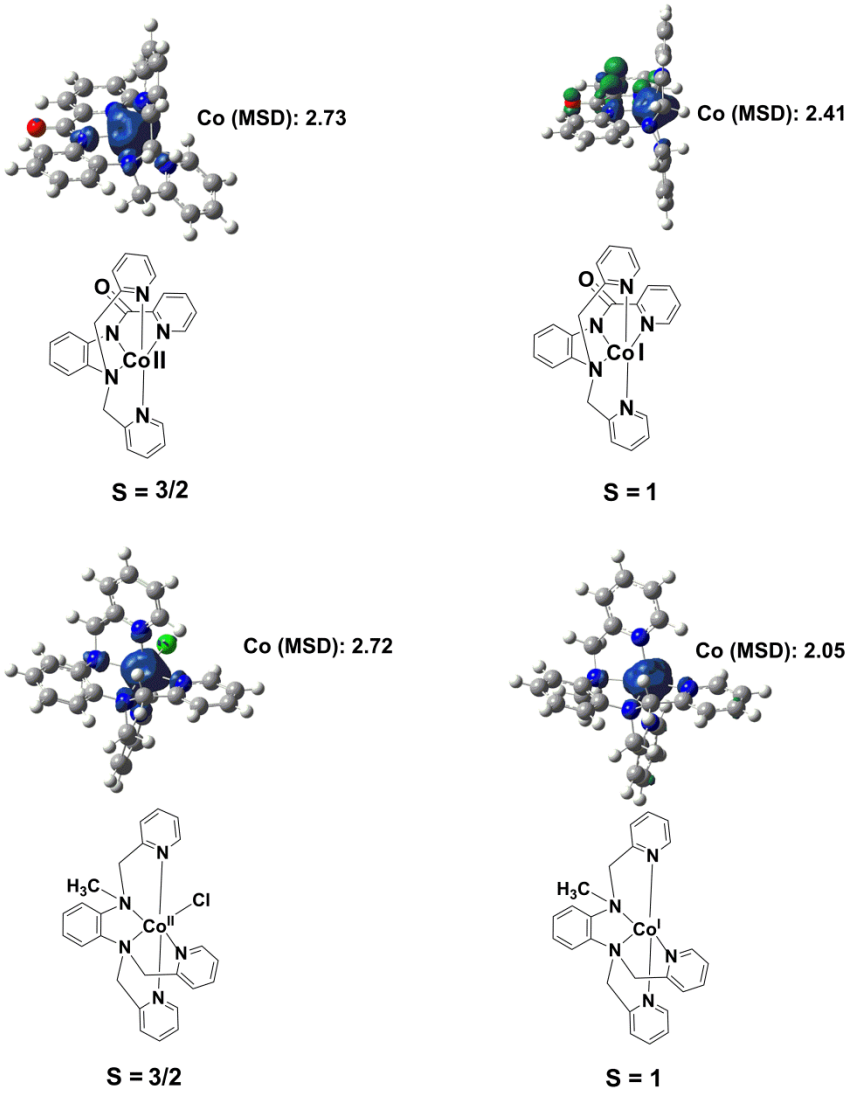

Figure 6.20. Spin density plots (isosurface value of 0.004 a.u.) of the redox-active species generated during the electrochemical reduction of Co-amide and Co-N-methylamine complexes.

Co^{II}-species are found to be high-spin (S=3/2) for both amide and N-methylamine complexes. Mulliken spin density (MSD) values calculated for the metal centers are about 2.7 which validates the presence of high-spin Co^{II}. The low-spin states (S=1/2) are found to be higher in energy by 16.9 and 13.3 kcal/mol for amide and N-methylamine complexes, respectively. Co^{I}-intermediates are found to be high-spin (S=1) as well. The low-spin states (S=0) are found to be

www.manaraa.com

higher in energy by 18.6 and 16.2 kcal/mol for amide and N-methylamine complexes, respectively. However, because of π-conjugation present in the planar amide ligand framework, latter shows some degree of redox non-innocence character as shown in the spin density plot of the Co^{I}-amide species (**Figure 6.20**).

6.3.7. Electrocatalytic properties

6.3.7.1. Proton reduction electrocatalysis

Electrocatalytic behavior was investigated with complexes **4** and **5** due to their stability and robust nature. The weak organic acids, triethyl ammonium chloride (Et_3NHCl) (**Figure 6.21**) and acetic acid (HOAc) (**Figure 6.22**) were used as the proton source. A catalytic peak was found near the second reduction process for **4** upon addition of various equivalents of HOAc in MeCN (**Figure 6.22a**). An observed catalytic current of 200 μA was measured after addition of 10 equiv. of HOAc and the overpotential was 0.740 V when the homoconjugation effect of the acid was considered.[10] The rate of H_2 generation (k_{obs}) was 7.39 s^{-1} and the identity of dihydrogen was confirmed by the bulk-electrolysis experiment at -1.7 $V_{Ag/AgCl}$. A turnover number (TON) of 15.44 after 3 h was calculated with 100 equiv. of acid. Faradaic efficiency was measured to be ~90%. Control experiments with HOAc in MeCN in absence of **4** exhibited catalytic peaks at significantly more negative potentials (**Figure 6.23**), thus validating the role of that species as a catalyst. Comparison of the charge *versus* time plots in presence and absence of **4** confirms the catalytic activity of the complex (**inset: Figure 6.22a**). Electrocatalytic measurements with complex **5** found a catalytic peak close to the second redox couple (**Figure 6.22b**) as observed with **4**. The catalytic current and k_{obs} were found to be 150 μA and 4.29 s^{-1}, respectively in presence of 10 equiv. of HOAc. An overpotential of 0.69 V was found and H_2 evolution was

www.manaraa.com

confirmed by electrolysis at -1.7 $V_{Ag/AgCl}$. A TON of 14.35 was observed after 3 h with 100 equiv. of acid. Faradaic efficiency was found to be 75%. Control experiments (**Figure 6.23**) and charge *versus* time plots (inset: **Figure 6.22b**) confirm the catalytic behavior of **5**. Comparison of the electrocatalytic behavior of **4** and **5** with that of a blank solution is also shown in **Figure 6.23**.

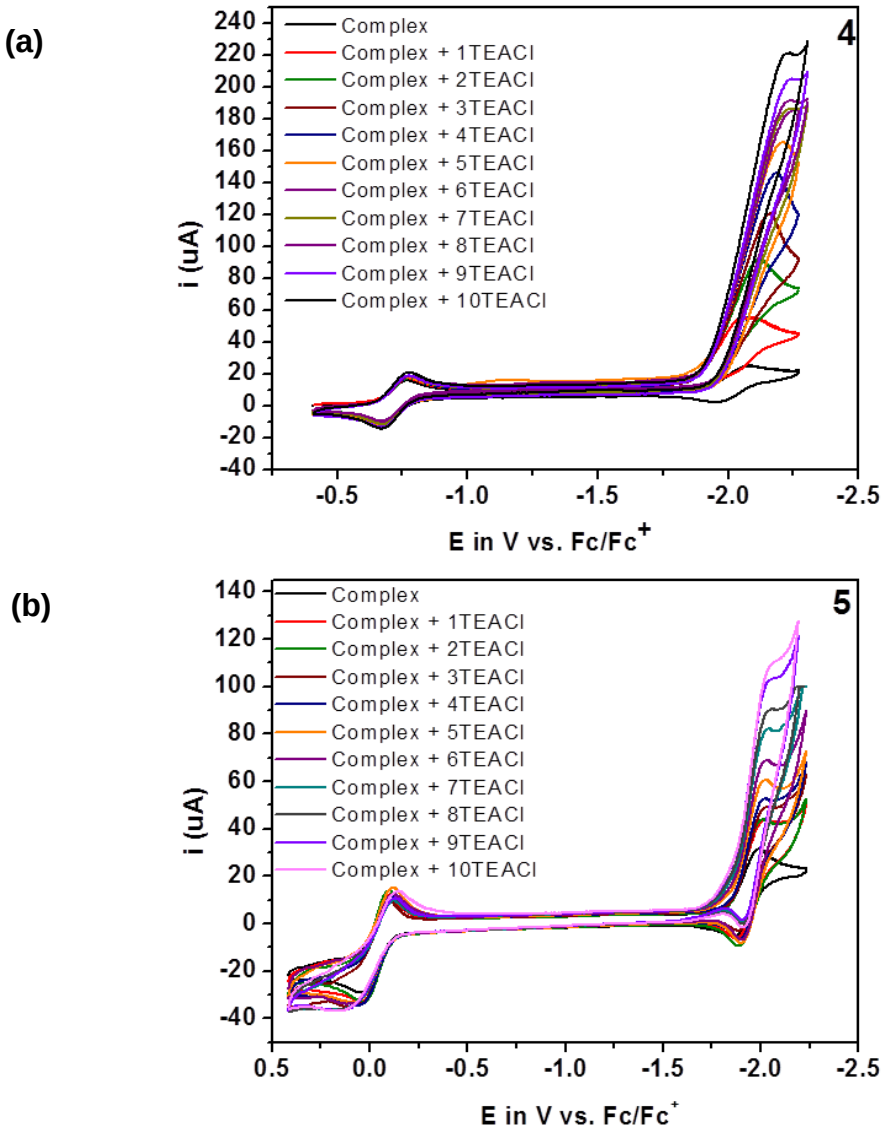

Figure 6.21. Catalytic CV experiments for **4,** and **5** with Et_3NHCl in CH_3CN.

www.manaraa.com

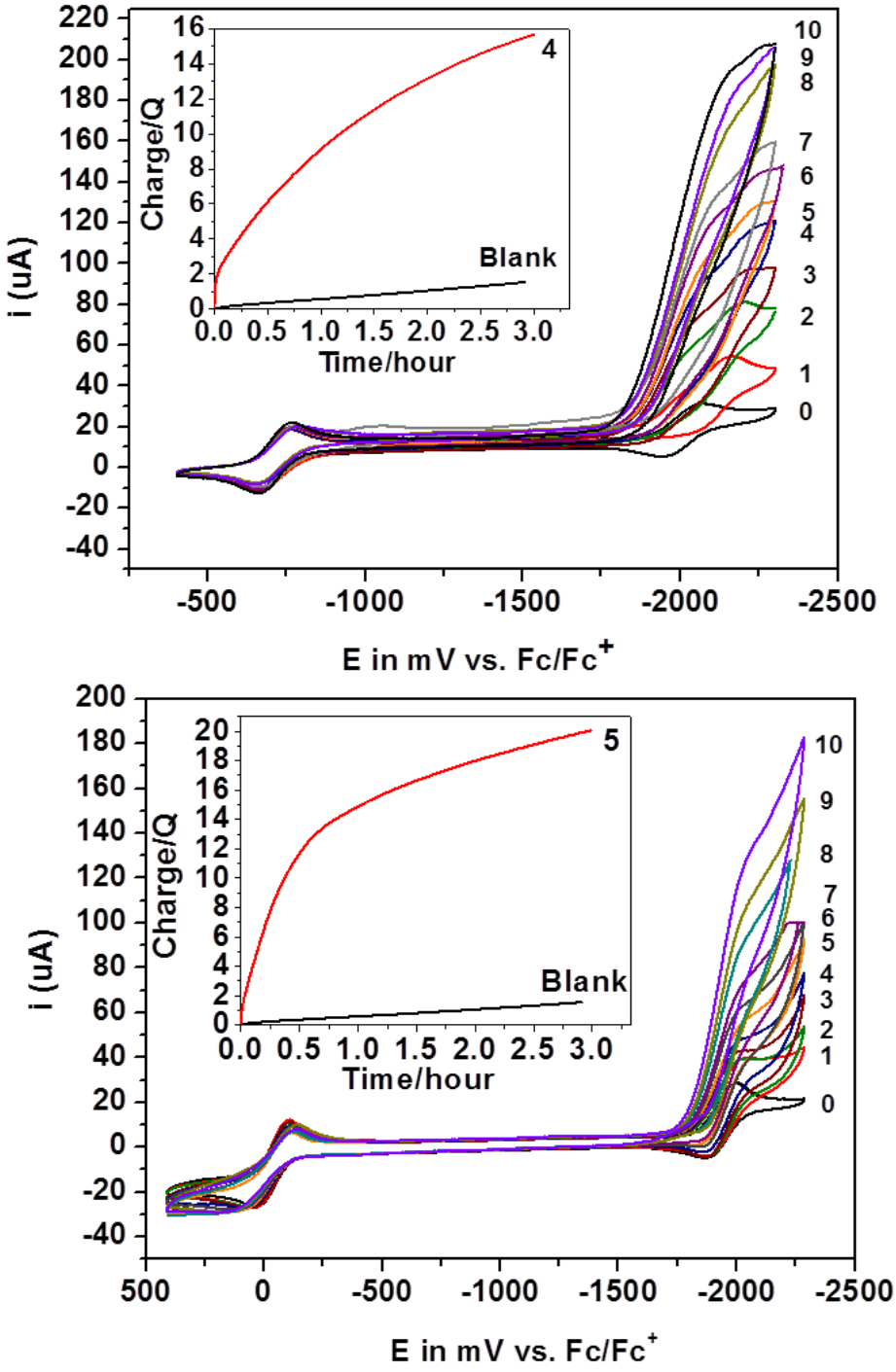

Figure 6.22. CV experiments of H_2 generation by **4** (**Figure 7.22a**) and **5** (**Figure 7.22b**) in MeCN. The numbers 0-10 indicate the HOAc equiv. used in comparison to the complex. Insets: Charge *versus* time plots during the bulk electrolysis of **4** and **5** (applied potential: -1.7 $V_{Ag/AgCl}$). Complex: 4 μmol; HOAc: 0.4 mmol during electrolysis.

www.manaraa.com

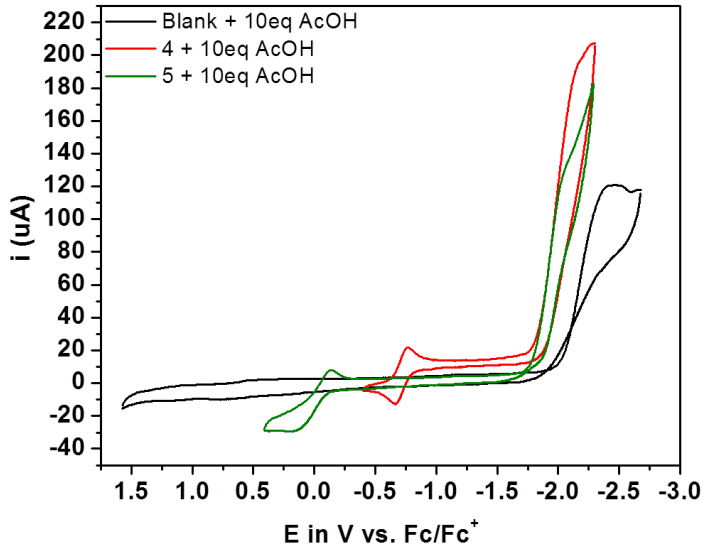

Figure 6.23. Comparison of CV for **4, 5,** and blank with HOAc in CH_3CN.

6.3.7.2. Water reduction electrocatalysis

The ultimate goal of electrocatalytic H_2 generation from neutral water (pH = 7) in phosphate buffer (1M) was attained with **4** and **5** (**Figure 6.24**). The catalytic peak appears at an onset overpotential of 0.55 V for **4**. Electrolysis at -1.7 $V_{Ag/AgCl}$ yielded a TON of 1,615 after 3 h with Faradaic efficiency of 95%. The TON reaches over 7,000 after 18 h without any obvious sign of catalyst decomposition (**Figure 6.25a**). The catalytic peak for **5** appears at a slightly more positive onset overpotential of 0.70 V, and electrolysis at -1.7 $V_{Ag/AgCl}$ confirmed dihydrogen generation. The TON and Faradaic efficiency were calculated to be 1,400 and 95%, respectively, over 3 h. No decomposition of the catalyst **5** was observed after 18 hours, when the TON reaches over 6,000 (**Figure 6.25b**). Control experiments generate some dihydrogen at more negative potentials than those with **4** and **5** (**Figures 6.24a** and **6.24b**). Charge consumption over time is much higher with both the complexes than that with the blank solution (**insets: Figures 6.24a and 6.24b**). Comparison of the electrocatalytic behavior of **4** and **5** in water is shown in Figure **6.26**. All the relevant catalytic parameters are reported in **Table 6.5**.

www.manaraa.com

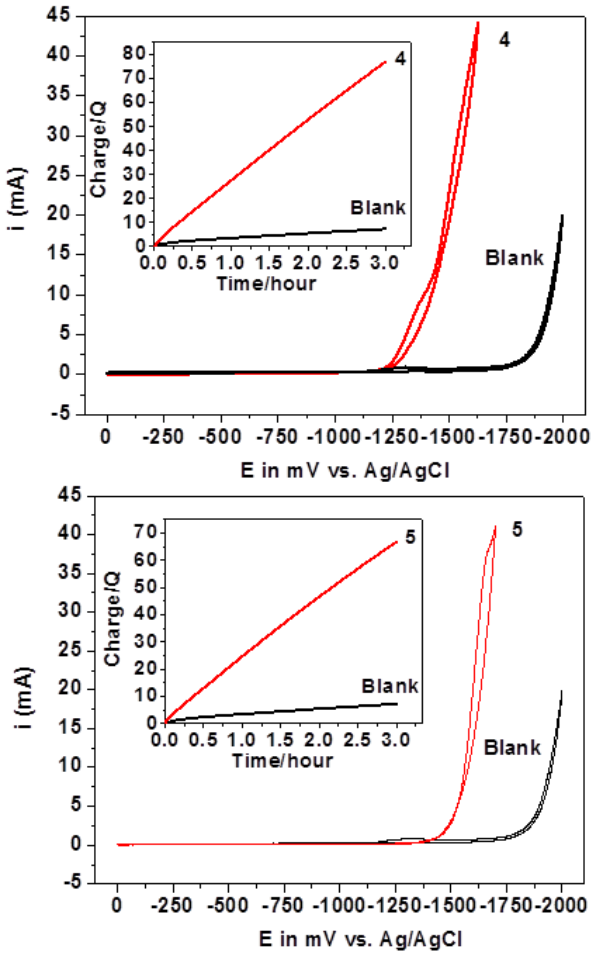

Figure 6.24. CV experiments of H_2 generation by **4** (**Figure 7.24a**) and **5** (**Figure 7.25b**) from water (pH = 7 with 1M phosphate buffer). Insets: charge *versus* time plots during the bulk electrolysis of **4** and **5** (applied potential: -1.7 $V_{Ag/AgCl}$). Complex: 0.2 µmol during electrolysis.

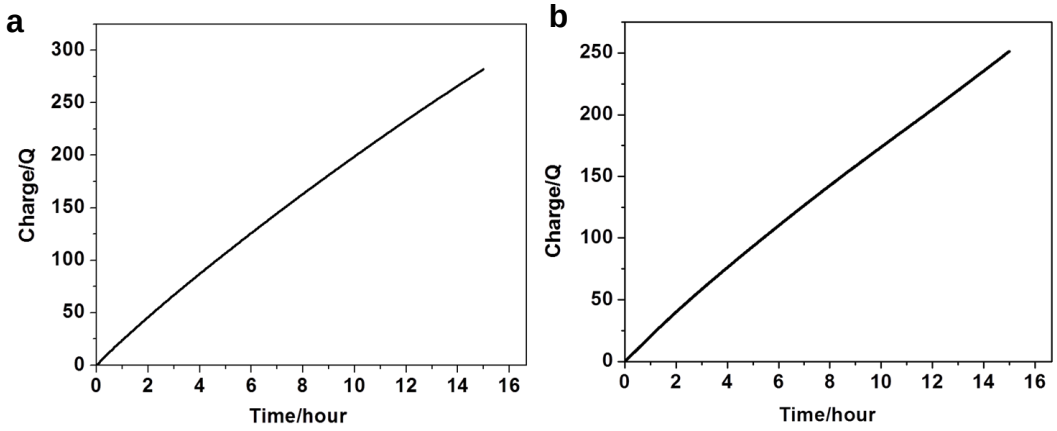

Figure 6.25. Charge *versus* time plot during bulk electrolysis for 18 hours of (a) **4**, TON/18 hours: 7150; Faradaic efficiency: 95%; and (b) **5,** TON/18 hours: 6000; Faradaic efficiency: 95%.

www.manaraa.com

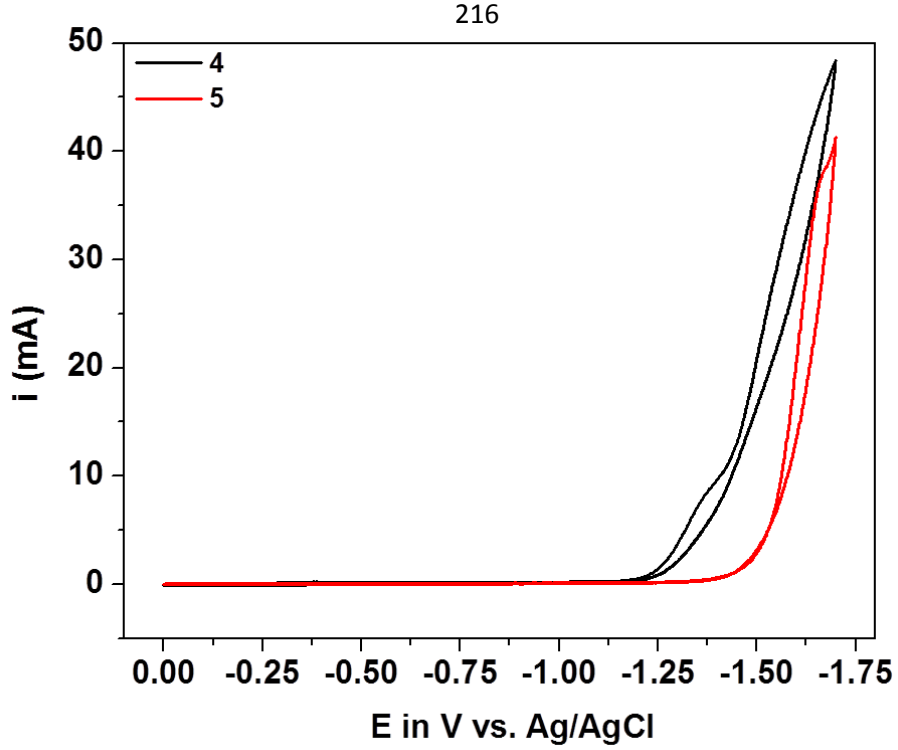

Figure 6.26. Comparison of CV for **4** and **5** with H_2O (phosphate buffer, pH: 7).

Table 6.5. Catalytic parameters with HOAc in CH_3CN and in water for **4** and **5** (bulk electrolysis (BE) for **4** and **5**: Applied potential (AP): -1.7 $V_{Ag/AgCl}$ with HOAc in CH_3CN; BE of **4** and **5** (AP: -1.7 $V_{Ag/AgCl}$) with water/phosphate buffer (pH: 7).

Parameters	**4 (HOAc)**	**4 (H_2O)**	**5 (HOAc)**	**5 (H_2O)**
Overpotential (V) (10 eq. HOAc) Onset Overpotential (H_2O) (10 mL 1M buffer)	0.74	0.55	0.69	0.70
k_{obs} (s^{-1}) (10 eq. HOAc)	7.39	N/A	4.29	N/A
TON/3h (4.0 X 10^{-6} mol) (100 eq HOAc) TON/3h (2.0 X 10^{-7} mol) (H_2O, 20 mL 1M buffer)	15.44	1615	14.35	1400
Faradaic efficiency (%)	90	95	75	95

www.manaraa.com

6.3.7.3. Catalytic mechanism

Mechanisms of electrocatalytic H_2 evolution by **4** and **5** have been elucidated by DFT calculations. **Figure 6.27** describes the catalytic pathway for complex **4** in MeCN. The five-coordinate Co^{II}-species, generated after dissociation of the chloro ligand, undergoes reduction to the corresponding Co^{I} complex. The reduction potential is calculated as -1.83$V_{Fc/Fc+}$. Uptake of a proton by the Co^{I} complex is favorable by 22.5 kcal/mol and results in the six-coordinate Co^{III}–H complex, which gets reduced to the more reactive $^{HS}Co^{II}$–H species. The latter species is high-spin in nature and occupation of the idealized e_g* MOs weakens the metal-ligand interactions. The Co–H bond elongates from 1.49 Å in the $^{LS}Co^{III}$-complex to 1.73 Å in the $^{HS}Co^{II}$-species. As a result, the hydride in the Co^{II}–H moiety is susceptible to heterolytic attack by an external proton. Uptake of a proton and generation of H_2 by this complex is favored by 54.0 kcal/mol (**Figure 6.27**), regenerating the five-coordinate Co^{II}-complex to restart the catalytic cycle. The reaction of a proton with the Co^{II}–H is expected to be activationless.[11] The homolytic pathway by the combination of two Co^{II}–H complexes is significantly less exothermic compared to the heterolytic mechanism. A proton-coupled electron transfer (PCET) event is not invoked for the Co^{II}/Co^{III}–H transformation since no anodic shift was found in the experimental electrocatalytic measurement of **4** with the decrease of pH. However, a PCET event for the Co^{I}/Co^{II}–H conversion, thereby bypassing the Co^{III}–H intermediate, may be plausible. Complex **5** follows a similar catalytic mechanism, as described in **Figure 6.28**. **Figure 6.28** describes the catalytic pathway of H_2 generation by complex **5** in CH_3CN. The reduction potential of **5** is calculated to be -1.75$V_{Fc/Fc+}$. The six-coordinate high-spin triplet Co^{I}-species, generated after the reduction, loses the chloride to obtain a vacant coordination site on the metal center. Loss of chloride is found to be favorable by 5.4 kcal/mol. Addition of a proton onto the vacant site of the Co^{I} center

www.manaraa.com

is calculated to be favorable by 11.7 kcal/mol. The resulting Co^{III}–H species can get reduced easily to the more reactive Co^{II}–H complex. The later species can accept one more proton on the hydride moiety and the generation of dihydrogen is calculated to be downhill by 41.5 kcal/mol. The five-coordinate Co^{II}-complex obtained after the release of dihydrogen, gets reduced at a potential of -1.29$V_{Fc/Fc+}$ to give rise to the corresponding Co^{I}-species that can restart the catalytic cycle. A proton-coupled electron transfer (PCET) event is not invoked for the Co^{II}/Co^{III}–H transformation since no anodic shift was found in the electrocatalytic measurement of **5** with the decrease of pH. However, a PCET event for the Co^{I}/Co^{II}–H conversion, thereby bypassing the Co^{III}–H intermediate, may be plausible.

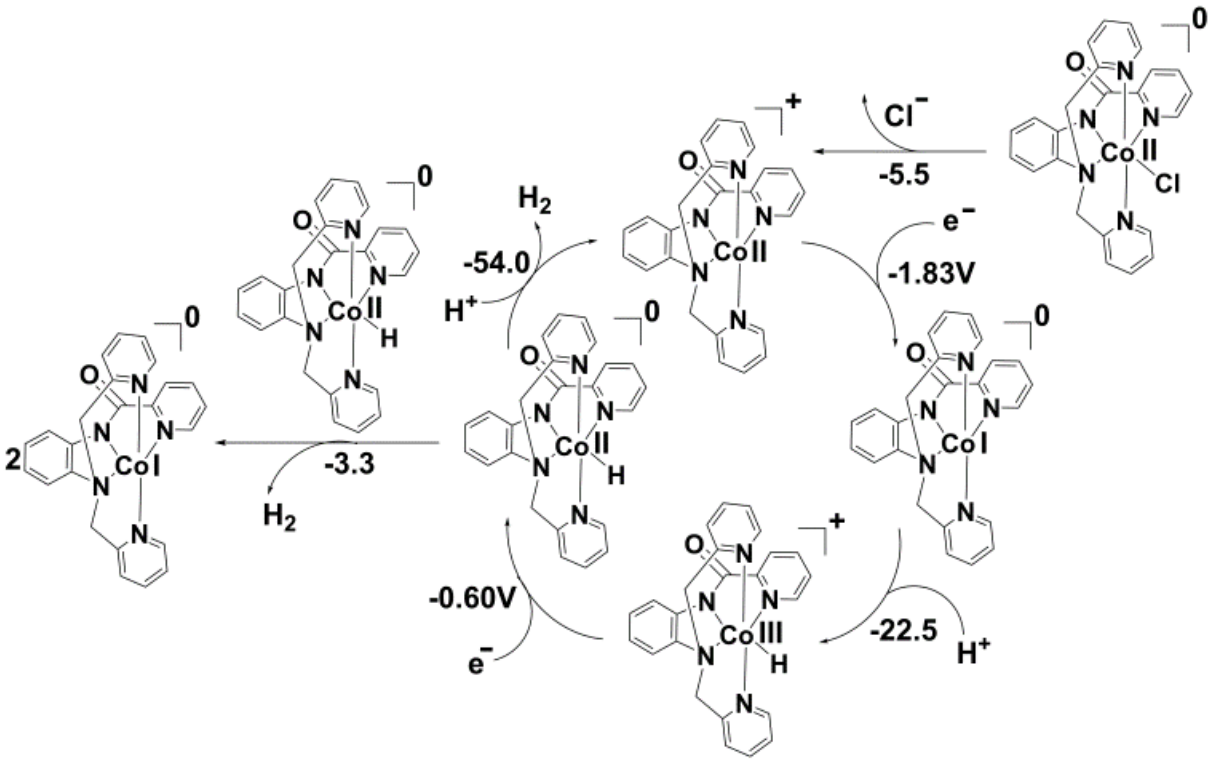

Figure 6.27. Catalytic mechanism of H_2 generation by 4 in MeCN. It involves a Co^{III}–H species that undergoes protonation to generate H_2. Bimolecular mechanism via the combination of two Co^{II}–H complexes is unlikely. Pathway involving a proton-coupled electron transfer event from the Co^{I}-complex to the Co^{II}–H species can contribute to the catalysis. The energetics for all events is reported as free energy changes in kcal/mol.

www.manaraa.com

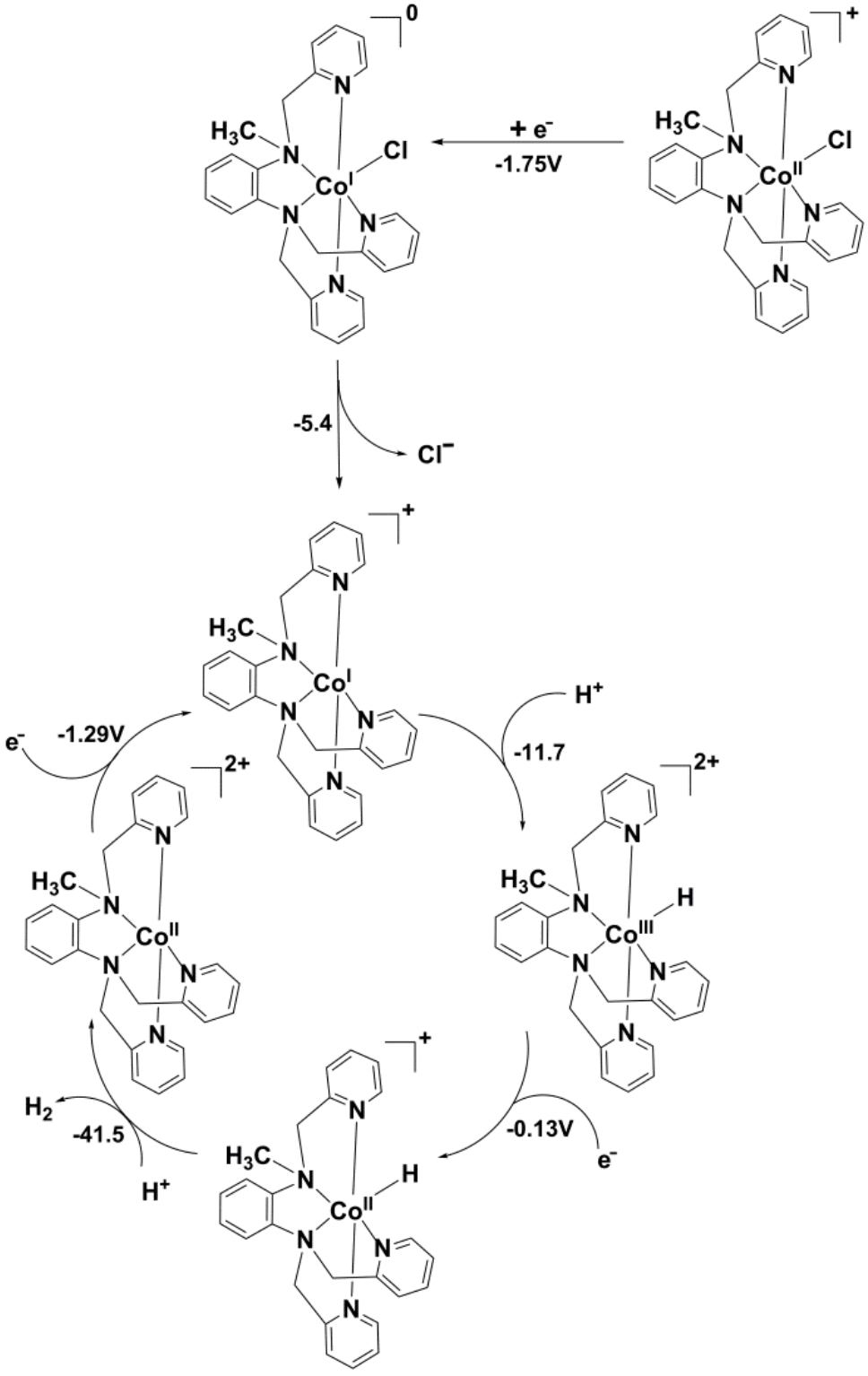

Figure 6.28. Catalytic mechanism of H_2 generation by **5** in CH_3CN. Energetics of all the chemical events is reported as free energy changes in kcal/mol.

www.manaraa.com

6.4. Conclusions

In conclusion, I have described the syntheses and characterization of a series of pentadentate, pyridine-rich Co-complexes **1**-**5** with amine, imine, methoxy, amide, and N-methylamine functionalities. The methoxy and amide species arise from the imine complex **2** *via* reaction with a solvent methanol or water, respectively. The Co^{III} imine **2** arises from aerial oxidation of the corresponding Co^{II}-amine species **1**. Introduction of an N-methyl function in **1** inhibits this oxidation and yields the $^{HS}Co^{II}$ N-methylamine **5**. Electrocatalytic experiments with **4** and **5** reveal H_2 generation with TONs of 15.44 and 14.35, respectively after 3 h in presence of acetic acid in MeCN solutions. Remarkably, **4** and **5** are excellent water reduction catalysts with TONs of 7,000 and 6,000, respectively after 18 h. The present TONs insert these two species among a select group of top catalysts for water reduction. Catalytic mechanisms obtained by DFT calculations involve the formation of a Co^{III}–H species that undergoes further reduction followed by protonation of the hydride on the cobalt center.

www.manaraa.com

REFERENCES

1. (a) Bigi, J. P.; Hanna, T. E.; Harman, W. H.; Chang, A.; Chang, C. J. *Chem. Commun.* **2010**, *46*, 958. (b) Stubbert, B. D.; Peters, J. C.; Gray, H. B. *J. Am.Chem.Soc.* **2011**, *133*, 18070. (c) Sun, Y.; Bigi, J. P.; Piro, N. A.; Tang, M. L.; Long, J. R.; Chang, C. J. *J. Am. Chem. Soc.* **2011**, *133*, 9212. (d) Leung, C. F.; Chen, Y. Z.; Yu, H. Q.; Yiu, S. M.; Ko, C. C.; Lau, T. C. *Int. J. Hydro. Energy* **2011**, *36*, 11640. (e) Singh, W. M.; Baine, T.; Kudo, S.; Tian, S.; Ma, X. A. N.; Zhou, H.; DeYonker, N. J.; Pham, T. C.; Bollinger, J. C.; Baker, D. L.; Yan, B.; Webster, C. E.; Zhao, X. *Angew. Chem. Int. Ed.* **2012**, *51*, 5941. (f) King, A. E.; Surendranath, Y.; Piro, N. A.; Bigi, J. P.; Long, J. R.; Chang, C. J. *Chem. Sci.* **2013**, *4*, 1578. (g) Nippe, M.; Khnayzer, R. S.; Panetier, J. A.; Zee, D. Z.; Olaiya, B. S.; Head-Gordon, M.; Chang, C. J.; Castellano, F. N.; Long, J. R. *Chem. Sci.* **2013**, *4*, 3934. (h) Zhang, P.; Wang, M.; Gloaguen, F.; Chen, L.; Quentel, F.; Sun, L. *Chem. Commun.* **2013**, *49*, 9455. (i) Singh, W. M.; Mirmohades, M.; Jane, R. T.; White, T. A.; Hammarström, L.; Thapper, A.; Lomoth, R.; Ott, Sascha *Chem. Commun.* **2013**, *49*, 8638. (j) Tong, L.; Zong, R.; Thummel, R. P. *J. Am. Chem. Soc.* **2014**, *136*, 4881. (k) Kawano, K.; Yamauchi, K.; Sakai, K. *Chem. Commun.* **2014**, *50*, 9872. (l) Call, A.; Codolà, Z.; Acuña-Parés, F.; Lloret-Fillol, J. *Chem. Eur. J.* **2014**, *20*, 6171.
2. (a) Lanznaster, M.; Hratchian, H. P.; Heeg, M. J.; Hryhorczuk, L. M.; McGarvey, B. R.; Schlegel, H. B.; Verani, C. N. *Inorg. Chem.* **2006**, *45*, 955. (b) Lanznaster, M.; Heeg, M. J.; Yee, G. T.; McGarvey, B. R.; Verani, C. N. *Inorg. Chem.* **2007,** *46*, 72. (c) Allard, M. M.; Sonk, J. A.; Heeg, M. J.; McGarvey, B. R.; Schlegel, H. B.; Verani, C. N. *Angew. Chem. Int. Ed.* **2012,** *51*, 3178. (d) Allard, M. M.; Xavier, F. R.; Heeg, M. J.; Schlegel, H. B.; Verani, C. N. *Eur. J. Inorg. Chem.* **2012**, 4622. (e) Wickramasinghe, L. D.; Perera, M.

www.manaraa.com

M.; Li, L.; Mao, G.; Zhou, Z.; Verani, C. N. *Angew. Chem. Int. Ed*. **2013**, *52*, 13346. (f) Wickramasinghe, L. D.; Mazumder, S.; Gonawala, S.; Perera, M. M.; Baydoun, H.; Thapa, B.; Li, L.; Xie, L.; Mao, G.; Zhou, Z.; Schlegel, H. B.; Verani, C. N. *Angew. Chem. Int. Ed*. **2014**, *53*, 14462. (g) Basu, D.; Allard, M. M.; Xavier, F. R.; Heeg, M. J.; Staples, R.; Schlegel, H. B.; Verani, C. N. *Dalton Trans.* **2015**, *44*, 3454.

3. (a) APEX2 V2010.11-3. Software *for the CCD Detector System*; Bruker Analytical X-ray Systems, Madison, WI, **2010**). (b) G. M. Sheldrick, *Acta Cryst*. **2008**, *A64*, 112. (c) Dolomanov, O. V.; Bourhis, L. J.; Gildea, R. J.; Howard, J. A. K.; Puschmann, H. *J. Appl. Cryst.* **2009**, *42*, 339.
4. (a) Parr, R. G.; Yang W. in *Density-functional theory of atoms and molecules; Oxford University Press: New York*, **1989**. (b) Frisch, M. J.; Trucks, G. W.; Schlegel, H. B.; Scuseria, G. E.; Robb, M. A.; Cheeseman, J. R.; Scalmani, G.; Barone, V.; Mennucci, B. ; Petersson, G. A.; Nakatsuji, H.; Caricato, M.; Li, X.; Hratchian, H. P.; Izmaylov, A. F.; Bloino, J.; Zheng, G.; Sonnenberg, J. L.; Hada, M.; Ehara, M.; Toyota, K.; Fukuda, R.; Hasegawa, J.; Ishida, M.; Nakajima, T.; Honda, Y.; Kitao, O.; Nakai, H.; Vreven, T. J., Montgomery, J. A.; Peralta, J. E.; Ogliaro, F.; Bearpark, M.; Heyd, J. J.; Brothers, E.; Kudin, K. N.; Staroverov, V. N.; Kobayashi, R.; Normand, J.; Raghavachari, K.; Rendell, A.; Burant, J. C.; Iyengar, S. S.; Tomasi, J.; Cossi, M.; Rega, N.; Millam, J. M.; Klene, M.; Knox, J. E.; Cross, J. B.; Bakken, V.; Adamo, C.; Jaramillo, J.; Gomperts, R.; Stratmann, R. E.; Yazyev, O.; Austin, A. J.; Cammi, R.; Pomelli, C.; Ochterski, J. W.; Salvador, P.; Dannenberg, J. J.; Dapprich, S.; Parandekar, P. V.; Mayhall, N. J.; Daniels, A. D.; Farkas, O.; Foresman, J. B.; Ortiz, J. V.; Cioslowski, J.; Fox, D. J. Gaussian Development Version; Revision H.31 ed.; Gaussian, Inc.: Wallingford, CT, **2010**. (c)

www.manaraa.com

Vosko, S. H.; Wilk, L.; Nusair, M. *Can. J. Phys.***1980**, *58*, 1200. (d) Lee, C. T.; Yang, W. T.; Parr, R. G. *Phys. Rev. B* **1988**, *37*, 785. (e) Dolg, M.; Wedig, U.; Stoll, H.; Preuss, H. *J. Chem. Phys*. **1987**, *86*, 866. (f) Francl, M. M.; Petro, W. J.; Hehre, W. J.; Binkley, J. S. ; Gordon, M. S.; DeFrees, D. J.; Pople, J. A. *J. Chem. Phys.* **1982**, *77*, 3654. (g) Hariharan, P. C.; Pople, J. A. *Theor.Chim.Acta* **1973**, *28*, 213. (h) Marenich, A. V.; Cramer, C. J.; Truhlar, D. G. *J. Phys. Chem. B* **2009**, *113*, 6378. (i) Seeger, R.; Pople, J. A. *J. Chem. Phys.* **1977,** *66*, 3045. (j) Schlegel, H. B.; McDouall, J. J. *In Computational Advances in Organic Chemistry, Ed.* C. Ögretir, I. G. Csizmadia, *Kluwer Academic: Amsterdam, The Netherlands*, **1991**, 167. (k) Bauernschmitt, R.; Ahlrichs, R. *J. Chem. Phys.* **1996**, *104*, 9047. (l) Dennington, R.; Keith, T.; Millam, J. M. *GaussView, Version 5*, Semichem, Inc.: Shawnee Mission, KS, **2009.** (m) Kelly, C. P.; Cramer, C. J.; Truhlar, D. G. *J. Phys. Chem. B* **2007**, *111*, 408.

5. Stoll, S.; Schweiger, A. EasySpin, a comprehensive software package for spectral simulation and analysis in EPR. *Journal of Magnetic Resonance* **2006**, *178*, 42.
6. Sato, M.; Mori, Y.; Iida, T. *Synthesis* **1992**, 539.
7. Tyler, L. A.; Olmstead, M. M.; Mascharak, P. K. *Inorg. Chem.* **2001**, *40*, 5408.
8. Parr, R. G.; Yang, W. Density-functional theory of atoms and molecules; Oxford University Press: New York, **1989**.
9. (a) Ballhausen, C. J *Introduction to Ligand Field Theory*, McGraw Hill New York **1962**, pp 259. (b) Figgis, B. N.; Hitchman, M. A. *Ligand Field Theory and its Applications*, Wiley-VCH New York, **2000**, pp139-140, 209-210.
10. Fourmond, V.; Jacques, P. A.; Fontecave, M.; Artero, V. *Inorg. Chem.* **2010,** *49*, 10338.
11. Muckermann, J. T.; Fujita, E. *Chem. Comm.* **2011**, *47*, 12456.

www.manaraa.com

CHAPTER 7

CONCLUSIONS

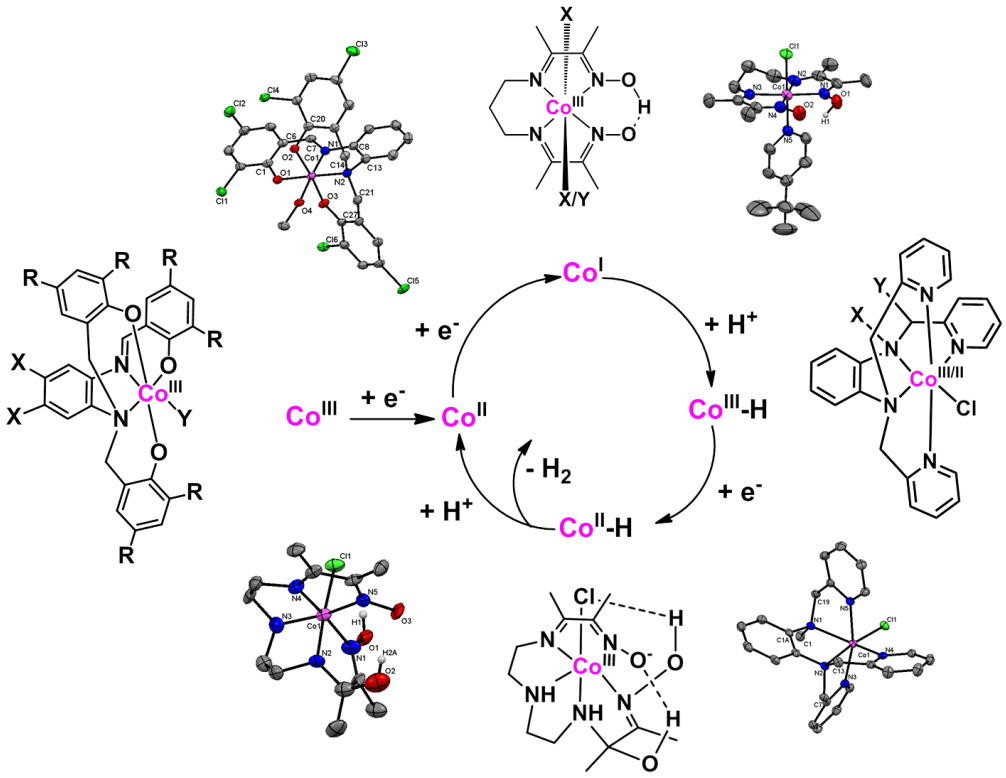

www.manaraa.com

CHAPTER 7

CONCLUSIONS

We designed several redox-active ligand architectures to optimize and understand the redox, electronic, and catalytic properties of their respective cobalt complexes towards proton and water reduction. The ligand design was varied from a pentadentate π-donor phenolate to a tetradentate acceptor oxime in order to reduce the overpotential of hydrogen generation in organic solvents (**Figure 7.1a**,**b**). We altered the substitution, axial ligands and axial ligand substitutions to vary electronic and catalytic properties for such tetra- or pentadentate ligand systems.

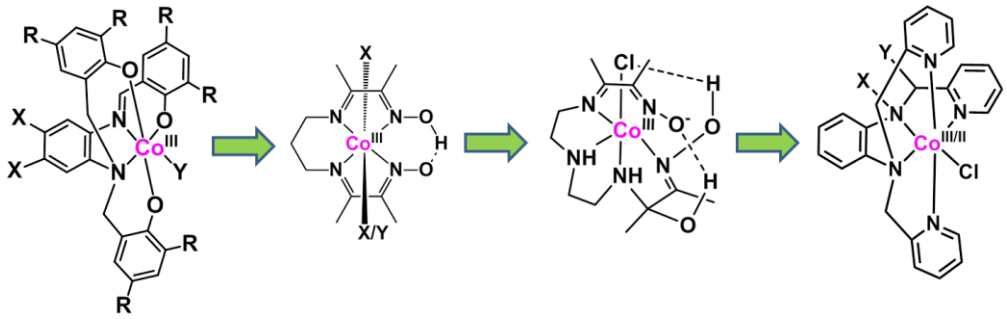

Figure 7.1. Modulation of ligand design towards proton and water reduction.

Knowledge of the nature of the active catalytic species enabled us to design the pentadentate oxime ligand which exhibited rich reaction chemistry along with suitable catalytic property in organic solvent (**Figure 7.1c**). The presence of several polar groups such as –OH and –NH and the absence of any aromatic rings make this complex water soluble, which is an added advantage.-Additionally, this complex exhibited excellent catalytic properties in water with low onset overpotential and high turnover number. We developed a similar redox-active π-acceptor pentadentate phenylene-bridged pyridine-rich ligand (**Figure 7.1d**) which provided extremely versatile reaction chemistry after complexation with cobalt. These complexes displayed catalytic properties at moderate to low-overpotential in acetonitrile with good turnover numbers.

www.manaraa.com

Furthermore, the water solubility and tunability of such complexes make them suitable candidates for water reduction. Therefore, water reduction was carried out with these complexes showing low onset overpotentials and high turnover numbers.

Finally, we incorporated $[Ru(bpy)_2]^{2+}$-based photosensitizer with one of the catalytic module (cobalt tetradentate oxime) to generate heterobimetallic $[Ru^{II}Co^{III}]$ species which displayed quenching of Co^{III} upon electron transfer from Ru^{II}* excited state.

In **Chapter 3**, cobalt(III) complexes of phenolate-rich $[N_2O_3]$ ligands were synthesized and characterized by multiple physico-chemical methods (**Figure 7.2**). Phenol substituents were varied from mild electron-withdrawing halogen to sterically bulky and electron-donating t-butyl group. A considerable change of electrochemical potential and electron acceptance rate were observed upon changing the phenolate substituents. The cobalt complex of chloro substitued phenolato ligand exhibited catalytic activity in the presence of weak acid such as acetic acid (HOAc) with an overpotential of 0.61 V. Bulk electrolysis at -1.8 $V_{Ag/AgCl}$ confirmed hydrogen generation with a TON of 11 after 3 hours with a Faradaic efficiency around 85 % in the presence of 100 equivalents of HOAc.

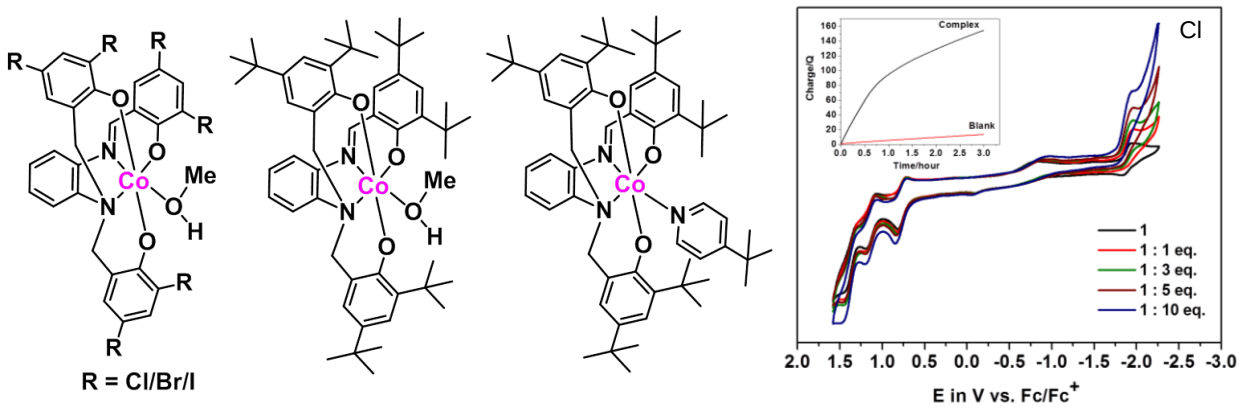

Figure 7.2. Various $Co^{III}[N_2O_3]$ systems and reactivity of chloro substituted complexes towards proton reduction in the presence of HOAc.

www.manaraa.com

In **Chapter 4**, cobalt(III) complexes of oxime-rich N_4 ligand were synthesized with chloride and substituted pyridine as axial ligands (**Figure 7.3**). Pyridine substitutions were altered from mild donating t-butyl, to strongly donating pyrrolidine, to electron-withdrawing benzoyl group. The identities of the redox species generated during electrochemistry were elucidated by means of CV, and ^{1}H-NMR titrations, EPR, and UV-visible spectroscopy, and DFT calculations. These complexes showed catalytic activity in the presence of mild-acid such as trifluoroacetic acid (TFA) with an overpotential of 0.35 V. Bulk electrolysis at -1.0 $V_{Ag/AgCl}$ confirmed hydrogen generation with a TON between 13-20 after 3 hours with a Faradaic efficiency around 85 % in the presence of 100 equivalents of TFA. A catalytic mechanism was proposed invoking a heterolytic pathway from Co^{II}-H species.

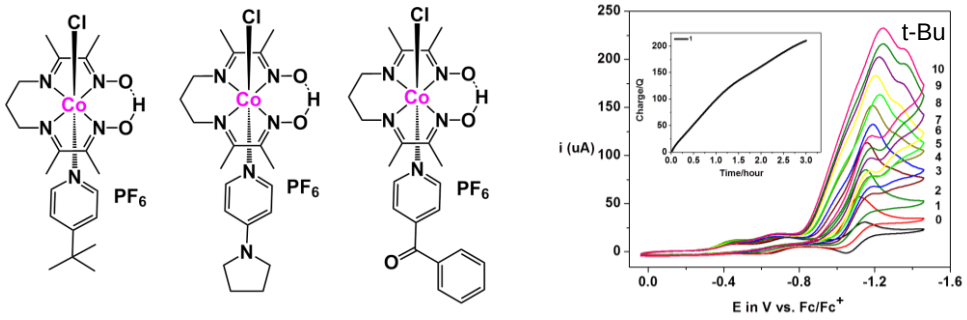

Figure 7.3. Various cobalt-oxime complexes with several axial substituents and its reactivity with TFA.

A heterobimetallic [$Ru^{II}Co^{III}$] complex based on this oxime as the bridging ligand was also synthesized and characterized by multiple physicochemical techniques (**Figure 7.4**). Both the cobalt module and [RuCo] complex exhibited electrocatalytic activity in the presence of TFA with the overpotential of 0.34 and 0.37 V, respectively. The hydrogen generation was confirmed by bulk-electrolysis experiment at -1.0 $V_{Ag/AgCl}$ in the presence of hundred equivalents of TFA. The corresponding TONs were found to be 7.2 and 7.0 after one hour, respectively, with a Faradaic efficiency of 70%. The transient absorption (TA) experiment reveals electron transfer

www.manaraa.com

from ruthenium to the cobalt center upon irradiating the complex at 500 nm light in either acetonitrile or in methanol. The photocatalytic activity of this complex towards hydrogen production is under investigation in the collaboration with Dr. Karen Mulfort at Argonne National Laboratory.

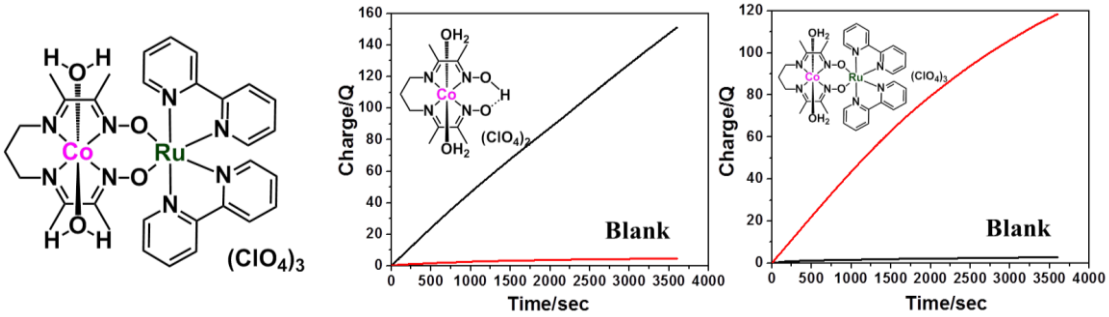

Figure 7.4. Cobalt and [RuCo] complexes based on oxime ligands and their activity with TFA.

In **Chapter 5**, cobalt(III) complex of pentadentate nitrogen-rich oxime ligand was synthesized and thoroughly characterized (**Figure 7.5**). Water incorporation was observed in the ligand framework during the complexation reaction. This complex displayed proton reduction activity in the presence of weak acid such as acetic acid and seems to operate in a molecular fashion. A catalytic mechanism was proposed invoking a heterolytic pathway from Co^{II}-H species. On the other hand, it can also generate hydrogen from neutral water at an overpotential of 0.65 V. This complex showed 6000 TON at -1.7 $V_{Ag/AgCl}$ after 18 hours period with neutral water and cobalt-based nanoparticles was found to be the active species for the catalysis.

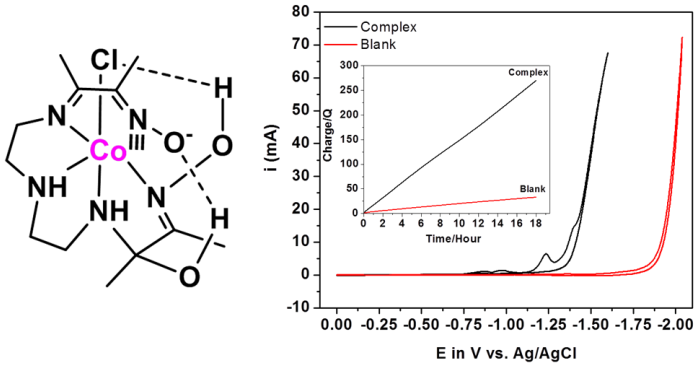

Figure 7.5. Cobalt complex of pentadentate oxime ligand and its activity towards water.

www.manaraa.com

In **Chapter 6**, Cobalt complexes of two pyridine-rich [$N_2N^{py}_3$] ligands were synthesized (**Figure 7.6**). Ligand transformation was observed from amine to imine to amide with the secondary amine containing ligand in the presence of cobalt, whereas this kind of oxidation can be prevented upon incorporating a methyl substituent on that particular nitrogen. The complexes exhibited proton reduction in the presence of weak acid such as acetic acid with an overpotential around 0.70 V. Bulk electrolysis at -1.7 $V_{Ag/AgCl}$ confirmed hydrogen generation with TON around 15 after three hours with Faradaic efficiency around 90 % in the presence of 100 equivalents of HOAc. These complexes was found to be water soluble and demonstrated water reduction activity with onset overpotential of 0.55 V (amide), and 0.70 V (amine). Bulk electrolysis at -1.7 $V_{Ag/AgCl}$ confirmed the presence of hydrogen with TON of 7200 and 6000 after 18 hours with a Faradaic efficiency around 95 % for amide and amine containing complexes, respectively. A catalytic mechanism was proposed invoking a heterolytic pathway from Co^{II}-H species.

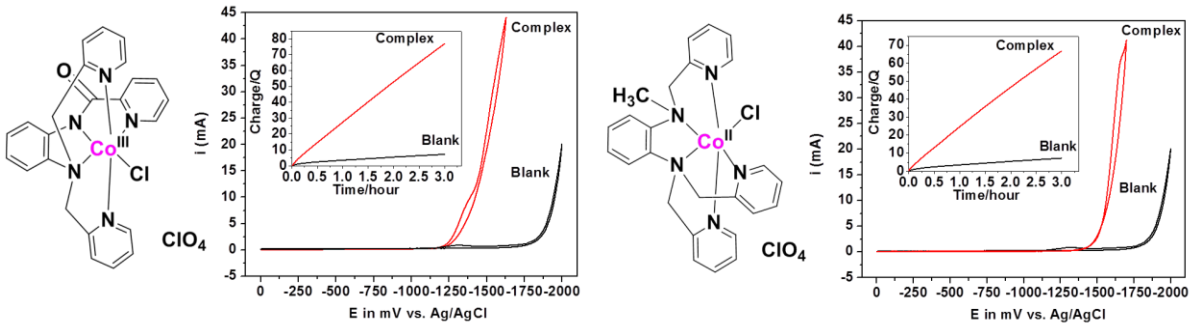

Figure 7.6. Cobalt complexes of pentadentate pyridine-rich ligand and its activity towards water.

In summary, we scanned a series of various ligand frameworks to optimize the electrocatalytic properties upon changing the electronic behavior. In addition, a [$Ru^{II}Co^{III}$]-based photocatalytic assembly was developed with selected catalytic module.

www.manaraa.com

A considerable understanding of the electronic and catalytic activity of cobalt complexes in various ligand frameworks enabled us to design and synthesize several heterobimetallic [RuCo] scaffolds based on phenanthroline ligand. Therefore, we synthesized complexes such as shown in **Figure 7.7**. The complex shown in the left side of **Figure 7.7** is a complex containing [$Ru^{II}Co^{III}$] scaffold whereas the complex in the other side is of [$Ru^{II}Co^{II}$] type. Generation of hydrogen by performing electron transfer from Ru^{II} to Co^{III} may not be viable, due to the lack of reactivity for the Co^{II} species to generate hydrogen.

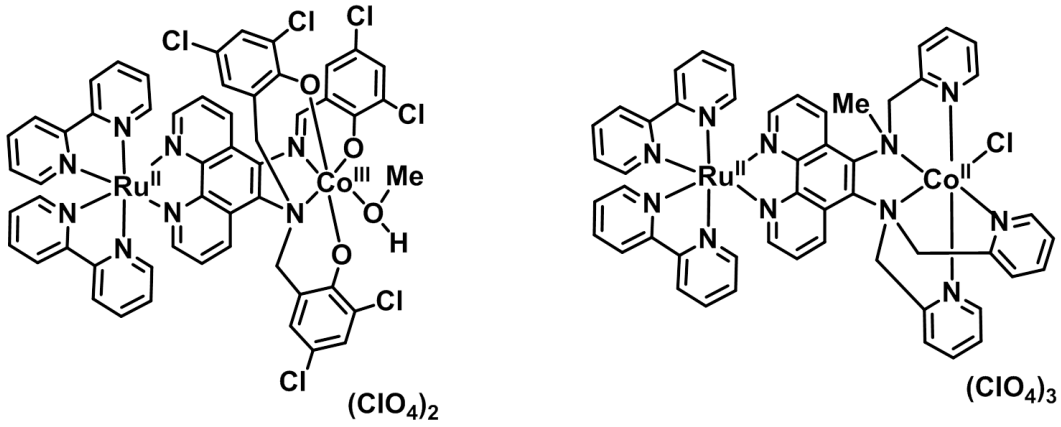

Figure 7.7. [$Ru^{II}Co^{III}$] and [$Ru^{II}Co^{II}$]-based heterobimetallic scaffold towards hydrogen production.

On the other hand, the [$Ru^{II}Co^{II}$] species can be promising due to the ease of formation of catalytically active Co^{I} species upon one electron transfer from Ru^{II} to Co^{II}. Although the transfer of electrons are theoretically feasible, a number of challenges are associated with this process, such as i) whether the electron will go to phenanthroline instead of bipyridine, ii) if it goes to phenanthroline (due to higher conjugation), whether it will stay there or reach to cobalt, and iii) when the electrons reach cobalt wheather it can do back electron transfer and recombine. Future studies will involve synthesis of such complexes and study of their electron transfer and photocatalytic activity towards hydrogen production.

www.manaraa.com

Appendix-I

Synthesis and Characterizations of the Complexes Not Included in Chapters

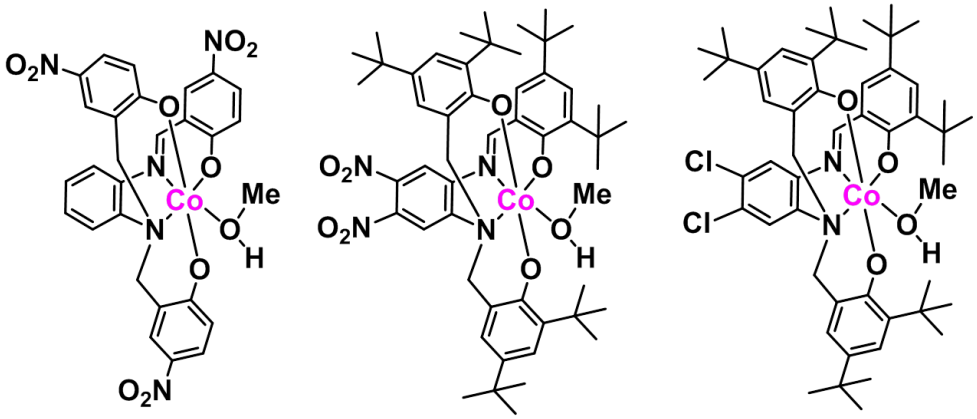

Figure AI.1. Cobalt(III) complexes of $[N_2O_3]$-based phenolate-rich ligands.

Synthesis of the precursors. The precursors 2-(chloromethyl)-4-nitrophenol, phenylenediamine and 4,5-dichlorobenzene-1,2-diamine were purchased from commercial sources whereas the other precursors 2,4-di-tert-butyl-6-(chloromethyl)phenol[8] and 4,5-dinitrobenzene-1,2-diamine[9] were synthesized according to methods already described in the literature.

Synthesis of the ligands. General procedure. Phenylenediamine (2 mmol) was treated with 2-(chloromethyl)-4-nitrophenol (6.2 mmol) in presence of triethylamine (8 mmol) in 80 mL of dichloromethane for three days under reflux to yield a yellow colored solution. The mixture was washed three times with brine solution (3 × 200 mL) to remove all the excess triethylamine, dried over anhydrous sodium sulfate and the crude product was isolated by solvent rotoevaporation. Unreacted chloride was removed by washing the solid with cold hexane to yield a yellow-colored solid. Similar procedure has been followed for the reaction of 4,5-dinitrobenzene-1,2-diamine or 4,5-dichlorobenzene-1,2-diamine with 2,4-di-tert-butyl-6-

www.manaraa.com

(chloromethyl)phenol in presence of triethylamine in dichloromethane to generate red and yellow color solution respectively.

2,2'-(((2-((2-hydroxy-5-nitrobenzyl)amino)phenyl)azanediyl)bis(methylene))bis(4-nitrophenol) – ***$H_3L^{\prime 4\text{-}NO_2}$***. Yield: 75%. IR (KBr, cm^{-1}) 3396(w) (OH); 3263(w) (NH); 3071(w) (Ar-CH); 2983(w), 2948(w) (alkyl-CH); 1591(m), 1490(m) (Ar-C-C); 1521(m), 1337(s), 1284(s) ($-NO_2$); 1162(m) (C-O). ^{1}H-NMR [400 MHz, d^6-DMSO, 300K] δ/ppm = 4.076 [s, 4H (CH_2)]; 4.372 [s, 2H (CH_2)]; 6.266 [d, 1H (aryl)]; 6.416 [t, 1H (aryl)]; 6.676 [d, 2H (aryl)]; 6.75 [t, 1H (aryl)]; 6.94 [d, 1H (aryl)]; 7.113 [d, 1H (aryl)]; 7.862 [dd, 2H (aryl)]; 7.944 [dd, 1H (aryl)]; 7.999 [d, 1H (aryl)]; 8.062 [d, 2H (aryl)]. ESI pos. in MeOH: m/z = 561.98 for $[H_3L^{\prime 4\text{-}NO_2} + H^+]^+$.

6,6'-(((2-((3,5-di-tert-butyl-2-hydroxybenzyl)amino)-4,5-dinitrophenyl)azanediyl) bis (methylene))bis(2,4-di-tert-butylphenol) – ***$(NO_2)_2H_3L^{\prime 2,4\text{-}t\text{-}bu}$***. Yield: 80%. IR (KBr, cm^{-1}) 3607(w), 3405(w) (OH); 3326(w) (NH); 3078(w) (Ar-CH); 2958(s), 2868(s) (alkyl-CH and t-bu); 1596(s), 1481(s) (Ar-C-C); 1545(s), 1364(s), 1273(s) (-NO2); 1149(m) (C-O). ^{1}H-NMR [400 MHz, $CDCl_3$, 300K] δ/ppm = 1.245 [s, 36H (t-butyl)]; 1.310 [s, 9H (t-butyl)]; 1.43 [s, 9H (t-butyl)]; 3.855 [s, 2H (CH_2)]; 4.248 [s, 2H (CH_2)]; 4.367 [s, 2H (CH_2)]; 5.691 [s, 1H (OH)]; 6.343 [s, 2H (OH)]; 6.942 [s, 1H (aryl)]; 7.031 [d, 2H (aryl)]; 7.157 [q, 3H (aryl)]; 7.329 [s, 1H (NH)]; 7.387 [d, 1H (aryl)]; 7.931 [s, 1H (aryl)]. ESI pos. in MeOH: m/z = 859.55 for $[(NO_2)_2H_3L^{\prime 2,4\text{-}t\text{-}bu} + Li^+]^+$.

6,6'-(((4,5-dichloro-2-((3,5-di-tert-butyl-2-hydroxybenzyl)amino) phenyl)azanediyl) bis (methylene))bis(2,4-di-tert-butylphenol) – ***$Cl_2H_3L^{\prime 2,4\text{-}t\text{-}bu}$***. Yield: 85%. IR (KBr, cm^{-1}) 3612(w) (OH); 3328(w) (NH); 3070(w) (Ar-CH); 2959(s), 2906(m), 2868(m) (alkyl-CH and t-bu); 1598(w), 1482(s) (Ar-C-C); 1162(m) (C-O). ^{1}H-NMR [400 MHz, $CDCl_3$, 300K] δ/ppm = 1.244

www.manaraa.com

[s, 36H (t-butyl)]; 1.323 [s, 9H (t-butyl)]; 1.426 [s, 9H (t-butyl)]; [3.803 [d, 2H (CH_2)]; 4.133 [d, 2H (CH_2)]; 4.253 [s, 2H (CH_2)]; 6.956 [s, 2H (aryl)]; 7.000 [s, 2H (aryl)]; 7.082 [s, 1H (aryl)]; 7.132 [s, 2H (aryl)]; 7.338 [s, 1H (aryl)]. ESI pos. in MeOH: m/z = 831.47 for $[Cl_2H_3L'^{2,4\text{-t-bu}} + H^+]^+$.

The complexes. Caution: Perchlorate salts are potentially explosive and should be handled with utmost care and in small quantities. Complexes **1**-**3** have been synthesized under aerobic conditions using the general procedure described as follows: To a 30 mL solution of ligand in dichloromethane (1 mmol) sodium methoxide (0.162 g, 3 mmol) in 30 mL of methanol was added and the mixture was stirred for 10 minutes. A 20 mL methanol solution of $[Co(H_2O)_6](ClO_4)_2$ (0.365 g, 1 mmol) was added dropwise to the mixture over period of 5 minutes. After the addition was complete, the solution was refluxed for 4 hours to ensure the completion of reaction and the mixture was concentrated to 10 mL. Slow evaporation of the solvent gave rise to brown colored precipitate which was collected by vaccum filtration. Further recrystalization form different solvent mixtures gave crystalline pure product.

$[Co^{III}(L^{4\text{-}NO_2})MeOH]$ **(1)**. *H_2O* X-ray quality crystal grown from DCM/ACN (1:1) to isolate water coordinated complex. For physical characterization, original methanol coordinated complex have been used. Yield. 80%. IR (KBr, cm^{-1}) 3421(w) (OH); 3063(w) (Ar-CH); 2930(w) (alkyl-CH); 1599(s), 1304(s) (NO_2); 1580(s) (C=N); 1481(s) (Ar-C-C); 1095(s) (C-O); No ClO_4^-. ^{1}H-NMR [400MHz, d^6-DMSO, 300K] δ/ppm = 3.151 [s, 3H (CH_3)]; 4.096 [s, 1H (OH)]; 4.18 [d, 2H (CH_2)]; 4.789 [d, 2H (CH_2)]; 6.398 [d, 2H (aryl)]; 7.161 [t, 1H (aryl)]; 7.375 [t, 1H (aryl)]; 7.435 [d, 1H (aryl)]; 7.554 [d, 2H (aryl)]; 7.756 [d, 1H (aryl)]; 7.801 [s, 1H (aryl)]; 8.205 [d, 1H (aryl)]; 8.260 [d, 2H (aryl)]; 8.692 [s, 1H (N=CH)];. ESI pos. in MeOH: m/z = 638.0336 for $[Co^{III}(L^{4\text{-}NO_2}) + Na^+]^+$. Anal. Calcd for $C_{28}H_{24}CoN_5O_{11}$: C, 50.54; H, 3.64; N, 10.52. Found: C,

www.manaraa.com

50.08; H, 3.87; N, 10.77.

[$Co^{III}((NO_2)_2(L^{2,4\text{-}t\text{-}bu}))MeOH$] **(2)**. *MeOH. 0.5* H_2**O** Recrystallized from MeOH/DCM (1:1). Yield. 85%. IR (KBr, cm^{-1}) 3459(w) (OH); 3060(w) (Ar-CH); 2954(s), 2868(m) (t-butyl and alkyl-CH); 1579(s) (C=N); 1541(s), 1525(s), 1360(s) (NO_2); 1473(m) (Ar-C-C); 1179(m) (C-O); No ClO_4^-. ^{1}H-NMR [400MHz, d^6-DMSO, 300K] δ/ppm = 0.849 [s, 18H (t-butyl)]; 0.987 [s, 18H (t-butyl)]; 1.218 [s, 9H (t-butyl)]; 1.590 [s, 9H (t-butyl)]; 3.145 [d, 3H (CH_3)]; 4.013 [d, 2H (CH_2)]; 4.184 [q, 1H (OH)]; 4.961 [d, 2H (CH_2)]; 6.508 [s, 2H (aryl)]; 6.579 [s, 2H (aryl)]; 7.035 [s, 1H (aryl)]; 7.345 [s, 1H (aryl)]; 7.623 [s, 1H (aryl)]; 8.380 [s, 1H (aryl)]; 9.152 [s, 1H (N=CH)]. ESI pos. in MeOH: m/z = 929.4259 for [$Co^{III}((NO_2)_2(L^{2,4\text{-}t\text{-}bu}))+ Na^+]^+$. Anal. Calcd for $C_{53}H_{76}CoN_4O_{9.5}$: C, 64.95; H, 7.82; N, 5.72. Found: C, 64.61; H, 7.51; N, 6.22.

[$Co^{III}(Cl_2L^{2,4\text{-}t\text{-}bu})MeOH$] **(3)**. *1.5* H_2O Recrystallized from MeOH/DCM (1:1). Yield. 90%. IR (KBr, cm^{-1}) 3443(w) (OH); 3047(w) (Ar-CH); 2958(s), 2904(m), 2868(m) (t-butyl and alkyl-CH); 1605(s) (C=N); 1470(s) (Ar-C-C); 1127(m) (C-O); No ClO_4^-. ^{1}H-NMR [400MHz, d^6 DMSO, 300K] δ/ppm = 0.864 [s, 18H (t-butyl)]; 1.032 [s, 18H (t-butyl)]; 1.243 [s, 9H (t-butyl)]; 1.618 [s, 9H (t-butyl)]; 3.154 [d, 3H (CH_3)]; 3.901 [d, 2H (CH_2)]; 4.087 [q, 1H (OH)]; 4.862 [d, 2H (CH_2)]; 6.490 [s, 2H (aryl)]; 6.569 [s, 2H (aryl)]; 7.078 [s, 1H (aryl)]; 7.296 [s, 1H (aryl)]; 7.544 [s, 1H (aryl)]; 7.958 [s, 1H (aryl)]; 8.520 [s, 1H (N=CH)]. ESI pos. in MeOH: m/z = 885.3900 for [$Co^{III}(Cl_2L^{2,4\text{-}t\text{-}bu})+ H^+]^+$. Anal. Calcd for $C_{52}H_{74}CoN_2O_{5.5}$: C, 66.09; H, 7.89; N, 2.96 Found: C, 65.92; H, 7.52; N, 3.56.

www.manaraa.com

Table AI.1. Crystal Data for the complexes **1**, **2**, and **3**.

	1	**2**	**3**
Empirical formula	$C_{33}H_{29}CoN_8O_{10}$	$C_{53.5}H_{78}CoN_4O_{10}$	$C_{52}H_{71}Cl_2CoN_2O_4$
Formula weight	756.57	996.13	917.94
Temperature (K)	100.1(2)	100(2)	100(2)
Wavelength (Å)	0.71073	0.71073	0.71073
Crystal system, space group	Triclinic, P-1	Monoclinic, P21/c	Triclinic, P-1
a (Å)	11.4337(8)	13.196(2)	12.2154(10)
b (Å)	12.5296(8)	38.556(6)	14.5086(12)
c (Å)	13.2100(9)	11.3194(16)	14.9325(11)
α (º)	88.368(4)	90	91.171(4)
β (º)	66.364(3)	111.054(5)	109.941(3)
γ (º)	77.712(4)	90	95.805(4)
Volume ($Å^3$)	1690.6(2)	5374.8(14)	2470.8(3)
Z	2	4	2
Calculated density (Mg/m^3)	1.486	1.231	1.234
Absorption coefficient (mm^{-1})	0.578	0.378	0.500
F (000)	780	2136	980
R(F) (%)	6.50	6.59	4.46
R_w(F) (%)	14.71	16.05	5.48

www.manaraa.com

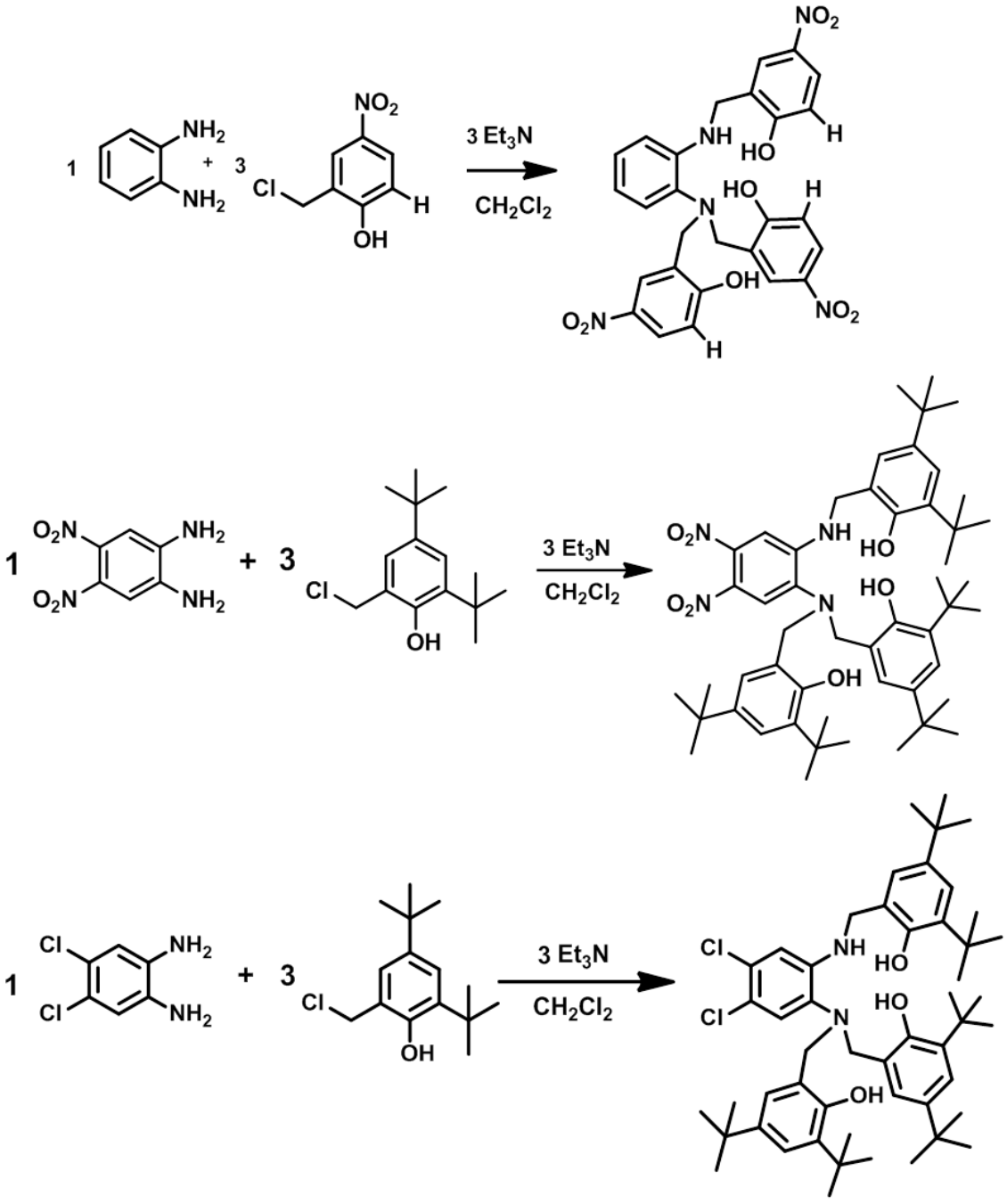

Figure AI.2. Synthetic scheme for the ligands.

www.manaraa.com

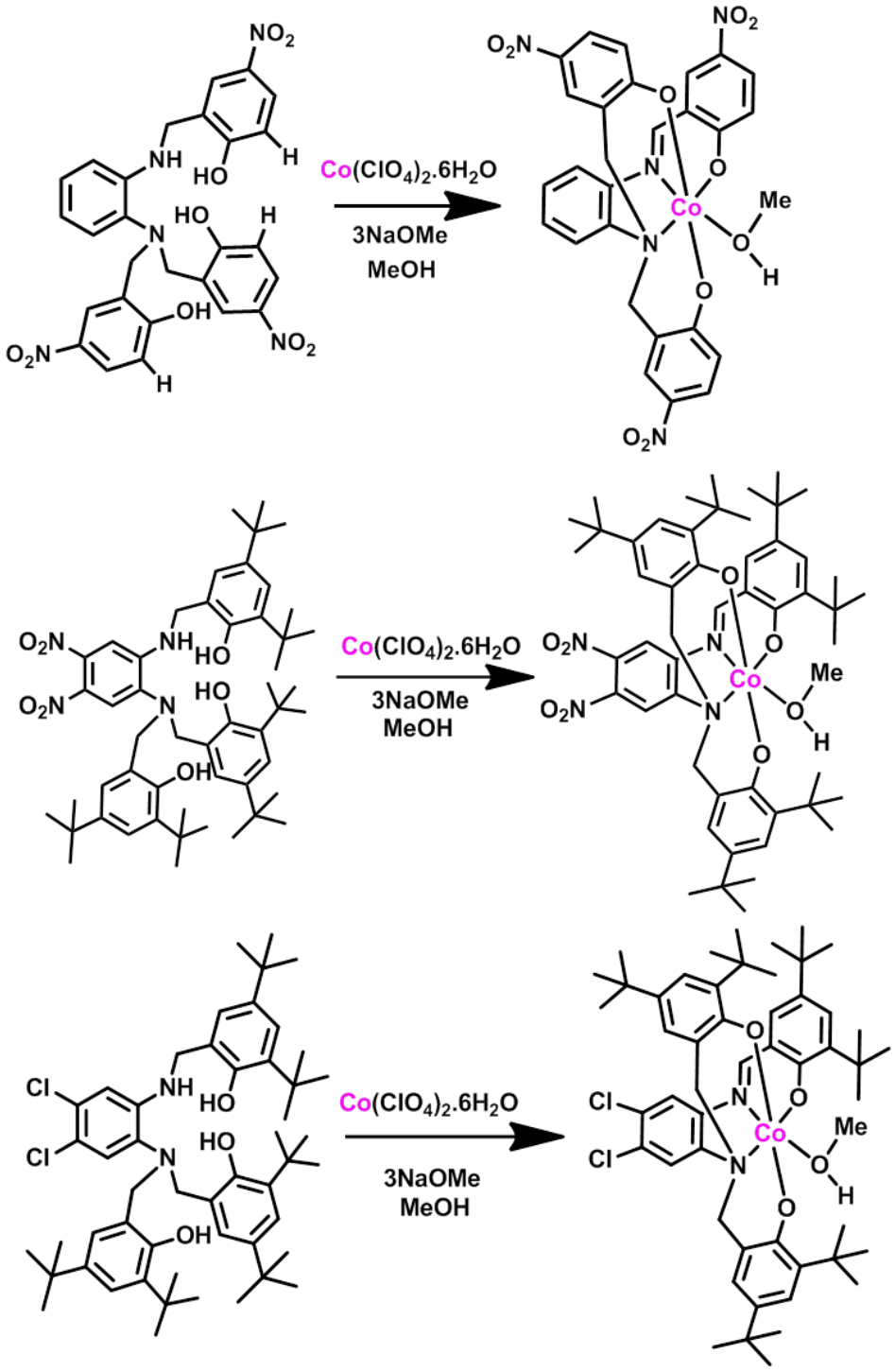

Figure AI.3. Synthetic scheme for the complexes **1-3** (top to bottom)**.**

www.manaraa.com

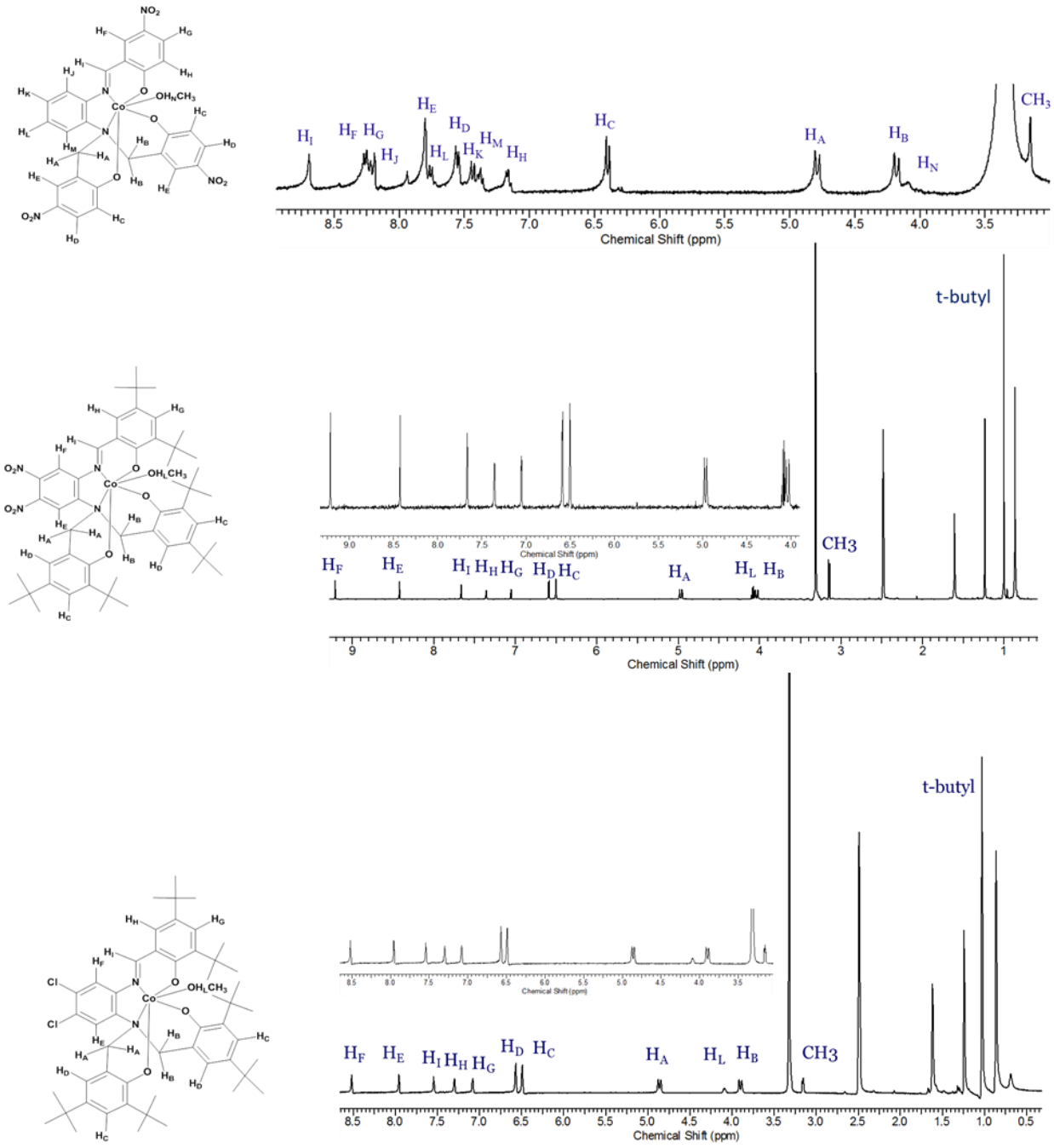

Figure AI.4. ^{1}H-NMR spectra for **1-3** in d^{6}-DMSO (top to bottom).

www.manaraa.com

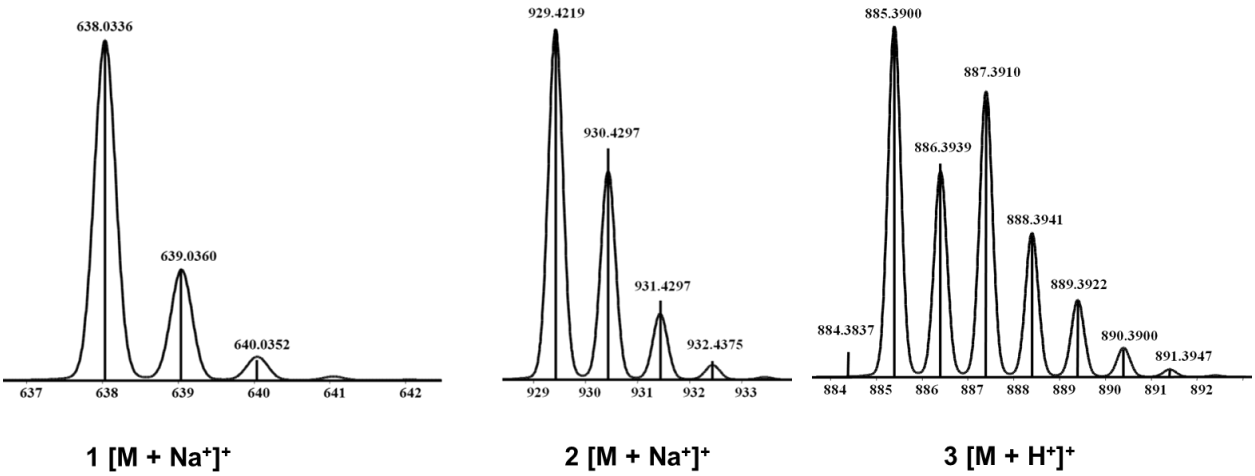

Figure AI.5. Experimental (bars) and simulated (line) isotopic distribution for the molecular ions of the complexes **1**-**3** (left to right) in CH_3OH.

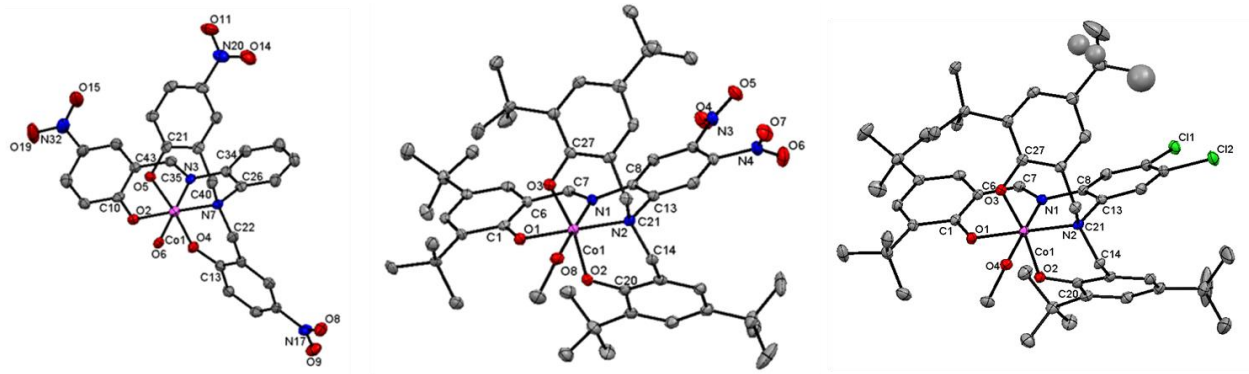

Figure AI.6. The ORTEP representation of the cations of **1**, **2**, and **3** at 50% ellipsoid probability. Bond lengths are in Å: For **1**: Co(1)-N(3): 1.874(3); Co(1)-N(7): 1.963(3); Co(1)-O(2): 1.874(3); Co(1)-O(4): 1.882(3); Co(1)-O(5): 1.897(3); Co(1)-O(6): 1.931(3). For **2**: Co(1)-N(1): 1.875(2); Co(1)-N(2): 1.981(2); Co(1)-O(1): 1.875(2); Co(1)-O(2): 1.888(2); Co(1)-O(3): 1.896(2); Co(1)-O(4): 1.984(2). For **3**: Co1-N1: 1.8565, Co1-N2: 1.984, Co1-O1: 1.882, Co1-O2: 1.9154, Co1-O3: 1.9407, Co1-O4: 1.9816.

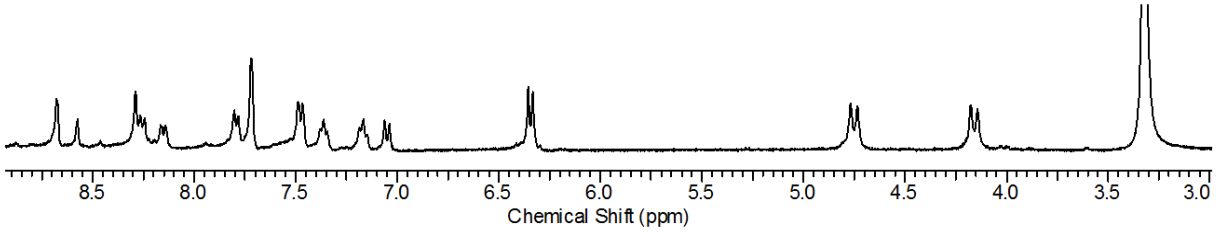

Figure AI.7. ^{1}H-NMR spectra for **1** in d^6-DMSO after recrystallization from CH_2Cl_2/CH_3CN (1:1) mixture.

www.manaraa.com

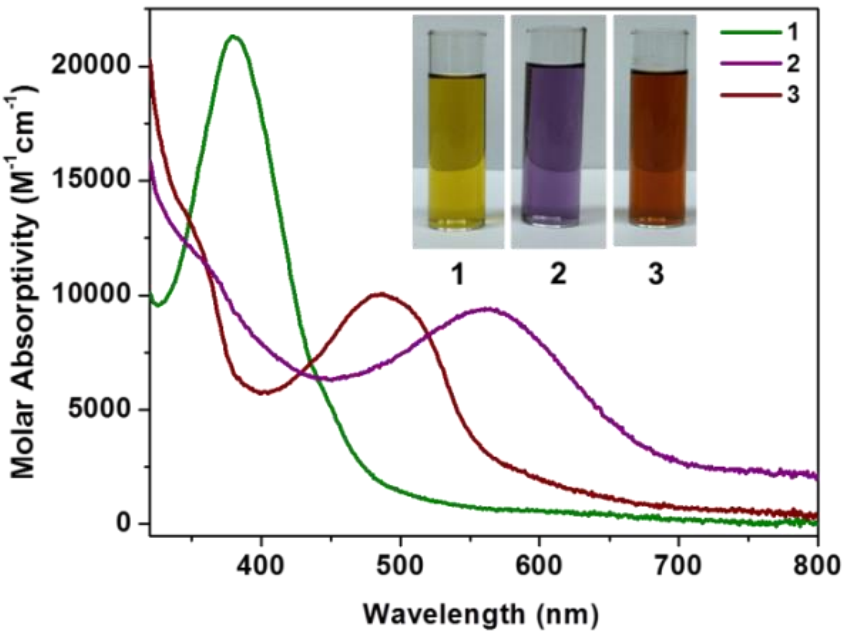

Figure AI.8. UV-visible spectra with the corresponding color for **1-3** in CH_3CN (1×10^{-5} M).

Table AI.2. UV-visible parameters of complex **1-3** in CH_3CN.

	λ (nm) |ε ($M^{-1}cm^{-1}$)|	λ (nm) |ε ($M^{-1}cm^{-1}$)|	λ (nm) |ε ($M^{-1}cm^{-1}$)|	λ (nm) |ε ($M^{-1}cm^{-1}$)|
1	379 |21216|			607 |1107|
2	365 |10880|		565 |9390|	777 |834|
3	356 |12183|	485 |10048|	507 |10060|	762 |1350|

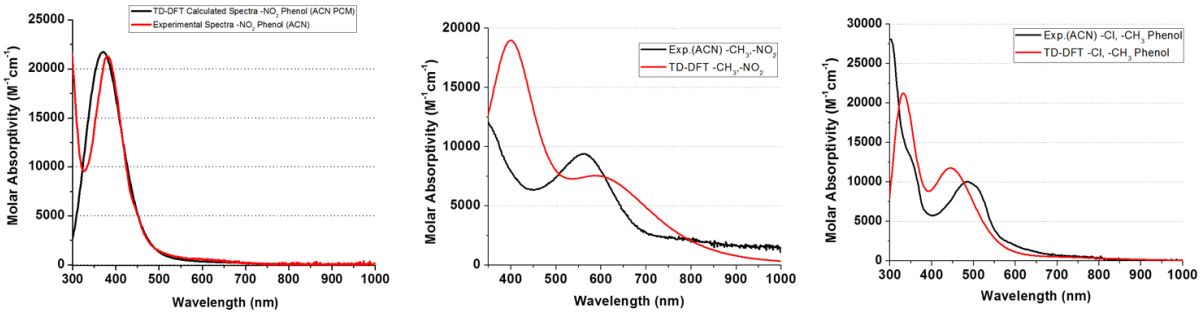

Figure AI.9. TD-DFT calculated UV-visible spectra for **1-3** by using CH_3CN as the solvent model.

www.manaraa.com

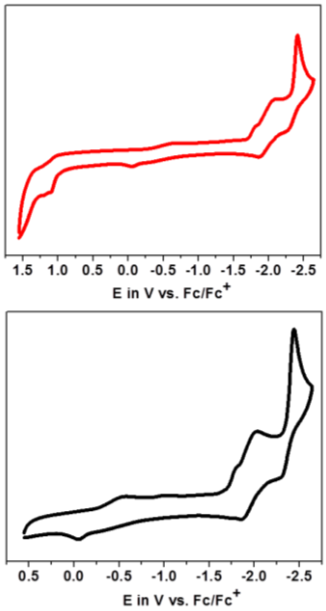

Figure AI.10. Cyclic voltammogram of complex **1** in CH_3CN.

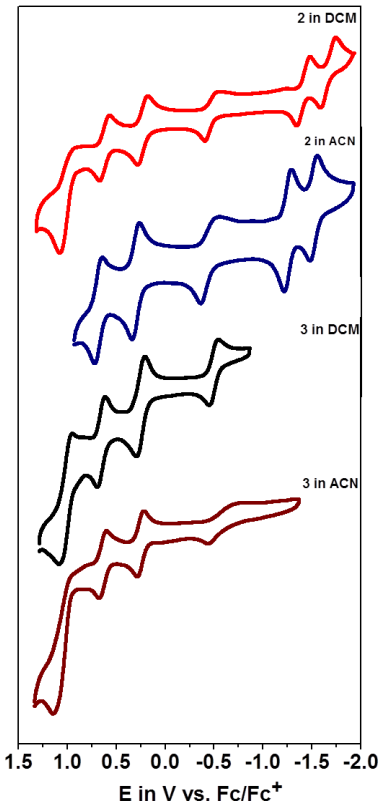

Figure AI.11. Cyclic voltammograms of **2** and **3** in dichloromethane and acetonitrile. Conditions: 0.1 M $TBAPF_6$ as supporting electrolyte; Glassy carbon (working), Pt wire (counter) and Ag/AgCl (reference); Scan rate: 100 mVs^{-1}**.**

www.manaraa.com

Table AI.3. Cyclic voltammetric parameters for complex **1-3** in (a) CH_2Cl_2 and (b) CH_3CN.

(a) CH_2Cl_2:

	3^{rd} $PhO^-/PhO^\bullet$ $E_{½}$, V (ΔE, V) $\lvert i_{pc}/i_{pa}\rvert$	2^{nd} $PhO^-/PhO^\bullet$ $E_{½}$, V (ΔE, V) $\lvert i_{pc}/i_{pa}\rvert$	1^{st} $PhO^-/PhO^\bullet$ $E_{½}$, V (ΔE, V) $\lvert i_{pc}/i_{pa}\rvert$	Co(III)/Co(II) $E_{½}$, V (ΔE, V) $\lvert i_{pc}/i_{pa}\rvert$	$NO2/^\bullet NO2^-$ $E_{½}$, V (ΔE, V) $\lvert i_{pc}/i_{pa}\rvert$
1	N/A	N/A	N/A	N/A	N/A
2	+1.00 (0.15) |N/A|	+0.68 (0.10) |0.81|	+0.28 (0.11) |0.80|	-0.38 (0.12) |0.75|	-1.32 (0.14) |1.18| -1.59 (0.15) |1.07|
3	+1.02 (0.13) |0.69|	+0.65 (0.09) |0.86|	+0.25 (0.09) |1.00|	-0.49 (0.09) |1.06|	N/A

(b) CH_3CN:

	3^{rd} $PhO^-/PhO^\bullet$ $E_{½}$, V (ΔE, V) $\lvert i_{pc}/i_{pa}\rvert$	2^{nd} $PhO^-/PhO^\bullet$ $E_{½}$, V (ΔE, V) $\lvert i_{pc}/i_{pa}\rvert$	1^{st} $PhO^-/PhO^\bullet$ $E_{½}$, V (ΔE, V) $\lvert i_{pc}/i_{pa}\rvert$	Co(III)/Co(II) $E_{½}$, [E_{pc}; E_{pa}], V (ΔE, V) $\lvert i_{pc}/i_{pa}\rvert$	$NO2/^\bullet NO2^-$ $E_{½}$, V (ΔE, V) $\lvert i_{pc}/i_{pa}\rvert$	$C{=}N/C^\bullet{-}N^-$ $E_{½}$, V (ΔE, V) $\lvert i_{pc}/i_{pa}\rvert$
1	N/A	N/A	-1.06 (N/A) |N/A|	E_{pc}: -0.57 E_{pa}: -0.32	-1.79 (N/A) |N/A| -1.96 (N/A) |N/A|	-2.35 (N/A) |N/A|
2	+1.18 (N/A) |N/A|	+0.67 (0.07) |0.64|	+0.30 (0.07) |0.91|	-0.44 (0.17) |0.75|	-1.24 (0.07) |1.01| -1.50 (0.07) |1.38|	E_{pc}: -2.20 E_{pa}: -1.94
3	+1.06 (0.18) |N/A|	+0.64 (0.08) |0.85|	+0.25 (0.07) |0.92|	E_{pc}: -0.71 E_{pa}: -0.43	N/A	-2.24 (0.11) |N/A| -2.47 (0.07) |N/A|

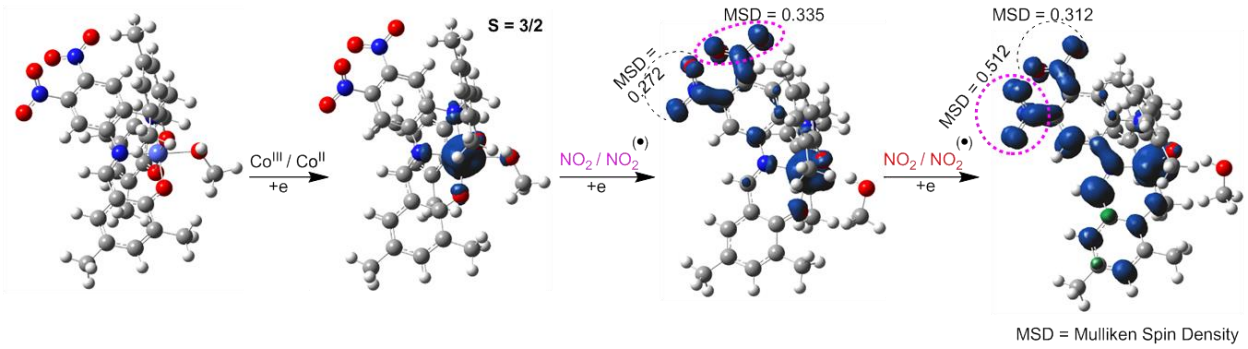

Figure AI.12. Spin-density plot for first three reductions of complex **2**.

www.manaraa.com

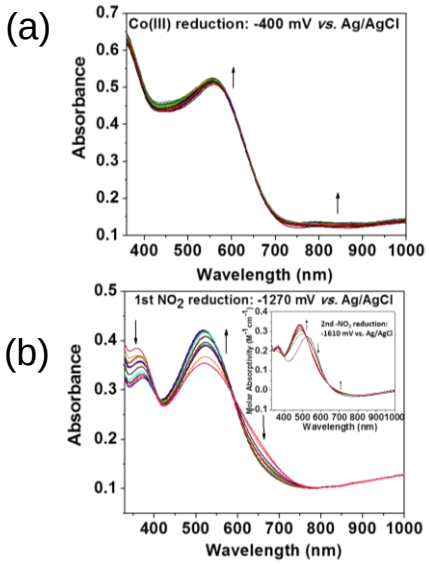

Figure AI.13. (a) Spectral changes upon electrochemical reduction of the Co^{III}/Co^{II} process in **2** in acetonitrile. The applied potential was –0.40 $V_{Ag/AgCl}$ over a period of 10 min.; (b) Spectral changes upon second reduction of **2** in acetonitrile. The applied potential was –1.27 $V_{Ag/AgCl}$ and the graph represents the behavior after 10 min. Inset: Spectral changes upon third reduction of **2** in acetonitrile. The applied potential was –1.61 $V_{Ag/AgCl}$.

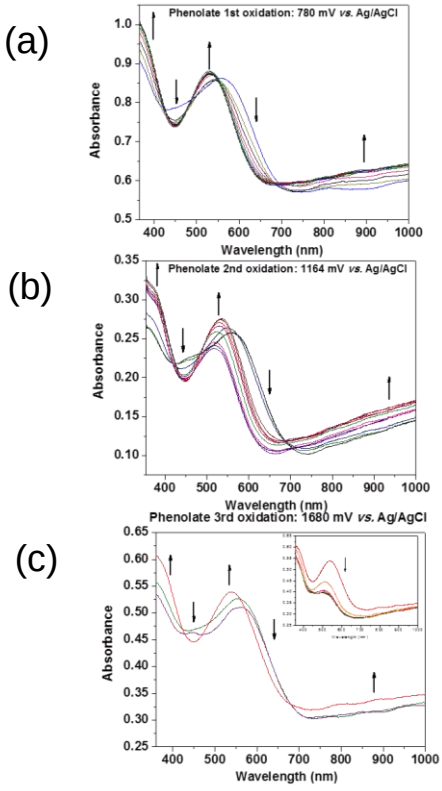

Figure AI.14. Spectroelectrochemical behavior after phenolate oxidations for complex **2**. (a) phenolate 1st oxidation (A.P.: 0.78 $V_{Ag/AgCl}$), (b) phenolate 2nd oxidation (A.P.: 1.16 $V_{Ag/AgCl}$) (c) phenolate 3rd oxidation (A. P.: 1.68 $V_{Ag/AgCl}$).

www.manaraa.com

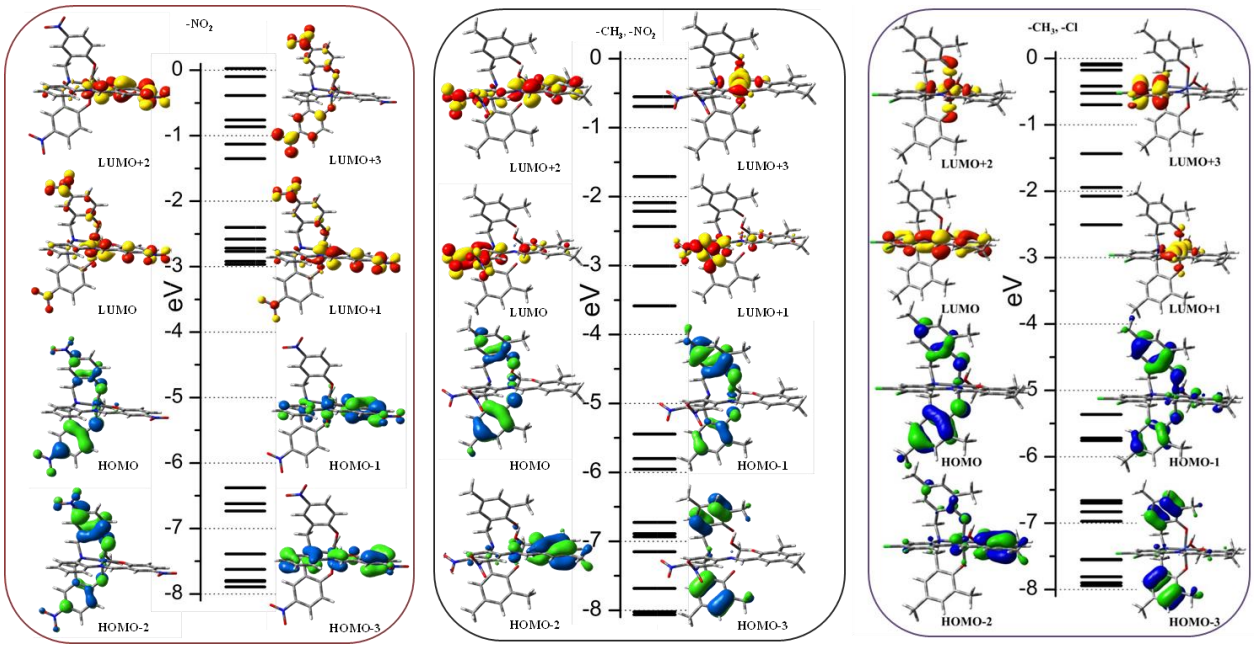

Figure AI.15. MO ladder for complex **1-3**.

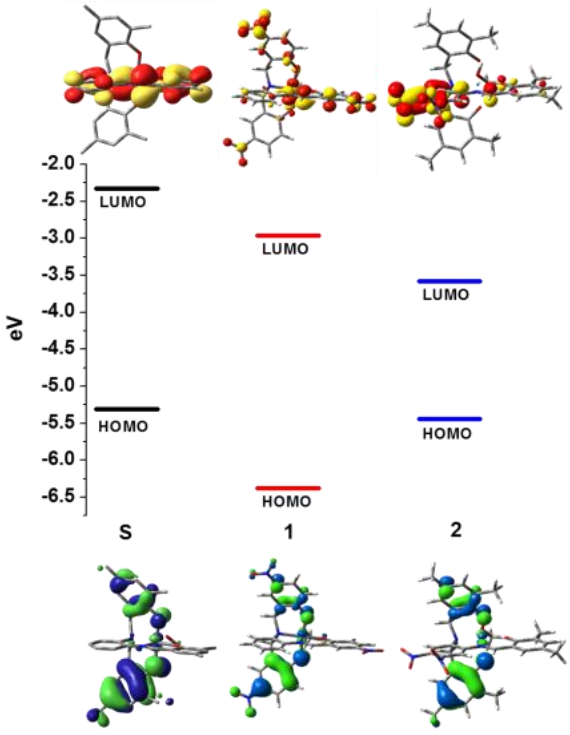

Figure AI.16. Comparison of MO ladder between HOMO and LUMO for complex **1** and **2** in comparison with *[Co^{III}(L$^{t\text{-}Bu}$)MeOH]* (Complex **4** from previous chapter).

www.manaraa.com

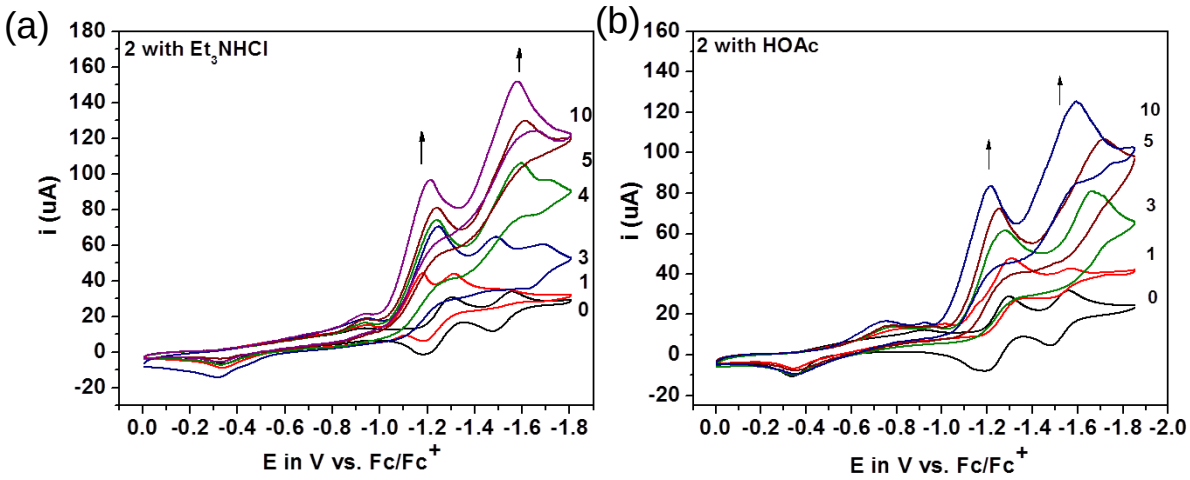

Figure AI.17. (a) Cyclic voltammetric experiment of **2** in CH_3CN in the presence of Et_3NHCl (0-10 eq) (a) Cyclic voltammetric experiment of **2** in CH_3CN in the presence of HOAc (0-10 eq).

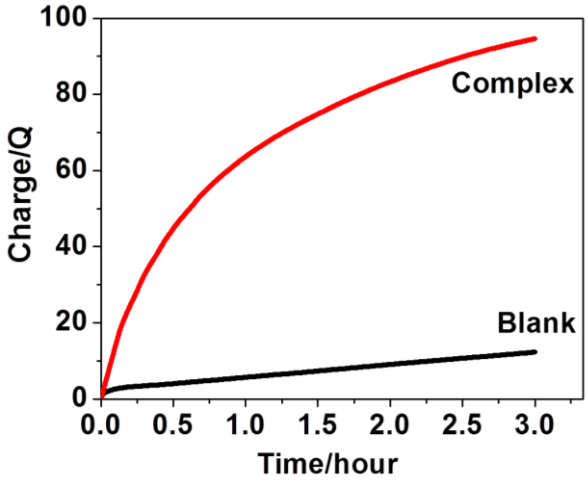

Figure AI.18. Plot of charge *versus* time during bulk electrolysis of 2 *versus* blank in presence of HOAc.

Table AI.4. Catalytic parameters for **2** in CH_3CN.

Parameters	**2 (HOAc)**
Overpotential (V) (10 eq. HOAc)	0.02
TON/3h (4.0×10^{-6} mol) (100 eq HOAc)	2.4
Faradaic efficiency (%)	50

www.manaraa.com

A pyridine-rich schiff-base ligand was synthesized following literature procedure.[1] Cobalt was introduced in the ligand framework as $Co(ClO_4)_2.6H_2O$ salt. This ligand exhibited unique reactivity towards complex formation as it rearranges to form imidazole containing bidentate ligand which forms hexa-coordinated complex with Co^{II} (**Figure AI.19**). We were able to obtain the crystal structure (**Figure AI.20**) of this complex (**4**) from methanol, which ascertains the identity of the rearranged product. Due to the hexacoordinated nature of the final complex we did not pursue proton reduction with this.

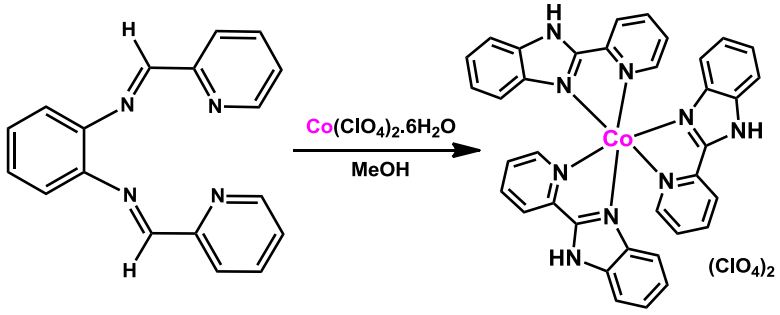

4

Figure AI.19. Synthetic scheme for the formation of rearranged Co^{II} complex (**4**).

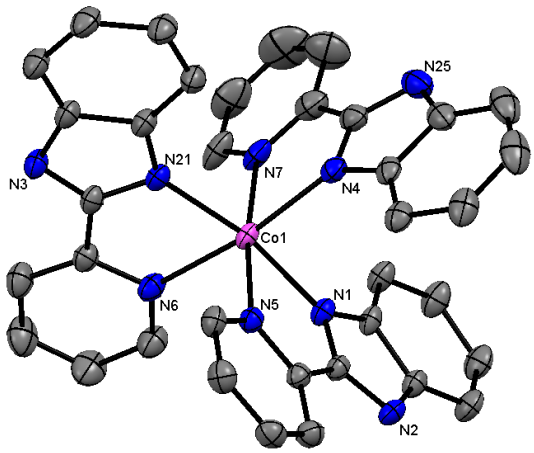

Figure AI.20. The ortep representation of complex **4** with 50% ellipsoidal probability.

C**omplex (4)**. CH_3OH. 2.5 H_2O: X-ray quality crystal grown from methanol. Yield. 45%. IR (KBr, cm^{-1}) 3421(s) (OH); 1607 (s) (C=N); 1442 (s) (Ar-C-C); 1090 (s) (ClO_4^-). ESI pos. in

www.manaraa.com

MeOH: m/z = 642.1565 for $[M - 2H^+]^+$. Anal. Calcd for $C_{37}H_{36}Cl_2CoN_9O_{11.5}$: C, 48.27; H, 3.94; N, 13.69. Found: C, 47.91; H, 3.58; N, 13.52. Evan's experiment suggested high-spin configuration.

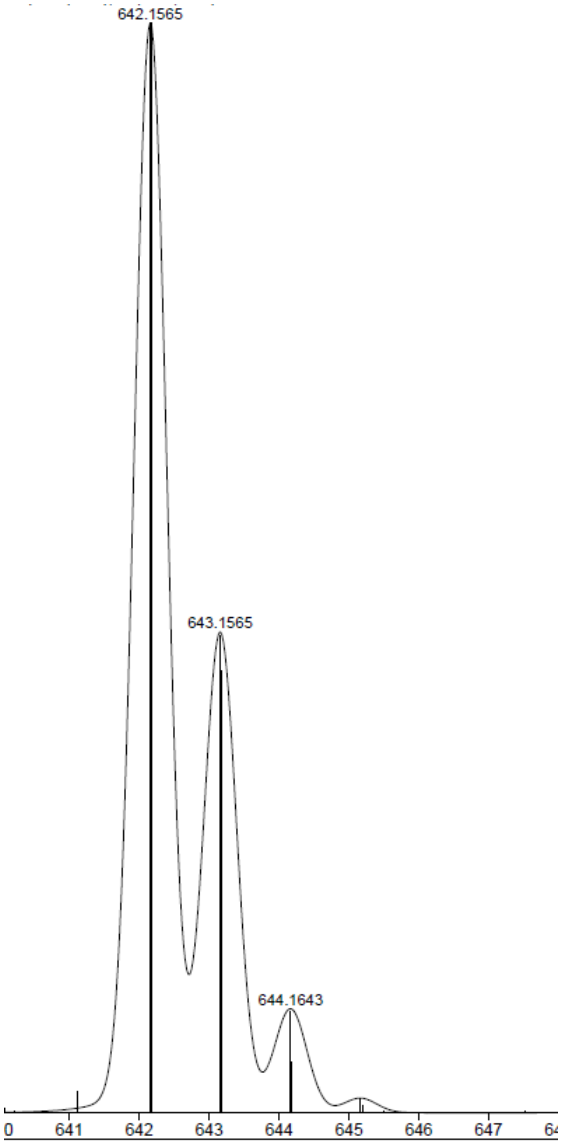

Figure AI.21. Experimental (bars) and simulated (line) isotopic distribution for the molecular ions of complex **4.**

www.manaraa.com

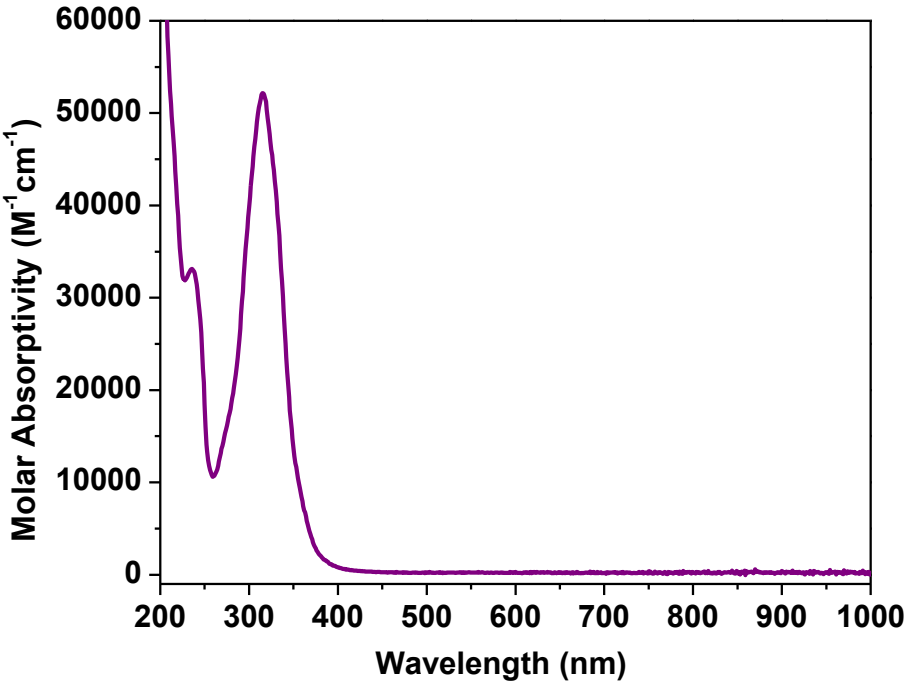

Figure AI.22. UV-visible spectra of **4** (Spectra: 10^{-5} M) in CH_3CN.

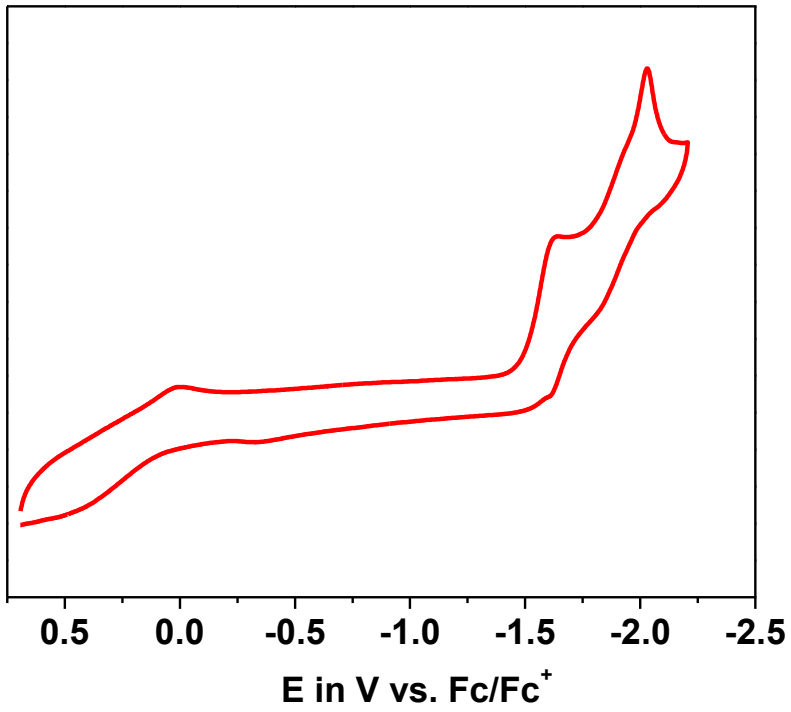

Figure AI.23. Cyclic voltammetry of **4** (Spectra: 10^{-5} M) in CH_3CN.

www.manaraa.com

The comparison between the crystal structure and the optimized structure revealed the high-spin nature of this complex (**Figure AI.24).**

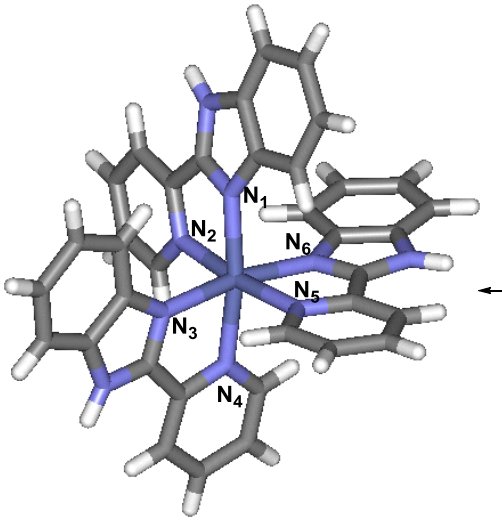

	Co-N_1	Co-N_2	Co-N_3	Co-N_4	Co-N_5	Co-N_6
Crystal Structure	2.093	2.156	2.110	2.164	2.154	2.099
High spin DFT	2.164	2.223	2.173	2.231	2.209	2.180
Deviation from crystal	0.071	0.067	0.063	0.067	0.055	0.081
Low spin DFT	2.250	2.039	2.028	2.316	2.032	2.021
Deviation from crystal	0.157	0.117	0.082	0.152	0.122	0.078

Bond distances are in Å

High spin (S=3/2) is lower in energy than low spin (S=1/2) structure by 13.5 kcal/mol (ΔG)

Figure AI.24. Comparison of bond lengths between the crystal structures with the corresponding DFT calculated high-spin and low-spin structure.

www.manaraa.com

A pyridine-rich water coordinated cobalt(III) complex (**5**) was synthesized. To a solution of complex (**4**) (from chapter **7**) (1 mmol, 0.589 g) in 10 mL of water, $AgClO_4$ (1 mmol, 0.207 g) in 5 mL of water added dropwise. The resulting solution was refluxed for 24 hours to generate this complex (**2**). After filtering AgCl precipitate, slow evaporation was performed to get precipitate from resulting filtrate. A yellowish colored complex was obtained after 3-4 days. X-ray quality Crystals were obtained by recrystallization from acetone/water mixture (1:1). Yield: 75 %. IR (KBr, cm^{-1}) 3540 (m) (OH); 3245 (w), 3112 (w) (Aromatic-CH); 3048 (w), 2972 (w) (aliphatic CH); 1635 (s) (C=O); 1600 (s) (C=N); 1444 (m) (C=C); 1094 (s) (ClO_4^-). ^{1}H-NMR [400MHz, CD_3CN, 300K] δ/ppm = 5.322 [d, 2H (CH_2)]; 5.654 [d, 2H (CH_2)]; 6.052 [s, 2H (H_2O)]; 6.991 [d, 2H (aryl)]; 7.289 [m, 2H (aryl)]; 7.390 [d, 2H (aryl)]; 7.579 [d, 2H (aryl)]; 8.026 [d, 2H (aryl)]; 8.100 [d, 1H (aryl)]; 8.260 [d, 1H (aryl)]; 8.537 [d, 2H (aryl)]; 8.706 [d, 1H (aryl)]; 9.169 [d, 1H (aryl)]. ESI pos. in MeOH: m/z = 470.1027 for $[[Co^{III}(^{C=O}L'1)(H_2O) - H^+]^+$

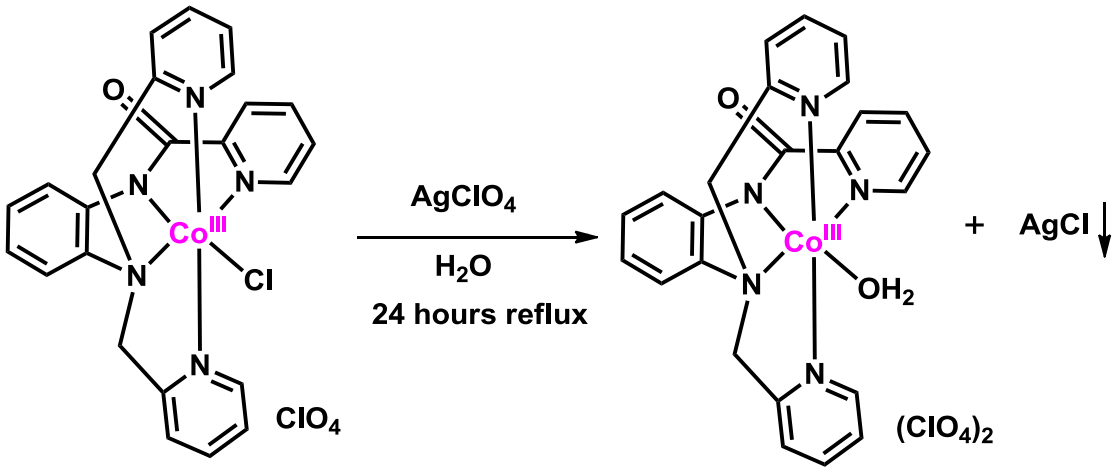

Figure AI.25. Synthetic scheme for the pyridine-rich water coordinated Co^{III} complex (**5**).

www.manaraa.com

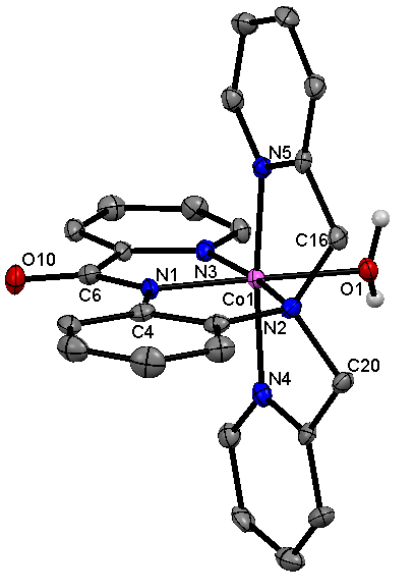

Figure AI.26. The ortep representation of complex **5** with 50% ellipsoidal probability.

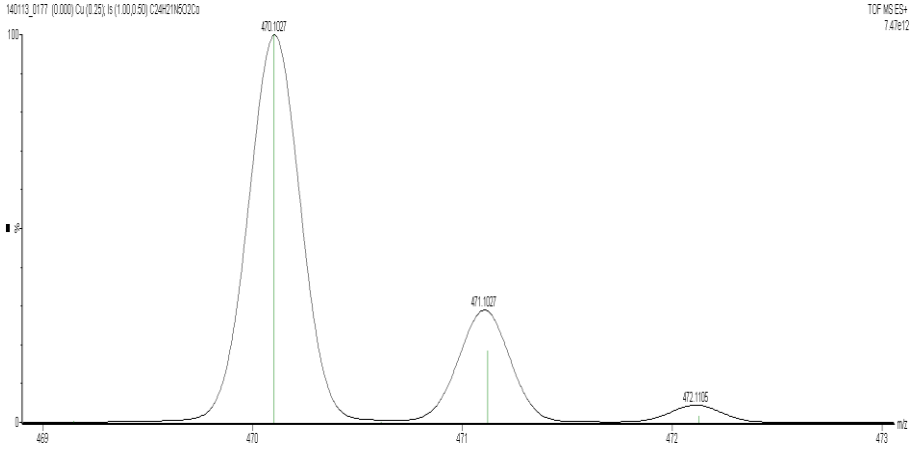

Figure AI.27. Experimental (bars) and simulated (line) isotopic distribution for the molecular ion ($[[Co^{III}(^{C=O}L'1)(H_2O) - H^+]^+$) of the complex **5** in CH_3OH.

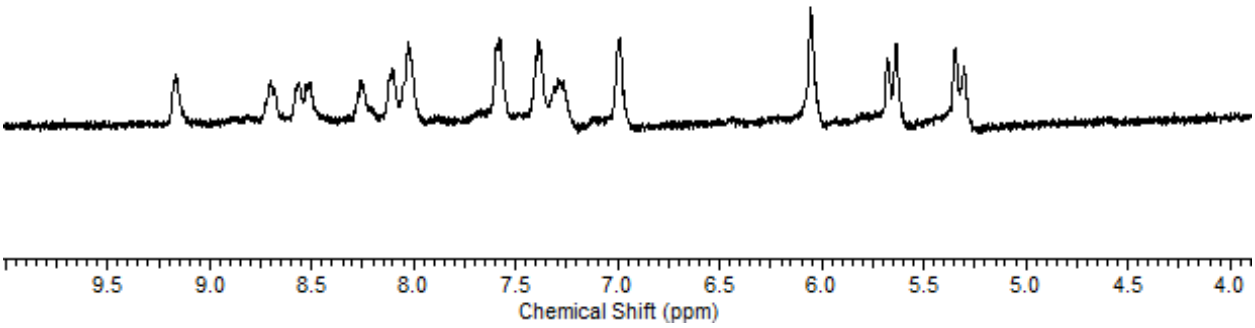

Figure AI.28. ^{1}H-NMR spectra for **5** in CD_3CN.

www.manaraa.com

Appendix-II

Crystal Structures

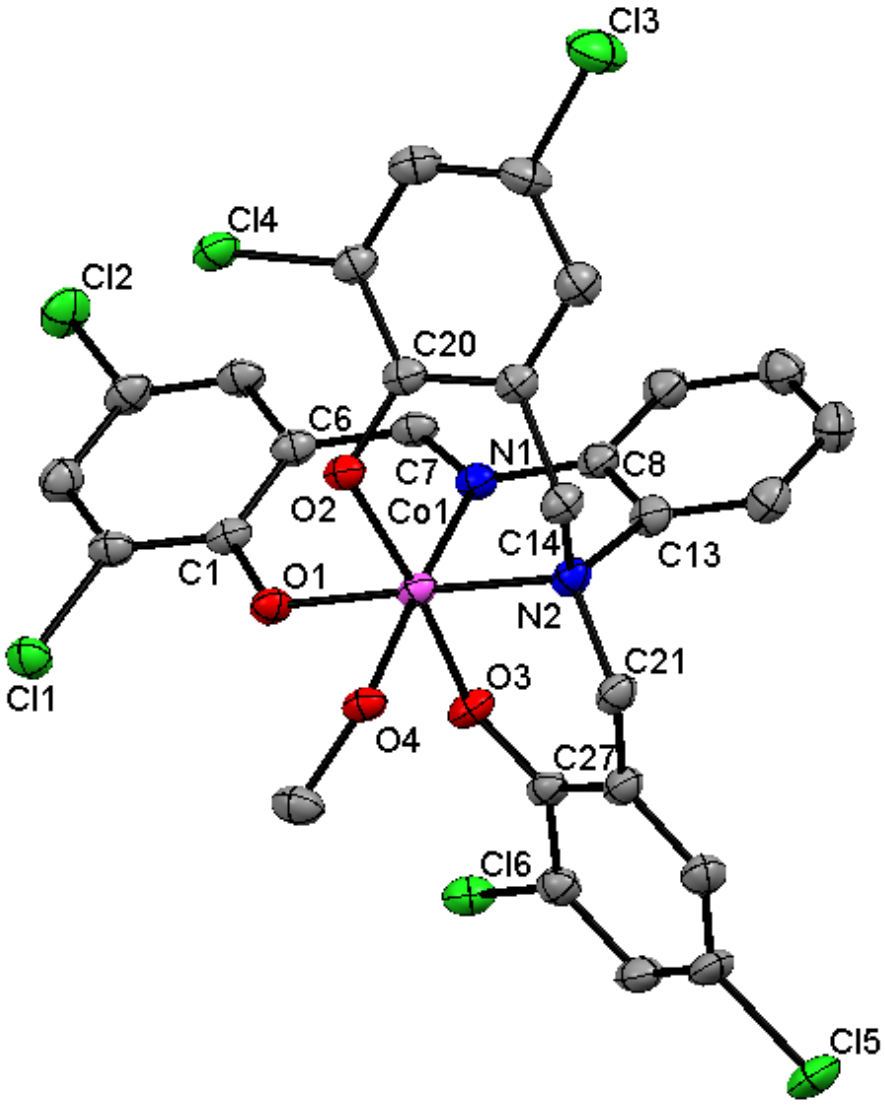

Figure AII.1. X-ray crystal structure of [$Co^{III}(L^{Cl})$MeOH] (from **chapter 3**).

www.manaraa.com

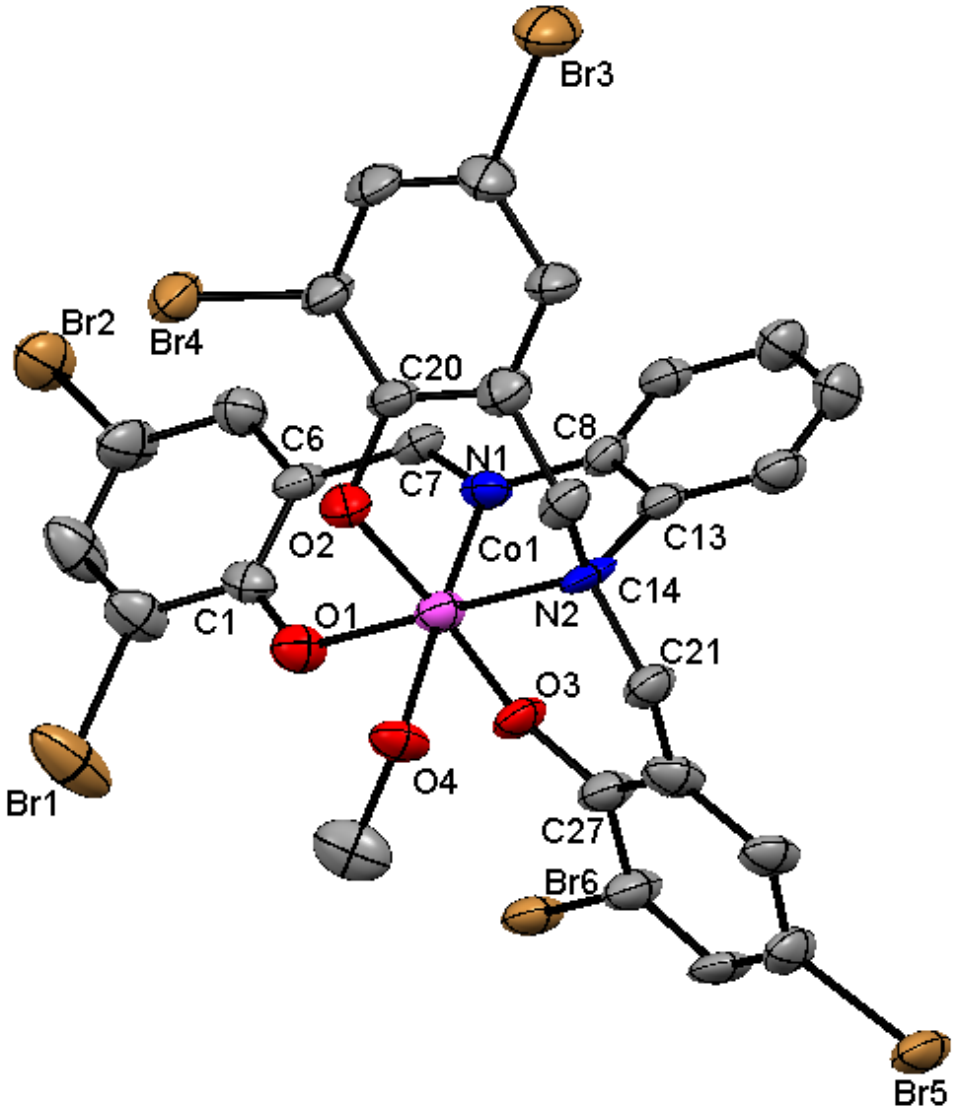

Figure AII.2. X-ray crystal structure of [$Co^{III}(L^{Cl})$MeOH] (from **chapter 3**).

www.manaraa.com

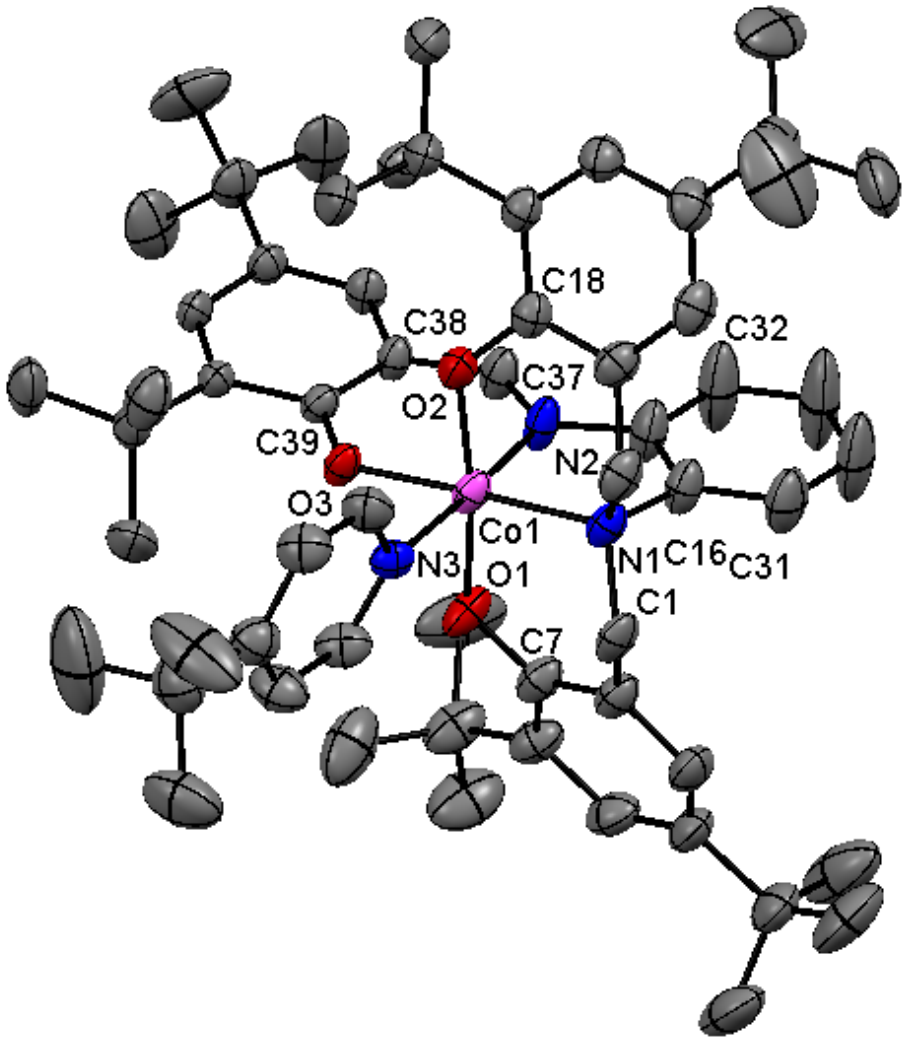

Figure AII.3. X-ray crystal structure of [$Co^{III}(L^{t\text{-}Bu}$)4-t-bu-pyridine] (from **chapter 3**).

www.manaraa.com

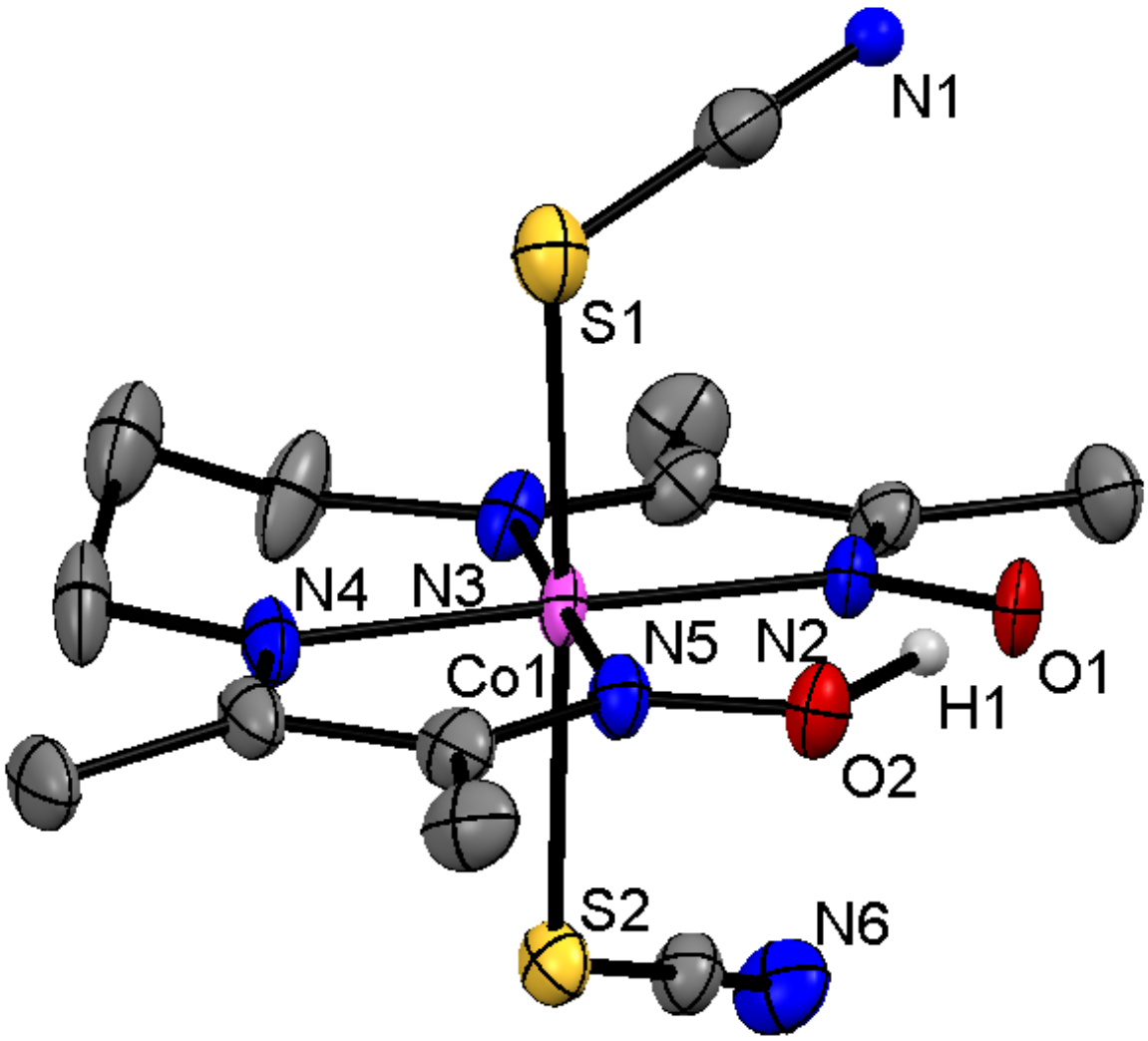

Figure AII.4. X-ray crystal structure of $[Co^{III}(HL^{oxime})(SCN)_2]$ (from **chapter 4**).

www.manaraa.com

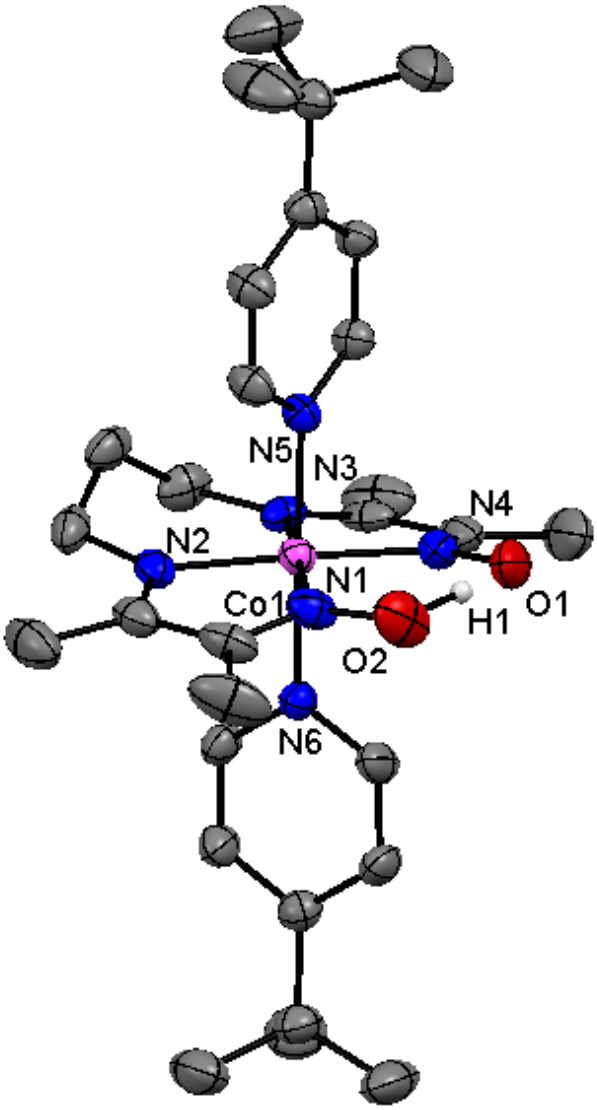

Figure AII.5. X-ray crystal structure of $[Co^{III}(HL^{oxime})(^{4\text{-}tBu}py)_2](PF_6)_2$ (from **chapter 4**).

www.manaraa.com

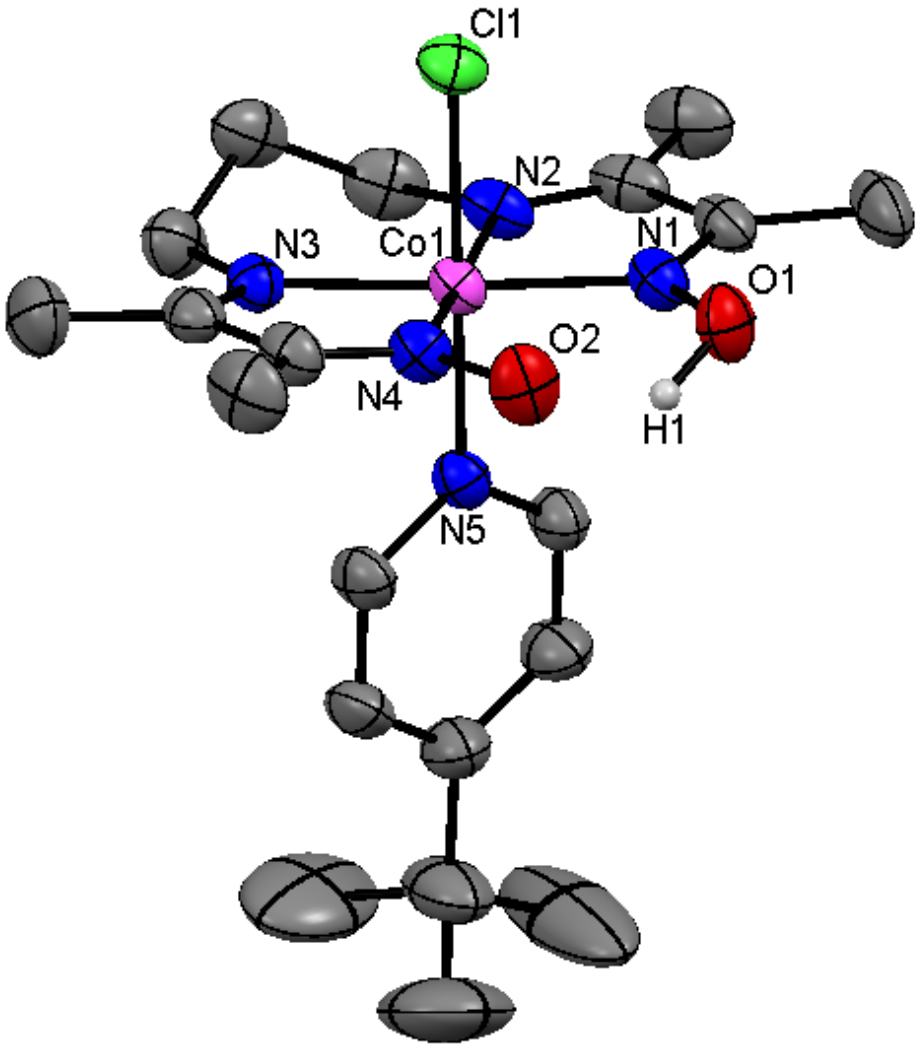

Figure AII.6. X-ray crystal structure of $[Co^{III}(^{4\text{-}tBu}py)(HL^{oxime})(Cl)]PF_6$ (from **chapter 4**).

www.manaraa.com

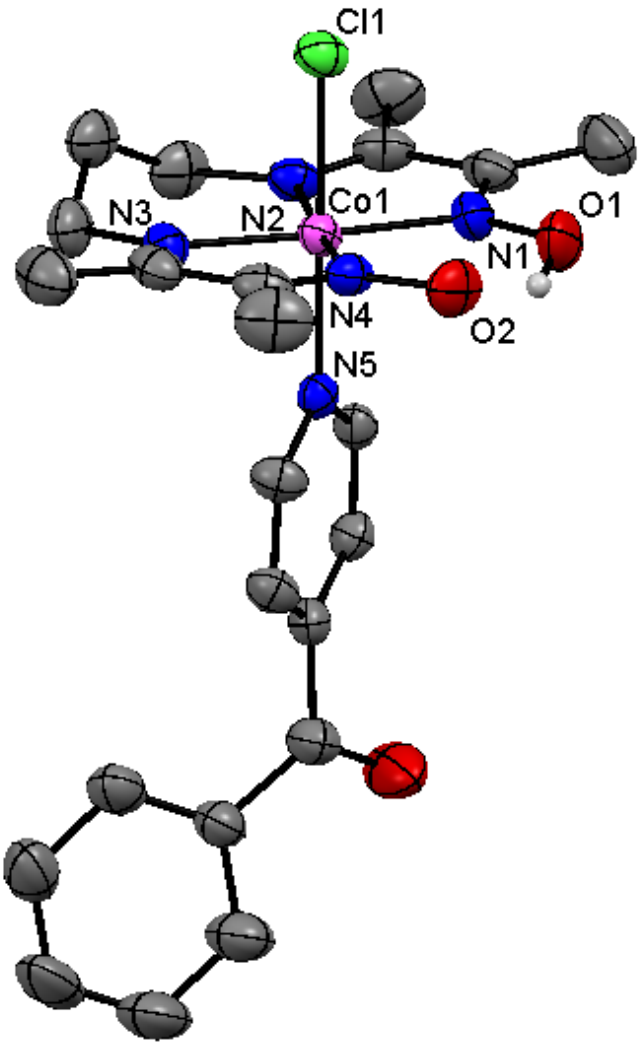

Figure AII.7. X-ray crystal structure of $[Co^{III}(^{4\text{-}Pyr}py)(HL^{oxime})(Cl)]PF_6$ (from **chapter 4**).

www.manaraa.com

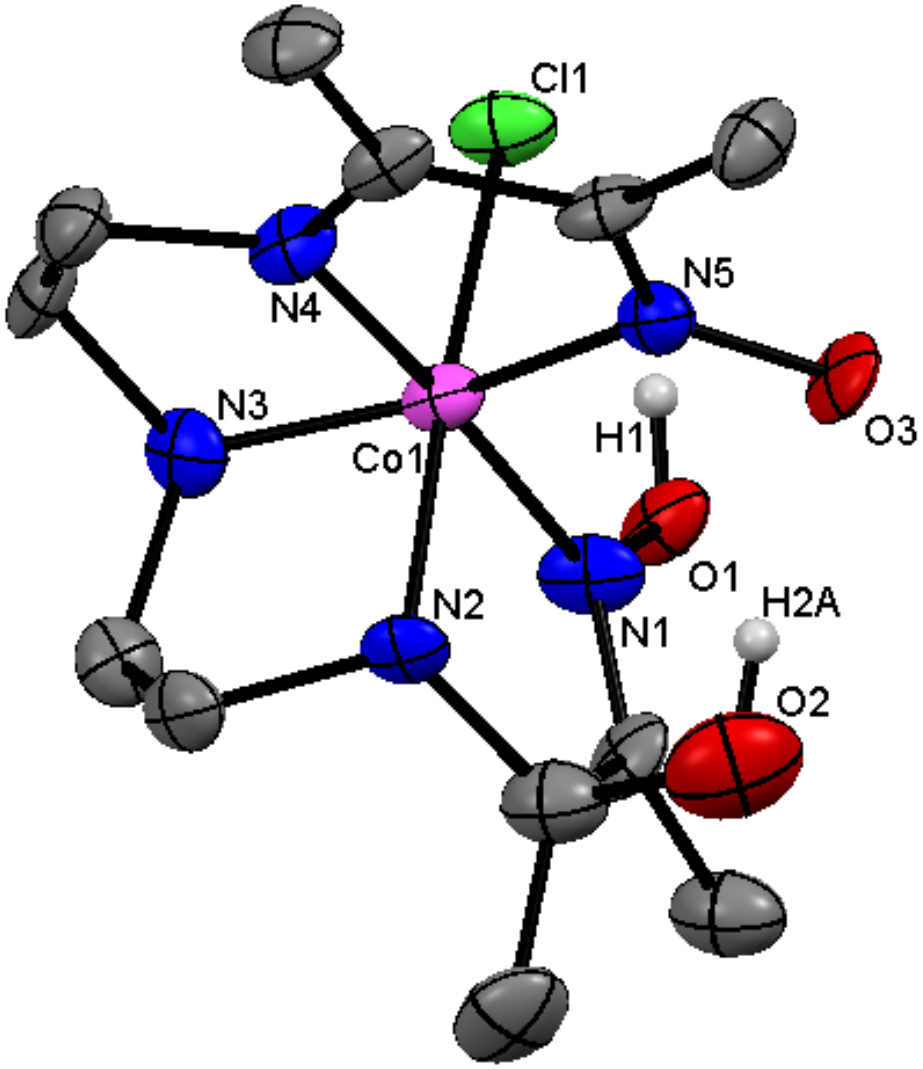

Figure AII.8. X-ray crystal structure of $[Co^{III}(^{H_2O}HL^{oxime})(Cl)]PF_6$ (from **chapter 5**).

www.manaraa.com

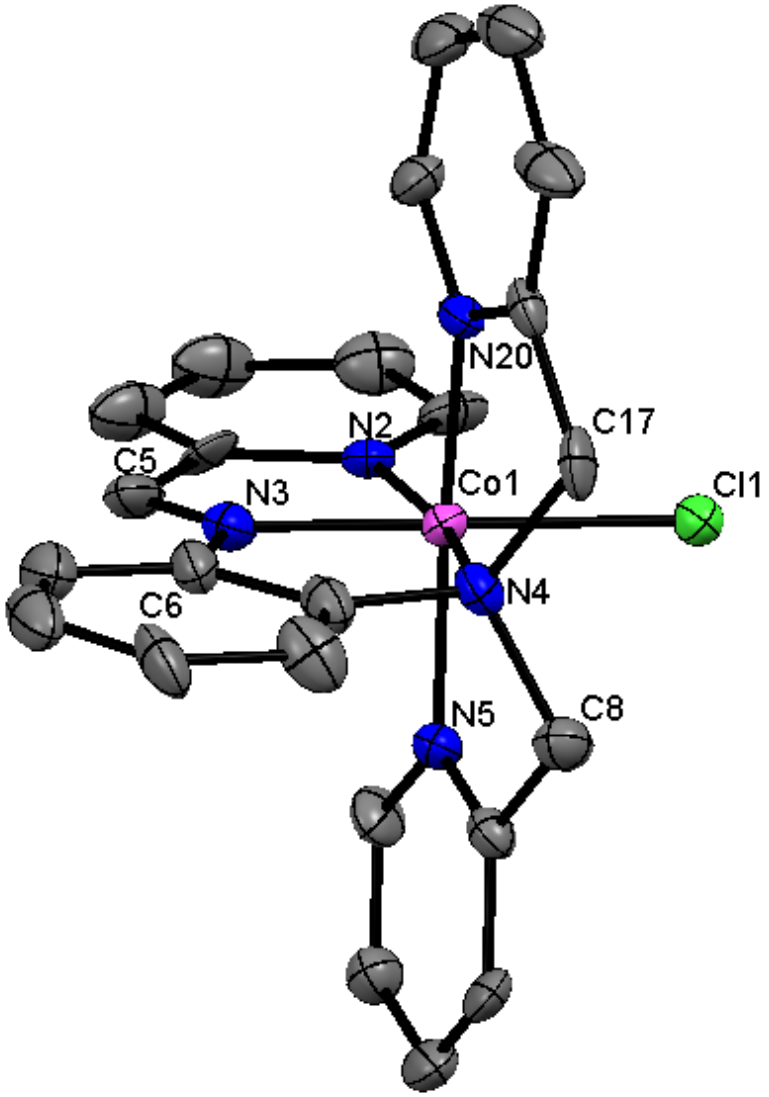

Figure AII.9. X-ray crystal structure of $[Co^{III}(^{imine}L^{1})(Cl)](ClO_4)_2$ (from **chapter 6**).

www.manaraa.com

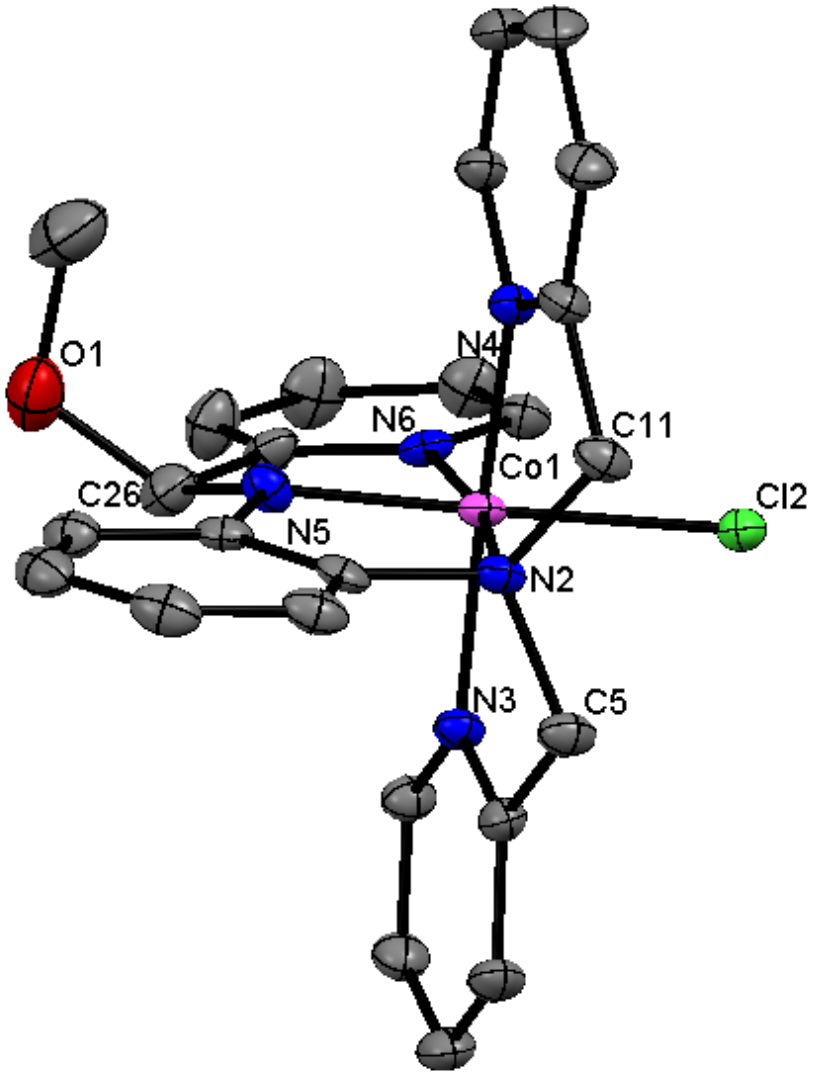

Figure AII.10. X-ray crystal structure of $[Co^{III}(^{OMe}L^{1})(Cl)]ClO_4$ (from **chapter 6**).

www.manaraa.com

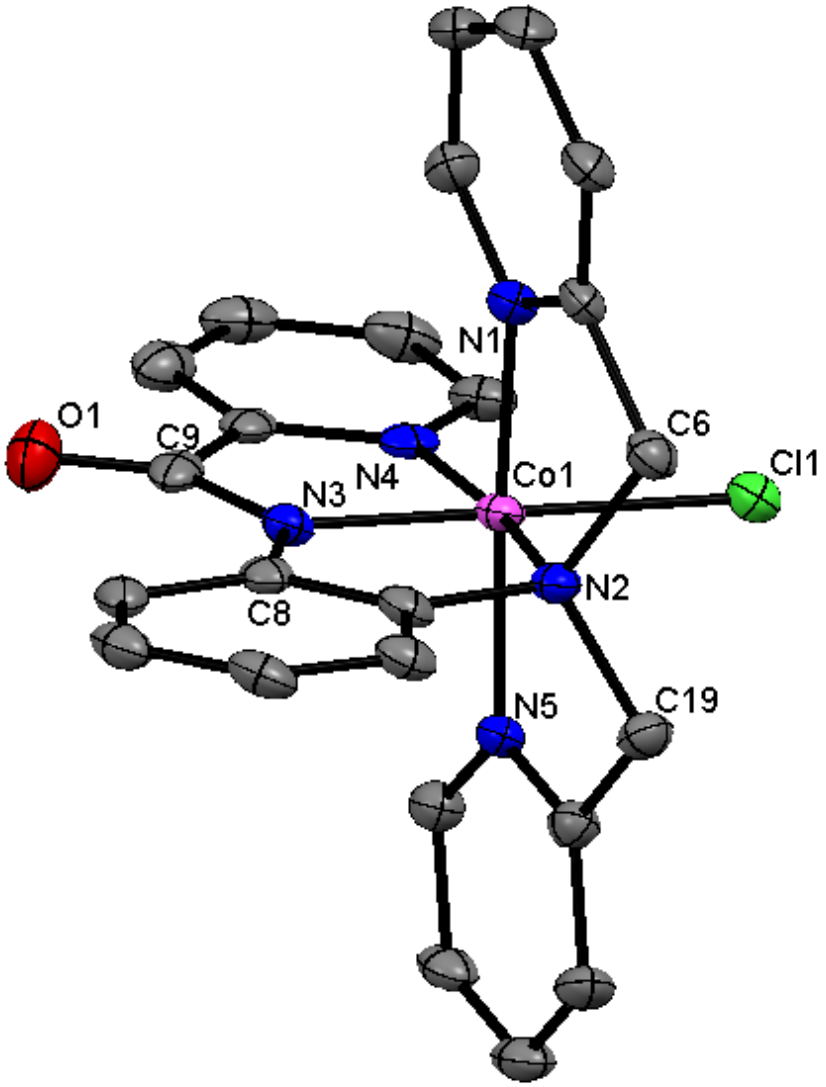

Figure AII.11. X-ray crystal structure of $[Co^{III}(^{amide}L^{1})(Cl)]ClO_4$ (from **chapter 6**).

www.manaraa.com

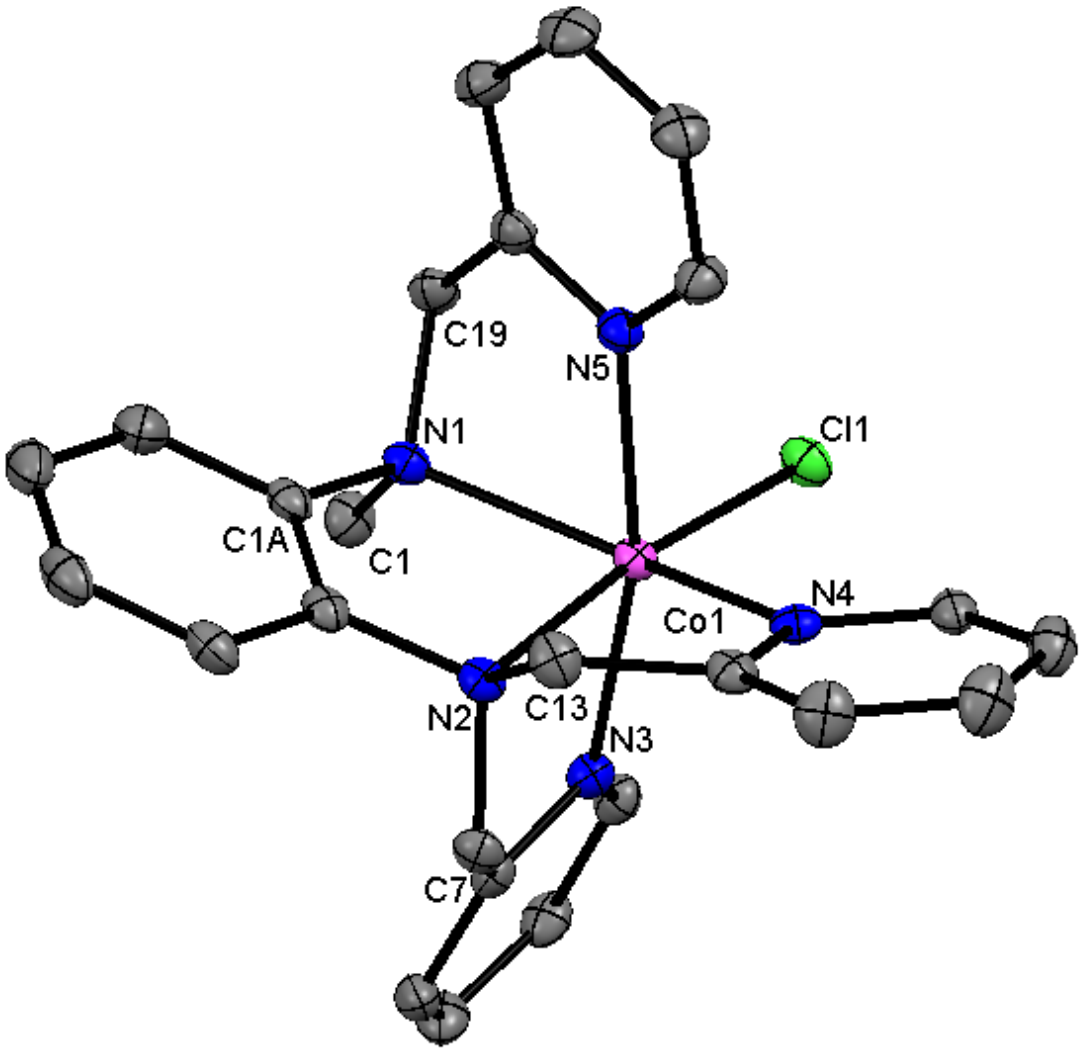

Figure AII.12. X-ray crystal structure of $[Co^{II}(MeL^{2})(Cl)]ClO_4$ (from **chapter 6**).

www.manaraa.com

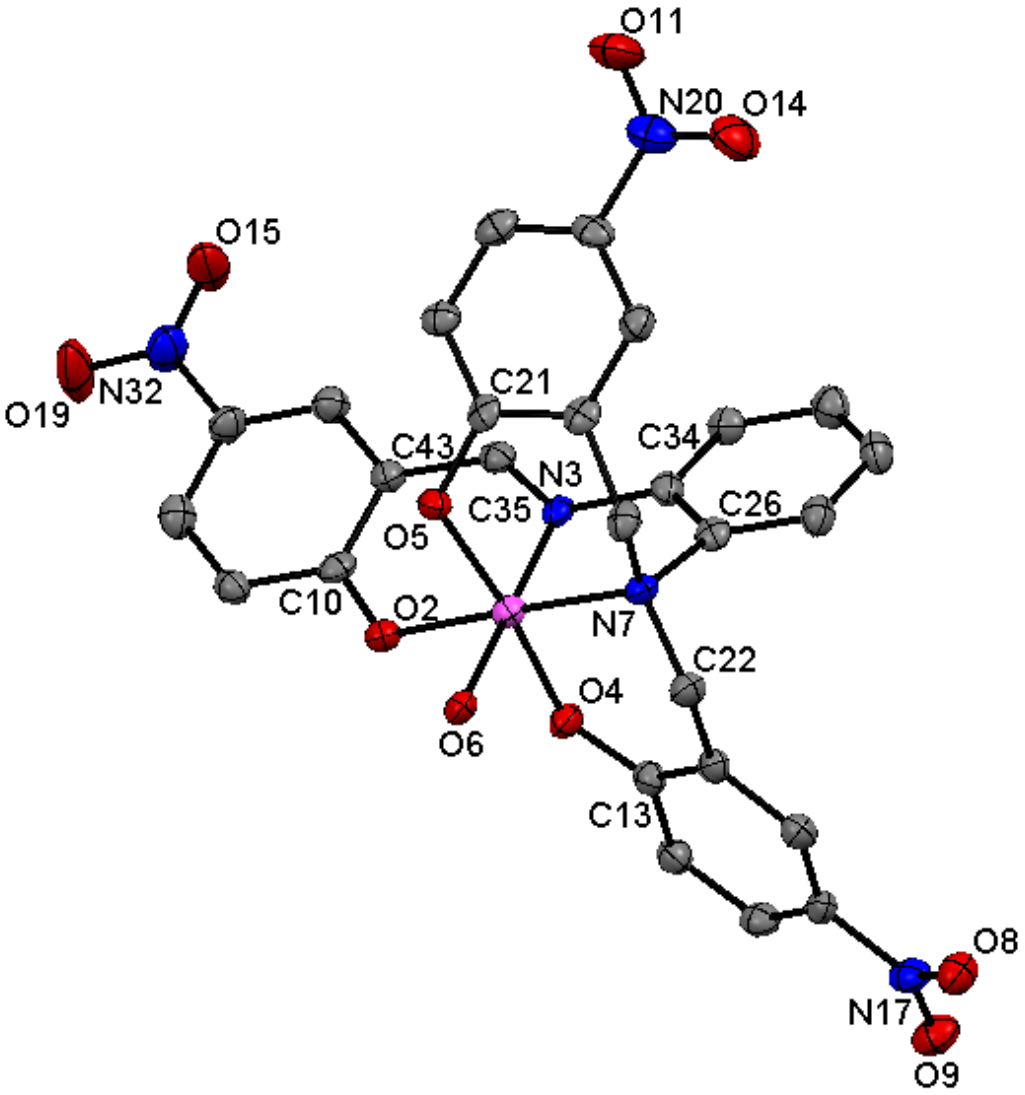

Figure AII.13. X-ray crystal structure of $[Co^{III}(L^{4\text{-}NO_2})H_2O]$ (from **appendix I**).

www.manaraa.com

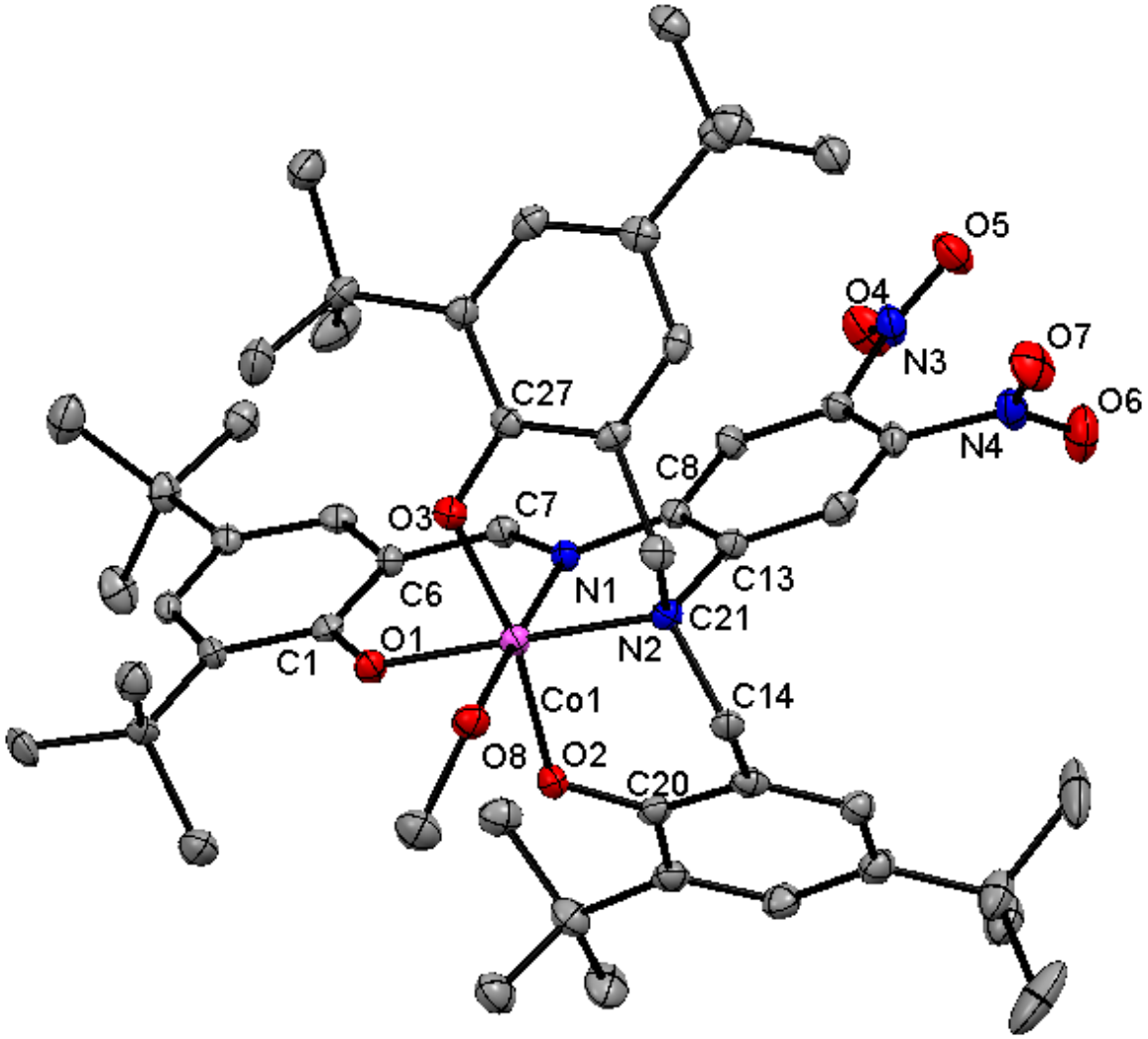

Figure AII.14. X-ray crystal structure of [$Co^{III}((NO_2)_2(L^{2,4\text{-t-bu}}))$MeOH] (from **appendix I**).

www.manaraa.com

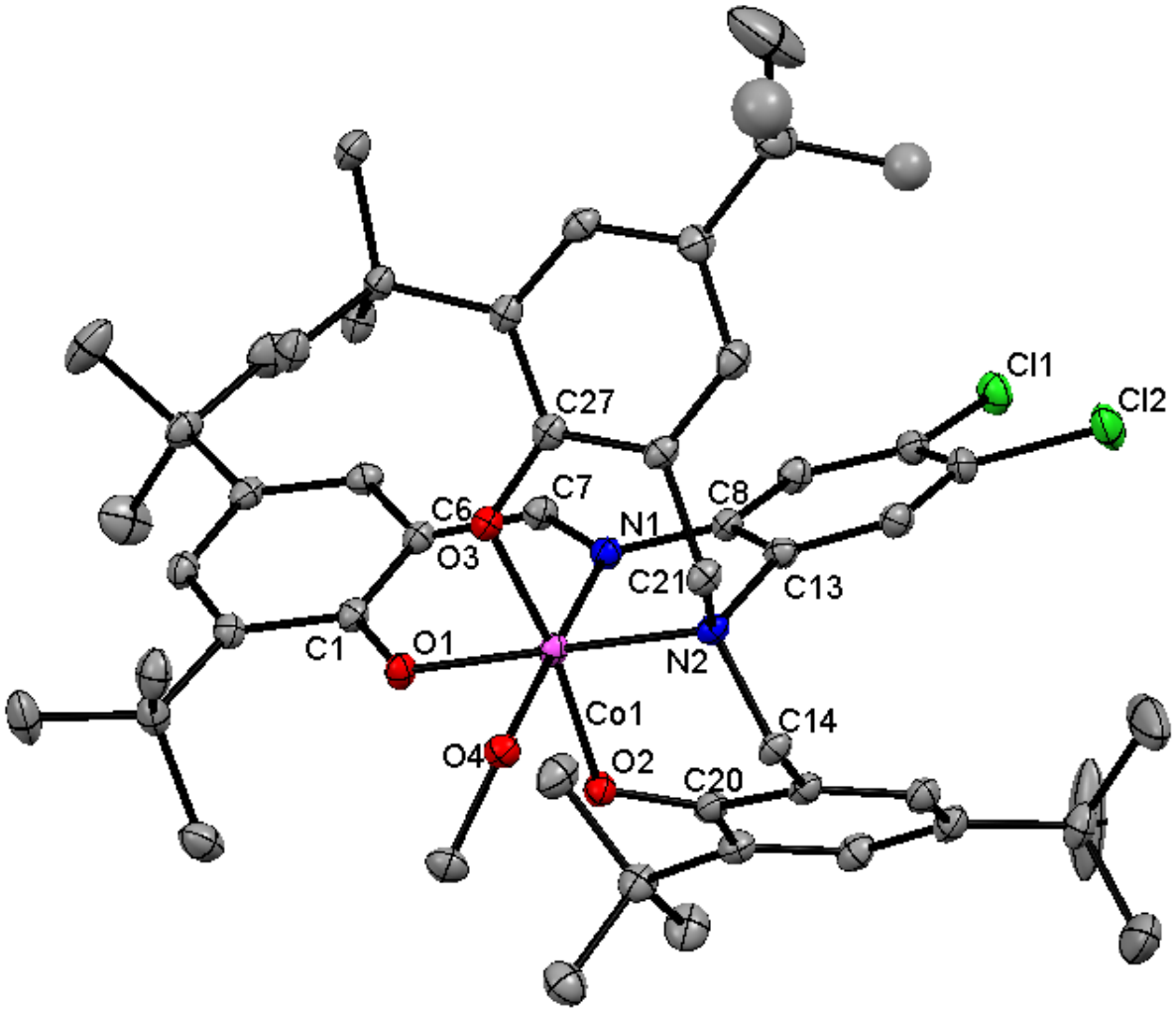

Figure AII.15. X-ray crystal structure of [$Co^{III}(Cl_2L^{2,4\text{-t-bu}})$MeOH] (from **appendix I**).

www.manaraa.com

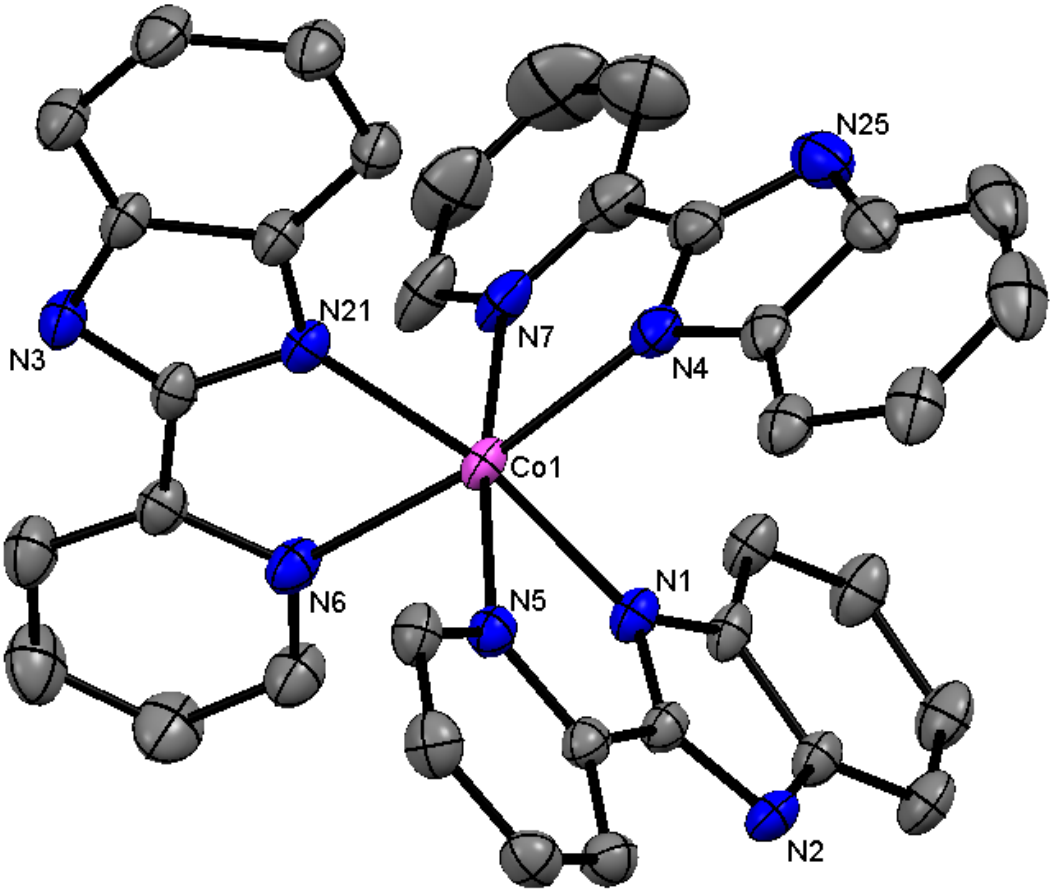

Figure AII.16. X-ray crystal structure of rearranged Co^{II} complex (from **appendix I**).

www.manaraa.com

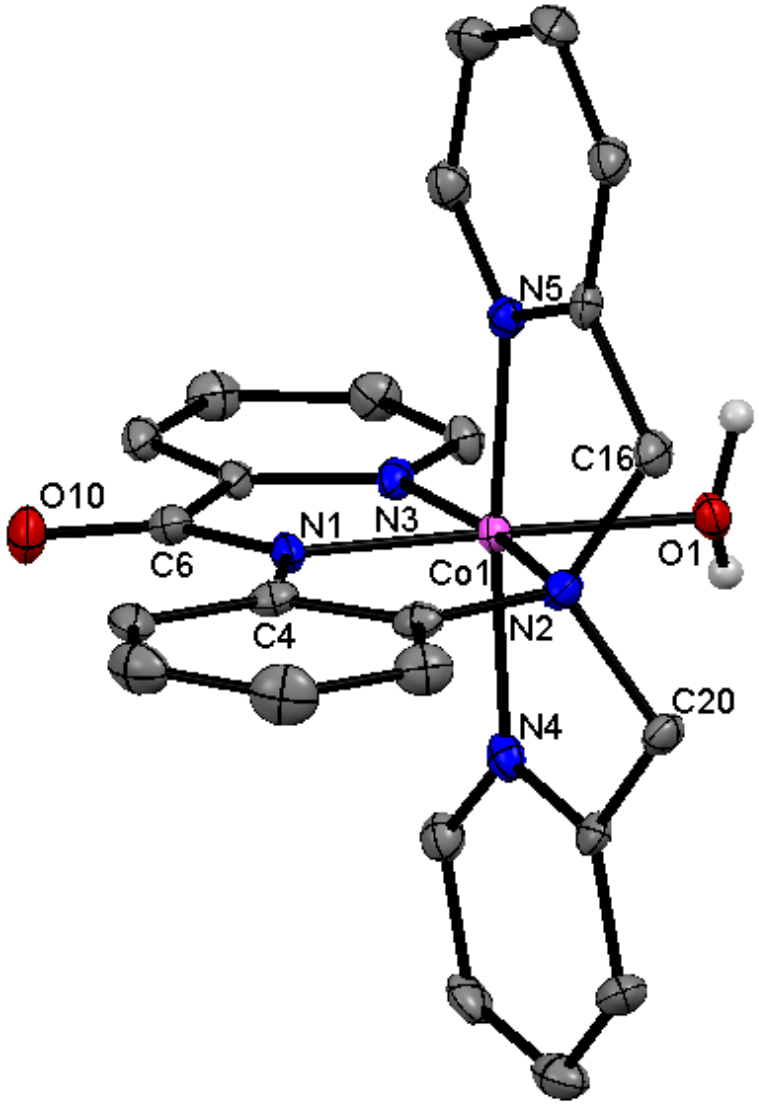

Figure AII.17. X-ray crystal structure of $[Co^{III}(^{amide}L^{1})(H_2O)](ClO_4)_2$ (from **appendix I**).

www.manaraa.com

Appendix-III

Permission/License Agreements for copyrighted Material

Basu, D.; Allard, M. M.; Xavier, F. R.; Heeg, M. J.; Schlegel, H. B.; Verani, C. N.* "Modulation of Electronic and Redox Properties in Phenolate-rich Cobalt(III) Complexes and their Implications for Catalytic Proton Reduction" Dalton Transactions **2015**, *44*, 3454 – Reproduced by permission of The Royal Society of Chemistry (Chapter **2** and **3**).

www.manaraa.com

Chapter 2 and **6** has been reproduced from **Basu, D.**; Mazumder, S.; Shi, X.; Baydoun, H.; Niklas, J.; Poluektov, O.; Schlegel, H. B.*; Verani, C. N.* "Ligand Transformations and Efficient Proton/Water Reduction with Cobalt Catalysts based on Pentadentate Pyridine-rich Environments" Angewandte Chemie International Edition **2015**, *54*, 2105. Here is the license agreement.

JOHN WILEY AND SONS LICENSE
TERMS AND CONDITIONS

Feb 19, 2015

This Agreement between Debashis Basu ("You") and John Wiley and Sons ("John Wiley and Sons") consists of your license details and the terms and conditions provided by John Wiley and Sons and Copyright Clearance Center.

License Number	3572550625818
License date	Feb 19, 2015
Licensed Content Publisher	John Wiley and Sons
Licensed Content Publication	Angewandte Chemie International Edition
Licensed Content Title	Ligand Transformations and Efficient Proton/Water Reduction with Cobalt Catalysts Based on Pentadentate Pyridine Rich Environments
Licensed Content Author	Debashis Basu, Shivnath Mazumder, Xuetao Shi, Habib Baydoun, Jens Niklas, Oleg Poluektov, H. Bernhard Schlegel, Cláudio N. Verani
Licensed Content Date	Dec 22, 2014
Pages	6
Type of use	Dissertation/Thesis
Requestor type	Author of this Wiley article
Format	Print and electronic
Portion	Full article
Will you be translating?	No
Title of your thesis / Dissertation	INVESTIGATION OF NEW LIGAND ARCHITECHTURES TOWARDS PROTON AND WATER REDUCTION CATALYSIS BY COBALT COMPLEXES
Expected completion date	May 2015
Expected size (number of pages)	350
Requestor Location	Debashis Basu 5101 Cass Avenue Department of Chemistry Wayne State University DETROIT, MI 48202

www.manaraa.com

	United States Attn: Debashis Basu
Billing Type	Invoice
Billing Address	Debashis Basu 5101 Cass Avenue Department of Chemistry Wayne State University DETROIT, MI 48202 United States Attn: Debashis Basu
Total	0.00 USD

Terms and Conditions

TERMS AND CONDITIONS

This copyrighted material is owned by or exclusively licensed to John Wiley & Sons, Inc. or one of its group companies (each a"Wiley Company") or handled on behalf of a society with which a Wiley Company has exclusive publishing rights in relation to a particular work (collectively "WILEY"). By clicking □accept□ in connection with completing this licensing transaction, you agree that the following terms and conditions apply to this transaction (along with the billing and payment terms and conditions established by the Copyright Clearance Center Inc., ("CCC's Billing and Payment terms and conditions"), at the time that you opened your Rightslink account (these are available at any time at http://myaccount.copyright.com).

Terms and Conditions

1. The materials you have requested permission to reproduce or reuse (the "Wiley Materials") are protected by copyright.

2. You are hereby granted a personal, nonexclusive, nonsublicensable (on a standalone basis), nontransferable, worldwide, limited license to reproduce the Wiley Materials for the purpose specified in the licensing process. This license is for a onetime use only and limited to any maximum distribution number specified in the license. The first instance of republication or reuse granted by this licence must be completed within two years of the date of the grant of this licence (although copies prepared before the end date may be distributed thereafter). The Wiley Materials shall not be used in any other manner or for any other purpose, beyond what is granted in the license. Permission is granted subject to an appropriate acknowledgement given to the author, title of the material/book/journal and the publisher. You shall also duplicate the copyright notice that appears in the Wiley publication in your use of the Wiley Material. Permission is also granted on the understanding that nowhere in the text is a previously published source acknowledged for all or part of this Wiley Material. Any third party content is expressly excluded from this permission.

3. With respect to the Wiley Materials, all rights are reserved. Except as expressly granted by the terms of the license, no part of the Wiley Materials may be copied, modified,

www.manaraa.com

adapted (except for minor reformatting required by the new Publication), translated, reproduced, transferred or distributed, in any form or by any means, and no derivative works may be made based on the Wiley Materials without the prior permission of the respective copyright owner. You may not alter, remove or suppress in any manner any copyright, trademark or other notices displayed by the Wiley Materials. You may not license, rent, sell, loan, lease, pledge, offer as security, transfer or assign the Wiley Materials on a standalone basis, or any of the rights granted to you hereunder to any other person.

4. The Wiley Materials and all of the intellectual property rights therein shall at all times remain the exclusive property of John Wiley & Sons Inc, the Wiley Companies, or their respective licensors, and your interest therein is only that of having possession of and the right to reproduce the Wiley Materials pursuant to Section 2 herein during the continuance of this Agreement. You agree that you own no right, title or interest in or to the Wiley Materials or any of the intellectual property rights therein. You shall have no rights hereunder other than the license as provided for above in Section 2. No right, license or interest to any trademark, trade name, service mark or other branding ("Marks") of WILEY or its licensors is granted hereunder, and you agree that you shall not assert any such right, license or interest with respect thereto.

5. NEITHER WILEY NOR ITS LICENSORS MAKES ANY WARRANTY OR REPRESENTATION OF ANY KIND TO YOU OR ANY THIRD PARTY, EXPRESS, IMPLIED OR STATUTORY, WITH RESPECT TO THE MATERIALS OR THE ACCURACY OF ANY INFORMATION CONTAINED IN THE MATERIALS, INCLUDING, WITHOUT LIMITATION, ANY IMPLIED WARRANTY OF MERCHANTABILITY, ACCURACY, SATISFACTORY QUALITY, FITNESS FOR A PARTICULAR PURPOSE, USABILITY, INTEGRATION OR NONINFRINGEMENT AND ALL SUCH WARRANTIES ARE HEREBY EXCLUDED BY WILEY AND ITS LICENSORS AND WAIVED BY YOU

6. WILEY shall have the right to terminate this Agreement immediately upon breach of this Agreement by you.

7. You shall indemnify, defend and hold harmless WILEY, its Licensors and their respective directors, officers, agents and employees, from and against any actual or threatened claims, demands, causes of action or proceedings arising from any breach of this Agreement by you.

8. IN NO EVENT SHALL WILEY OR ITS LICENSORS BE LIABLE TO YOU OR ANY OTHER PARTY OR ANY OTHER PERSON OR ENTITY FOR ANY SPECIAL, CONSEQUENTIAL, INCIDENTAL, INDIRECT, EXEMPLARY OR PUNITIVE DAMAGES, HOWEVER CAUSED, ARISING OUT OF OR IN CONNECTION WITH THE DOWNLOADING, PROVISIONING, VIEWING OR USE OF THE MATERIALS REGARDLESS OF THE FORM OF ACTION, WHETHER FOR BREACH OF CONTRACT, BREACH OF WARRANTY, TORT, NEGLIGENCE, INFRINGEMENT OR OTHERWISE (INCLUDING, WITHOUT LIMITATION, DAMAGES BASED ON

www.manaraa.com

LOSS OF PROFITS, DATA, FILES, USE, BUSINESS OPPORTUNITY OR CLAIMS OF THIRD PARTIES), AND WHETHER OR NOT THE PARTY HAS BEEN ADVISED OF THE POSSIBILITY OF SUCH DAMAGES. THIS LIMITATION SHALL APPLY NOTWITHSTANDING ANY FAILURE OF ESSENTIAL PURPOSE OF ANY LIMITED REMEDY PROVIDED HEREIN.

9. Should any provision of this Agreement be held by a court of competent jurisdiction to be illegal, invalid, or unenforceable, that provision shall be deemed amended to achieve as nearly as possible the same economic effect as the original provision, and the legality, validity and enforceability of the remaining provisions of this Agreement shall not be affected or impaired thereby.

10. The failure of either party to enforce any term or condition of this Agreement shall not constitute a waiver of either party's right to enforce each and every term and condition of this Agreement. No breach under this agreement shall be deemed waived or excused by either party unless such waiver or consent is in writing signed by the party granting such waiver or consent. The waiver by or consent of a party to a breach of any provision of this Agreement shall not operate or be construed as a waiver of or consent to any other or subsequent breach by such other party.

11. This Agreement may not be assigned (including by operation of law or otherwise) by you without WILEY's prior written consent.

12. Any fee required for this permission shall be nonrefundable after thirty (30) days from receipt by the CCC.

13. These terms and conditions together with CCC□s Billing and Payment terms and conditions (which are incorporated herein) form the entire agreement between you and WILEY concerning this licensing transaction and (in the absence of fraud) supersedes all prior agreements and representations of the parties, oral or written. This Agreement may not be amended except in writing signed by both parties. This Agreement shall be binding upon and inure to the benefit of the parties' successors, legal representatives, and authorized assigns.

14. In the event of any conflict between your obligations established by these terms and conditions and those established by CCC□s Billing and Payment terms and conditions, these terms and conditions shall prevail.

15. WILEY expressly reserves all rights not specifically granted in the combination of (i) the license details provided by you and accepted in the course of this licensing transaction, (ii) these terms and conditions and (iii) CCC□s Billing and Payment terms and conditions.

16. This Agreement will be void if the Type of Use, Format, Circulation, or Requestor Type was misrepresented during the licensing process.

www.manaraa.com

17. This Agreement shall be governed by and construed in accordance with the laws of the State of New York, USA, without regards to such state□s conflict of law rules. Any legal action, suit or proceeding arising out of or relating to these Terms and Conditions or the breach thereof shall be instituted in a court of competent jurisdiction in New York County in the State of New York in the United States of America and each party hereby consents and submits to the personal jurisdiction of such court, waives any objection to venue in such court and consents to service of process by registered or certified mail, return receipt requested, at the last known address of such party.

WILEY OPEN ACCESS TERMS AND CONDITIONS

Wiley Publishes Open Access Articles in fully Open Access Journals and in Subscription journals offering Online Open. Although most of the fully Open Access journals publish open access articles under the terms of the Creative Commons Attribution (CC BY) License only, the subscription journals and a few of the Open Access Journals offer a choice of Creative Commons Licenses:: Creative Commons Attribution (CCBY) license Creative Commons Attribution NonCommercial (CCBYNC) license and Creative Commons Attribution NonCommercialNoDerivs (CCBYNCND) License. The license type is clearly identified on the article.

Copyright in any research article in a journal published as Open Access under a Creative Commons License is retained by the author(s). Authors grant Wiley a license to publish the article and identify itself as the original publisher. Authors also grant any third party the right to use the article freely as long as its integrity is maintained and its original authors, citation details and publisher are identified as follows: [Title of Article/Author/Journal Title and Volume/Issue. Copyright (c) [year] [copyright owner as specified in the Journal]. Links to the final article on Wiley□s website are encouraged where applicable.

The Creative Commons Attribution License

The Creative Commons Attribution License (CCBY) allows users to copy, distribute and transmit an article, adapt the article and make commercial use of the article. The CCBY license permits commercial and noncommercial reuse of an open access article, as long as the author is properly attributed.

The Creative Commons Attribution License does not affect the moral rights of authors, including without limitation the right not to have their work subjected to derogatory treatment. It also does not affect any other rights held by authors or third parties in the article, including without limitation the rights of privacy and publicity. Use of the article must not assert or imply, whether implicitly or explicitly, any connection with, endorsement or sponsorship of such use by the author, publisher or any other party associated with the article.

For any reuse or distribution, users must include the copyright notice and make clear to others that the article is made available under a Creative Commons Attribution license, linking to the relevant Creative Commons web page.

www.manaraa.com

To the fullest extent permitted by applicable law, the article is made available as is and without representation or warranties of any kind whether express, implied, statutory or otherwise and including, without limitation, warranties of title, merchantability, fitness for a particular purpose, noninfringement, absence of defects, accuracy, or the presence or absence of errors.

Creative Commons Attribution NonCommercial License

The Creative Commons Attribution NonCommercial (CCBYNC) License permits use, distribution and reproduction in any medium, provided the original work is properly cited and is not used for commercial purposes.(see below)

Creative Commons AttributionNonCommercial-NoDerivs License

The Creative Commons Attribution NonCommercialNoDerivs License (CCBYNCND) permits use, distribution and reproduction in any medium, provided the original work is properly cited, is not used for commercial purposes and no modifications or adaptations are made. (see below)

Use by noncommercial users

For noncommercial and nonpromotional purposes, individual users may access, download, copy, display and redistribute to colleagues Wiley Open Access articles, as well as adapt, translate, text and datamine the content subject to the following conditions:

1. The authors' moral rights are not compromised. These rights include the right of "paternity" (also known as "attribution" the right for the author to be identified as such) and "integrity" (the right for the author not to have the work altered in such away that the author's reputation or integrity may be impugned).

2. Where content in the article is identified as belonging to a third party, it is the obligation of the user to ensure that any reuse complies with the copyright policies of the owner of that content.

3. If article content is copied, downloaded or otherwise reused for noncommercial research and education purposes, a link to the appropriate bibliographic citation (authors, journal, article title, volume, issue, page numbers, DOI and the link to the definitive published version on **Wiley Online Library**) should be maintained. Copyright notices and disclaimers must not be deleted.

4. Any translations, for which a prior translation agreement with Wiley has not been agreed, must prominently display the statement: "This is an unofficial translation of an article that appeared in a Wiley publication. The publisher has not endorsed this translation."

Use by commercial "forprofit" organisations

Use of Wiley Open Access articles for commercial, promotional, or marketing purposes requires further explicit permission from Wiley and will be subject to a fee. Commercial purposes

www.manaraa.com

include:

1. Copying or downloading of articles, or linking to such articles for further redistribution, sale or licensing;

2. Copying, downloading or posting by a site or service that incorporates advertising with such content;

3. The inclusion or incorporation of article content in other works or services (other than normal quotations with an appropriate citation) that is then available for sale or licensing, for a fee (for example, a compilation produced for marketing purposes, inclusion in a sales pack)

4. Use of article content (other than normal quotations with appropriate citation) by forprofit organisations for promotional purposes

5. Linking to article content in emails redistributed for promotional, marketing or educational purposes;

6. Use for the purposes of monetary reward by means of sale, resale, licence, loan, transfer or other form of commercial exploitation such as marketing products

7. Print reprints of Wiley Open Access articles can be purchased from: corporatesales@wiley.com

Further details can be found on Wiley Online Library
http://olabout.wiley.com/WileyCDA/Section/id410895.html

Other Terms and Conditions:

v1.9

Questions? customercare@copyright.com or +18552393415 (toll free in the US) or +19786462777.

Gratis licenses (referencing $0 in the Total field) are free. Please retain this printable license for your reference. No payment is required.

www.manaraa.com

ABSTRACT

INVESTIGATION OF NEW LIGAND ARCHITECTURES TOWARDS PROTON AND WATER REDUCTION CATALYSIS BY COBALT COMPLEXES

by

DEBASHIS BASU

August 2015

Advisor: Prof. Cláudio N. Verani

Major: Chemistry (Inorganic)

Degree: Doctor of Philosophy

During my PhD training in the Verani group at WSU, I designed several ligand architectures to optimize and understand the redox, electronic, and catalytic properties of their respective cobalt complexes towards proton and water reduction.

A series of π-donor phenolate ligands of the [N_2O_3] type were synthesized upon varying phenolate substituents from electron-withdrawing halogens to -donating t-butyl. The incorporation of cobalt in such ligand systems under aerobic condition generates the Co(III) complexes with the ligand oxidized to imine form from its amine counterpart. The redox, electronic, and electron transfer properties are greatly altered upon varying these substituents. The cobalt complex of chloro-substituted phenolato ligand exhibits catalytic activity in the presence of a weak acid such as acetic acid (HOAc) with an overpotential of 0.61 V, whereas the cobalt complex of t-butyl substituted phenolato ligand shows catalysis with a much higher overpotential of 0.90 V. Bulk electrolysis for the former complex at -1.8 $V_{Ag/AgCl}$ confirms hydrogen generation with a TON of 11 after 3 hours with a Faradaic efficiency of 85 % in the

www.manaraa.com

presence of 100 equivalents of HOAc. This work suggests that electron-withdrawing group may reduce the overpotential needed for proton reduction catalysis. Therefore, we synthesized cobalt(III) complexes of nitro containing phenolate-rich [N_2O_3] ligands. The nitro substituents are incorporated either in the phenylene bridge or in the phenolate arm. The complex containing two nitro groups on the phenylene bridge stabilizes multiple redox species in the reduction side of the electrochemical window, and subsequently greatly reduces the overpotential (0.6 to 0.1 V) for hydrogen generation from a weak acid such as acetic acid.

We also investigated a π-acceptor ligand such as an oxime instead of a π-donor ligand framework to reduce the overpotential for the proton reduction with the corresponding cobalt complexes. Homoaxially and heteroaxially substituted cobalt(III) complexes of such oxime-rich N_4 ligand were synthesized. Extensive characterization of the various redox species by means of CV, and ^{1}H-NMR titrations, EPR, and UV-Visible spectroscopy and DFT calculations reveal the electrochemical equilibria operating for these systems. The Co(I) redox species, the active intermediate for the catalysis is found to be 5-coordinate in nature. Hydrogen generation is observed in the presense of these complexes with a mild-acid such as trifluoroacetic acid (TFA) with an overpotential of 0.35 V, and subsequently confirmed by bulk electrolysis measurements at -1.0 $V_{Ag/AgCl}$ with a TON between 13-20 after 3 hours with a Faradaic efficiency of 85 %. A catalytic mechanism is proposed invoking a heterolytic pathway from Co^{II}-H species. To incorporate a photosensitizer with this catalytic module, a heterobimetallic [$Ru^{II}Co^{III}$] complex based on such an oxime as the bridging ligand was synthesized and characterized. This [RuCo] complex exhibits electrocatalytic activity in the presence of TFA with the overpotential of 0.37 V and TON of 7.0 after one hour at -1.0 $V_{Ag/AgCl}$ with a Faradaic efficiency of 70%. The electron transfer study and the photocatalytic activity of this complex towards hydrogen production are

www.manaraa.com

under investigation in collaboration with Dr. Karen Mulfort in Argon National Lab.

We designed a ligand framework based on a pentadentate oxime due to the 5-coordinate nature of the Co(I) active species towards proton reduction. Therefore, a Co(III) complex of such [$NN'_2N''_2$] ligand was synthesized. This complex incorporates an aqua ligand during the complexation reaction. Proton reduction activity is shown by this complex in the presence of acetic acid with a very low overpotential of 0.24 V and TON of 14.7 after 3 hours at -1.7 $V_{Ag/AgCl}$. A catalytic mechanism is proposed invoking a heterolytic pathway from Co^{II}-H species. This complex is water soluble due to the presence of various polar groups such as -NH and -OH. Water reduction activity is observed with an overpotential of 0.65 V with a TON of 6,000 at -1.7 $V_{Ag/AgCl}$ after 18 hours. The active species for catalysis in water is found to be cobalt-based nanoparticles.

To continue to explore and study complexes capable of performing catalytic water reduction, cobalt complexes of two pentadentate pyridine-rich [$N_2N^{py}_3$] ligands were synthesized. One of the ligands is susceptible towards oxidation upon complexation and forms the corresponding Co^{III}-amide complex. This oxidation is prevented by incorporating a methyl substituent on that particular nitrogen. Both complexes show catalytic proton reduction in the presence of acetic acid with an overpotential around 0.70 V with TON of 15 after three hours at -1.7 $V_{Ag/AgCl}$ with a Faradaic efficiency of 90 % in the presence of 100 equivalents of HOAc *via* a heterolytic pathway from a Co^{II}-H species. These complexes are water soluble and perform water reduction activity with an onset overpotential of 0.55 V (amide), and 0.70 V (amine). Bulk electrolysis at -1.7 $V_{Ag/AgCl}$ confirms the presence of hydrogen with TONs of 7,200 and 6,000 after 18 hours with a Faradaic efficiency around 95 % for amide and amine containing complexes, respectively.

www.manaraa.com

AUTOBIOGRAPHICAL STATEMENT

Debashis Basu

Professional Preparation: Education

Wayne State University, MI (USA), Inorganic Chemistry, Ph. D., 2015
Indian Institute of Technology, Delhi (India), Chemistry, M. Sc., 2008
Jadavpur University, Kolkata (India), Chemistry, B. Sc. (Honors), 2006

Appointments

2011-2015: Graduate Research Assistant, Department of Chemistry, Wayne State University
2009-2011: Graduate Teaching Assistant, Department of Chemistry, Wayne State University
2008-2009: Research Project Associate, Department of Chemical Engineering, IIT Delhi

Publications

1. Basu, D.; Allard, M. M.; Xavier, F. R.; Heeg, M. J.; Schlegel, H. B.; Verani, C. N.* "Modulation of Electronic and Redox Properties in Phenolate-rich Cobalt(III) Complexes and their Implications for Catalytic Proton Reduction" *Dalton Trans.* **2015**, *44*, 3454.
2. Basu, D.; Mazumder, S.; Shi, X.; Baydoun, H.; Niklas, J.; Poluektov, O.; Schlegel, H. B.*; Verani, C. N.* "Ligand Transformations and Efficient Proton/Water Reduction with Cobalt Catalysts based on Pentadentate Pyridine-rich Environments" *Angew. Chem. Int. Ed.* **2015**, *54*, 2105.
3. Basu, D.; Mazumder, S.; Shi, X.; Staples, R.; Schlegel, H. B.*; Verani, C. N.* "Distinct Proton and Water Reduction Behavior with a Cobalt(III) Electrocatalyst Based on Pentadentate Oximes" *Angew. Chem. Int. Ed.* **2015**, *54*, DOI: 10.1002/anie.201501410.
4. Basu, D.; Mazumder, S.; Shi, X.; Wanniarachchi, D.; Niklas, J.; Poluektov, O.; Staples, R.; Schlegel, H. B.*; Verani, C. N.* "Evaluation of the Mechanistic and Catalytic Behavior of Heteroaxial Co^{III}-oximes towards Hydrogen Generation" *Final manuscript under revision by authors* targeting Chemical Science.
5. Basu, D.; Mazumder, S.; Schlegel, H. B.*; Verani, C. N.* "Inference of Mechanisms from Cobalt-based Proton and Water Reduction Catalysts" *Manuscript in preparation* targeting Coordination Chemistry Reviews.

Presentations

1. "Investigation of the Electronic and Catalytic Properties of Monometallic Cobalt(III) and Heterobimetallic [$Ru^{II}Co^{III}$] System towards Proton Reduction." Debashis Basu, Claudio Verani **20th International Symposium on the Photophysics and Photochemistry of Coordination Compounds**, Traverse City, MI, July 7-11, **2013, poster presentation**.
2. "Towards Proton Reduction Catalysis: Redox, Electronic and Catalytic Properties of New Co^{III} Complexes and their [$Ru^{II}Co^{III}$] Analogues." Debashis Basu, Claudio Verani **246th ACS National Meeting**, Indianapolis, IN, September 8-12, **2013**, **oral presentation**.

Skills

Synthesis and characterization, qualitative and quantitative analysis, thin layer and column chromatography, FTIR, NMR, and UV-visible spectroscopy, ESI-MS spectrometry, electro- and spectroelectrochemistry, bulk electrolysis, gas chromatography, computer skills.

www.manaraa.com